

# **Micro- to Nano-Scale Architecture and Aspects of Skeletal Growth in Marine Calcifiers**

Laura Meret Otter

Department of Earth and Planetary Sciences  
Macquarie University

For the degree of Doctor of Philosophy

Principal Supervisor: Prof Dorrit E. Jacob

Co-Supervision: Dr Matthew A. Kosnik

April, 2019



*...dedicated to my parents: Anne & Ron.*

## STATEMENT OF ORIGINALITY

I declare that the work in this thesis entitled “Micro- to Nano-Scale Architecture and Aspects of Skeletal Growth in Marine Calcifiers” has not been previously submitted for a degree to any other university or institution.

Further, I certify that the thesis is an original piece of research and it has been written by me. Any help and assistance that I have received as well as the preparation of the thesis itself have been appropriately referenced and/or acknowledged.

**Laura Meret Otter**

April 12, 2019

# ABSTRACT

Bivalve shells are nano-composite materials consisting of crystalline calcium carbonate phases (i.e. aragonite and calcite) that are intimately arranged with organic constituents into different hierarchical architectures. This explains their enhanced mechanical properties that outperform their monolithic geological counterparts. Shells grow incrementally throughout their lifetime and record environmental conditions in their trace element and isotopic signatures. Our understanding of how shells grow has seen a recent paradigm change away from classical ion-by-ion crystallization models to non-classical crystallization pathways via colloid attachment and transformation of nanogranular amorphous calcium carbonate precursor phases. These findings complicate any paleo-environmental reconstructions and lead to fundamental questions, such as: which impact do the new crystallization pathways have on trace element partitioning? How are these pathways affected by physiological effects on sub-micron growth processes?

These questions are addressed in this thesis by using living shells in controlled aquaculture conditions. Four different bivalve species with different architectural ultrastructures were studied here: *Anadara trapezia* (crossed-lamellar and complex crossed-lamellar architectures), *Katelysia rhytiphora* (compound composite prismatic and crossed-acicular), *Mytilus galloprovincialis* (simple prismatic and nacre) and *Pinctada imbricata fucata* (simple prismatic and nacre). These bivalves were periodically subjected to pulse-chase labelling experiments with strontium-enriched seawater to create “snapshots” of submicron shell growth processes correlatively visualized with micro- to nano-analytical instrumentation such as EPMA, FEG-SEM, Nano-SIMS, Micro-Raman, EBSD, HR-(S)TEM, and Atom Probe Tomography.

As non-nacreous architectures are virtually not studied, pulse-chase labelling experiments combined with architectural investigations provide a powerful tool for detailed characterization at the micron scale: the Sr-label in the shell is shown to cut across all architectural units independent of hierarchy and local orientation, indicating growth rates across a uniform growth front during shell mineralization. While this growth process may appear intuitive, this thesis presents here the first direct evidence compared to previous inferences from natural environments without rigorous time-resolution. This growth process across all architectural hierarchies in the shell is fundamentally different to that of nacropismatic shells, which are thought to grow in a two-step process of forming organic compartments prior to calcification.

Material properties of non-nacreous shells are investigated via stereographic visualization of Young’s moduli and reveal a girdle-like arrangement of elastically stiffer orientations that result in quasi-isotropic planes perpendicular to the growth direction across the entire shell. For nacropismatic shells at the nano-scale, the thesis presents new insights into the toughening processes investigated via innovative TEM-based nanoindentation experiments. At low compression, it is found that organic interfaces confine strain propagation within each tablet and nanogranules as well as organic inclusions rotate and deform, while at high compression tablets interlock and fully recover to their original state.



Nacre is by far the best-studied biomineral, but its insulating properties and high organic content presents significant challenges when taking geochemical investigations to the nano-scale. Therefore, a best practice methodological protocol for Atom Probe Tomography is developed for nacre that minimises the generation of artefacts in the mass spectrum and allows for correlative analysis of the insulating material. This protocol paves the way for innovative studies focussing on the growth dynamics within individual nacre tablets.

The correlated, multianalytical approach is further used to study the ultrastructure and composition of bimineralic cheilostome bryozoan skeletons that consist of primary, calcitic lateral walls that are covered with fine-grained fibrous aragonite on their distal side while the colony's frontal and basal walls are fully aragonitic. This arrangement of mineral phases was previously unknown in cheilostome bryozoa. Further, an organic membrane is situated between both mineral phases that may serve as a template for biomineralisation.

The last part of the thesis investigates another facet of nacre – lustrous pearls by mapping out the knowledge gaps existing in the area of provenance identification and presenting the world's only source of untreated Akoya cultured pearls. These untreated pearls are an invaluable source to investigate the natural colour-palette that are linked to pigments within the nacre.

#### **Contribution highlights of this PhD thesis to the area of research:**

- Aquaculture based pulse-chase labelling of bivalves combined with architectural investigations has great potential to visualize growth dynamics of different hierarchical orders at the micron scale.
- Pulse-chase labelling using elemental Sr and visualisation via correlated backscattered electron images provides more detailed high-resolution insights compared to fluorescent dyes without requiring an isotopic label.
- Non-nacreous shell architectures have commonalities with nacre, as they are enveloped by organic sheaths, have nanometre sized organic inclusions, and consist of nanogranules.
- The growth front within non-nacreous shells cuts across different hierarchical architectural units. This contrasts to nacre that has a two-stage formation of the interlamellar membrane followed by calcification.
- Sub-nanometre scale investigations of nacre by means of atom probe tomography (APT) are challenging due to the insulating character and organic-rich nature of the material. To overcome this, a new correlative best practice is presented that improves data collection and interpretation.
- Nacre's exceptional mechanical resilience is shown to derive at least partly from the material's capacity to interlock tightly across several nacre tablets during compression, while simultaneously, nanogranules and organic inclusions rotate and deform.

## ACKNOWLEDGEMENTS

I acknowledge the traditional owners of the land on which Macquarie University is built upon: the Wattamattagal clan of the Darug nation, and I pay my deepest respects to their Elders past, present, and future.

My deepest gratitude goes to my primary supervisor, Dorrit Jacob, for her ongoing support and mentoring that go far beyond just supervising this thesis: thank you for being such an expert, inclusive and powerful role-model, for helping me become a braver character, and to follow my dreams irrespective of conditions.

I kindly thank my co-supervisor Matthew Kosnik for his very constructive feedback and support throughout my candidature and for always having a fresh point of view on my work.

I express my greatest gratitude to all of my numerous collaborators who always provided skilful advice and kind support. I thoroughly enjoyed working with and learning from all of you: Hadrien Henry, Timothy Murphy, Yi-Jen Lai, Olivier Alard (Department of Earth and Planetary Sciences, Macquarie University), Sue Lindsay and Chao Shen (Macquarie University Faculty of Science and Engineering Microscope Facility MQFoSE MF), Patrick Trimby, Katja Eder, Limei Yang, Matthew Foley, Julie Cairney, Hongwei Liu, Steven Moody (Australian Centre for Microscopy & Microanalysis at the University of Sydney), Oscar Branson, Stephen Eggins, Levi Beeching (the Australian National University), Matt Kilburn and Paul Guagliardo (Centre for Microscopy, Characterisation & Analysis, the University of Western Australia), Nicholas Sturman (The Gemological Institute of America), Peter Hoppe, Klaus Peter Jochum, Brigitte Stoll, Jan Leitner, and Antje Sorowka (Max Planck Institute for Chemistry), Stephan Buhre, Nora Groschopf, Mihail Mondeshki, Tobias Häger, and Ursula Wehrmeister (Johannes Gutenberg University Mainz), Joachim Scholz (Senckenberg Research Institute and Natural History Museum Frankfurt, Marine Invertebrates III), Richard Wirth and Anja Schreiber (GFZ German Research Centre for Geosciences), Frédéric Marin (Université de Bourgogne Franche-Comté, Dijon, France), Stephan Wolf (Institute of Glass and Ceramics, Friedrich–Alexander University Erlangen–Nürnberg), Le Thi Thu Huong (University of Graz) and Christoph Lenz (University of Vienna). I especially thank Robert Hovden for inviting me into his group at the University of Michigan to present my PhD studies and to engage in lab work with his group. I warmly extend these thanks to Jiseok Gim and Noah Schnitzer, who have made me feel very welcome in the Hovden group and made long days and night in the lab to such a great experience!

I gratefully acknowledge James Brown and “Pearls of Australia” for providing cultured pearls used in this thesis and extend my gratitude also to Celeste Boonaerts and Rose Crisp for granting me insights into aspects of pearling and jewellery.

This project wouldn’t have been feasible without the expert support of Jane Williamson, Josh Aldridge and Peter Schlegel from the Macquarie Seawater Facility as well as expert advice on bivalve husbandry

protocols from Wayne O'Connor from Port Stephens Fisheries Centre, NSW Department of Primary Industries. I kindly thank Jacob Bynes, Stephan Buhre, Michael Förster, and Steve Craven for skilful advice on sample preparation. I kindly acknowledge the current and former administration team for their endless assistance with paperwork: Aida Pujol, Alarnah Jade-Cullen, Amid Shresta, Fiona Yang, Jennifer Rowland, Jenny Fang, Phil Dartnell, and Wendy Southwell. Special thanks to Aida for always having my back as I was travelling abroad for my PGRF.

I thank my group members Oluwatoosin Agbaje, Benedikt Demmert, Dilmi Herath, Gabriel Dominguez, and Shiladitya Mazumdar for their collaboration and kind support.

I dearly thank all my friends, colleagues, lab, and office mates of the Macquarie University EPS PhD cohort – for fun discussions, lunch, and coffee breaks, Friday evening socials, movie nights, amazing weekends and most of all for always helping and supporting each other: Alexander Wellhäuser, Francesca Mirolo, Halimulati Ananue, Hindol Ghatak, Jonathan Munnikhuis, Jonathon Wasiliev, Kui Han, Maria “Coti” Manassero, Marina Veter, Milena Schoenhofen, Rosa Didonna, Sarath Kumara, Thusitha Nimalsiri, and Zairong Liu.

I thank Gudrun Daniels for helping Michael and me settle in and start our new household in Sydney and to Tatiana Chapman for being the most wonderful (and geologist!) landlady welcoming us to warmly into her family.

I dedicate this thesis to my parents, Anne and Ron, for their endless love and unconditional support. Thank you for having faith in my journey to the other side of the world. And to my partner, Michael, for sharing this adventure with me and for always being my safe haven.

This thesis was supported by an Australian Government International Postgraduate Research Scholarship (IPRS) awarded to Laura M. Otter. Additionally, research costs were covered through the Australian Research Council via a Future Fellowship (FT120100462) and a Discovery Grant (DP160102081) to Dorrit E. Jacob. Financial support for a research visit to the to the University of Michigan and for attending the Gordon Research Conference on Biomineralisation (2018) was provided by an Macquarie University Postgraduate Research Fund (MQ PGRF) including Deputy Vice-Chancellor of-Research Commendation awarded to Laura M. Otter.

# TABLE OF CONTENTS

Statement of originality.....	3
Abstract.....	4
Acknowledgements.....	6
Table of contents.....	8
List of figures.....	14
List of tables.....	17
List of supplementary figures.....	18
List of supplementary tables.....	21
Outline of the thesis.....	22
Published parts of the thesis.....	24
Talk and poster presentations related to this thesis.....	25
Awards and grants related to this thesis.....	26
1. Introduction.....	27
1.1 Background: what is biomineralisation?.....	27
1.2 Modes of biomineralisation.....	27
1.2.1 Biologically induced mineralization (BIM).....	27
1.2.2 Biologically controlled mineralization (BCM).....	28
1.3 Crystallization pathways for nucleation and growth of biominerals.....	28
1.3.1 Classical nucleation pathways.....	28
1.3.2 Non-classical crystallization models and the role of amorphous calcium carbonate.....	29
1.4 The bivalve shell.....	30
1.4.1 The periostracum.....	30
1.4.2 Nacropismatic shells.....	31
1.4.3 Non-nacreous shells.....	32
1.4.4 The organic moiety in shells.....	33
1.5 Pearls.....	34
1.6 Nacre formation models.....	35
1.6.1 The heteroepitaxial growth model.....	36
1.6.2 The homoepitaxial growth model via transmembrane mineral bridges.....	36

1.7	Motivation and aim of the thesis .....	38
1.8	Approach of the thesis .....	39
2.	Insights into architecture, growth dynamics, and biomineralization from pulsed Sr-labelled <i>Katelysia rhytiphora</i> shells (Mollusca, Bivalvia) .....	40
	Abstract .....	41
2.1	Introduction .....	41
2.2	Materials and methods .....	42
2.2.1	Aquaculture and labelling experiments .....	42
2.2.2	Sample preparation .....	43
2.2.3	Optical microscopy .....	43
2.2.4	Electron probe micro analyser (EPMA), field emission gun scanning electron microscopy (FEG-SEM) and electron backscatter diffraction (EBSD) .....	44
2.2.5	Micro-Raman spectroscopy .....	44
2.2.6	NanoSIMS analysis .....	45
2.2.7	Thermal gravimetric analysis (TGA) .....	45
2.3	Results .....	45
2.3.1	Ultrastructure and growth .....	45
2.3.2	Validation of Sr-incorporation .....	47
2.3.3	Raman spectroscopy .....	48
2.3.4	Architecture of the outer shell layer .....	49
2.3.5	Crystallographic preferred orientations .....	51
2.3.6	Local growth rates .....	52
2.4	Discussion .....	55
2.4.1	Multiscale architecture .....	55
2.4.2	Mechanical properties .....	56
2.4.3	Growth features and growth in the wild .....	57
2.4.4	Implications for growth dynamics and biomineralization in pulse Sr labelled shells .....	59
2.4.5	Strontium/calcium ratios in the shell .....	60
2.4.6	Effects of aquaculture and pulsed Sr-labelling on growth and composition of the shells .....	61
2.5	Conclusion .....	62
	Acknowledgements .....	62
	Supporting material .....	64

Supplementary figures .....	64
Supplementary tables .....	76
3. Micro- to nano-scale architecture and growth dynamics of bivalve shells: crossed-lamellar architecture of <i>Anadara trapezia</i> (Mollusca, Bivalvia) .....	84
Abstract .....	85
3.1 Introduction .....	85
3.2 Materials and methods .....	87
3.2.1 Aquaculture experiments .....	87
3.2.2 Sample preparation .....	87
3.2.3 Optical microscopy .....	88
3.2.4 Scanning electron microscopy (SEM) .....	88
3.2.5 Transmission electron microscopy (TEM) and scanning transmission electron microscopy (STEM) .....	88
3.2.6 Electron backscatter diffraction (EBSD) .....	88
3.2.7 Electron probe micro analyser (EPMA).....	89
3.2.8 NanoSIMS analysis.....	89
3.2.9 Micro-Raman mapping .....	89
3.3 Results.....	89
3.3.1 General shell characteristics.....	89
3.3.2 Strontium enrichment and pulse labelled shell increments .....	91
3.3.3 Shell architecture and crystallographic preferred orientations.....	94
3.4 Discussion .....	97
3.4.1 Shell geochemistry .....	97
3.4.2 Strontium incorporation .....	97
3.4.3 Growth dynamics of <i>A. trapezia</i> shells .....	98
3.4.4 Macro- to micro-scale properties of crossed-lamellar shells.....	99
3.4.5 Nanoscale properties of crossed-lamellar shells .....	100
3.4.6 Aspects of shell mechanical properties .....	100
3.5 Conclusion .....	102
Acknowledgements .....	102
Supporting material .....	104
Supplementary figures .....	104

Analytical challenges associated with EBSD.....	110
Supplementary table.....	111
4. Overcoming challenges associated with the analysis of nacre in the atom probe.....	112
Abstract.....	113
4.1 Introduction.....	113
4.2 Materials and methods.....	115
4.2.1 Challenges associated with sample preparation.....	116
4.3 Results and discussion.....	118
4.3.1 Challenges during atom probe experiments.....	118
4.3.2 Discussion of experimental conditions.....	121
4.4 Conclusion.....	125
Acknowledgements.....	125
Supporting material.....	126
5. A pearl identification challenge.....	128
Abstract.....	129
5.1 Introduction.....	129
5.2 Materials and methods.....	130
5.3 Results.....	131
5.3.1 External appearance.....	131
5.3.2 Real-time microradiography (RTX) and $\mu$ -computed tomography ( $\mu$ -CT) analysis.....	132
5.3.3 Energy dispersive X-ray fluorescence (EDXRF).....	135
5.3.4 Optical X-ray fluorescence.....	136
5.3.5 Laser ablation-inductively coupled plasma-mass spectrometry (LA-ICP-MS) analyses....	137
5.3.6 UV radiation and DiamondView reactions.....	140
5.4 Discussion.....	140
5.5 Conclusion.....	142
Acknowledgements.....	143
6. Akoya cultured pearl farming in eastern Australia.....	144
Abstract.....	145
6.1 Introduction.....	145
6.1.1 Hatchery and spat production.....	146

6.1.2 Seeding and maintaining of Australian akoya pearl oysters .....	147
6.1.3 Harvesting and general farming procedures of Australian akoya cultured pearls.....	150
6.2 Materials and methods .....	154
6.3 Results and discussion.....	155
6.3.1 Raman spectrometry .....	155
6.3.2 Photoluminescence spectrometry .....	156
6.3.3 Mid-FTIR spectrometry .....	157
6.3.4 UV-Vis spectrometry .....	158
6.4 Conclusion .....	160
Acknowledgements .....	161
7. General conclusions of the thesis .....	162
7.1 Aspects of trace element incorporation and pulse Sr-labelling .....	162
7.2 Aspects of shell architecture and crystallographic orientations of marine calcifiers .....	163
7.3 Aspects of mechanical properties of marine calcifiers.....	164
7.4 Future directions .....	165
References .....	167
APPENDIX.....	187
8. Nanoscale deformation processes revealed in nacre of <i>Pinna nobilis</i> mollusc shell .....	188
Abstract .....	189
8.1 Introduction .....	189
8.2 Materials and methods .....	191
8.2.1 Sample material.....	191
8.2.2 Sample preparation .....	191
8.2.3 Electron microscopy .....	192
8.2.4 In-situ nanoindentation.....	193
8.2.5 Triboindentation.....	193
8.2 Results .....	194
8.2.1 Nanoscale deformation and toughening processes.....	194
8.2.2 Highly recoverable nacre tablet locking.....	195
8.2.3 Preservation of mechanical strength .....	196
8.2.4 Damage-tolerance of nacre's architecture.....	198



Discussion .....	200
Acknowledgements .....	200
Supporting material .....	201
Crystal structure of inorganic bridges .....	201
Quantifying organic concentration from HAADF intensity .....	201
Deformation and recovery of nacre tablets .....	202
Strain attenuation in nacre .....	205
Comparison of mechanical properties on the cross-sectional and bulk specimen of nacre, prismatic calcite, and geological monolithic aragonite .....	210
9. Architecture of <i>Anoteropora latirostris</i> (Bryozoa, Cheilostomata) and implications for their biomineralization .....	213
Abstract .....	214
9.1 Introduction .....	214
9.2 Materials and methods .....	216
9.2.1 Systematic account .....	216
9.2.2 Collection and repository of material .....	216
9.2.3 Sample preparation, light and electron microscopy .....	216
9.2.4 X-ray micro -CT .....	217
9.2.5 Electron backscatter diffraction .....	217
9.2.6 NanoSIMS analysis .....	218
9.3 Results .....	219
9.3.1 Colony morphology via X-ray Micro Computed Tomography (Micro-CT) .....	219
9.3.2 Micron-scale architecture and mineral phase composition .....	220
9.4 Discussion .....	226
9.4.1 Bimineralic bryozoan skeletons .....	226
9.4.2 Ultrastructure and mechanical properties .....	226
9.4.3 Insights into the biomineralization processes .....	228
Acknowledgements .....	229
Supporting material .....	230
Supplementary methods .....	236
Stations and sampling: .....	237

# LIST OF FIGURES

Figure 1.1: Crystallisation pathways.....	28
Figure 1.2: Schematic diagrams depicting the maturation process from primary ACC to aragonite.....	29
Figure 1.3: Schematic cross-sections through a nacropismatic bivalve shell .....	30
Figure 1.4: Schematic block diagrams of the most abundant bivalve shell ultrastructures .....	32
Figure 1.5: Schematic cross-section through nacre.....	34
Figure 1.6: Schematic cross-sections through a nacreous bead cultured pearl .....	35
Figure 1.7: Mineral bridge structure connecting two nacre tables of <i>Pinctada margaritifera</i> .....	37
Figure 2.1: Outer and inner shell surface of an unlabelled <i>K. rhytiphora</i> shell with cross-section .....	46
Figure 2.2: FEG-SEM BSE images and NanoSims maps of the oOSL and iOSL of a <i>K. rhytiphora</i> shell .....	47
Figure 2.3: Micro-Raman maps showing the effect of Sr concentrations on the FWHM of peak $\nu_1$ at $1084.8\text{ cm}^{-1}$ in the oOSL and iOSL.....	49
Figure 2.4: SE and BSE images showing cross-sections of Sr-labelled <i>K. rhytiphora</i> shells.....	50
Figure 2.5: EBSD map for aragonite of a pulsed Sr-labelled shell overlain on the BSE image and pole figures .....	52
Figure 2.6: Average growth of the compound composite prismatic (oOSL) layer and crossed-acicular layer (iOSL) .....	53
Figure 2.7: Young's moduli of <i>K. rhytiphora</i> .....	57
Figure 2.8: Schematic of the compound composite prismatic and crossed-acicular architecture transected by Sr-labels .....	60
Figure 3.1: Shell of the bivalve <i>Anadara trapezia</i> .....	90
Figure 3.2: NanoSIMS maps of a Sr-labelled <i>A. trapezia</i> shell .....	92
Figure 3.3: BSE images showing the growth fronts along the tip and umbo of the same specimen with crossed-lamellar and complex crossed-lamellar shell ultrastructure.....	93
Figure 3.4: Micro-Raman maps showing the effect of Sr concentrations on the FWHM and peak position shift of peak for a Sr-labelled <i>A. trapezia</i> .....	94
Figure 3.5: Electron images depicting the shell of <i>A. trapezia</i> .....	96
Figure 3.6: Average daily local growth rates of labelled and unlabelled shell layers.....	97

Figure 3.7: Young's modulus of <i>A. trapezia</i> .....	101
Figure 4.1: Image of <i>Mytilus galloprovincialis</i> shell .....	114
Figure 4.2: TEM images of two APT tips after annular milling .....	117
Figure 4.3: SEM images of atom probe tips .....	118
Figure 4.4: Voltage curves of several different APT datasets with their corresponding mass spectra .....	119
Figure 4.5: Reconstruction of the data shown in Figure 4.4c .....	120
Figure 4.6: Bright field TEM images at different magnifications of the APT tip shown in (d).....	121
Figure 4.7: Comparison of the mass resolution ( $M/\Delta M$ ) to the experimental APT parameters .....	123
Figure 4.8: Concentration profile crossing the membrane, providing a qualitative guide to the relative composition of the matrix and membrane region.....	124
Figure 5.1: Photo of the two challenging pearls discussed in this study.....	129
Figure 5.2: Platy structure typical of nacreous pearls was evident on both pearls.....	132
Figure 5.3: Three $\mu$ -CT slices obtained during the analysis of pearl A in Bangkok.....	133
Figure 5.4: Three $\mu$ -CT slices obtained during the analysis of pearl B in Bangkok .....	133
Figure 5.5: Three $\mu$ -CT slices obtained during the analysis of pearl A in Germany .....	134
Figure 5.6: Three $\mu$ -CT slices obtained during the analysis of pearl B in Germany.....	134
Figure 5.7: 3D XCT software analysis.....	134
Figure 5.8: Optical X-ray fluorescence reactions.....	136
Figure 5.9: Depth profiles obtained by LA-ICP-MS.....	139
Figure 5.10: DiamondView results for pearl A (left) and pearl (B) right .....	140
Figure 6.1: A bracelet showing naturally coloured blue, cream, yellow, and silver akoya cultured pearls from Broken Bay Pearls.....	145
Figure 6.2: The map of Australia indicates the location of the Broken Bay Pearls farm near Woy Woy in New South Wales.....	146
Figure 6.3: Australian <i>Pinctada imbricata fucata</i> larvae .....	147
Figure 6.4: Steps involved in the seeding of Australian akoya pearls .....	149
Figure 6.5: Steps involved in the process of harvesting Australian akoya pearls .....	152
Figure 6.6: This silver pendant features a round 7.5 mm silver akoya pearl from Broken Bay .....	153

Figure 6.7: Naturally white cultured pearls from Broken Bay.....	153
Figure 6.8: Proportions of bodycolours produced at Broken Bay Pearls.....	154
Figure 6.9: Raman spectra of seven Broken Bay akoya cultured pearls.....	156
Figure 6.10: Photoluminescence (PL) spectra of the seven akoya cultured pearls .....	157
Figure 6.11: Mid-FTIR spectrum of an orange sample from Broken Bay Pearls .....	158
Figure 6.12: UV-Vis specular reflectance spectra of 14 Australian akoya pearls.....	159
Figure 8.1: Highly deformed and recovered nacre during nanoindentation.....	194
Figure 8.2: Strain propagation confined by organic interfaces .....	196
Figure 8.3: Recoverable mechanical strength of nacre and crack blunting.....	197
Figure 8.4: Toughening processes of nacre, prismatic calcite, and monolithic aragonite.....	198
Figure 9.1: General aspects of <i>Anoteropora latirostris</i> .....	215
Figure 9.2: Endocasts from microCT of a colony of <i>Anoteropora latirostris</i> .....	220
Figure 9.3: Mineralogy of <i>Anoteropora latirostris</i> .....	221
Figure 9.4: SEM images of a skeleton of <i>Anoteropora latirostris</i> .....	222
Figure 9.5: SEM images and NanoSIMS maps of <i>Anoteropora latirostris</i> .....	223
Figure 9.6: Crystallographic preferred orientations in the skeleton of <i>Anoteropora latirostris</i> . .....	224
Figure 9.7: Pole figures for aragonite and calcite in the skeleton of <i>Anoteropora latirostris</i> .....	225

## LIST OF TABLES

Table 1.1: Overview of taxa studied in this thesis presented together with mineralogical, and ultrastructural information .....	39
Table 2.1: Geochemical composition of <i>K. rhytiphora</i> .....	48
Table 2.2: Average daily local growth rates from pulsed Sr-labelling experiments .....	54
Table 2.3: Distribution coefficients of Ca and Sr between shell and seawater .....	61
Table 3.1: Major and minor element concentrations of unlabelled <i>A. trapezia</i> shell.....	91
Table 3.2: FWHM and position shifts of $\nu_1[\text{CO}_3]$ obtained from micro-Raman maps .....	94
Table 4.1: Experimental conditions for individual atom probe runs.....	122
Table 5.1: EDXRF results in $\mu\text{g}\cdot\text{g}^{-1}$ obtained from the pearls in six different positions.....	135
Table 5.2: LA-ICP-MS data in $\mu\text{g}\cdot\text{g}^{-1}$ obtained in three different laboratories for both pearls.....	138
Table 6.1: Characteristics of natural-colour cultured pearls from <i>Pinctada imbricata fucata</i> bivalves from eastern Australia .....	151
Table 6.2: Summary of colour and corresponding absorption centres of untreated cultured pearls from <i>P. fucata</i> , <i>P. margaritifera</i> , and <i>P. maxima</i> .....	160

## LIST OF SUPPLEMENTARY FIGURES

Supplementary Figure 2.1: Representative micro-Raman spectra obtained from both ultrastructures (iOSL-blue, oOSL-red) .....	64
Supplementary Figure 2.2: Micro-Raman maps overlain on BSE images of a polished cross-section of a Sr labelled <i>K. rhytiphora</i> shell .....	64
Supplementary Figure 2.3: SE-images of a <i>K. rhytiphora</i> shell broken radially .....	65
Supplementary Figure 2.4: BSE image of a polished longitudinal cross-section of <i>K. rhytiphora</i> .....	65
Supplementary Figure 2.5: BSE image showing a polished cross-section of the innermost (first) Sr label (LE1) in the compound composite prismatic ultrastructure oOSL. ....	66
Supplementary Figure 2.6: SE image of a radially broken shell exposing detail in the compound composite prismatic ultrastructure (oOSL). ....	66
Supplementary Figure 2.7: BSE image showing a polished cross-section of Sr label LE1 within the crossed-acicular ultrastructure (iOSL) .....	67
Supplementary Figure 2.8: SE image showing a radially broken surface of the crossed-acicular ultrastructure (iOSL) .....	68
Supplementary Figure 2.9: Differential thermal analysis (a) and thermal gravimetric analysis (b) show thermal stability and total organic matrix contents of iOSL and oOSL .....	68
Supplementary Figure 2.10: Orientation maps for aragonite in oOSL .....	69
Supplementary Figure 2.11: SE image showing a broken radial cross-section of the compound composite prismatic ultrastructure (oOSL) .....	70
Supplementary Figure 2.12: Orientation map for aragonite in iOSL .....	71
Supplementary Figure 2.13: First-order prisms (separated by organic sheaths) have undulated growth fronts with the individual apex co-aligned with the centre of each prism .....	72
Supplementary Figure 2.14: BSE images of polished cross-sections of compound composite prismatic shell at the growth front of the ventral margin .....	73
Supplementary Figure 2.15: BSE images of polished cross-sections of crossed-acicular shell layers (iOSL) near the growth front of the ventral margin .....	74
Supplementary Figure 2.16: BSE images of a polished cross-section .....	75
Supplementary Figure 2.17: BSE images of polished cross-sections of a Sr-labelled shell .....	76
Supplementary Figure 3.1: Polished cross-section of an <i>Anadara trapezia</i> shell .....	104

Supplementary Figure 3.2: Representative micro-Raman spectra of the inner and outer layer of an <i>A. trapezia</i> shell cross-section .....	104
Supplementary Figure 3.3: Scanning transmission electron microscopy (STEM, bright-field) images showing nanometre sizes voids in <i>A. trapezia</i> .....	105
Supplementary Figure 3.4: Scanning transmission electron microscopy (STEM, bright-field) images showing the compound composite prismatic ultrastructure in the outer shell layer of the venerid bivalve <i>K. rhytiphora</i> .....	105
Supplementary Figure 3.5: Crystallographic orientation map for aragonite with crossed-lamellar structure.....	106
Supplementary Figure 3.6: High resolution crystallographic orientation map for aragonite with crossed-lamellar structure obtained.....	107
Supplementary Figure 3.7: High resolution Kernel average misorientation EBSD map .....	108
Supplementary Figure 3.8: BSE image compilation as shown in the main text of this study.....	109
Supplementary Figure 4.1: Mass spectra of the APT dataset containing the organic membrane .....	127
Supplementary Figure 8.1: Shared crystal orientation between two adjacent nacre tablets .....	201
Supplementary Figure 8.2: Relative organic concentration in nacre tablets using the ratio of high-angle elastic electron scattering intensity .....	202
Supplementary Figure 8.3: Cross-sectional view of nacre deformation and recovery at tablet interfaces using HAADF STEM.....	202
Supplementary Figure 8.4: Cross-sectional view of nacre deformation and recovery at tablet interfaces using HAADF STEM.....	203
Supplementary Figure 8.5: <i>In situ</i> TEM nanoindentation along a-axis of nacre tablets .....	204
Supplementary Figure 8.6: Strain attenuation from 1 <sup>st</sup> to 2 <sup>nd</sup> tablet from indenter tip .....	205
Supplementary Figure 8.7: Rotation and deformation of aragonite nanograins and organic inclusions in nacre at the nano-scale .....	206
Supplementary Figure 8.8: Cracks blunted by organic boundaries and inclusions in nacre .....	207
Supplementary Figure 8.9: Video stills of nacreous aragonite extracted from in-situ BF-TEM nanoindentation.....	208
Supplementary Figure 8.10: Video stills of prismatic calcite extracted from in-situ BF-TEM nanoindentation.....	209

Supplementary Figure 8.11: Video stills of geological monolithic aragonite extracted from in-situ BF-TEM nanoindentation .....	210
Supplementary Figure 8.12: Literature survey of elastic modulus of nacre, prismatic calcite, and monolithic aragonite .....	211
Supplementary Figure 8.13: Literature survey of strength of nacre, prismatic calcite, and monolithic aragonite.....	212
Supplementary Figure 9.1: BSE image of a sectioned and polished colony of <i>Anoteropora latirostris</i> with measurements of wall thicknesses for calcitic and aragonitic layers .....	231
Supplementary Figure 9.2: Backscatter Electron image of polished section of sample SMF60007 ...	232
Supplementary Figure 9.3: SEM images showing fractured walls defining the chambers of individual autozooids (Sample ZSM20190252).....	233
Supplementary Figure 9.4: BSE images and NanoSIMS maps of the sectioned and polished specimen in epoxy.....	234
Supplementary Figure 9.5: NanoSIMS maps (mirrored) of $^{28}\text{Si}^-/^{12}\text{C}^-$ .....	235
Supplementary Figure 9.6: Grain sizes in micrometre of calcite (blue) and aragonite (red) grains for the segment mapped by EBSD.....	236
Supplementary Figure 9.7: Map of the sampling stations during RV Meteor expedition 5/2 .....	236



## LIST OF SUPPLEMENTARY TABLES

Supplementary Table 2.1: WDX Electron Probe Micro Analyser (EPMA) parameters.....	76
Supplementary Table 2.2: Geochemical composition of <i>K. rhytiphora</i> shells .....	77
Supplementary Table 2.3: Raman band parameters of $\nu_1[\text{CO}_3]$ as obtained from micro-Raman hyperspectral mapping .....	78
Supplementary Table 2.4: Local growth rates (three replicate measurements) under pulsed Sr-labelling aquaculture conditions for the compound composite prismatic (oOSL) layer.....	79
Supplementary Table 2.5: Local growth rates (three replicate measurements) under pulsed Sr-labelling aquaculture conditions for the crossed-acicular (iOSL) layer.....	81
Supplementary Table 3.1: Growth rates of an <i>A. trapezia</i> shell, formed during aquaculture experiments with ambient and enriched Sr-concentrations .....	111
Supplementary Table 4.1: List of (complex) ions present in mass spectrum of APT dataset containing organic membrane.....	126
Supplementary Table 9.1: List of colonies of <i>Anoteropora latirostris</i> used in this study .....	230
Supplementary Table 9.2: Measured $\text{CN}^-/\text{C}^-$ and $\text{Si}^-/\text{C}^-$ ratios for four sample areas and selected sub-regions.....	230

# OUTLINE OF THE THESIS

This thesis has been prepared as thesis by publication and consists of seven original research chapters (chapters 2 to 8) excluding the introduction (chapter 1) and thesis summary (chapter 9):

**Chapter 1: introduction** provides a literature review by introducing different modes of biomineralisation and highlighting the difference between classical and non-classical crystallization pathways. Further, this chapter focusses on the different ultrastructures of bivalve shells and compares them to nacreous pearls. A review of recently debated nacre formation models concludes this chapter.

**Chapter 2: insights into architecture, growth dynamics, and biomineralization from pulsed Sr-labelled *Katelysia rhytiphora* shells (Mollusca, Bivalvia)** presents the first study utilizing pulsed-chase labelling experiments and subsequent correlative analysis of the labelled and unlabelled shell architectures, namely compound composite prismatic (outer) and crossed-acicular (inner) ultrastructure. This chapter evaluates the use of aquaculture-based labelling experiments, furthers our understanding about non- nacreous shell architectures and adds to our knowledge of shell growth by presenting aspects of material properties, crystallographic twinning, organic content, and nanogranularity.

**Chapter 3: micro- to nano-scale architecture and growth dynamics of bivalve shells: crossed-lamellar architecture of *Anadara trapezia* (Mollusca, Bivalvia)** focusses on the architecture, material properties, and results of pulse-labelled *Anadara trapezia* shells. High-resolution scanning/transmission electron microscopy (S/TEM) allows for nano-scale observations of organic inclusions that are compared to nacreous and other crossed-lamellar shells.

**Chapter 4: overcoming challenges associated with the analysis of nacre in the atom probe** evaluates the potential of Atom Probe Tomography (APT) as the most promising techniques to study the geochemical composition alongside the ultrastructure and morphology of nacre at sub-nanometre resolution. However, the insulating properties and beam sensitivity of the material pose significant challenges in the preparation, analysis, and data interpretation that had to be addressed and better understood prior to answering deeper research questions. This chapter presents a best practice methodological protocol for the analysis of nacre in the atom probe using pulse-chase labelled nacre of *Mytilus galloprovincialis* shells.

**Chapter 5: a pearl identification challenge** explores and maps out the boundaries of pearl identification using methods commonly utilized by gemmological laboratories. These institutions take large efforts to decipher aspects of provenance, species, habitat, cultivation, and treatments encoded in the trace element content within the nacre of lustrous pearls.

**Chapter 6: akoya cultured pearl farming in eastern Australia** presents the world's only source of untreated (i.e. neither bleached nor dyed) Akoya cultured pearls. These specimens offered an excellent chance to investigate their natural colour-palette that is otherwise not accessible on the gemmological market. These untreated pearls show a wider range of colour that are linked to pigments within the nacre.

Within the context of this thesis, this chapter is treated as a “spin-off” that will allow for future biomineralogical studies of the organic and inorganic moiety in pearl and shell material.

**Chapter 7: summary and conclusions of the thesis:** assesses and discusses the key findings of the previously presented main research chapters and closes by pointing out the directions of future research.

The thesis appendix contains two additional chapters that are part of this PhD project:

**Chapter 8: nanoscale deformation processes revealed in nacre of *Pinna nobilis* mollusc shell** presents innovative high-resolution *in situ* nano-indentation experiments performed during S/TEM to deeper investigate nano-toughening processes in nacre. This approach allows for the direct observation of deformation processes in nacre and its exceptional resilience to recover its original morphology without leaving any noticeable damage after releasing compression. A special focus is given to the crack inhibiting properties of organic inclusions, the recoverability of the interlamellar membrane after tablet interlocking and the behaviour of nano-asperities and mineral bridges.

**Chapter 9: architecture of *Anoteropora latirostris* (Bryozoa, Cheilostomata) and implications for their biomineralization** is the first multi-scale study of the composition and ultrastructure of a bimineralic bryozoa. Both aragonitic and calcitic layers are characterized as well as the organic membrane situated at their interface. Architectural aspects including the amounts of crystallographic twinning and material properties allow for a comparison with bivalve shells.

## PUBLISHED PARTS OF THE THESIS

All main research chapters in this thesis are either published, have been submitted for publication or are in preparation for submission:

**Thesis Chapter 2 is published in Biogeosciences since September 2019:**

L.M. Otter, O.B. Agbaje, M.R. Kilburn, C. Lenz, H. Henry, P. Trimby, P. Hoppe, D. E. Jacob: Insights into architecture, growth dynamics, and biomineralization from pulsed Sr-labelled *Katelysia rhytiphora* shells (Mollusca, Bivalvia).

**Thesis Chapter 3 is in preparation for Chemical Geology:**

L.M. Otter, Patrick Trimby, Hadrien Henry, Robert Hovden, Jiseok Gim, Frédéric Marin, Matt R. Kilburn, Oluwatoosin B.A. Agbaje, Matthew A Kosnik, Dorrit E. Jacob: Micro - to Nano-Scale Architecture and Growth Dynamics of bivalve shells: Crossed-Lamellar architecture of *Anadara trapezia* (Mollusca, Bivalvia).

**Thesis Chapter 4 is published in Geostandards and Geoanalytical Research since June 2019:**

K. Eder, L.M. Otter, L. Yang, D.E. Jacob, J.M. Cairney: Overcoming Challenges associated with the analysis of nacre in the atom probe.

**Thesis Chapter 5 is published in Gems & Gemology since August 2019:**

N. Sturman, L.M. Otter, A. Homkrajae, A. Manustrong, N. Nilpetploy, K. Lawanwong, P. Kessrapong, K.P. Jochum, B. Stoll, H. Götz, D.E. Jacob: A Pearl Identification Challenge.

**Thesis Chapter 6 is published in Gems & Gemology since January 2018:**

L.M. Otter, O.B. Agbaje, L.T.T. Huong, T. Häger, D.E. Jacob: Akoya Cultured Pearl Farming in Eastern Australia, *Gems & Gemology*, Vol. 53, No. 4, pp. 423–437. Doi: 10.5741/GEMS.53.4.423

Research chapters within the appendix are published as follows:

**Appendix Chapter 8 is accepted for publication in Nature Communications since May 2019:**

J. Gim, N. Schnitzer, L.M. Otter, Y. Cui, S. Motreuil, Frédéric Marin<sup>3</sup>, S.E. Wolf, D.E. Jacob, A. Misra, R. Hovden: Nanoscale deformation processes revealed in nacre of *Pinna nobilis* mollusc shell.

**Appendix Chapter 9 is published in Nature Scientific Reports since July 2019:**

D.E. Jacob, B. Ruthensteiner, P. Trimby, H. Henry, S.O. Martha, L.M. Otter, J. Scholz: Architecture of *Anoteropora latirostris* (Bryozoa, Cheilostomata) and implications for their biomineralization.

# TALK AND POSTER PRESENTATIONS RELATED TO THIS THESIS

## 2019:

L.M. Otter, P. Trimby, H. Henry, M.R. Kilburn, K. Eder, O.B.A. Agbaje, J. Gim, R. Hovden, J.M. Cairney, S. Mazumdar, D.E. Jacob: Bivalve Shell Architectures: New Insights from Pulsed Sr-Labeling and Correlative Micro/Nanoanalysis. Goldschmidt2019 conference, 18-23. August, 2019, Barcelona, Spain.

K. Eder, L.M. Otter, L. Yang, D.E. Jacob, J.M. Cairney: Challenges associated with the analysis of nacre in the atom probe. ICTMS 2019 - International Conference on Tomography of Materials & Structures, 22 - 26 July 2019, Cairns, Australia.

P. Trimby, A. Bewick, D. Abou-Ras, P. Caprioglio, D. Neher and L.M. Otter: The Analysis of “Sensitive” Materials Using EBSD: The Importance of Beam Conditions and Detector Sensitivity. Microscopy & Microanalysis 2019, August 4-8, Portland, Oregon, USA.

J. Gim, N. Schnitzer, Y. Cui, L.M. Otter, S.E. Wolf, D.E. Jacob, A. Misra, and R. Hovden (2019): Nanoscale Deformation Processes Revealed in Nacre of *Pinna nobilis* Mollusc Shells. Microscopy & Microanalysis 2019, August 4-8, Portland, Oregon, USA.

P. Trimby, A. Bewick, D. Abou-Ras, P. Caprioglio and L.M. Otter: Analyses of “sensitive” materials: a new dawn for EBSD? Royal Microscopical Society RMS EBSD 2019 Meeting, April 1-3, London England.

## 2018:

K. Eder, L.M. Otter, O. Branson, L. Yang, D.E. Jacob, J.M. Cairney: Challenges associated with the analysis of nacre in the atom probe. International Microscopy Congress, September 9-14, Sydney, NSW, Australia.

N. Sturman, L.M. Otter, A. Homkrajae, A. Manustrong, N. Nilpetploy, K. Lawanwong, P. Kessrapong, K.P. Jochum, B. Stoll, H. Götz, D.E. Jacob: A Pearl Identification Challenge. 2018 GIA Symposium, October 7- 9. 2018, Carlsbad, California, USA.

L.M. Otter, M.R. Kilburn, P. Trimby, K. Eder, D.E. Jacob: Submicron Architecture and Growth Dynamics of Bivalve Shells: Insights from Pulsed Strontium Labeling Experiments. Gordon Research Conference on Biomineralisation, July 29-August 3, 2018, New London, NH, USA.

L.M. Otter, K. Eder, O. Branson, J.M. Cairney, L. Yang, D.E. Jacob: Nanoscale Inhomogeneities in Nacre: New Analytical Challenges for the Atom Probe. Geoanalysis Conference, June, 8-13, 2018, Sydney, Australia.

D.E. Jacob, B. Ruthensteiner, P. Trimby, H. Henry, S.O. Martha, L.M. Otter, J. Scholz: Biomineralisation and microstructure of *Anoteropora latirostris* (Silén, 1947) from the Gulf

of Aden. VIII. Australarwood Meeting of Australasian Bryozoologists, February, 2018, Australian Museum, Sydney, Australia.

**2017:**

L.M. Otter, M.R. Kilburn, R. Wirth, S. Buhre, K. Eder, S.J. Moody, D.E. Jacob: High-Resolution Microanalytical Methods for the Investigation of Bivalve Shell Ultrastructures – Relevance for Paleoclimate Reconstructions. CCFS Whole-of-Centre Meeting, November 2017, Cairns, Australia.

L.M. Otter, M.A. Kosnik, M.R. Kilburn, A. Sorowka, P. Hoppe, J.E. Williamson, D.E. Jacob: Submicron Architecture of Bivalve Shells revealed by Microbeam Techniques. Goldschmidt Conference, August, 2017, Paris, France.

## **AWARDS AND GRANTS RELATED TO THIS THESIS**

**January 2016 to April 2019:**

International Postgraduate Research Scholarship "IPRS" funded through the Australian Government

**July 2018:**

Geoanalysis conference registration funded by NSW Government

**April 2018:**

Macquarie University Postgraduate Research Fund “PGRF” including Deputy Vice-Chancellor (Research) Commendation for international travel to Gordon Research Conference and Seminar and collaboration work at the University of Michigan, Ann Arbor, MI-USA

**June 2017:**

Best oral presentation HDR 2017 Conference, Macquarie University

# 1. INTRODUCTION

## 1.1 Background: what is biomineralisation?

Biomineralisation refers to various processes by which organisms form minerals (Weiner and Dove, 2003). The difference between this process and abiotic mineral formation lies in the influence that these organisms exert on the composition, location and timing of mineral deposition. Another difference is that the formation of biominerals requires two basic components: the inorganic mineral phase and an organic phase (Lowenstam and Weiner, 1989; Mann, 2001). The scientific discipline investigating all aspects around nucleation and growth of these mineralised structures and tissues is referred to as 'biomineralisation'. The ability to synthesize minerals evolved multiple times across the three domains of life: bacteria, archaea, and eucaryota (Cuif et al., 2010; Lowenstam and Weiner, 1989). This field is highly interdisciplinary in nature and combines crystallography, biology, geochemistry, materials sciences, medicine, mineralogy, and physics. Different scientific disciplines make routine use of biominerals: In geochemistry and palaeontology, recent and fossil biominerals are used to analyse trace element and isotopes (Weiner and Dove, 2003). These signatures are relevant to reconstruct climatic and environmental information and to make predictions about the future. Another example are bioinspired material design applications that make advantage of the excellent material properties of biominerals (Currey, 1977; Jackson et al., 1988; Munch et al., 2008).

## 1.2 Modes of biomineralisation

There are two superordinate modes describing how organisms produce biominerals: biologically induced mineralization (BIM) and biologically controlled mineralization (BCM, also sometime referred to as "organic matrix-mediated") (Lowenstam, 1981; Lowenstam and Weiner, 1989). While both types require a nucleation template, the biominerals produced differ significantly in ultrastructure and complexity.

### *1.2.1 Biologically induced mineralization (BIM)*

Biominerals formed by BIM nucleate and grow mostly extracellularly on cell surfaces as slime or sheets as metabolic by-products (Frankel and Bazylnski, 2003; Weiner and Dove, 2003). Mineral nucleation is initiated by fluctuations of i.e. pH, Eh, and pCO<sub>2</sub> in the local microenvironment of cells (e.g. Tebo, 1997). This implies that this type of mineralization occurs beyond the direct control of the organism, which is generally reflected in a poorer crystallinity of the material (Frankel and Bazylnski, 2003). Examples for BIM are bacteria that produce magnetite by Fe(III) reduction (Zhang et al., 1997). Other aspects in which BIM products are discriminated from their inorganic and BCM-derived counterparts are microstructure, morphology, particle size, trace element signatures, and water content (Weiner and Dove, 2003).

### 1.2.2 Biologically controlled mineralization (BCM)

BCM is strongly regulated by the genetic program of the specific organism and the mineralized products are, in general, more complex and sophisticated than those produced by BIM and their inorganic counterparts (Weiner and Dove, 2003). Further, while both BIM and BCM produce minerals that are composites of mineral and organic phases, only BCM derived biominerals have complex hierarchical architectures or ultrastructures (Weiner and Dove, 2003). These differences arise from the organism's control over all aspects of nucleation and growth of the biomineral (e.g. Cusack et al., 2008). Depending on the location of the mineralization front, it can be differentiated between three sub-types of BCM:

- Biologically controlled intracellular mineralization: → e.g. frustules (walls) of diatoms (Weiner and Dove, 2003)
- Biologically controlled intercellular mineralization → e.g. calcareous algae (Borowitzka, 1982)
- Biologically controlled extracellular mineralization → e.g. mollusc shells (Weiner and Dove, 2003) and bryozoa exoskeletons (Lowenstam, 1981; Rucker and Carver, 1969)

## 1.3 Crystallization pathways for nucleation and growth of biominerals

There are two distinct theories describing nucleation and growth of minerals: The classical nucleation pathway (Figure 1.1, blue arrow) and the non-classical nucleation pathways (Figure 1.1, red arrows).

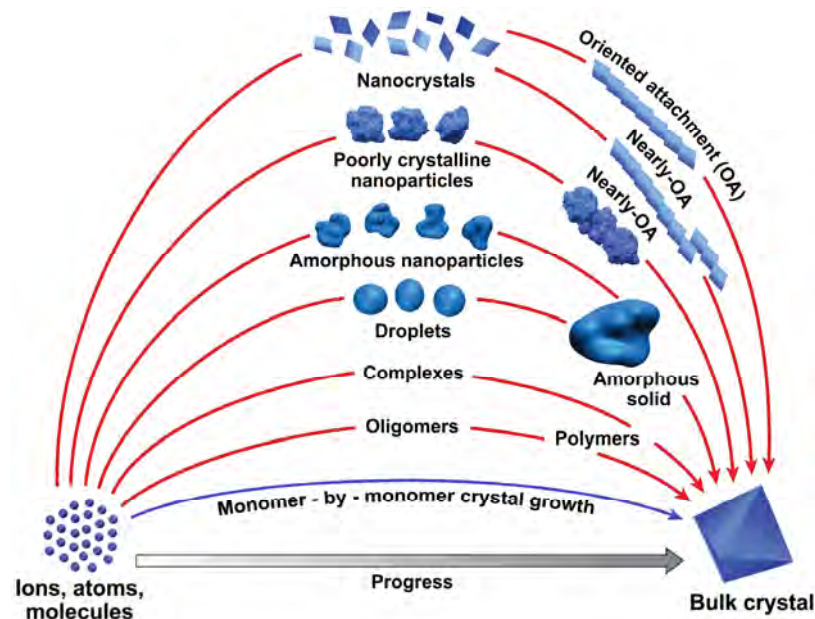


Figure 1.1: Crystallisation pathways from individual free ions, atoms, or molecules to a bulk crystal via classical (blue arrow) and different non-classical pathways (red arrows) modified after De Yoreo et al. (2015).

### 1.3.1 Classical nucleation pathways

Classical nucleation requires supersaturation of a liquid, melt or even gas at which particles begin to cluster (or nucleate) at a certain critical size depending on prevailing pressure and temperature conditions (Gibbs, 1879; Turnbull and Fisher, 1949). The critical size (also referred to as Gibbs-Thomson effect) plays an important role in the nucleation of particles and is defined as a threshold in the system, which separates a regime where nuclei randomly form and dissolve in a steady state, from

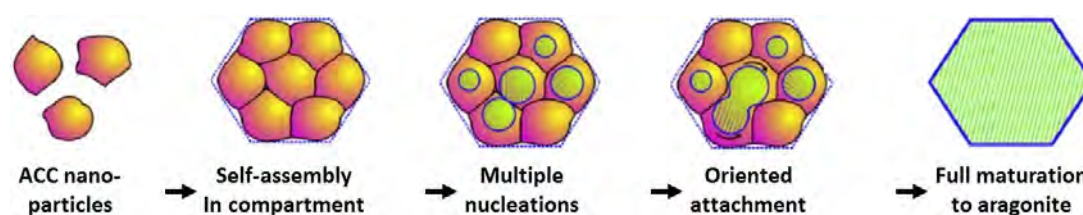


one where nuclei are stable and continue growing (Cölfen and Mann, 2003; De Yoreo et al., 2015; De Yoreo and Vekilov, 2003). Further growth continues as the positive surface potentials of these nuclei continuously adsorbing new monomeric building blocks (i.e. atoms, ions or molecules) (see Figure 1.1, black arrow) either by attaching to preexisting kinks, steps and island structures on the crystal face or by forming new kinks (Cölfen and Mann, 2003; De Yoreo et al., 2015; De Yoreo and Vekilov, 2003; Volmer and Weber, 1926).

Classical crystal growth proceeds following the Ostwald step rule via several phases of increasing thermodynamic stability (Ostwald, 1897). However, this mechanism alone cannot explain the control that the organic template and lastly the organism has over nucleation and growth in the system, which is why other, non-classical pathways are required.

### *1.3.2 Non-classical crystallization models and the role of amorphous calcium carbonate*

Over the last twenty years, amorphous calcium carbonate (ACC) (Cölfen, 2008) was discovered as a precursor phase in different calcifiers such as sea urchin spines (Beniash et al., 1999; Politi et al., 2004), calcite sponge spicules (Sethmann et al., 2006), as well as in the larval stages of gastropods and bivalves (Hasse et al., 2000; Weiss et al., 2002). Addadi et al. (2006) suspected adult shells to form via ACC, and evidence was indeed provided first in the case of cultured pearls (Jacob et al., 2008) then in shells of adult Unionoida (Jacob et al., 2011). The discovery of a precursor phase for aragonite led to a paradigm shift in our understanding of how biominerals form – away from the classical ion by ion attachment pathway to crystallization by colloid attachment and transformation (CAT), which is a sub-form of the non-classical oriented attachment pathway depicted in Figure 1.1, uppermost red arrow (Addadi et al., 2003; Gower, 2008). Today, the CAT pathway is closely associated with the formation of nacreous bivalve shells, where aragonite is observed to mineralize via its colloidal, nanogranular ACC precursor phase and subsequent maturation to aragonite (Figure 1.2) (De Yoreo et al., 2015; Wolf et al., 2016; Zhang and Xu, 2013).



**Figure 1.2: Schematic diagrams depicting the maturation process from primary ACC nanoparticles via a multistep process of self-assembling, nucleation, oriented attachment and transformation to mature aragonite modified after Zhang and Xu (2013).**

The nanogranules are enveloped in thin organic sheaths and have sizes ranging from 20 nm to a few hundred nanometres and were observed using different Transmission Electron Microscopy (TEM) and Atomic Force Microscopy (AFM) based techniques (Hovden et al., 2015; Jacob et al., 2008; Jacob et al., 2011; Wolf et al., 2016).

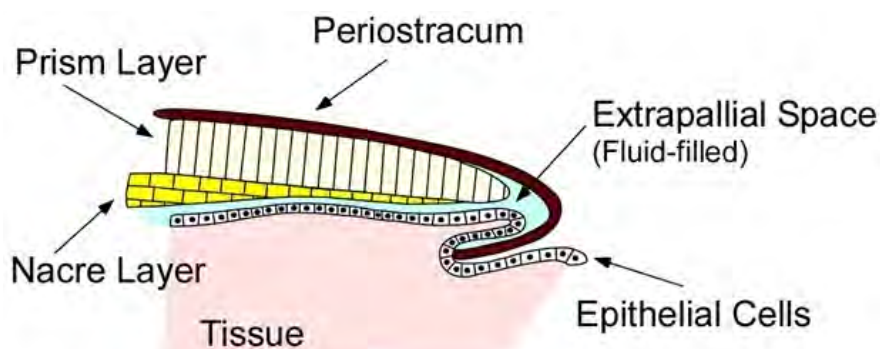
Recently, Jacob et al. (2017) showed that planktic foraminifera form their shells via vaterite, which is another unstable calcium carbonate polymorph that transforms at some point to calcite. Hence, also foraminifera use a non-classical crystallization pathway involving a metastable precursor phase (Jacob

et al., 2017). The steadily increasing number of calcifiers that mineralise via transient precursors allow us to speculate that there are yet undiscovered taxa e.g. cheilostome bryozoa that might take advantage of non-classical crystallization pathways.

## 1.4 The bivalve shell

A continuous fossil shell record since the early Cambrian (ca. 543 Ma) demonstrates the successful evolution of the phylum Mollusca to which the bivalves belongs (Lowenstam and Weiner, 1989). Today, molluscs (bivalves, gastropods and some cephalopods) live in almost all habitats from the deep marine trenches, over inter- and subtidal planes, to rivers and lakes. Most molluscs have calcareous exoskeletons, which support and shelter the animal's soft body (Carter, 1989; Lowenstam and Weiner, 1989). The organ that is responsible for the formation of the calcareous shell is the mantle epithelium – a thin membranous tissue situated in between the soft-body and the shell (Nakahara and Bevelander, 1971; Suzuki and Nagasawa, 2013). Calcium carbonate is produced along the entire surface of the mantle epithelium, however, the mantle edge along the ventral margin of the shell has the highest calcification rate and is responsible for growth in length, while other parts calcify at lower rates in order to thicken the shell (e.g. Carré et al., 2006; Foster et al., 2009).

Macroscopically, the bivalve shell consists generally of three layers (Figure 1.3): an organic periostracum, a middle layer, and an inner layer. Both calcareous layers (i.e. middle and inner layers) can have different architectures. Boggild (1930) , for example, differentiated 8 superordinate shell architectures, namely: homogeneous, prismatic, foliated, nacreous, grained, larger crystal individuals, crossed-lamellar, and complex crossed-lamellar, of which some are more common as middle (e.g. prismatic Figure 1.3, crossed- lamellar), while others occur predominantly as inner layers (e.g. nacre Figure 1.3, complex crossed-lamellar) depending on the bivalve species. Microbeam techniques-based investigations at higher magnification reveal surface roughness with a nanogranular texture that are enveloped by thin organic sheaths that seem to be a common motif in all architectures (Checa et al., 2005; Dauphin et al., 2019).



**Figure 1.3: Schematic cross-sections through a nacropismatic bivalve shell (not to scale) modified from Jacob et al. (2008).**

### 1.4.1 The periostracum

The periostracum is the thin, organic, dark, outer layer that generally covers the whole external surface of the shell. Its main functions are to camouflage the animal (Marin et al., 2012), to prevent chemical

damage to the underlying calcareous layers (Marin et al., 2012) and biofouling (Bers et al., 2006). It comprises a high proportion of cross-linked proteins and insoluble biopolymers and serves as a template for nucleation and growth of the initial mineralized shell layers in bivalve larval stages (Auzoux-Bordenave et al., 2010; Checa, 2000; Nudelman, 2015; Weiss et al., 2002).

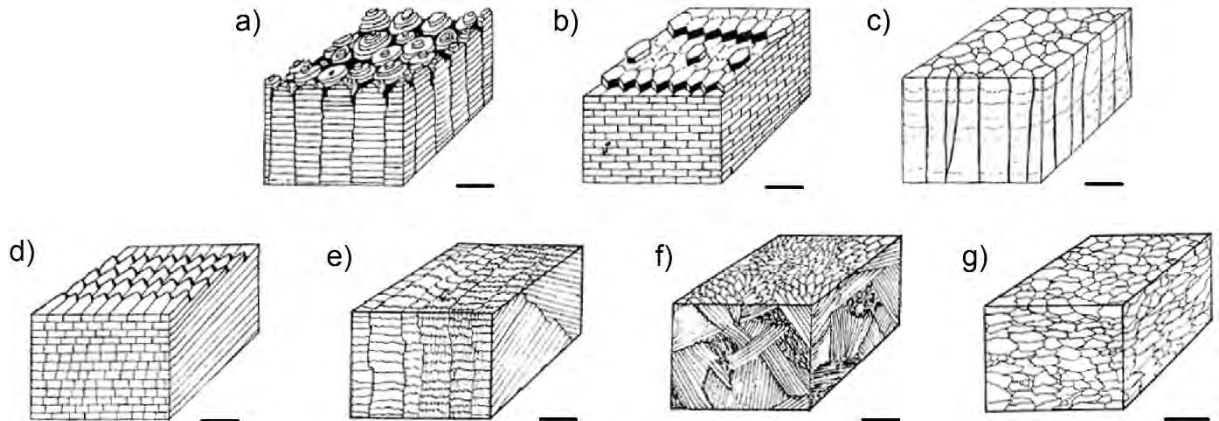
#### 1.4.2 Nacropismatic shells

Nacropismatic bivalve shells are characterized by a middle layer of simple prismatic and an inner layer of nacre (Figure 1.3). The simple prismatic architecture is generally thicker than the inner nacreous layer, and provides stability (Boggild, 1930; Taylor, 1969)). Prisms are generally columnar with irregular hexagonal, pentagonal, or square cross-sections that are most commonly arranged perpendicular to the growth surface (Checa et al., 2005; Taylor, 1969). The prisms can be calcitic, common in marine species, or aragonitic, commonly in freshwater species (Boggild, 1930; Taylor, 1969). They are thought to have spherulitic initial growth stages situated in contact with the periostracum that can only significantly extend away from the outer surface via the principle of competition for space (Checa et al., 2005; Taylor, 1969). Crystallographic investigations show that two types of prismatic orientation are dominant: In the genera *Pinna* and *Atrina*, the crystallographic c-axis is oriented parallel to the long side of the prism and, thus parallel to their growth direction (Dauphin et al., 2019; Pokroy et al., 2006), while in *Pinctada* the long axis of the prisms is aligned perpendicularly with the crystallographic c-axis (Dauphin et al., 2019).

The inner layer of nacre (or mother-of-pearl) consists of polygonal tablets of aragonite with sizes of ca. 15  $\mu\text{m}$  in diameter and a thickness of ca. 0.5  $\mu\text{m}$  (Boggild, 1930; Carter, 1989; Checa et al., 2006; Nudelman, 2015; Taylor, 1969). There are two patterns in which nacre occurs that are distinct for bivalves and gastropods and are genetically unrelated (Jackson et al., 2009): In gastropods, it can be arranged as “columnar nacre” in which tablets are stacked, whereas in bivalves it is expressed as “sheet nacre” with a so-called “brick and mortar” ultrastructure, where the “bricks” refer to the mineral phase and the “mortar” describes the interlamellar organic matrix (Chateigner et al., 2000; Kobayashi and Samata, 2006; Taylor, 1969). The cephalopod *Nautilus* shows even a mix of both nacre types (Mitchell et al., 1995). For a long time it has been believed that nacre has strictly co-oriented crystallographic c-axes, which follow the curvature of the shell surface with a perpendicular orientation (Suzuki et al., 2009). However, recent studies show c-axes tilts of up to 10 degrees (Dimasi and Sarikaya, 2004) as well as a high disorder at the nacropismatic boundary (Gilbert et al., 2008; Olson et al., 2013b) (Gilbert et al., 2008). At the nano-scale, nacre tablets show a granular substructure consisting of 20 to 120 nm sized globular granules (Checa et al., 2011; Checa et al., 2013; Dauphin, 2001; Jacob et al., 2008; Metzler et al., 2008; Mutvei and Dunca, 2010). Individual granules are enveloped by thin organic sheaths i.e. vesicles (Checa et al., 2013; Jacob et al., 2008). These granules are believed to result from the initial ACC nanogranular assemblage of the nacre tablet prior to its maturation to aragonite (discussed earlier in chapter 1.3.2 of this thesis).

### 1.4.3 Non-nacreous shells

Traditionally, studies on shell formation and their mechanical and geochemical properties have been focusing on nacre (both columnar and sheet, Figure 1.4a and b, respectively) as well as the simple prismatic ultrastructure (Figure 1.4c) that is generally associated with this architecture. However, different types of prismatic ultrastructures exist, such as the compound composite prismatic architecture, and these, similarly to other non-nacreous molluscan shells, have received less attention up to now. (Figure 1.4d-g).



**Figure 1.4: Schematic block diagrams of the most abundant bivalve shell ultrastructures: (a) columnar nacre, (b) sheet nacre, (c) prismatic, (d) foliated, (e) crossed-lamellar, (f) complex crossed-lamellar, (g) homogeneous. Scale bars are 5  $\mu\text{m}$  (a, b, d, g) and 500  $\mu\text{m}$  (c, e, f). Modified after Currey and Taylor (1974).**

The *foliated ultrastructure* (Figure 1.4c) is a common though not much studied inner layer of molluscs and is generally calcitic (Boggild, 1930; Checa et al., 2009; Taylor, 1969). It consists of co-oriented laths that are usually aligned parallel to the inner shell surface (Boggild, 1930, 1930; Taylor, 1969). Hence, it resembles a high similarity to the “brick and mortar” ultrastructure of sheet nacre.

The *crossed-lamellar ultrastructure* (Figure 1.4e) is the most abundant shell architecture in the phylum Mollusca and has an even higher fracture toughness than nacre (Almagro et al., 2016; Böhm et al., 2016; Dauphin and Denis, 2000). Also, it is the next best studied architecture after the nacropismatic ultrastructures. It is always aragonitic and consists of a hierarchy of up to four orders of lamellae: First order lamellae are parallel with wide and flat aspects and have alternating orientations (Boggild, 1930; Dauphin and Denis, 2000; Kamat et al., 2000; Pokroy and Zolotoyabko, 2003; Taylor, 1973). They consist of stacked second order lamellae that comprise thin and elongated third order lamellae that in turn exhibit a granular surface roughness associated with nanometre sized fourth order lamellae (Agbaje et al., 2017b; Almagro et al., 2016; Böhm et al., 2016; Pokroy and Zolotoyabko, 2003). However, the architecture varies in detail among different species and can be separated into groups by crystallographic properties (Almagro et al., 2016; Böhm et al., 2016).

The *complex crossed-lamellar ultrastructure* (Figure 1.4f) is also aragonitic and has a similar hierarchical arrangement as the crossed-lamellar type with the addition that the laths are arranged in four or more radial directions and have more than two dip directions (Chateigner et al., 2000). The

lamellae and their arrangements can vary significantly in shape that can be grouped to different e.g. regular and irregular sub-types (Chateigner et al., 2000; Taylor, 1969).

The homogeneous *ultrastructure* (Figure 1.4g) is always aragonitic (Taylor, 1969) and is characterized as an aggregation of granular particles that lack a distinct and organized substructure (Carter, 1989; Chateigner et al., 2000; Taylor, 1969). However, the shell areas show parallel extinction over wide parts of the shell when viewed with crossed nichols indicating that at least the crystallographic axes are well aligned (Boggild, 1930; Kobayashi, 1971).

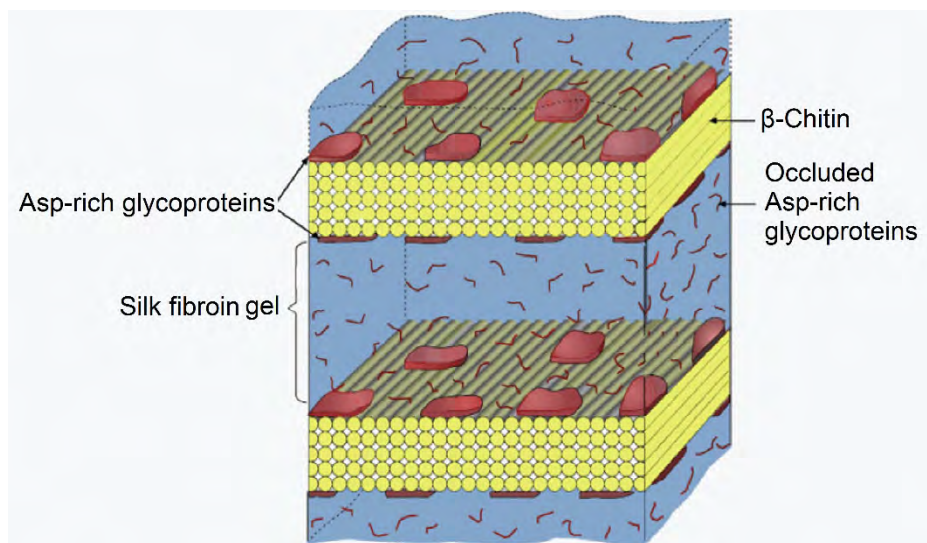
#### *1.4.4 The organic moiety in shells*

Each hierarchical order of architectural units is enveloped in organic membranes that can be wider or thinner depending on the present ultrastructure type (Checa et al., 2005; Dauphin et al., 2019). Total organic content of shells has been investigated for several ultrastructures by means of differential thermal analysis (DTA) and thermogravimetric analysis (TGA) and range from about 0.1 wt.% in highly mineralised crossed-lamellar shells (Agbaje et al., 2017b) to up to 5 wt.% in nacre (Hare, 1965).

Three types of organic matrix components have been differentiated: (1) the interlamellar membrane referring to the 30 nm thick, well-defined sheaths separating generations of aragonite tablets, (2) intertabular membranes between neighbouring nacre tablets and (3) the intracrystalline organic content i.e. organic inclusions (for review see Marin and Luquet, 2004; Nudelman, 2015) that describe nanometre-sized pores within the aragonite thought to be filled with organic material (Gries et al., 2009a; Younis et al., 2012a). However, only the first two types have been widely investigated regarding their composition, formation, and ultrastructure. In comparison, these aspects are barely touched in the case of organic inclusions as their size of only few nanometres poses challenges to the current analytical limits and are so far only known to contain greater amounts of carbon (Gries et al., 2009a).

*In vitro* experiments showed that macromolecules extracted from the organic matrix of nacre control polymorph nucleation actively as it induces aragonite formation despite calcite being more stable under ambient conditions (Watabe and Wilbur, 1960). It is understood today that the organic matrix provides a template for mineralization (Bevelander and Nakahara, 1969; Levi-Kalishman et al., 2001) and that they consist of three main components: (1) the highly oriented, water-insoluble polysaccharide  $\beta$ -chitin, (2) relatively hydrophobic alanine- and glycine-rich silk-like fibre proteins, and (3) water-soluble acidic macromolecules such as glycoproteins that are rich in aspartic and glutamic acid and are often associated with polysaccharides (Addadi et al., 2006; Belcher et al., 1996; Falini et al., 1996; Keith et al., 1993; Levi-Kalishman et al., 2001; Marie et al., 2007; Peters, 1972; Weiner et al., 1983; Weiner and Traub, 1980).  $\beta$ -chitin occurs as a core-layer in the inter-lamellar matrix in a crystalline biopolymer state where it serves as a scaffold for mineralization (Addadi et al., 2006; Falini et al., 1996; Weiner et al., 1984). It is “sandwiched” between layers of the water-soluble aspartic-rich glycoproteins (Figure 1.5), while the compartments between the scaffolds are thought to be filled with silk fibroin-like proteins in a hydrated gel-like state with some minor proportion of the aspartic-rich glycoproteins (Levi-Kalishman et al., 2001; Nudelman et al., 2008). Sudo et al. (1997) showed that the Ala- and Gly-rich silk-like proteins have

amino acid sequences similar to those found in spider silk. However, Agbaje et al. (2018) showed recently with Solid State NMR that chitin in the organic matrix is not as abundant as previously proposed to the extent that it may even be completely absent in some species.



**Figure 1.5: Schematic cross-section through nacre (aragonite transparent and not to scale) depicting the components of the organic matrix modified after Levi-Kalisman et al. (2001).**

The water-soluble polysaccharides often associated with aspartic-rich glycoproteins and glutamic acid have been demonstrated to occur together with high concentrations of sulphates that serve as nucleating centres for aragonite (Addadi et al., 1987; Belcher et al., 1996; Crenshaw and Ristedt, 1976; Falini et al., 1996; Nudelman et al., 2006). However, ultrastructure, components and associated functions regarding nucleation and growth of the mineral phase are not yet fully understood. This is especially the case for non-nacreous shells and remain an area of ongoing research.

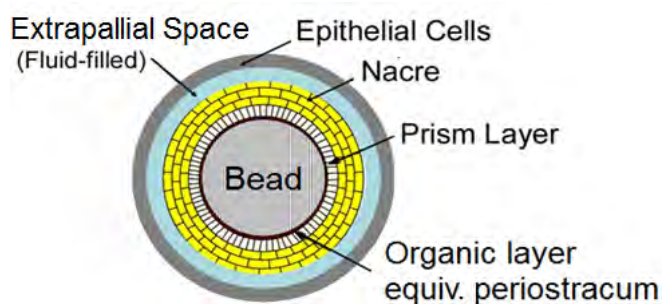
## 1.5 Pearls

Pearls are defined as mineralized, lustrous concretion that are produced within the soft tissue of molluscs such as pearl-oysters and pearl-mussels. The nacreous inner lining in shells and the nacreous material of lustrous pearls are produced by the same mineralizing tissue: the mantle epithelial cells (Jacob et al., 2008; Strack, 2006). Natural loose concentric pearls can form after an injury with subsequent detachment of epithelial cells that can develop into a cyst within the tissue of the bivalve, sometimes but not necessarily around an irritant (Landman et al., 2001; Strack, 2006). Mankind has valued pearls since prehistoric times because of their lustre and rarity (Strack, 2006). There were several attempts throughout history to manipulate bivalves and encourage pearl formation: the earliest pearly objects formed through human intervention were blisters in the shape of Buddha figures produced since ca. 100 B.C. throughout China (Akamatsu et al., 2001; Strack, 2006). Today, half-round Mabe-pearls are grown by using mainly the marine pearl-oysters *Pteria penguin*, *Pinctada maxima* and *Pinctada margaritifera* (Edwards et al., 2018; Kripa et al., 2008; Strack, 2006). Round cultured pearls were far more challenging to produce and the first reproducible method for the mass production of round pearls was successfully established as the “Mise-Nishikawa method” by Tokichi Nishikawa, Tatsuhei Mise, and Kokichi Mikimoto in 1916 (Strack, 2006). The “Mise-Nishikawa method” is still state of the art for producing



bead cultured pearls (e.g. Otter et al., 2017). Here, a small piece of nacre-producing outer mantle epithelium (graft) of a sacrificed donor bivalve is cut and inserted together with a calcareous bead into the gonad (i.e. reproductive organ) of a host bivalve. Within the first 21 days after seeding, the tissue graft undergoes cellular proliferation and produces a closed cyst or pearl sac around the bead and generally deposits a 20-30  $\mu\text{m}$  thick organic coating onto the bead (Cuif et al., 2011). Subsequently, calcitic prisms and aragonitic nacre layers are produced until the cultured pearl is harvested.

Kawakami (1952) was the first to describe the three layered mineralization sequence in pearls (Figure 1.6) and their similarity with the ones observed in the shells of the corresponding bivalves and coined the term of the “reversed shell”. The structural relationship was speculated to arise from the transformation of the tissue into the pearl sac that likely causes some regenerative metabolic changes in the mineralizing epithelium (Kawakami, 1952; Taylor and Strack, 2008). However, Cuif et al. (2011) criticize this term as too simplistic since microstructures in pearls can show far more complexity as well as “confused” architectures such as prismatic microcrystalline aragonite that are not expressed in the corresponding shells, which they believe to arise as an effect of the artificially curved bead surface.



**Figure 1.6: Simplified schematic cross-sections through a nacreous bead cultured pearl and predominant structural layers (not to scale) modified from Jacob et al. (2008). Note the structural similarity with the schematic cross-sections through a nacropismatic bivalve shell shown in Figure 1.3.**

Nonetheless, as both pearls and shells are produced by the same tissue and only differ in some structural variations as an effect of adaptation to two distinct substrates both systems provide the opportunity to study the microstructure, geochemistry, mechanical properties and biomineralisation processes in nacre.

## 1.6 Nacre formation models

Amongst all eight types of shell architectures only the nacreous ultrastructures has a differentiated history of formation models, while the formation of other shell architectures is inferred based on the nacre models. Although much is known about the individual constituents of both organic and inorganic components the exact dynamics and sequence are still not fully understood (Addadi et al., 2006; Mutvei, 1979; Nudelman, 2015; Olson et al., 2013a; Schäffer et al., 1997). There are two main groups of models that try to explain the nucleation and growth of nacre: (1) different heteroepitaxial models explain tablet growth to be initiated by the organic template, and (2) the homoepitaxial or mineral bridge models that explain growth to be a continuous process spreading from one tablet to the next. Lastly, there are some well as some complementary models such as those on stop and start molecules.

### 1.6.1 The heteroepitaxial growth model

The heteroepitaxial nucleation model describes nacre growth to be induced by organic macromolecules e.g. in the interlamellar membrane that act as a template for biomineralisation (Belcher et al., 1996; Falini et al., 1996; Metzler et al., 2010; Watabe and Wilbur, 1960; Weiner et al., 1984; Weiner and Hood, 1975; Weiner and Lowenstam, 1986; Weiner and Traub, 1980). Organic templates play an important role as they provide nucleation sites by lowering the interfacial energy (De Yoreo and Vekilov, 2003 and references therein), thus providing the organism with control over nucleation and growth of the mineral phase (De Yoreo and Vekilov, 2003). It has long been speculated that the organic matrix of mollusc shells initiates aragonite growth *in vivo* (Belcher et al., 1996; Falini et al., 1996; Watabe and Wilbur, 1960) as well as that the interlamellar matrix is formed prior to mineralization (Bevelander and Nakahara, 1969). Later, the first nacre growth model was proposed by Weiner et al. that explained nacre tablets to grow via templating on the interlamellar membrane (Weiner et al., 1984; Weiner and Hood, 1975; Weiner and Lowenstam, 1986; Weiner and Traub, 1980). This model was further evolved by Levi-Kalishman et al. (2001), who postulated that chitin forms a rigid compartmentalizing scaffold, while the silk-like proteins fill in the compartmental space between the interlamellar membranes in the state of a gel (Figure 1.5). This gel is thought to be subsequently overgrown by the mineral (Levi-Kalishman et al., 2001). Although Levi-Kalishman et al. (2001) could not provide direct evidence for the gel-like organic constituent, this was later provided by Nudelman (2015), who confirmed the presence of the silk-like proteins by means of cryo-environmental-SEM and located it indeed within the compartments sandwiched between the chitin-like organic material of the interlamellar membrane. Further, distinct areas with high concentrations of sulphate occurring together with carboxylates were found in the interlamellar membrane as well as at the centre of nacre tablets and are both thought to act as a strong anionic component that attract calcium and thereby inducing the ordered/orientated growth of calcium carbonate (Addadi et al., 1987; Crenshaw and Ristedt, 1976; Nudelman et al., 2006). Hence, a new model was proposed that comprises a round, organic and sulphate-rich “Nudelman site” of about 1  $\mu\text{m}$  in diameter per tablet that initiates nucleation and growth of aragonite (Nudelman et al., 2006).

Metzler et al. (2007) proposed that interlamellar membranes may comprise two distinct nucleation sites situated opposite each other within each interlamellar membrane that may coincide with “Nudelman sites” and regulate aragonite growth from an older generation of nacre tablets to the next younger one. The STOP molecule is hypothesized to sit on the interlamellar membrane facing the older nacre tablet generation and becomes activated as the growing aragonite approaches. This activates the START molecule on the opposite side of the interlamellar membrane and creates a new nucleation site with shared crystallographic orientation of both generations.

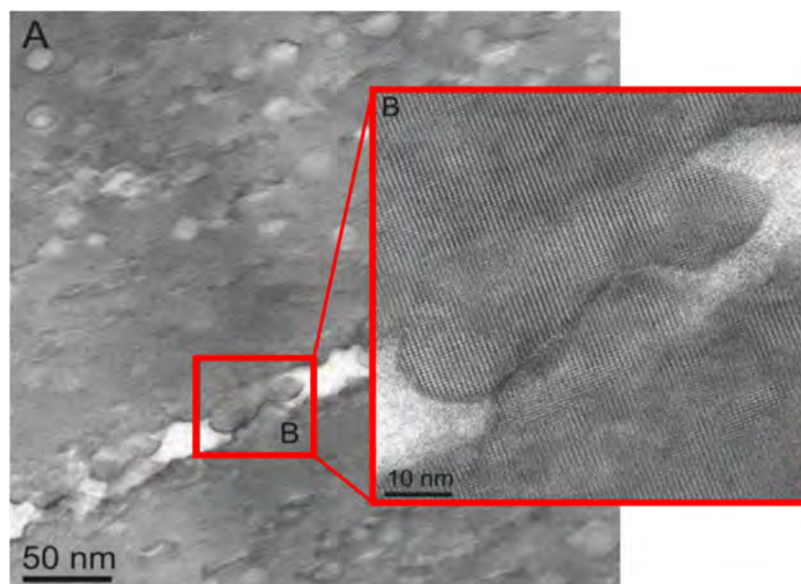
### 1.6.2 The homoepitaxial growth model via transmembrane mineral bridges

Schäffer et al. (1997) was the first to hypothesize that new generations of nacre tablets may also form by protruding through ion conductive pores in the interlamellar membrane that allow for continued



growth of the mineral phase. Hence, only one nucleation event at the beginning of a nacre tablet stack is needed and successive tablets form homoepitaxially (Nudelman, 2015 and references therein). The connectivity of tablets explains excellently the shared crystallographic orientation within each nacre tablet stack (Gries et al., 2009b; Nudelman, 2015; Saruwatari et al., 2009). Pore sizes proposed by Schäffer et al. (1997) were 5-50 nm in diameter spaced apart in a distance of about 50 nm on average and compare well to other studies (Barthelat et al., 2006; Lin et al., 2008; Song et al., 2003). However, regarding these early studies of mineral bridges there has been some speculation if some of the pores were artefacts induced by excessive sample preparation that involved decalcification and drying of the organics that can cause shrinkage of the interlamellar membranes (Nudelman, 2015). Also, most of these early studies were based on gastropod nacre and do not necessarily apply to bivalve nacre.

Checa et al. (2011) showed that minor mineral bridges with diameters ranging from 10–50 nm are indeed interrupted by the organic matrix and are, hence, not continuous across the interlamellar membrane (Figure 1.7). This was only discovered by systematically testing different focal points during TEM analysis along the suspected bridge structure. Moreover, it was proposed that these “minor bridges” result from coincidentally closely spaced asperity or hillock structures from both sides of the interlamellar membrane and, hence, do not share continuous crystal lattice orientations (Checa et al., 2011; Gries et al., 2009b; Younis et al., 2012a). Further, gastropod and cephalopod nacre was found to communicate across wide pores of the interlamellar membrane aligned along the centre axes of the columnar nacre stacks, whereas in the sheet nacre of bivalves, major interruptions were found to occur only close to the edges of tablets and are the only mineral bridge structures truly associated with shared crystallographic alignments of the tablet generations, while minor bridges and asperities may actually serve mechanical functions and prevent tablet sliding (Barthelat et al., 2006).



**Figure 1.7: Mineral bridge structure connecting two nacre tables of *Pinctada margaritifera* across the interlamellar membrane (B) enlarged section of (A) modified from Checa et al. (2011).**

## 1.7 Motivation and aim of the thesis

Bivalves grow their shells incrementally throughout their lifetime, which can easily exceed 200 years depending on the species (Forsythe et al., 2003). During growth, they record changing environmental conditions encoded in trace element and isotopic signatures. These signatures, if deciphered correctly, are an invaluable resource of geochemical information that can be used to reconstruct many different environmental parameters such as water temperature, salinity (e.g. Klein et al., 1996b), and pH (e.g. Zhao et al., 2017b). However, these reconstructions are often complicated by factors like the shell's nano-scale architectural complexity compared to its pure geological counterparts (e.g. Jackson et al., 1988; Katti et al., 2006) as well as the fact that trace elements are incorporated not directly into mature aragonite but into transient precursor phases (De Yoreo et al., 2015; Wolf et al., 2016; Zhang and Xu, 2013). Missing growth models for the non-nacreous shells further complicate their applicability. It is therefore perhaps not surprising that some paleoclimate reconstructions show yet inexplicable deviations from the thermodynamic equilibrium behaviour for some elements and isotope ratios (Epstein et al., 1951). Within this context we can identify several primary and secondary aims to further our general understanding of bivalve shell biomineralisation within a multi-disciplinary context:

Primary goals of the thesis:

1. Evaluate the feasibility and potential of pulse-chase labelling as a tool to further our understanding of growth dynamics in different bivalve ultrastructures
2. Better understanding of architectural growth processes and sub-micron growth dynamics of bivalve shells, through direct study and comparison studies with bryozoa skeletons
3. Further our understanding regarding the role of sub-micron organic inclusions that are abundant in bivalve shells with different architectures

Secondary goals of the thesis:

4. Provide a basis for future pearl provenance investigations by applying the results from this thesis on shell growth processes.
5. Compare mechanical properties of shells and other marine calcifiers (bryozoa)

## 1.8 Approach of the thesis

As bivalves are easy to culture, shell growth and the influence of metabolic activity on the composition of the shell are best studied in living shells in a controlled aquaculture setup. These aquaculture experiments were performed using four different bivalve species (Table 1.1) sourced from their natural environments and acclimated in the Macquarie University Seawater Facility. These bivalves were then subjected to pulse-chase labelling experiments by repeatedly incubating them for a limited time in strontium (Sr)-enriched seawater to create “snapshots” of submicron shell growth dynamics. After the aquaculture period, bivalves were sacrificed and shell architectures, material properties, and chemical composition were visualized with a correlative, stepwise spatially downscaled high-resolution micro- and nano-analytical approach using a range of state-of-the-art instrumentation.

Similar combinations of instruments were used to characterize the architectures and material properties of different types of pearls and bryozoa skeletons to provide comparison studies on biomineralisation in marine calcifiers. A comprehensive list of pulse-labelled and unlabelled species used in this thesis is presented in Table 1.1.

**Table 1.1: Overview of taxa studied in this thesis presented together with mineralogical, and ultrastructural information. All species are from the marine environment. Chapters in which the taxa were used are referenced for clarity.**

Taxa:	Shell Composition:	Architecture:	Pulse Labelling Experiments:	Thesis chapter #:
<i>Anadara trapezia</i> (Deshayes, 1839) Family: Arcidae Order: Arcida	Aragonite	Crossed-lamellar & Complex crossed-lamellar	Yes	3
<i>Katelysia rhytiphora</i> (Lamy, 1935) Family: Veneridae Order: Venerida	Aragonite	Compound composite prismatic & Crossed-acicular	Yes	2
<i>Mytilus galloprovincialis</i> (Lamarck, 1819) Family: Mytilidae Order: Mytilida	Calcite Aragonite	Simple Prismatic & Nacre	Yes	4
<i>Pinctada imbricata fucata</i> (Gould, 1850) Family: Pteriidae Order: Pterioida	Calcite Aragonite	Simple Prismatic & Nacre	Yes (shells) No (pearls)	6*
<i>Pinna nobilis</i> (Linnaeus, 1758) Family: Pinnidae Order: Ostreida	Calcite Aragonite	Simple Prismatic & Nacre	No	8 in appendix
<i>Anoteropora latirostris</i> (Silén, 1947) Family: Mamilloporidae Order: Cheilostomatida	Calcite Aragonite	-	No	9 in appendix

\*Chapter contains only pearls. Pulse labelled shells are part of ongoing research project. Samples presented in thesis research chapter 6 are of unknown origin and are, hence, excluded from this table.

## 2. INSIGHTS INTO ARCHITECTURE, GROWTH DYNAMICS, AND BIOMINERALIZATION FROM PULSED SR-LABELLED *KATELYSIA RHYTIPHORA* SHELLS (MOLLUSCA, BIVALVIA)

Laura M. Otter<sup>1\*</sup>, Oluwatoosin B. A. Agbaje<sup>1</sup>, Matt R. Kilburn<sup>2</sup>, Christoph Lenz<sup>3,4</sup>, Hadrien Henry<sup>1,3</sup>,  
Patrick Trimby<sup>5</sup>, Peter Hoppe<sup>6</sup>, Dorrit E. Jacob<sup>1,3</sup>

<sup>1</sup>Department of Earth & Planetary Science, Macquarie University, Sydney, NSW 2109, Australia

<sup>2</sup>Centre for Microscopy Characterisation and Analysis, University of Western Australia, Perth, WA 6009, Australia

<sup>3</sup>Australian Research Council Centre of Excellence for Core to Crust Fluid System (CCFS) / GEMOC

<sup>4</sup>Institute of Mineralogy and Crystallography, University of Vienna, Althanstr. 14, 1090 Vienna, Austria

<sup>5</sup>Oxford Instruments NanoAnalysis, High Wycombe, HP12 3SE, United Kingdom

<sup>6</sup>Particle Chemistry Department, Max Planck Institute for Chemistry, Hahn-Meitner-Weg 1, 55128 Mainz, Germany

\*Corresponding Author: [laura.otter@mq.edu.au](mailto:laura.otter@mq.edu.au)

This chapter has been published in Biogeosciences as:

**L.M. Otter**, O.B. Agbaje, M.R. Kilburn, C. Lenz, H. Henry, P. Trimby, P. Hoppe, D.E. Jacob (2019): Insights into architecture, growth dynamics, and biomineralization from pulsed Sr-labelled *Katelysia rhytiphora* shells (Mollusca, Bivalvia), Biogeosciences, Vol. 16, pp. 3439–3455. Doi: 10.5194/bg-16-3439-2019. Open Access at: <https://www.biogeosciences.net/16/3439/2019>

The author's contribution to the publication is as follows: LMO designed the study with the supervisor, acquired the bivalves and diet, conducted aquaculture experiments, sample preparation as well as performed optical microscopy, SEM, micro-Raman analysis and evaluated the data. Further, LMO supported NanoSIMS, EBSD EPMA and TGA analysis as well as data evaluation and drafted the manuscript. All co-authors participated in editing the draft and gave final approval for publication.

## Abstract

The intertidal bivalve *Katelysia rhytiphora*, endemic to south Australia and Tasmania, is used here for pulsed Sr-labelling experiments in aquaculture experiments to visualize shell growth at the micro- to nano-scale. The ventral margin area of the outer shell layer composed of (i) an outermost outer shell layer (oOSL) with compound composite prismatic architecture with three hierarchical orders of prisms and an (ii) innermost outer shell layer (iOSL) with crossed-acicular architecture consisting of intersecting lamellae bundles. All structural orders in both layers are enveloped by an organic sheath and the smallest mineralized units are nanogranules. Electron Backscatter Diffraction reveals a strong preferred orientation of the aragonite c-axes perpendicular to the growth layers, while the a- and b-axis are scattered within a plane normal to the local growth direction and >46 % twin grain boundaries are detected. The Young's modulus shows a girdle-like maximum of elastically stiffer orientations for the shell following the inner shell surface.

The bivalves were subjected for 6 days twice to seawater with an increased Sr concentration of 18x mean ocean water by dissolving  $144 \mu\text{g}\cdot\text{g}^{-1}$  Sr ( $159.88 \text{ Sr/Ca mmol/mol}$ ) in seawater. The pulse labelling intervals in the shell are 17x (oOSL) and 12x (iOSL) enriched in Sr relative to the Sr spiked seawater. All architectural units in the shell are transected by the Sr label, demonstrating shell growth to progress homogeneously instead of forming one individual architectural unit after the other.  $D_{\text{Sr/Ca}}$  for labelled and unlabelled shell are similar to shell portions formed in the wild (0.12 to 0.15). All  $D_{\text{Sr/Ca}}$  are lower than values for equilibrium partitioning of Sr in synthetic aragonite.

## 2.1 Introduction

The shells of bivalves are bio-composites with a complex, hierarchical 3D arrangement of crystalline calcium carbonate (aragonite and/or calcite), intimately conjoined by organic macromolecules that control nucleation and growth of the mineral entity across all length scales (Addadi et al., 2006; Cusack et al., 2008; Rodriguez-Navarro et al., 2012; Simkiss, 1965; Weiner et al., 1984; Weiner and Traub, 1980). This arrangement significantly enhances the physical and mechanical properties of the shell and explains its high mechanical strength and fracture resistance (Currey and Kohn, 1976; Jackson et al., 1988; Kamat et al., 2000).

Trace elements incorporated in the carbonate phase of shells are used to monitor and reconstruct (paleo)environmental parameters, e.g. water salinity (Klein et al., 1996b), temperature (Klein et al., 1996a; Schöne et al., 2011; Zhao et al., 2017a), and pH (Zhao et al., 2017b). While the incorporation mechanisms of trace elements in mollusc shells are not yet fully understood, we do know that the incorporation of some trace elements, such as strontium, are influenced by local growth rates between different growth axes, shell curvature along the same axis, and physiological effects (Carré et al., 2005; Foster et al., 2009; Gillikin et al., 2005; Gillikin et al., 2008; Urey et al., 1951). Organic carboxyl-groups play a critical role for the incorporation of Mg into the shell (Shirai et al., 2012; Stephenson et al., 2008; Wang et al., 2009), but direct evidence for a similar role of organic molecules in the incorporations of

other trace elements is lacking. Indeed, different trace elements (e.g. Mg, K, Ca, Sr) show distinctly different interaction with organic molecules and influence on mineral growth (Sand et al., 2017) showing that generalisation for the role of trace elements in biomineralisation are not straightforward.

A critical step forward in our understanding of how trace elements are incorporated into the growing biomineral is to gain better insight across all spatial scales into how different shell architectures are formed. Traditionally, studies on shell formation have been focusing on the nacreous ultrastructure (Checa et al., 2006; Nudelman, 2015), while more recently other ultrastructures, such as the crossed-lamellar architecture received increasing attention (Agbaje et al., 2017b; Almagro et al., 2016; Böhm et al., 2016). Here we present data and detailed characterization of two rarely investigated ultrastructures, namely the compound composite prismatic and the crossed-acicular ultrastructure, which are common to bivalves of the *Veneridae* family (Shimamoto, 1986).

We are using a combination of pulse Sr labelling aquaculture experiments and high-resolution microanalytical methods to gain insight into submicron architecture and growth dynamics in the two different portions of the outer shell layer. Pulse Sr labelling experiments have contributed significantly to our understanding of submicron scale growth mechanisms in marine calcifiers such as scleractinian corals, echinoderms and foraminifera (Domart-Coulon et al., 2014; Gorzelak et al., 2014; Gutner-Hoch et al., 2016; Nehrke et al., 2013; Shirai et al., 2012). Since pulse Sr labelling experiments provide time gauges for shell growth at high spatial resolution, this method enables study of time-resolved growth of individual submicron sized architectural units in the shell relative to local growth, which, due to the curvature of the shell, can vary by up to 90° in direction from the direction of dorso-ventral shell extension in bivalves.

## 2.2 Materials and methods

### 2.2.1 Aquaculture and labelling experiments

The “common cockle” or “ridged venus” *Katelysia rhytiphora* (Lamy) is a temperate, shallow burrowing, intertidal species that occurs along the shorelines of Tasmania and south-eastern to south-western Australia (Edgar, 2000). Some species of the genus *Katelysia* are edible (*K. peronei*, *K. rhytiphora*, and *K. scalarina*) and have been a historical food source in Australia as seen by their occurrence in aboriginal shell middens (Cann et al., 1991). Today, *Katelysia* are produced in aquaculture (Nell et al., 1994), and shells in the wild are used to extract environmental parameters (Nell and Paterson, 1997). *K. rhytiphora* shells were collected alive at Port Lincoln, South Australia from fine- to medium-grained sand in the intertidal zone. Twenty-nine bivalves were placed in polyethylene boxes (20 x 40 x 10 cm, 7 bivalves per box) filled with sterilized beach sand and placed within 50 litre polyethylene tanks at the seawater facility at Macquarie University in September 2016. All tanks were connected to a recirculating system with filtered, sterilized natural seawater. Temperature and water chemistry, including salinity, pH matched ocean values. The setup in smaller sand-filled boxes enabled easy and quick transfer of the bivalves between the larger tanks, thus minimizing handling stress. Indeed, the

bivalves were observed to continue filter-feeding while being transferred, which is a reliable sign for the absence of handling stress. Acclimatisation period was 3 weeks and experiments lasted 36 days. A 12h/12h day/night light cycle was maintained throughout the experiment and the water was homogenized using an air-stone. The bivalves were fed daily with a mix of microalgae “Shellfish Diet 1800” (Reed Mariculture Inc., USA) containing *Isochrysis sp.*, *Pavlova sp.*, *Tetraselmis sp.*, *Chaetoceros calcitrans*, *Thalassiosira weissflogii*, and *Thalassiosira pseudonana*. After acclimatisation, bivalves were transferred twice for 6 days each to labelling seawater conditions at 18 x mean ocean water average of  $144 \mu\text{g}\cdot\text{g}^{-1}$  Sr ( $4.380 \text{ g SrCl}_2 \times 6\text{H}_2\text{O}$  in 10 l seawater). Between labelling events, bivalves spent 12 days at normal seawater conditions (ca.  $8 \mu\text{g}\cdot\text{g}^{-1}$  Sr). After the last labelling event, some bivalves were collected after 6 days at ambient conditions, while the remaining specimens were collected after 12 days. The pulsed Sr labelled periods are referred to as “labelling events”, LE1 and LE2, whereas “normal events” NE1 and NE2 refer to background conditions, with ambient marine Sr levels. The water quality was maintained by fully renewing the spiked seawater every 48 hours with a freshly produced batch (using  $4.380 \text{ g SrCl}_2 \times 6\text{H}_2\text{O}$  per 10 l seawater). Over the entire course of aquaculture an effort was made to keep the conditions (temperature, salinity, pH, lighting), including food availability, as stable as possible, so that Sr-concentration in the seawater was the only altered variable. After the experiments, bivalves were deep-frozen at  $-20^\circ\text{C}$ . After thawing and removing of soft tissues, shells were rinsed in deionized water and air-dried.

### 2.2.2 Sample preparation

Valves were cut along the maximum growth axis using an IsoMet low speed precision sectioning saw (Buehler, IL, USA). Left valves were mounted using EpoFix epoxy resin (Struers, Australia), while 3 mm-thick shell slabs from right valves were fixed on microscopy glass slides using metal bisphenol-A-epoxy resin (Permatex, Hartford, CT, USA). After curing at room temperature, sample surfaces were ground and polished using sandpaper (P400-P2000) as well as 3 and  $1 \mu\text{m}$  diamond pastes. Left valves were further polished using a final chemical polishing step with a diluted suspension of colloidal silica ( $0.05 \mu\text{m}$ ) for one minute on a neoprene polishing cloth to ensure optimum conditions for high-resolution analyses. Additional shell pieces were immersed in a solution of 1% wt./vol. ethylenediaminetetracetic acid disodium salt dihydrate (EDTA; Sigma-Aldrich), ultra-sonicated for 6 minutes, rinsed with Milli-Q water and air-dried. For SE-images un-etched broken shell pieces and some etched with EDTA (1 % wt./vol) were mounted on aluminium stubs using carbon glue, and gold-coated with a thickness of 15 nm.

### 2.2.3 Optical microscopy

A Leica M205C binocular stereomicroscope with reflective light was used to image shell slabs along the entire shell cross-section. Images were stitched and contrast improved in Adobe Photoshop CS5. To obtain greyscale line profiles, the image part containing the prismatic oOSL was cropped and further improved in contrast. Greyscale line profiles were acquired using ImageJ (Schindelin et al., 2015).

#### *2.2.4 Electron probe micro analyser (EPMA), field emission gun scanning electron microscopy (FEG-SEM) and electron backscatter diffraction (EBSD)*

Quantitative wavelength-dispersive X-ray spectroscopy (WDS) was carried out using a JEOL JXA 8200 electron probe micro analyser (EPMA) at the University of Mainz, Germany, with a defocused beam in rastering mode at 20,000 x magnification to obtain concentrations of Na, Mg, P, S, Cl, K, Ca, Mn, Fe, Sr, and Ba calibrated against a variety of minerals and synthetic reference materials (Supplementary Table 2.1). Backscattered electron (BSE) images at lower magnification were acquired from carbon-coated polished cross-sections. Specimens were imaged with 15 kV acceleration voltage and 8 nA beam current at 11 mm working distance. Epoxy mounts and broken pieces of shells were imaged with field-emission gun scanning electron microscopes (FEG-SEM), namely a JEOL JSM- 7100F and a Phenom XL at Macquarie University (BSE images at 15 kV and 8 nA), and a ZEISS Leo 1530 at the Max Planck Institute for Chemistry, Germany, for secondary electron (SE) images (at 3 kV and 2 nA).

Electron backscatter diffraction (EBSD) data were acquired at Oxford Instruments NanoAnalysis, High Wycombe, United Kingdom, using a Hitachi SU70 FE-SEM equipped with an Oxford Instruments AZtec 3.4 EBSD-EDS system, with an X-Max 150 mm<sup>2</sup> EDS detector and a CMOS-based Symmetry EBSD detector. Three EBSD maps were collected along the axis of maximum growth in different regions of interest using 15 kV accelerating voltage, a beam current of 10 nA and a step size of 0.1  $\mu\text{m}$ . The EBSD pattern resolution was 156 x 128 pixels at a collection rate of 195 patterns per second. Noise reduction was performed using the HKL software and datasets were processed using the MTEX toolbox in Matlab (Bachmann et al., 2010; Mainprice et al., 2011) following the protocol in Henry et al. (2017). All EBSD data points were used for the calculation of the Young's modulus.

#### *2.2.5 Micro-Raman spectroscopy*

Raman spectra were recorded at room temperature using a Horiba Jobin Yvon LabRAM HR Evolution spectrometer coupled to an Olympus optical microscope with the laser beam path aligned through the microscope objective (quasi-backscattering configuration). A diode-pumped solid-state laser with 473 nm ( $\sim 15$  mW at sample surface) and a He-Ne laser with 633 nm ( $\sim 10$  mW at sample surface) excitation wavelength were used. Spectra recorded in the red spectral range ( $\lambda_{\text{exc}} = 633$  nm) have a spectral resolution of 0.8  $\text{cm}^{-1}$  and a pixel resolution of 0.3  $\text{cm}^{-1}$ ; those recorded in the blue spectral range ( $\lambda_{\text{exc}} = 473$  nm) have a spectral resolution of 1.6  $\text{cm}^{-1}$  and 0.6  $\text{cm}^{-1}$  pixel resolution using a grating with 1800 lines/mm.

Hyperspectral images were obtained using a software-controlled x-y table and a step width of 0.6  $\mu\text{m}$ . All instrument set-up parameters and measurement conditions were kept constant during automated point-by-point spectra acquisition to guarantee subtle changes of Raman band parameters to be recorded reliably. Minute modification of Raman band parameters as obtained from hyperspectral mapping were interpreted only qualitatively. Data reduction included background subtraction and peak fitting using Lorentzian-Gaussian (pseudo-Voigt) function. All FWHM values were corrected for the instrumental apparatus function using the empirical correction published in Váczi (2014).



### 2.2.6 NanoSIMS analysis

Epoxy mounts were gold-coated prior to introduction into a new generation CAMECA NanoSIMS 50L ion probe equipped with a Hyperion RF plasma oxygen ion source, at the University of Western Australia. The primary oxygen ion beam was focused to a diameter of 100 nm and images were acquired from  $100 \times 100 \mu\text{m}^2$  areas at a resolution of  $1024 \times 1024$  pixels with a dwell time of 3.6 ms/pixel.  $^{24}\text{Mg}$ ,  $^{40}\text{Ca}$ , and  $^{88}\text{Sr}$  were measured on electron multipliers at a mass resolving power of 5000. The imaged areas were pre-sputtered at a slightly larger map area prior to acquisition. Images were processed using the OpenMIMS plugin for ImageJ/FIJI, where a correction for detector dead time was applied and the ratio of  $^{88}\text{Sr}/^{40}\text{Ca}$  are expressed as a Hue-Saturation-Intensity (HSI) colour scale – min (blue) = 10, max (magenta) = 100.

### 2.2.7 Thermal gravimetric analysis (TGA)

Using a DREMEL power tool, fractions of both portions of the outer shell layer were obtained by removing the iOSL in one shell fragment and the oOSL in another. Both samples were soaked in  $\text{H}_2\text{O}_2$  (Merck KGaA, Darmstadt; Germany) for 1 hr at room temperature and washed with Milli-Q water. After air-drying, each sample was powdered using an agate mortar and pestle. Total amounts of organics were determined with a TGA 2050 thermogravimetric analyser (TA Instruments, USA). About 10 mg of powdered sample was measured (two replicates). The analysis was carried out under a nitrogen atmosphere, at a linear heating rate of  $10^\circ\text{C}/\text{min}$ , between  $25\text{--}1000^\circ\text{C}$ .

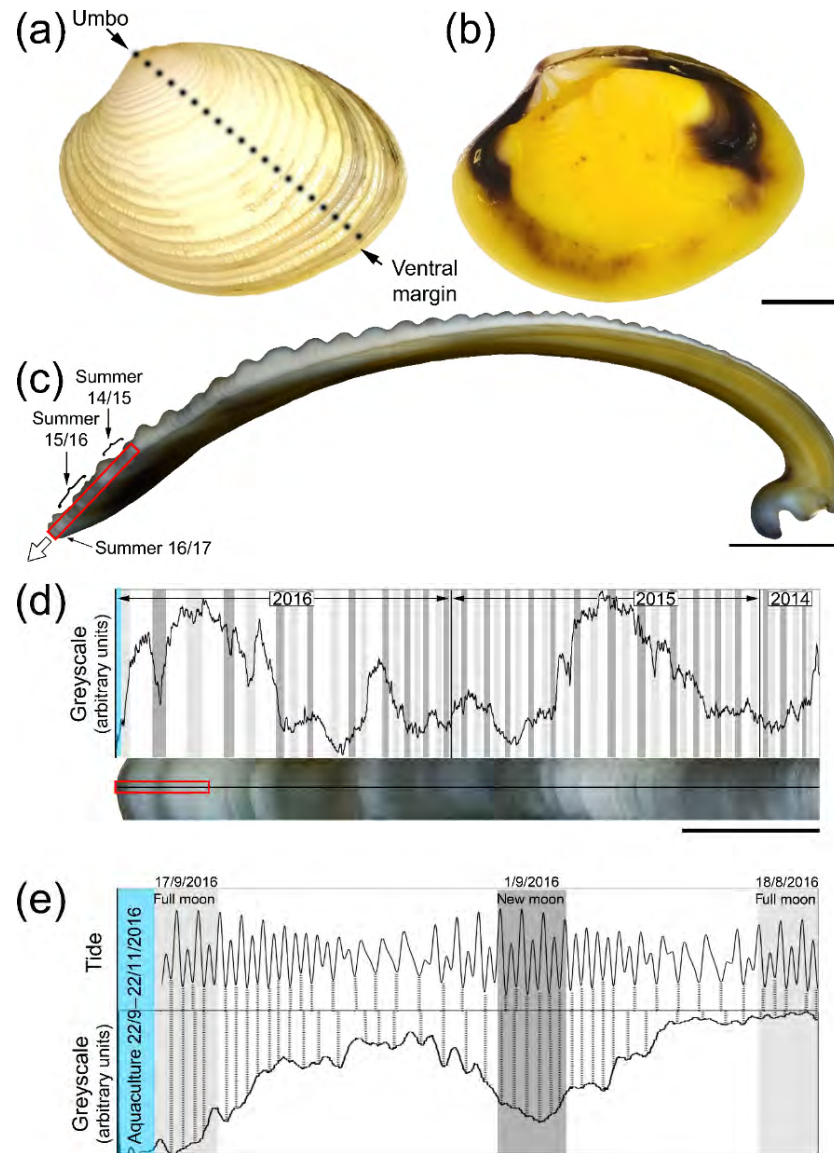
## 2.3 Results

### 2.3.1 Ultrastructure and growth

The outer surface of *K. rhytiphora* shells show prominent, concentric ridges (Figure 2.1a) and a yellow and purple to brown pigmentation on the inside (Figure 2.1b). The shell is fully aragonitic (Supplementary Figure 2.1) and our study focussed on the two architecturally different outer layers of the shell, to the outside of the pallial line. Underneath a very thin periostracum (see subchapter 2.3.4), the outermost outer shell layer (oOSL) consists of a compound composite prismatic architecture, while the innermost outer shell layer (iOSL) has a crossed-acicular ultrastructure. General thickening of the whole shell is achieved by the inner layer beyond the pallial line (Figure 2.1c). The oOSL of *K. rhytiphora* shells studied here is characterised by three dark bands near the ventral margin (Figure 2.1c-e). A minor dark band at the very tip of the shell corresponds to growth in November when the bivalves were sacrificed (Figure 2.1c-e).

The compound composite prismatic ultrastructure, which is considered to be one of the most complex shell architectures known represents an umbrella-term for a family of differently arranged hierarchical prismatic ultrastructures (Popov, 1986; Shimamoto, 1986; Taylor, 1969). First-order prisms in the oOSL have thicknesses between  $10\text{--}30 \mu\text{m}$  and run parallel to the outer shell surface, with the long axis of the prisms oriented parallel to the main growth axis (Popov, 1986). These first-order units consist of  $0.3 \mu\text{m}$

thick second-order prisms (Shimamoto, 1986) that protrude radially from the central axis of first-order prisms creating a feather-like appearance when viewed in cross-section (Shimamoto, 1986; Taylor, 1969). Each prism in both hierarchical orders is covered by a thin organic sheath (Shimamoto, 1986; Taylor, 1969). Taylor (1969) also observed smaller units within second-order prisms delineated by organic matrix and we refer to these units as third-order prisms here.



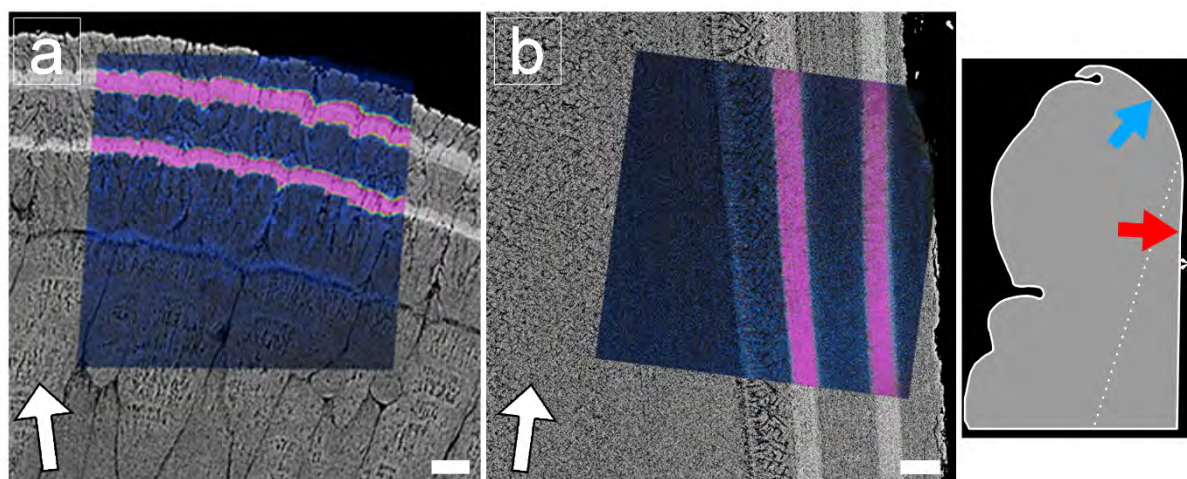
**Figure 2.1:** Outer (a) and inner shell surface (b) of an unlabelled *K. rhytiphora* shell. Dashed black line in (a) indicates where the shell was cut to produce the cross-section where a white arrow in (c) indicates the general growth direction of the shell. All cross-sections in this study are prepared as radial sections along the maximum growth axis unless otherwise specified. Dark bands (indicated by arrows in c) result from growth during summer between lighter coloured winter periods and are magnified in d (red box in c) with a greyscale line profile. Darker greyscale intensities correlate with 48 out of 50 spring tides in two years from the collection site of the bivalves (full moon: light grey, new moon: dark grey) suggesting a fortnightly growth resolution in this shell area. Greyscale line profiles (e) of the area marked by the red box in D shows the most recent dark shell growth increment formed in the wild (mid-August to mid-September 2016). In this shell part, tides correlate with most shell increments (black dashed lines), while this correlation is lost after start of aquaculture (blue area). Blue area in d, e marks the aquaculture period with lower than normal growth rates. Scale bars are 10 mm (a-b), 5 mm (c), 1 mm (d), 0.1 mm (e).

Two different schools of thought group the crossed-acicular ultrastructure with other structurally related architectures: Shimamoto (1986) classifies the crossed-acicular ultrastructure as a subtype of the homogeneous ultrastructure, while Marin et al. (2012) groups the crossed-lamellar, complex crossed-

lamellar, and crossed-acicular ultrastructures together. The crossed-acicular ultrastructure has previously been comprehensively described for the marine gastropod *Cuvierina* (Carter, 1989) and consists of single lamellae that are arranged into bundles intersecting at angles of 120-150° with dipping angles of 30 to 40° relative to the inner shell surface (Carter, 1989).

### 2.3.2 Validation of Sr-incorporation

Qualitative NanoSIMS mapping revealed two distinct bands of elevated Sr concentration in the oOSL at the ventral margin (Figure 2.2a) as well as in the iOSL ca. 0.5 mm away from the ventral margin (Figure 2.2b). Correlation of NanoSIMS maps with BSE images verify that light greyscales in BSE images are indeed caused by higher concentrations of Sr in the shell.



**Figure 2.2: FEG-SEM BSE images showing polished cross-sections of the oOSL (a) and iOSL (b) of a Sr-labelled *K. rhytiphora* shell (specimen ID: K2-06) overlain with NanoSIMS  $^{88}\text{Sr}/^{40}\text{Ca}$  maps. Shell layers grown in ambient seawater  $^{88}\text{Sr}/^{40}\text{Ca}$  ratios are depicted in blue, while shell formed during Sr-enriched incubations are shown in pink. White arrows point towards the general growth direction of the shell, while the Sr-labelled shell layers from the underlying BSE image visualise the local growth directions for each ultrastructure. A schematic of the shell tip shows the exact location of the NanoSIMS maps with a blue and red arrow pointing towards the locations of the prismatic oOSL (a) and crossed-acicular iOSL (b) sampling location, respectively. Asterisk marks the inner shell surface. Scale bars are 10  $\mu\text{m}$ .**

EPMA-based WDS analyses (Tables 2.1 and Supplementary Table 2.2) show that Sr contents are generally higher in the oOSL than in the iOSL, averaging 19,500  $\mu\text{g}\cdot\text{g}^{-1}$  for the oOSL and 12,000  $\mu\text{g}\cdot\text{g}^{-1}$  for the iOSL (note that the value for iOSL is a minimum value as the analysed area slightly exceeds the label width). Strontium concentrations in growth regions formed before aquaculture (pre-aqua), during acclimatisation (pre-LE 1) and between labelling events (NE 1) are around 1,120  $\mu\text{g}\cdot\text{g}^{-1}$  for oOSL and again lower (1,010  $\mu\text{g}\cdot\text{g}^{-1}$ ) for the iOSL (Table 2.1 and Supplementary Table 2.2). Likewise, average molar ratios of Sr/Ca (mmol/mol) range from 1.32 (oOSL) and 1.18 (iOSL) in shell sections grown during ambient conditions in aquaculture to 14.55 (iOSL) and up to 23.60 (oOSL) in shell portions grown during pulse labelling. Hence, the increase of 18x mean ocean water concentrations (144  $\mu\text{g}\cdot\text{g}^{-1}$  Sr) in seawater resulted in a 17x increase in Sr in the oOSL (18,500  $\mu\text{g}\cdot\text{g}^{-1}$ ) in the labelled compared to the unlabelled conditions and in about 12x increase for the iOSL (>10,970  $\mu\text{g}\cdot\text{g}^{-1}$ ). Concentrations of other minor elements (Na, Mg, S, Cl) are generally lower in the iOSL and were identical within uncertainty between labelling and non-labelling experiments. Molar ratios for Na/Ca and Mg/Ca range

from 13.56 to 25.91 and from 0.76 to 1.05, respectively, and do not correlate with high Sr concentrations. Concentrations of Mn, Ba, P, K, and Fe in the shells are below detection limits.

**Table 2.1: Geochemical composition of *K. rhytiphora* obtained from wavelength-dispersive X-ray spectrometry (WDS) electron probe micro analyser (EPMA) provided as  $\mu\text{g}\cdot\text{g}^{-1}$  averages (Avg.) and standard deviations (Stdev.) as well as molar element/Ca ratios for shell compositions grown under different conditions in the wild (“pre-aqua”), in aquaculture during pulsed Sr-labelling (“LE 1” and “LE 2”), and non-labelling (“pre-NE 1” and “NE 1”) periods.**

			Na	Mg	S	Cl	Ca	Sr	Na/Ca	Mg/Ca	Sr/Ca
Compound composite prismatic	Pre-Aqua	Avg.	5,300	180	400	400	389,000	1,000	23.95	0.77	1.19
	(n=5)	Stdev	450	120	160	100	1,400	300	2.00	0.51	0.30
	Pre-LE 1	Avg.	4,200	240	560	400	391,000	1,100	18.84	1.02	1.29
	(n=3)	Stdev	300	60	120	100	500	90	1.32	0.25	0.10
	LE 1	Avg.	4,200	240	480	300	378,000	20,000	19.17	1.05	24.16
	(n=3)	Stdev	300	60	80	100	600	600	1.37	0.26	0.72
	NE 1	Avg.	3,000	180	680	300	391,000	1,350	13.56	0.76	1.58
	(n=3)	Stdev	70	180	200	200	3,100	90	0.33	0.76	0.10
	LE 2	Avg.	4,800	240	480	200	385,000	19,000	21.86	1.03	23.04
	(n=3)	Stdev	300	60	120	100	1,100	200	1.35	0.26	0.20
Crossed- Acicular*	Pre-Aqua	Avg.	5,600	bdl	200	200	386,000	900	25.12	bdl	1.10
	(n=5)	Stdev	670	-	240	100	400	300	3.01	-	0.40
	Pre-LE 1	Avg.	5,700	bdl	200	200	384,000	900	25.91	bdl	1.01
	(n=3)	Stdev	670	-	120	200	500	300	3.03	-	0.40
	LE 1	Avg.	5,600	bdl	520	300	380,000	>12,000	25.52	bdl	>14.55
	(n=3)	Stdev	670	-	280	100	400	300	3.06	-	0.41
	NE 1	Avg.	5,300	180	800	200	390,000	1,300	23.89	0.77	1.49
	(n=3)	Stdev	670	300	280	200	400	300	2.99	1.28	0.40
Limits of Detection:			400	100	100	100	300	200	-	-	-

Mn, Ba, P, K, and Fe, were analysed and were always below detection limits ( $200 \mu\text{g}\cdot\text{g}^{-1}$  for Mn, Ba, Fe and  $100 \mu\text{g}\cdot\text{g}^{-1}$  for P, K). \*LE2 and NE 2 in the crossed-acicular ultrastructure (iOSL) were too close to the edge and are excluded, LE1 is a minimum value as the analysed area slightly exceeds label width. See Supplementary Table 2.2 for data in wt.% ( $\text{g}\cdot\text{g}^{-1}$ ) oxide.

### 2.3.3 Raman spectroscopy

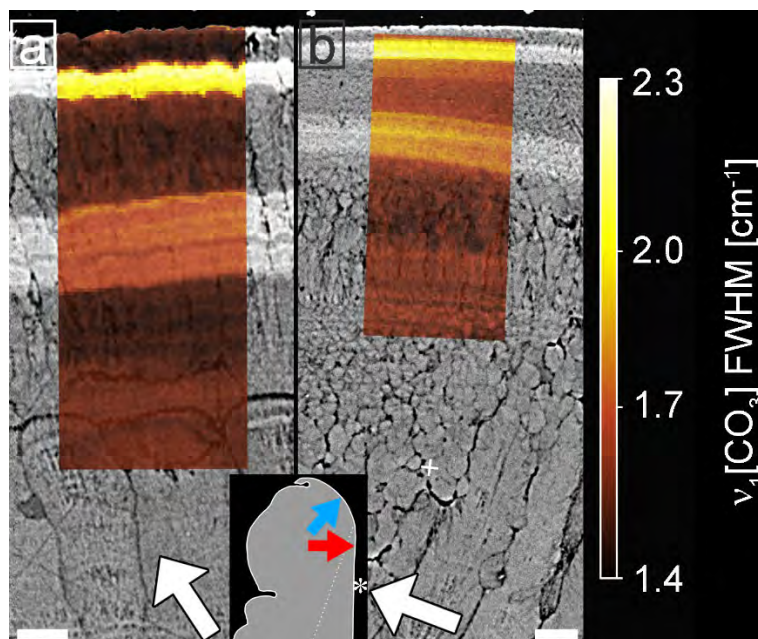
Raman spot analyses in both studied shell layers show peak positions characteristic for aragonite (Supplementary Figure 2.1), namely a doublet at 701 and 705  $\text{cm}^{-1}$  ( $\nu_4$ ,  $\text{CO}_3$  in-plane bending), a peak at 1084.8  $\text{cm}^{-1}$  ( $\nu_1$ ,  $\text{CO}_3$  symmetric stretching), and several modes between 170 and 300  $\text{cm}^{-1}$  that are due to rotations and translations of  $\text{Ca}^{2+}$  and  $\text{CO}_3^{2-}$  units (Carteret et al., 2013; Urmos et al., 1991; Wehrmeister et al., 2010). In addition, broad bands centred at 1134 and 1532  $\text{cm}^{-1}$  represent C-C single bond ( $\nu_2$  stretching mode) and C=C double bond ( $\nu_1$  stretching mode) vibrations of polyene chains in organic pigments in the shell (Otter et al., 2017).

Micro-Raman hyperspectral mapping of the most intensive peak at 1084.8  $\text{cm}^{-1}$  revealed that band widths (full-width at half-maximum, FWHM) differ between Sr labelled and unlabelled areas (Figure 2.3). Two regions with systematic peak broadening in both ultrastructures correspond to the Sr labels seen as bands of light greyscale in BSE images and represent a change in concentration from 19,500  $\mu\text{g}\cdot\text{g}^{-1}$  Sr in labelled to 1,120  $\mu\text{g}\cdot\text{g}^{-1}$  in shell portions grown in ambient conditions. Although Sr concentrations in the seawater and duration of labelling conditions were identical for all labelling periods, the more recent outer label (LE 2) is narrower and brighter than in the earlier label (LE 1), reflecting different shell growth rates. Band width distribution shows distinct narrow increments within both labels.

Highest FWHM values within each labelled area are 2.2 and 2.7  $\text{cm}^{-1}$  for the oOSL (Figure 2.3a) and 1.8 and 2.4  $\text{cm}^{-1}$  for the iOSL (Figure 2.3b, Supplementary Table 2.3), while FWHMs in unlabelled



areas are less than  $1.8 \text{ cm}^{-1}$ . The  $\nu_1$  symmetric stretching band shows a shift in peak position to lower wavenumbers in areas of high Sr concentration (Supplementary Figure 2.2, Supplementary Table 2.3). Note that FWHMs and peak positions do not vary among different architectural features in the unlabelled shell architecture, and hence, are not influenced by grain size effects.



**Figure 2.3:** Micro-Raman maps (sample K2-04) showing the effect of Sr concentrations on the FWHM of peak  $\nu_1$  at  $1084.8 \text{ cm}^{-1}$  in the oOSL (a) and iOSL (b). Raman maps are overlain on BSE images. White arrows point towards the general growth direction of the shell, while the Sr-labelled shell layers from the underlying BSE image visualise the local growth directions for each ultrastructure. For Micro-Raman maps of peak shifts see Supplementary Figure 2.2. All values are bandwidth corrected after Váczi (2014). A schematic of the shell tip shows the exact location of the Raman maps with a blue and red arrow pointing towards the locations of the prismatic oOSL and crossed-acicular iOSL sampling location, respectively. Asterisk marks the inner shell surface. Scale bars are  $10 \mu\text{m}$ .

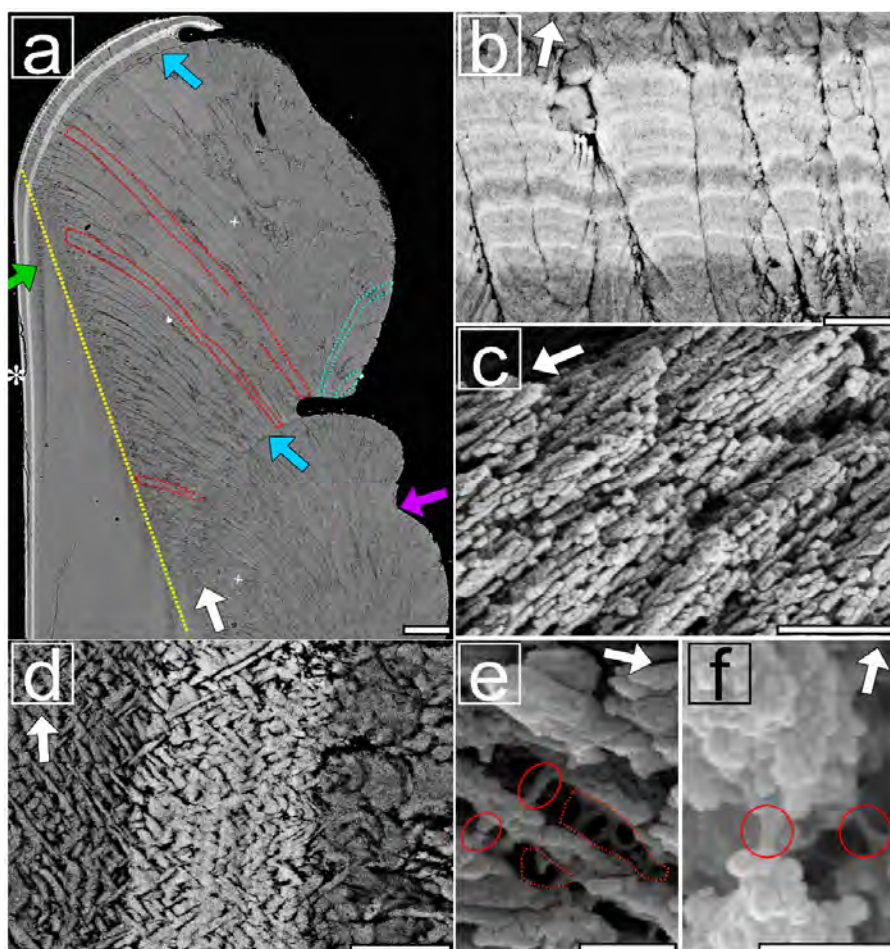
### 2.3.4 Architecture of the outer shell layer

#### 2.3.4.1 The compound composite prismatic layer (oOSL)

As visible in radial sections of the oOSL (Figure 2.4a) first-order prisms are oriented with their long sides parallel to the umbo-ventral margin axis and form a fan-like arrangement resulting in the ridged outer surface (Popov, 1986; Shimamoto, 1986; Taylor, 1969). First-order prisms originate and end at the organic-rich growth checks (Figure 2.4a) and can reach sizes of  $>700 \mu\text{m}$  (projected 2D length) and widths of  $17 \mu\text{m}$  (aspect ratio of  $>40$ ). Growth checks can be organic rich as observed here, or are fully mineralized with a different morphology, such as a thin layer of prisms (see below; Ropes et al., 1984). In contrast to studies that reported first-order prisms to exhibit square shapes in longitudinal cross-sections (e.g., Taylor, 1969), we observed irregular six-sided prism cross-sections in these *Katelsysia* shells (Supplementary Figure 2.4). Measured widths of around  $17 \mu\text{m}$  compare to literature values of around  $10 \mu\text{m}$  for other venerid shells (Shimamoto, 1986). First-order prisms consist of second-order prisms arranged radially around their central axis at an angle of  $68^\circ$  (Figure 4b, Supplementary Figure 5), resulting in a feathery arrangement of second-order prisms in cross-sections (Popov, 1986; Shimamoto, 1986). Individual second-order prisms have projected lengths and widths of  $3 \pm 0.3 \mu\text{m}$  and  $0.3 \pm 0.06 \mu\text{m}$  ( $n=8$ ), with an aspect ratio of 10. The widths are in accordance with values provided by

Shimamoto (1986) for the shells of other venerid shells. Both first- and second-order prisms were found to be enveloped by organic sheaths as indicated by darker greyscales in the BSE images (Figures 4a-b, Supplementary Figure 4) supporting literature findings for this ultrastructure (Shimamoto, 1986; Taylor, 1969).

Second-order prisms consist of third-order prisms (Figure 2.4c), which are arranged with their long axes parallel to each other. They have lengths of  $496 \pm 129$  nm and widths of  $67 \pm 16$  nm ( $n=8$ , Supplementary Figure 2.6) with a lower aspect ratio of 8 compared to first- and second-order prism. Lastly, the smallest building blocks revealed by SEM images in etched shell samples are nano-granules with sizes in the range of 70 nm (Figure 2.4e, f).



**Figure 2.4:** Electron images showing a cross-sections along the maximum growth axis of Sr-labelled *K. rhytiphora* shells: (a) BSE image shows the ventral margin of the shell. First-order prisms in the prismatic oOSL bend inwards (red outlined) reach lengths of up to 700  $\mu\text{m}$  with widths of 17  $\mu\text{m}$ . Outward bending prisms (blue outlined) form the ridged surface ornamentation of the shell. Growth checks (blue arrows) are observed to occur directly at the end of ridge feature, while not all ridge features are concluded by growth checks (purple arrow). The yellow dashed line marks the boundary between iOSL and oOSL. Both Sr labels show bright greyscales and follow the growth front of the shell. In the iOSL, the growth check continues as a prismatic layer (green arrow). Strontium-labels within the oOSL (b) show first-order prisms that consist of radially arranged second-order prisms, which in turn consist of third-order prisms with their long axis parallel to each other, as seen in a broken piece of shell (c, SE-image). The iOSL has a crossed-acicular ultrastructure (d, BSE image) that is composed of needle-like lamellae intersecting at an angle of ca.  $82^\circ$ . Etched specimens (e, f: SE images) reveal the nano-granular texture of the mineral phase as well as organic compounds with fibre (red circles) and sheet-like structures (dashed red lines) in the prismatic (e) and crossed-acicular (f) layers. White arrows point towards the general growth direction of the shell, while the Sr-labelled shell layers in BSE images visualises the local growth directions for each ultrastructure. For more details see Supplementary Figure 2.3-2.8. Scale bars: 100  $\mu\text{m}$  (a), 5  $\mu\text{m}$  (b and d), and 500 nm (c, e and f).

#### 2.3.4.2 The crossed-acicular layer (iOSL)

The acicular-prismatic boundary is marked by a ca. 30  $\mu\text{m}$  wide transitional layer of granular texture comprising high numbers of short first-order prisms and spherulitic grains (Supplementary Figure 2.3). The growth check, which is organic rich in the oOSL, continues as a thin prismatic layer into the crossed-acicular ultrastructure of the iOSL (Figure 2.4a, green arrow). Bundles of cross-layered lamellae in the iOSL are enveloped by organic sheaths (dark grey, Figure 4d, Supplementary Figure 7) and measure up to 1.4 x 0.8 x 0.2  $\mu\text{m}$  (Supplementary Figure 2.8). Individual acicular lamellae are  $1.8 \pm 0.4 \mu\text{m}$  long and  $0.22 \pm 0.05 \mu\text{m}$  (n=19) wide with aspect ratios of about 8 (Figure 4d, Supplementary Figure 7). The angle between acicular lamellae is  $81 \pm 8^\circ$  (n=6). Similarly, to the oOSL, etching revealed a nano-granular texture in this layer (Figure 2.4f).

#### 2.3.4.3 Organic content

Thermal gravimetric analysis (TGA) was used to determine the total amount of organic macromolecules in the shell, which amounts to  $1.42 \pm 0.03 \text{ wt.}\%$  and  $2.19 \pm 0.04 \text{ wt.}\%$  for the iOSL and oOSL, respectively (Supplementary Figure 2.9). The organic phases are visible after etching the mineral phase and exhibit fibre- and sheet-like shapes (Figure 2.4e, f).

#### 2.3.5 Crystallographic preferred orientations

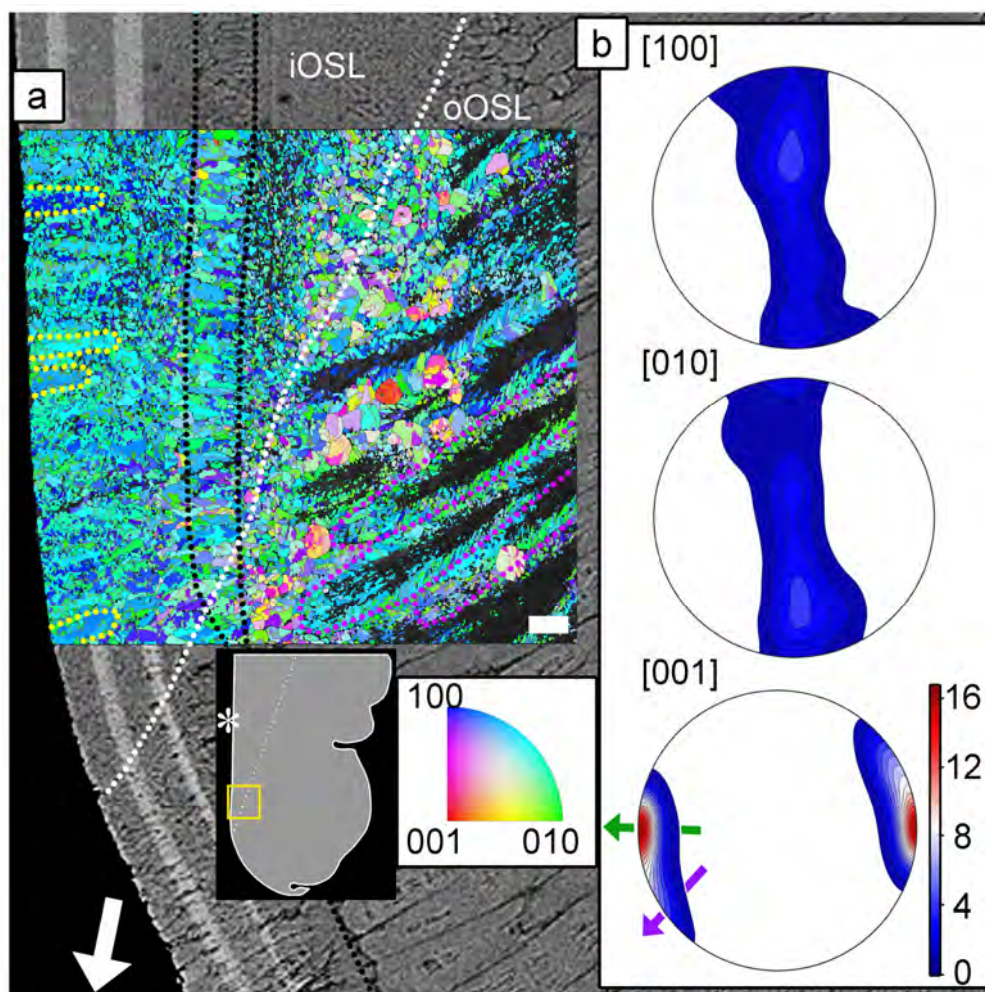
The ultrastructure of the aragonite grains in the oOSL and iOSL shell layers is shown in the orientation map in Figure 2.5a. The map is colour-coded using an inverse pole figure colour scheme and shows the crystal direction in the orientation map facing the reader with blue, green, and red for the crystallographic a- [100], b- [010], and c-axis [001], respectively. Figure 2.5a shows the feathery arrangement of the second-order prisms within the first-order prisms (outlined in green) as described above. The rims of the first-order prisms in the oOSL are well-resolved in the orientation map (Figure 5, Supplementary Figure 10), while most of their cores remains dark and unindexed, indicative of poor or non-existent diffraction patterns as measured during the EBSD indexing cycle. We believe this effect is an artefact of sample polishing arising from preferential removal of the nearly vertically oriented second-order prisms in these areas (Supplementary Figure 2.11). The alternative explanation, namely reduced crystallinity in these areas is highly unlikely as this would have been detected in Raman maps via significant band-width changes (Figure 3, Supplementary Figure 2).

The iOSL with crossed-acicular architecture shows ca. 17  $\mu\text{m}$  by ca. 10  $\mu\text{m}$  large areas of lamellae, where the aragonite crystallographic axes are well co-orientated (Figure 2.5a, outlined in yellow) and have high amounts of crystallographic twin boundaries (Figure 5 and Supplementary Figure 12).

Pole figures (Figure 2.5b) show a strong preferred orientation of the aragonite c-axes perpendicular to the growth layers in the crossed-acicular architecture, while the crystallographic a and b axes are scattered on a plane normal to the local growth direction. The local growth direction in the crossed-acicular ultrastructure (green arrow in Figure 2.5b) is perpendicular to the light grey Sr labels in the underlying BSE image and at this locality differs by ca.  $90^\circ$  from the general shell growth direction (white arrow). In comparison, the local growth direction of the compound composite prismatic layer



(oOSL: purple arrow in Figure 2.5b) has a smaller angle with the general shell growth direction. We identified a high abundance of twinning with 46 % (oOSL) and 56 % (iOSL) of the grains showing at least one twin (i.e.  $63.8^\circ \pm 5^\circ$  rotation around the 001 axis).



**Figure 2.5:** Orientation map for aragonite (a) of a pulsed Sr-labelled shell (specimen ID: K2-11) overlain on the BSE image of the same area. The dotted white line indicates the boundary between the crossed-acicular iOSL and prismatic oOSL shell layer portions. The organic growth check in the oOSL that continues as a prismatic layer in the iOSL is highlighted with black dotted lines. Blue, green, and red colours depict the crystallographic a- [100], b- [010], and c-axes [001] of aragonite, respectively. Twinned grain boundaries are presented in red. The map is color-coded to show the crystallographic orientation normal to the image plane. Predominantly green and blue colours in the map indicate that the a-[100] and b-[010] axes are randomly aligned mainly normal to the image plane. First-order prisms in the oOSL (some outlined in purple) have unindexed cores, and feathery arranged second-order prisms are visible at their rims. Individual lamellae of the iOSL form co-oriented stacks up to 17  $\mu\text{m}$  in size (circled in yellow). Pole figures (b) (lower hemisphere, equal area projection) show a strong clustering of the [001] axes for both layers. The local growth direction of the iOSL (green arrow), perpendicular to the light grey Sr-labelled layers in the underlying BSE image, differs by about  $90^\circ$  from the general growth direction (white arrow in (a)). The local growth direction of the oOSL (purple arrow) has a smaller angle with the general shell growth direction. The crystallographic a- and b-axes are randomly distributed in a plane normal to the local growth direction (i.e. parallel to the growth lines of the iOSL). Maximum density values of pole figures are colour-coded according to scale with the [001] axes achieving 16.8 times uniform. A schematic of the shell tip shows the location of the orientation map and the BSE image. Asterisk marks the inner shell surface. Scale bar is 10  $\mu\text{m}$ .

### 2.3.6 Local growth rates

The pulsed Sr labels are easily visible in both the oOSL and the iOSL in BSE images as bands of bright greyscale (Figure 2.4a). In general, greyscale values in BSE images cannot be relied on for trace element



quantification. In this study, however, we have calibrated the BSE grey scale using quantitative WDS-based EPMA measurements in the same analytical session. Moreover, correlative mapping of the Sr distribution with NanoSIMS and micro-Raman spectroscopy (Figure 2 and 3, Supplementary Figure 2) clearly correlates the bright greyscales in the BSE images spatially with the Sr-labelled areas. Thus, in this study, greyscales in the BSE images reflect variations in Sr concentrations on the shells without any doubt. Commonly, bivalve shell growth rates are reported as the macroscopic linear dorso-ventral shell extension (“general growth direction” in this study). Our high magnification images require us to take into account that local growth directions of the architectural units differ from the macroscopic linear dorso-ventral shell extension axis. Previously, these have been referred to as “crystal growth rate” (Carré et al., 2006; Gillikin et al., 2005). Instead, we use the term “local growth rate”, because “crystal growth rate” does not reflect recent research that established the mesocrystalline nature of the material, initially formed as amorphous calcium carbonate.

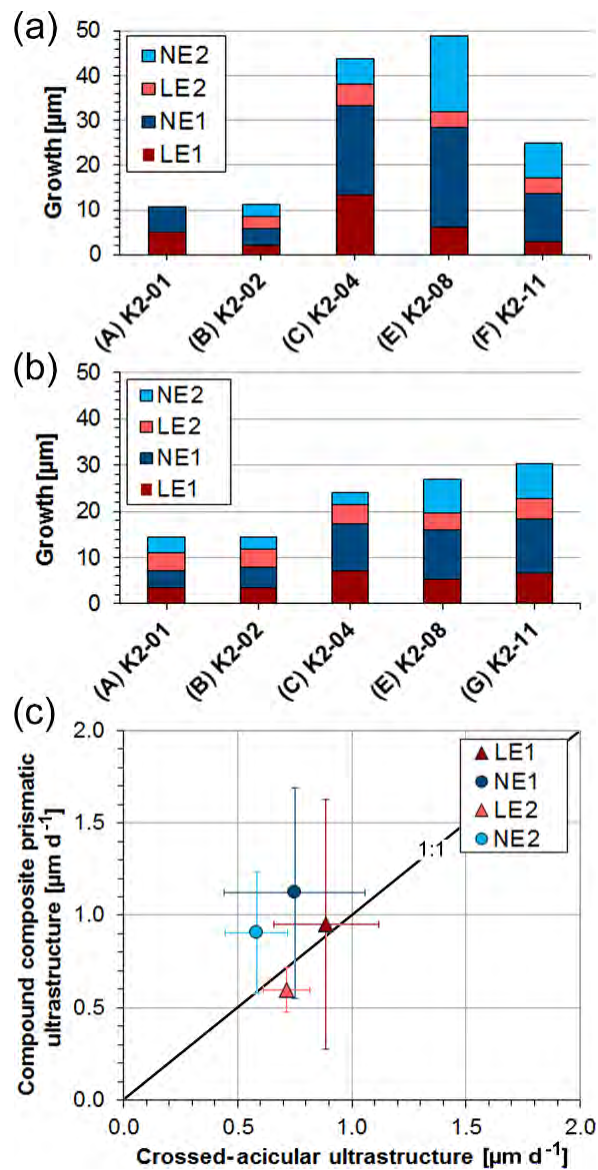


Figure 2.6: Average growth of the compound composite prismatic (oOSL) layer (a) and crossed-acicular layer (iOSL) (b) (for values see Table 2.2). Distances were measured in triplicate at 5 different locations (Supplementary Figure 2.14, 2.15) along the axis of maximum growth using the software ImageJ. Local growth rates shown in (c) agree well within the first standard deviation between labelling and ambient conditions.

Table 2.2 summarises the average local daily growth rates for all experiments (for detailed dataset see Supplementary Table 2.4 and 2.5). Length measurements were acquired in triplicate at five different locations on cross-sections along the maximum growth axis using the software ImageJ (Supplementary Figures 14, 15, Supplementary Table 2.4 and 2.5). Although sizes and ages of the bivalve shells are similar, absolute local growth rates vary among specimens, especially for the oOSL (Figure 2.6a, b). On a daily average within 6 days of pulsed Sr-labelling procedure, layer LE1 grew  $0.93 \pm 0.15 \mu\text{m}$  (range:  $0.37 - 2.22 \mu\text{m}$ ), while layer LE2 grew  $0.60 \pm 0.12 \mu\text{m}$  (range:  $0.43 - 0.80 \mu\text{m}$ ; Table 2.2 and Supplementary Table 2.4). A 12-day ambient period (NE1) resulted in an average daily growth of  $1.02 \pm 0.09 \mu\text{m}$  (range:  $0.31 - 1.86 \mu\text{m}$ ). The last 12-day ambient period (NE2) resulted in an average daily growth of  $0.76 \pm 0.08 \mu\text{m}$  (range:  $0.47 - 1.41 \mu\text{m}$ ). In comparison, the crossed-acicular ultrastructure (iOSL) grew only  $0.88 \pm 0.10 \mu\text{m}$  (range:  $0.58 - 1.17 \mu\text{m}$ ) during LE1 and  $0.72 \pm 0.05 \mu\text{m}$  ( $0.62 - 0.92 \mu\text{m}$ ) during LE2. Twelve days of ambient conditions (NE1) resulted in  $0.75 \pm 0.04 \mu\text{m}$  ( $0.31 - 1.13 \mu\text{m}$ ) daily average growth and for NE2 in  $0.47 \pm 0.03$  ( $0.43 - 0.84$ ). Based on average daily growth rates, oOSL grew 17 % faster than iOSL, which showed steadier growth (i.e. smaller standard deviations). Growth rates decrease with increasing distance to the ventral margin along iOSL (Figure 2.4a). Individual Sr labels offer further detail and comprise several narrow increments of varying width and greyscale intensity in both ultrastructures (Figures 4b, d). A systematic shift towards faster or slower local growth rates during Sr incubation was not observed (Figure 2.6c).

**Table 2.2: Average daily local growth rates from pulsed Sr-labelling experiments. Rates in bold in NE2 were formed within 6 days (K2-01 to K2-04), all other rates in this column are within 12 days (K2-06 to K2-11). Average daily local growth rates for the entire experimental period are  $0.85 \mu\text{m}$  (oOSL) and  $0.73 \mu\text{m}$  (iOSL). For full details lists of all measurements see Supplementary Table 2.3 and 2.4.**

Sample ID:	Shell layer	LE 1 [ $\mu\text{m}/\text{d}$ ]	NE 1 [ $\mu\text{m}/\text{d}$ ]	LE 2 [ $\mu\text{m}/\text{d}$ ]	NE 2 [ $\mu\text{m}/\text{d}$ ]	Total growth period [ $\mu\text{m}/30\text{d}$ ], [ $\mu\text{m}/36\text{d}$ ]	Daily growth period [ $\mu\text{m}/\text{d}$ ]
K2-01*	oOSL	$0.85 \pm 0.10$	$0.48 \pm 0.05$	n.a.	n.a.	<b><math>10.8 \pm 1.1</math></b>	$0.66 \pm 0.08$
	iOSL	$0.58 \pm 0.03$	$0.31 \pm 0.03$	$0.67 \pm 0.03$	$0.55 \pm 0.03$	<b><math>14.5 \pm 0.9</math></b>	$0.53 \pm 0.03$
K2-02	oOSL	$0.37 \pm 0.07$	$0.31 \pm 0.04$	$0.43 \pm 0.08$	$0.47 \pm 0.05$	<b><math>11.3 \pm 1.6</math></b>	$0.39 \pm 0.08$
	iOSL	$0.60 \pm 0.05$	$0.36 \pm 0.03$	$0.65 \pm 0.03$	$0.43 \pm 0.05$	<b><math>14.4 \pm 1.1</math></b>	$0.45 \pm 0.05$
K2-04	oOSL	$2.22 \pm 0.15$	$1.67 \pm 0.05$	$0.80 \pm 0.12$	$0.97 \pm 0.13$	<b><math>43.9 \pm 2.9</math></b>	$1.41 \pm 0.15$
	iOSL	$1.17 \pm 0.32$	$0.85 \pm 0.08$	$0.72 \pm 0.07$	$0.43 \pm 0.12$	<b><math>24.0 \pm 3.9</math></b>	$0.79 \pm 0.17$
K2-06	oOSL	$0.63 \pm 0.20$	$0.88 \pm 0.14$	$0.58 \pm 0.12$	$1.03 \pm 0.13$	$30.1 \pm 1.3$	$0.78 \pm 0.12$
	iOSL	$1.00 \pm 0.10$	$1.13 \pm 0.05$	$0.92 \pm 0.03$	$0.84 \pm 0.03$	$35.1 \pm 1.8$	$0.97 \pm 0.05$
K2-08	oOSL	$1.07 \pm 0.30$	$1.86 \pm 0.13$	$0.58 \pm 0.15$	$1.41 \pm 0.04$	$49.2 \pm 1.2$	$1.23 \pm 0.13$
	iOSL	$0.87 \pm 0.08$	$0.89 \pm 0.03$	$0.62 \pm 0.05$	$0.61 \pm 0.03$	$26.9 \pm 1.4$	$0.75 \pm 0.08$
K2-11	oOSL	$0.46 \pm 0.12$	$0.90 \pm 0.11$	$0.60 \pm 0.15$	$0.64 \pm 0.11$	$24.9 \pm 4.2$	$0.65 \pm 0.11$
	iOSL	$1.12 \pm 0.05$	$0.97 \pm 0.17$	$0.73 \pm 0.03$	$0.63 \pm 0.03$	$30.3 \pm 0.9$	$0.86 \pm 0.02$
	Av. oOSL	<b><math>0.93 \pm 0.15</math></b>	<b><math>1.02 \pm 0.09</math></b>	<b><math>0.60 \pm 0.12</math></b>	<b><math>0.76 \pm 0.08</math></b>	<b><math>28.4 \pm 2.1</math></b>	<b><math>0.85 \pm 0.11</math></b>
	Av. iOSL	<b><math>0.88 \pm 0.10</math></b>	<b><math>0.75 \pm 0.04</math></b>	<b><math>0.72 \pm 0.05</math></b>	<b><math>0.47 \pm 0.03</math></b>	<b><math>24.2 \pm 1.7</math></b>	<b><math>0.73 \pm 0.07</math></b>

\*This individual did not show prismatic growth after NE1, while the crossed-acicular ultrastructure kept growing.

## 2.4 Discussion

### 2.4.1 Multiscale architecture

Compared to simple prisms in the nacreprismatic bivalve ultrastructure the compound composite prismatic ultrastructure of *K. rhytiphora* is far more complex, containing three orders of prisms with sizes ranging from mm (first-order prisms) to nm (third-order prisms; Figures 4a-c, Supplementary Figure 11). With respect to the number of hierarchically distinct units, the compound composite prismatic ultrastructure shares more similarity with the crossed-lamellar architecture than with the simple prism ultrastructure (Agbaje et al., 2017b). In *K. rhytiphora*, the first-order prisms run perpendicular to the growth checks and radially with respect to the radial cross-section (Figure 2.4a) and comprise two orders of acicular prisms with high aspect ratios that are arranged feathery (radially in 3D around the central prism axis) in the case of second-order prisms and parallel in the case of third-order prisms (Figure 2.4b, c).

Organic contents of both shell layers, namely 2.2 wt.% in the oOSL and 1.4 wt.% in the iOSL (Figure 4e-f, Supplementary Figure 9), are intermediate between nacreprismatic shells (3-5 wt.% total organic content) and the highly mineralized crossed-lamellar shells with less than 1 wt.% organic content (Agbaje et al., 2017a).

Second-order prisms in the oOSL are co-oriented across their thin organic envelopes and, likewise, lamellae in the iOSL show co-orientation over 10  $\mu\text{m}$  (Figure 6a, Supplementary Figure 10). Co-orientation across the delineating organic sheath in the shell is a general observation for all bivalve shell architectures (e.g., Agbaje et al., 2017b; Gilbert et al., 2008) and is the result of the epitaxial growth mechanism via mineral bridges across the organic scaffolding (Checa et al., 2011). This model involving mineral bridges was developed for growth mechanisms in nacre, which has comparatively thick organic interlamellar sheets of ca. 30 nm and where 150-200 nm sized mineral bridges are indeed visible (Checa et al., 2011; Nudelman, 2015). The organic sheaths in the *K. rhytiphora* shells are significantly thinner than the interlamellar membranes in nacre and mineral bridges across these would only require a few nanogranules of  $\text{CaCO}_3$ , the 30-50 nm sized basic building blocks in bivalve shells (Wolf et al., 2016).

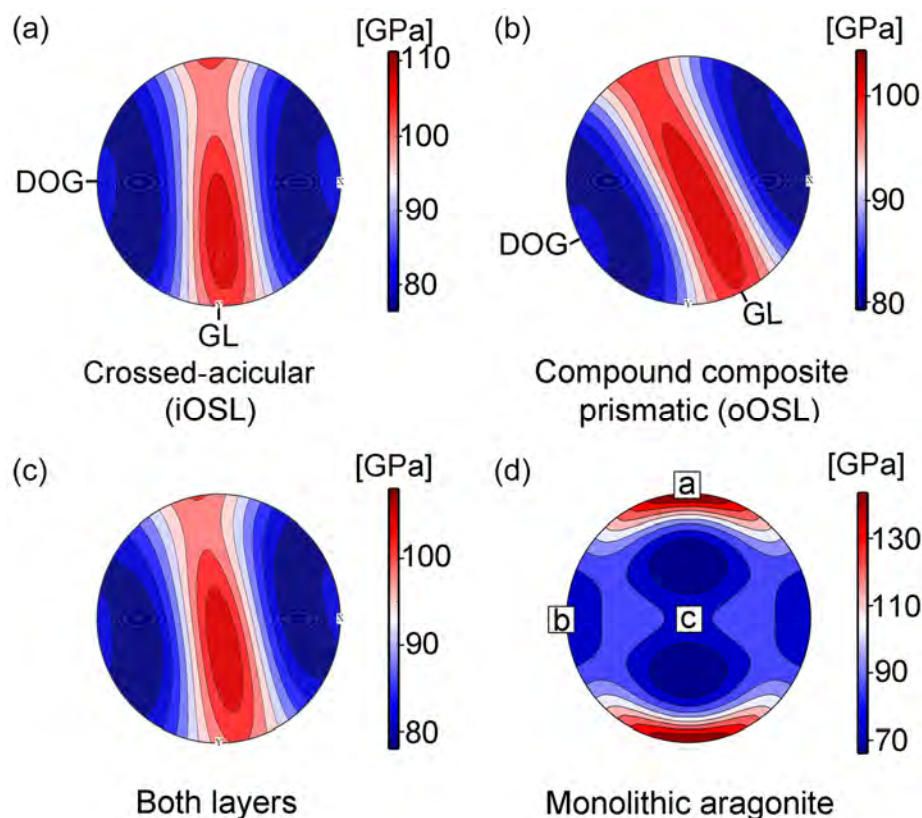
The crossed-acicular ultrastructure (iOSL) is built less complex than the prismatic ultrastructure (oOSL) and consists of only two architectural orders: (i) cross-layered individual lamellae of a few microns in length are angled at approx.  $80^\circ$  to each other and have dipping angles of  $<20^\circ$  towards the inner shell surface, and (ii) cross-layered bundles of co-oriented lamellae at a higher hierarchical order (Supplementary Figure 2.8). Similar bundle-like arrangements of crossed-acicular lamellae were observed by Carter (1989) in the marine gastropod *Cuvierina*, but these show larger angles to each other and smaller dipping angles than those observed in this study. In orientation maps for the iOSL (Figure 5a, Supplementary Figure 12), some pseudo-prisms (Pérez-Huerta et al., 2014) can be identified (outlined in yellow) that consist of co-oriented lamellas.

A common structural motif of aragonitic bivalve shells is the high amount of crystallographic twinning. In *K. rhytiphora*, we observed 46 % (oOSL) and 56 % (iOSL) twin boundaries. Similar to amounts reported for crossed-lamellar (26 %) and nacreous (20-65 %) ultrastructures (Agbaje et al., 2017b; Chateigner et al., 2000). Aragonite twinning in bivalve shells encompasses all length scales including the nano-scale (Kobayashi and Akai, 1994) and values obtained by EBSD are minimum values as they are a function of the spatial resolution.

The smallest mineralized unit of both ultrastructures in the shells are granules with sizes of tens of nanometres (Figure 2.4e). These granules are similar in size to the nano-granular texture observed in nacropismatic and crossed-lamellar shell samples and have been found to be a common motif for bivalve shells (Agbaje et al., 2017b; Jacob et al., 2008; Wolf et al., 2016). Previous studies showed that these granules are often less well-crystallized or even amorphous and are enveloped by thin organic sheaths (Jacob et al., 2008; Wolf et al., 2012). They are most often the vestiges of a non-classical crystallization pathway via amorphous calcium carbonate ACC (De Yoreo et al., 2015).

#### 2.4.2 Mechanical properties

The mechanical properties of shells i.e. stiffness, impact resistance, and toughness outcompete aragonite single crystals by several magnitudes (Jackson et al., 1988; Katti et al., 2006; Wang et al., 2001). Through evolutionary fine-tuning bivalve shells optimize their mechanical properties via their hierarchical organization, crystallographic twinning, nano-granularity, and the intimate intergrowth of mineral and organic phases at the nanoscale and aim at minimizing anisotropy in certain directions of the shell (Weiner et al., 2000). An important parameter to describe the stiffness of a material in response to stress and strain is the Young's modulus (Hashin, 1962). Young's moduli for *K. rhytiphora* shells, calculated from the EBSD dataset and the elastic constants of aragonite single crystals (Liu et al., 2005) yield a maximum of 139 GPa for the iOSL (Figure 2.7a), 132 GPa for the oOSL (Figure 2.7b), resulting in 135 GPa for both shell layers together (Figure 2.7c). These values are in the range of those reported for crossed-lamellar (Agbaje et al., 2017b) and nacreous shells (Fitzer et al., 2015). The mechanical anisotropy can be defined as  $200 \cdot (\max - \min) / (\max + \min)$  with max and min being the maximum and minimum values in GPa. For both layers, the mechanical anisotropy reaches 30 %. The stereographic projection of the Young's modulus (Figure 2.7a-c) reveals a girdle-like maximum of elastically stiffer orientations for the shell that differs significantly from aragonite single crystals (Figure 2.7d), but is similar to results for other bivalve shells (Agbaje et al., 2017b). In reference to the shell morphology, this non-random arrangement of crystallographic orientations results in a quasi-isotropic plane of maximum fracture resistance parallel to the local growth lines (GL, Figure 2.7a-c) and perpendicular to the local growth direction (and thus curvature) of the shell. Hence, the strongest, most fracture-resistant direction in the shell is parallel to its surface, thus maximising the shell's protective function.



**Figure 2.7:** Young's moduli (upper hemisphere and equal area projection), for the compound composite prismatic (oOsl, a) and crossed-acicular ultrastructure (iOsl, b) as well as for both layers together (c). Calculations were made with the Hill averaging scheme (colour scale on the right). (d) The Young's modulus for a aragonite single crystal is calculated with the Voigt–Reuss–Hill averaging scheme and is based on the elastic constants published in De Villiers (1971). We used the aragonite single crystal elastic properties of Liu et al. (2005) and the EBSD data collected from *K. rhytiphora* from this study as inputs (GL – local growth line, DOG – local direction of growth). Note the reference frame for (d) is given by the aragonite crystallographic axes.

#### 2.4.3 Growth features and growth in the wild

*K. rhytiphora* shells form ornamental ridges on their outer shell surface (Figure 2.1), and it is an interesting question how these ridges relate to shell growth. In the case of specimen K2-04 (Figure 2.4), the ridge feature spans the area between the two most recent growth checks (Figure 2.4a), suggesting a one year growth period for the ridge feature, which is also supported by estimating the growth period using growth rates for this specimen (2.2  $\mu\text{m}/\text{day}$  using LE1). However, ridge features are not always associated with growth checks (Figure 2.4a, purple arrow). Ridges are evenly distributed and similar in width (Figure 2.1c), resulting in a decrease in the number of ridges per year with ontogenetic age of the shell. Similar to our findings for *K. rhytiphora* the surface spines of the gastropod *Strombus gigas* were found to be produced at different periods of time across different individuals, suggesting a genetic rather than an environmental control (Radermacher et al., 2009).

Looking at the formation of the ridge features in more detail, specimen K2-04 shows that the beginning of a new ridge as a fine protruding tip (Figure 4a, Supplementary Figure 16), is associated with the highest local growth rates (2.2  $\mu\text{m}/\text{day}$  using LE1, Table 2.2, Supplementary Figure 2.14). Evaluating this observation across all shells shows that at the same point in time, those shells with higher growth rates (e.g. 1.86, Table 2.2, Supplementary Figure 2.14) started producing their next ridge feature

(Supplementary Figure 2.14d, e) while those shells with lower growth rates (e.g. 0.37, 0.46, Table 2.2, Supplementary Figure 2.14) lag behind (Supplementary Figure 2.14b, f). Supporting the delicate protruding tip of a new ridge by modulating growth rates could be a protective mechanism for this growth feature.

A major difference in the growth patterns between both layers of ultrastructures is that while the growth front in the iOSL is homogeneous and runs straight (Figure 2.4d), the growth front in the oOSL is undulated (Figure 2.4b and outlined in Supplementary Figure 2.13). The centres of first-order prisms in the oOSL protrude compared to their rims (Supplementary Figure 13) and the constant thickness of the Sr-labelled shell demonstrates that growth rates, measured perpendicular to the growth front, are homogeneous across this area. This undulation is not observed in other prismatic ultrastructures (simple prismatic ultrastructure: Dauphin et al., 2018) and the underlying reasons for this are yet unknown.

Total growth for oOSL and iOSL in aquaculture is on average 28.4  $\mu\text{m}$  (oOSL) and 24.2  $\mu\text{m}$  (iOSL) with daily growth rates of  $0.85 \pm 0.11 \mu\text{m}$  for oOSL and  $0.73 \pm 0.07 \mu\text{m}$  for iOSL (Table 2.2). Consistent with the curved geometry of the shell and as previously documented (Carré et al., 2005; Foster et al., 2009) the oOSL in *K. rhytiphora* grows 17 % faster than iOSL (Table 2.2, Figure 2.6), and growth rates for this layer are less variable than for the oOSL, both within individual specimens and across the population (Table 2.2, Supplementary Table 2.4, 2.5). While first-order prisms extend between two growth lines and are likely annual, second-order prisms (3 to 6  $\mu\text{m}$  long, Supplementary Figure 2.5) and crossed-acicular lamellae (1.8  $\mu\text{m}$ , Supplementary Figure 2.7) grow at rates of days in our aquaculture experiment, while nanometre-sized third-order prisms (Supplementary Figure 2.6) form within hours. Note however, that while growth rates for the architectural units relative to each other are valid, absolute growth rates in the wild are likely higher compared to aquaculture.

In fact, some insight into shell growth in the wild can be gained from shell portions predating the aquaculture experiments and are described here for the shell section depicted in Figure 2.1, which is representative for three specimens in which these observations were made: Alternating light and dark bands seen in the shell cross-section (Figure 2.1c-e) represent winter (light bands) and summer (dark bands) shell growth. This is verified from the final dark band at the tip of the shell that corresponds to growth in late November when the bivalves were sacrificed. Cyclic changes in the greyscale line profile across these bands (Figure 2.1c, d) correlate with tidal cycles: light grey and dark grey portions fall together with full and new moon cycles, respectively (Figure 2.1d) and indicate that this shell section was deposited over the period two years. Intervals between grey-shaded areas in Figure 2.1d correlate well with neap tides. This growth pattern is in accordance with findings that shell growth is strongly influenced by tidal cycles (Evans, 1972; Hallmann et al., 2009; Schöne, 2008), whereby neap tides result in light coloured increments that are generally wider than the dark increments (Carré et al., 2005; Carré et al., 2006; Rhoads and Lutz, 1980; Schöne et al., 2002). Hence, *K. rhytiphora* shells in the wild show a well-defined fortnightly shell increment resolution. Micro-growth bands at the outermost shell tip (Figure 2.1d, red box) can be correlated with tides at the sampling locality at Port Lincoln, South

Australia from mid-August to mid-September 2016 (Figure 2.1e) and indicate that these micro-growth bands formed over this period in 2016 and prior to aquaculture (started mid-September 2016). From this time onward, the line profile ceases to correlate with tides (Figure 2.1d, e blue band) and shell increments formed during aquaculture are very dark, reflecting lower than normal growth rates.

Analysis of the Sr labelled bands in the shell at high magnification by Backscatter Electron Microscopy allows further insight into growth conditions in aquaculture: Sr label LE1, for example, (Figure 2.4b, oOSL) consists of pairs of bright, narrow and darker, wide increments (Supplementary Figure 2.17a). Identical patterns can be seen in the micro-Raman maps (Figure 3, Supplementary Figure 2) and confirm that these variations in greyscale observed in BSE are caused by variable Sr concentrations in the labelled shell portion. A similar pattern is observed in the iOSL (Supplementary Figure 2.17b). It is noteworthy that the number of increment pairs in the label matches the number of days in Sr-enriched conditions (Supplementary Figure 2.17a, b) although the bivalves were maintained at constant conditions (including amount and timing of feeding) with Sr concentrations being the only varied parameter. This indicates that the acclimatisation period of three weeks at the start of the aquaculture experiments was enough for the bivalves to adjust from their circatidal and circalunidian cycles in the wild to the circadian cycle in aquaculture.

#### *2.4.4 Implications for growth dynamics and biomineralization in pulse Sr labelled shells*

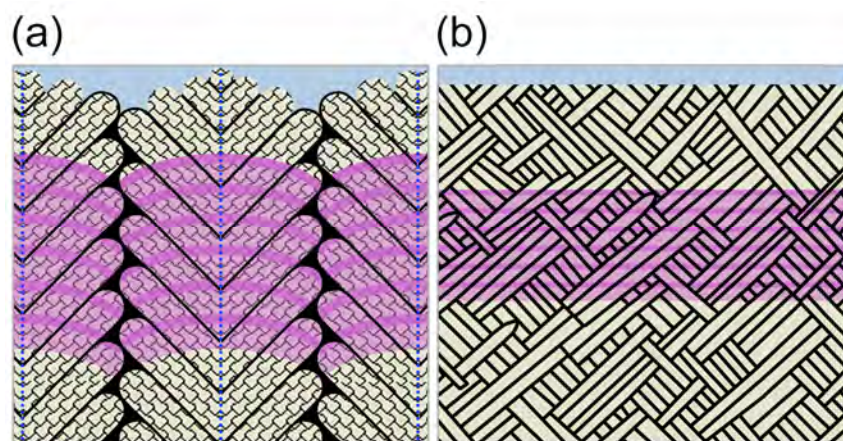
Rather than gradual transitions in greyscale, the changeover between labelled and unlabelled areas in the shells is characterized by a ca. 500 nm narrow greyscale transition in the oOSL (ca. 150 nm in the iOSL), which is roughly equivalent to shell growth over 5 hours at the growth rates for this shell and this particular local growth rate (K2-04: 2.22  $\mu\text{m}/\text{day}$  (oOSL) and 0.72  $\mu\text{m}/\text{day}$ , Table 2.2). The activation volume of the incident electron beam, which could falsify the width estimate of the transition in greyscale is ca. 250 nm (Goldstein et al., 2017); Figure 17a, b), thus does not affect our estimate here. These short-term Sr-concentration changes in the shell thus mirror the immediate change in experimental conditions reasonably well, where seawater was replaced completely both at the start and the end of each Sr-enriched incubation and show that there is no significant lag between change in seawater Sr concentration and Sr incorporation in the shell. This suggests that in the biomineralization of this bivalve species there is no role for a significant ‘Sr-reservoir’, which would otherwise retain Sr-concentrations different to the respective batch of seawater and cause gradual changes in greyscale in the BSE images of the shells over a wider shell portion.

One such biomineralization reservoir in bivalves is thought to reside in the space between the mantle epithelium and the growth front of the shell, namely the extrapallial space. The fluid in this space contains high concentrations of  $\text{Ca}^{2+}$ -binding proteins, important agents in biomineralization (Cusack et al., 2008; Rousseau et al., 2009). Our findings that the change in Sr-concentration in the shell closely mirrors the batch-changes of seawater suggest however, that the extrapallial fluid cannot be very voluminous, if it exists at all (Addadi et al., 2006; Marin et al., 2012). These results also demonstrate that changes in Sr concentrations (and, by inference also changes in concentrations of other trace



elements) are recorded in the shell without significant temporal delay, which underscores the high suitability of bivalve shells as high-resolution archives of environmental change (Schöne et al., 2005).

An important finding of this study is that all hierarchical architectural units in both shell layers are transected by the Sr label (Figure 2.4b, d, summarised in Figure 2.8). Thus, rather than forming one individual architectural unit after the other, the growth front in the shell progresses homogeneously, transecting not only all mineral units, but also their individual organic envelopes. Naturally, and consistent with other pulse labelling studies on marine calcifiers the macroscopic morphology of the growth front follows the outside morphology of the skeleton. Nevertheless, at the micron to submicron scale, the homogeneous growth front observed here highlights a fundamental difference to growth processes in other calcifying organisms, where growth fronts are extremely heterogeneous in morphology and in growth rate (Domart-Coulon et al., 2014; Gorzelak et al., 2014). Our observation also potentially challenges the prevailing model for the formation of nacre by successive filling of pre-existing empty organic envelopes (Bevelander and Nakahara, 1969; Levi-Kalisman et al., 2001). Instead, our results for *K. rhytiphora* call for a more dynamic shell growth mechanism that allows for simultaneous formation of organic sheaths and mineral components, perhaps along the lines of models of calcification via directional solidification as recently proposed by Schoeppler et al. (2018).



**Figure 2.8:** Schematic (not to scale) of the compound composite prismatic (oOSL, a) and crossed-acicular architecture (iOSL, b; modified after Bandel (1977)) transected by Sr-labels (purple) summarizing the observations in this study. Unlabelled aragonitic architectural units (beige) are outlined by organic sheaths (black). First-order prisms in (a) have thick organic sheaths, curved growth fronts, and consist of second-order prisms that are arranged at ca. 60° to the central axis of each first-order prism (a, blue dashed lines). Third-order prisms (a, tiled pattern) are oriented parallel to each other within second-order prisms. The shading in the pink Sr labels illustrates the internal BSE greyscale variations in the Sr labels reflecting variable Sr-concentrations within the Sr-label in the shells. The Sr-label is generally wider in the oOSL compared to the iOSL and transects all architectural units in both ultrastructures.

#### 2.4.5 Strontium/calcium ratios in the shell

The Sr/Ca ratio in bivalve shells has been used as a proxy for sea surface temperature (e.g., Dodd, 1965; Swan, 1956; Zhao et al., 2017a). However, a plethora of studies argues that Sr/Ca ratios in bivalve shells are mainly influenced by growth rate (e.g., Takesue and van Geen, 2004) and metabolic rate (Bailey and Lear, 2006; Foster et al., 2009; Gillikin et al., 2005; Purton et al., 1999) rather than by temperature. Distribution coefficients  $D_{\text{Sr/Ca}}$  calculated as  $(\text{Sr/Ca}_{\text{unlabelled shell}})/(\text{Sr/Ca}_{\text{mean ocean water}})$  for both shell layers in this study are very similar for labelled and ambient aquaculture conditions (0.14 and 0.15, Table 2.3)



and are only slightly higher than those in the wild before aquaculture (0.13 for oOSL and 0.12 for iOSL). These  $D_{\text{Sr/Ca}}$  values are in a similar range as aquaculture-derived  $D_{\text{Sr/Ca}}$  for shells of the freshwater bivalve *Corbicula fluminea* (0.19 - 0.29, Zhao et al., 2017a), however these values, both for *K. rhytiphora* and *C. fluminea* are significantly smaller than  $D_{\text{Sr/Ca}}$  for equilibrium incorporation of Sr/Ca in synthetic aragonite of 1.19 at 20 °C (Gaetani and Cohen, 2006). This discrepancy once again highlights the complexities involved in the interpretation of the chemical signatures in biominerals and their correct application to arrive at accurate reconstructions of past environments. While the exact reasons for the large difference between synthetic and biomineralised aragonite are yet unknown, multi-step fractionation mechanisms connected with the step-wise nonclassical crystallization pathway (Jacob et al., 2017), which is the confirmed formation pathway for many calcifying organisms (De Yoreo et al., 2015) could play a major role.

**Table 2.3: Distribution coefficients of Ca and Sr between shell and seawater for both ultrastructures as well as for pulse Sr-labelled and unlabelled conditions. Concentrations for Ca and Sr in shell are from Table 2.1, while seawater values are mean ocean water.**

Distribution coefficients:	Compound composite prismatic (oOSL) ultrastructure	Crossed-acicular (iOSL) ultrastructure
$D_{\text{Sr}}$ labelled ( $\text{Sr/Ca}_{\text{labelled shell}}/\text{Sr/Ca}_{\text{seawater}}$ )	0.15	>0.09*
$D_{\text{Sr}}$ unlabelled ( $\text{Sr/Ca}_{\text{unlabelled shell}}/\text{Sr/Ca}_{\text{seawater}}$ )	0.14	0.14
$D_{\text{Sr}}$ natural environment ( $\text{Sr/Ca}_{\text{natural shell}}/\text{Sr/Ca}_{\text{seawater}}$ )	0.13	0.12

\*Minimum value as the analysed area slightly exceeds label width.

#### 2.4.6 Effects of aquaculture and pulsed Sr-labelling on growth and composition of the shells

Reduced growth rates are a common observation for bivalves held in aquaculture and *K. rhytiphora* in this study is no exception. A major contributing factor to reduced growth rates in aquaculture for intertidal bivalves such as *K. rhytiphora*, is the very different environment with respect to tidal cycles and lower water depths (e.g., Pannella and MacClintock, 1968). The strong influence of tides on shell growth for intertidal bivalves is well known (Carré et al., 2005; Carré et al., 2006; Rhoads and Lutz, 1980; Schöne et al., 2002), hence an aquaculture protocol that takes increased water pressures into account would be expected to enhance growth rates in future experiments.

The Micro-Raman maps demonstrate the influence of the incorporation of high Sr concentrations on the aragonite crystal structure: In the Sr- labels the  $\nu_1[\text{CO}_3]$  symmetric-stretching band-position is broadened by ca.  $0.5 \text{ cm}^{-1}$  (Figure 2.3) and down shifted by ca.  $0.5 \text{ cm}^{-1}$  (Supplementary Figure 2.2, Supplementary Table 2.3) compared to the areas formed at ambient conditions. This peak shift as well as the peak broadening results from changes in the interatomic distances in the aragonite crystal structure and slightly increase in structural disorder due to the incorporation of the larger Sr ion on nine-fold coordinated smaller Ca-sites (Alia et al., 1997). These effects on the Raman bands of the anionic complexes in minerals are typical when larger cations are substituted in the crystal lattice (Bischoff et al., 1985; O'Donnell et al., 2008; Ruschel et al., 2012).

Hence, while Raman spectra show that Sr-labelling has a measurable effect on the crystal structure of the aragonitic shell, this effect is minor, because (i) Sr substitution into the shell aragonite does not result in formation of a discrete  $\text{SrCO}_3$  phase, which would have been detected as a band at  $1073 \text{ cm}^{-1}$  (Alia et

al., 1997), and (2) analysis of the EBSD data (Figure 2.6, Supplementary Figures 10 and 12) does not show systematic deviations between the labelled and ambient areas in the shell. Furthermore, daily local growth rates of Sr-labelled and unlabelled areas, do not show systematic trends (Figure 2.5c). Hence, while shell growth rates are downscaled during aquaculture, the multi-scale architecture of the shell down to the atom-level show no significant deviation from natural shells, indicating that the shell growth processes in aquaculture under the conditions chosen in this study are comparable to those in the wild.

Hence, pulsed Sr-labelling experiments offer the potential to study calcification processes down to the sub-micron range without apparent alteration of the growth processes and offer excellent analytical detectability for a wide range of micro-beam techniques. Pulse Sr-labelling is thus superior to experiments with fluorescent markers that are limited to the spatial resolution of light microscopy and have been shown to impact vitality and biomineralization processes in some calcifiers (Allison et al., 2011; Gorzelak et al., 2014; Russell and Urbaniak, 2004; Thébault et al., 2006).

## 2.5 Conclusion

Pulsed Sr-labelling experiments and correlated, *in situ* NanoSIMS and Raman mapping together with WDS spot analysis and FEG-SEM BSE imaging resolve local growth rates at the nanometre scale and show compelling potential to shed light on submicron growth mechanism in bivalve shells:

- All hierarchical architectural units and intercalated organic sheaths are transected by the Sr label and demonstrated bivalve shell growth to progress homogeneously instead of forming one individual architectural unit after the other.
- Sharp transitions between labelled and unlabelled shell areas indicate that physiological transport processes for Sr have no significant lag and suggest that the extrapallial fluid cannot be very voluminous.
- Both architectures have similar  $D_{\text{Sr}/\text{Ca}}$  for labelled and unlabelled shells that agree well with those of shell formed in the wild and are all significantly below  $D_{\text{Sr}/\text{Ca}}$  for equilibrium incorporation of Sr/Ca in synthetic aragonite.

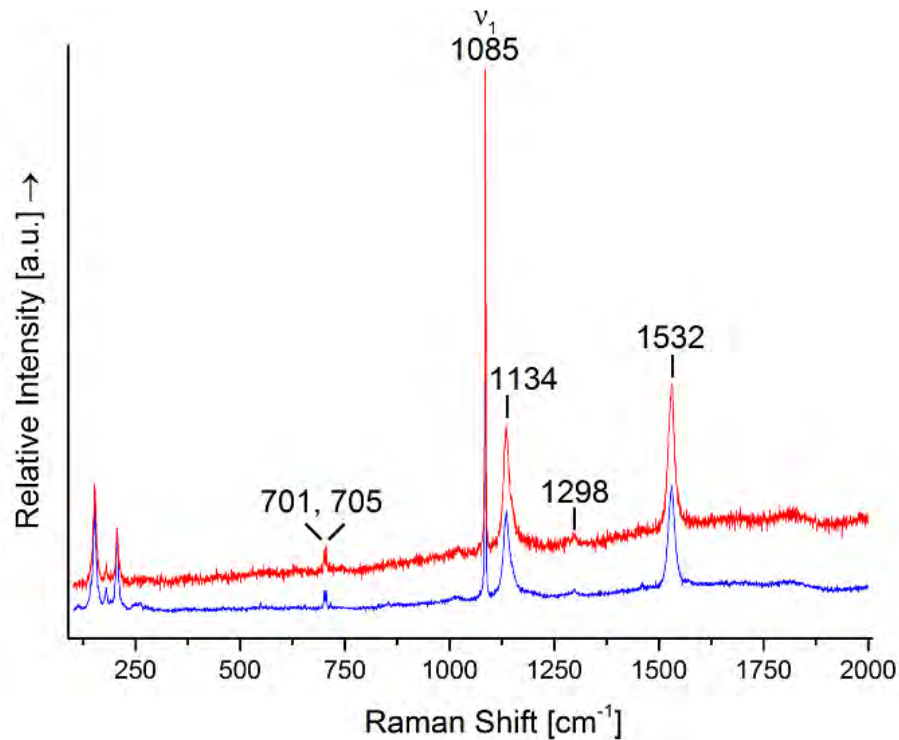
## Acknowledgements

We acknowledge Michael W. Förster, Antje Sorowka, Steve Craven, and Jacob Bynes for help and advice on sample preparation. Stephan Buhre is kindly thanked for calibrating the EPMA system. We thank the Macquarie University Faculty of Science and Engineering Microscope Facility (MQFoSE MF) for access to its instrumentation and support from its staff members Sue Lindsay and Chao Shen. Jane Williamson and Josh Aldridge are thanked for access and assistance at the Macquarie Seawater Facility. Wayne O'Connor from Port Stephens Fisheries Centre, NSW Department of Primary Industries is thanked for insightful discussions on husbandry protocols. The authors received financial support through an Australian Government International Postgraduate Research Scholarship (IPRS) awarded to LMO, a Macquarie University Research Excellence Scholarship (iMQRES) awarded to OBA, and DEJ

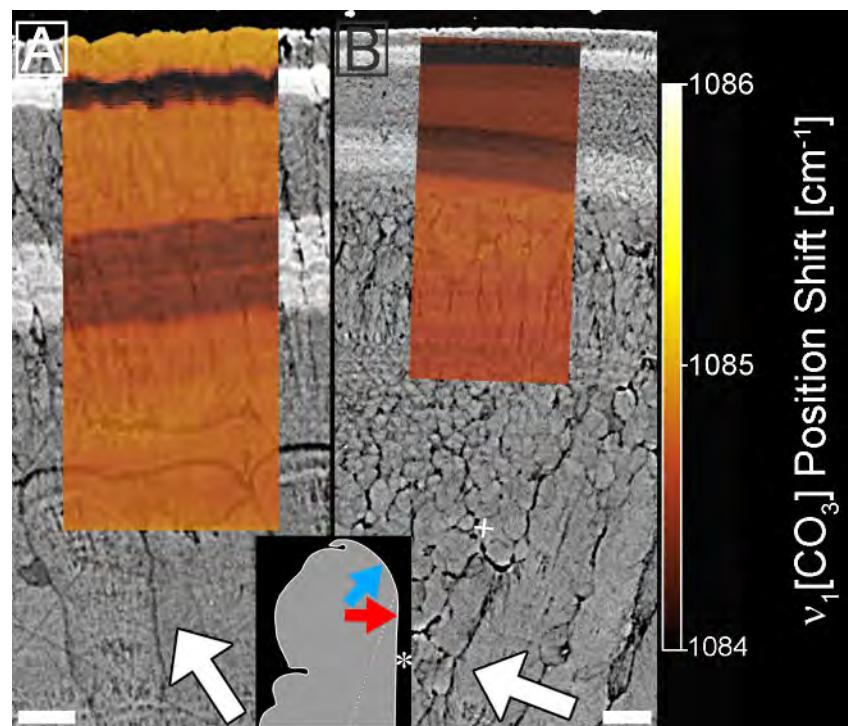
is supported via the Australian Research Council through a Discovery Grant (DP160102081). C.L. gratefully acknowledge the use of instrumentation funded through an honorary-associate agreement with the ARC CFSS/GEMOC at Macquarie University, Sydney and financial support by the Austrian Science Fund (FWF), through project J3662-N19. The authors acknowledge Microscopy Australia, the Science and Industry Endowment Fund, and the State Government of Western Australian for contributing to the Ion Probe Facility at the University of Western Australia.

## Supporting material

### Supplementary figures

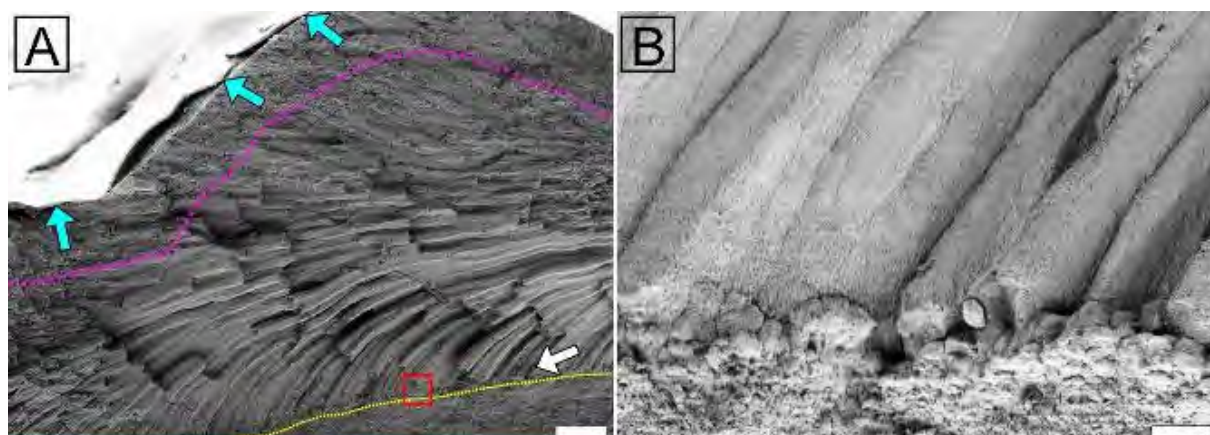


Supplementary Figure 2.1: Representative micro-Raman spectra obtained from both ultrastructures (iOSL-blue, oOSL-red). Relative Raman intensities were normalized to the highest intensity peak, no baseline correction.

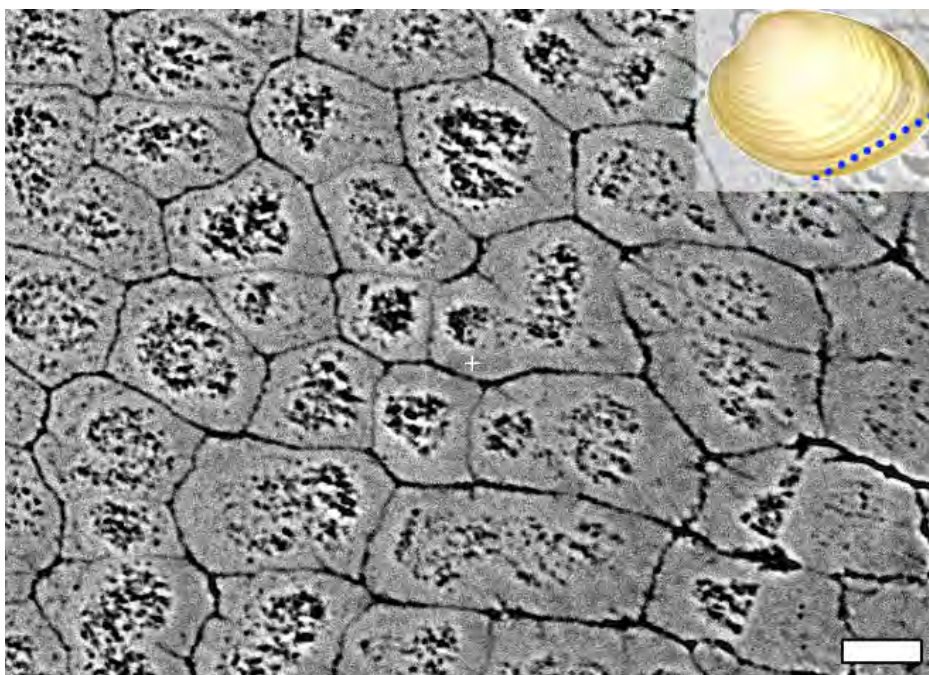


Supplementary Figure 2.2: Micro-Raman maps overlain on BSE images of a polished cross-section of a Sr labelled *K. rhytiphora* shell showing the effect of variable Sr concentrations on the peak position of  $\nu_1$  located at  $1084.8 \text{ cm}^{-1}$  in oOSL ((a) - compound composite prismatic ultrastructure) and iOSL ((b)- crossed-acicular architecture) Colour-scale on the right indicates the peak position and shift. All cross-sections are prepared as radial sections along the maximum growth axis unless otherwise specified. Lighter grey areas in the BSE

images have elevated Sr contents as confirmed by nanoSIMS and EPMA and show excellent correlation with position shifts to lower wavenumbers of about  $0.5\text{ cm}^{-1}$ . White arrows indicate the general shell growth direction. The local growth direction is orthogonal to the light grey bands of the Sr-label in the BSE image. The inset shows a schematic of the shell tip with the location of the Raman maps (blue arrow – oOSL, red arrow – iOSL, dashed line marks the border between the layers), asterisk marks the inner shell surface. Scale bars are 10  $\mu\text{m}$ .

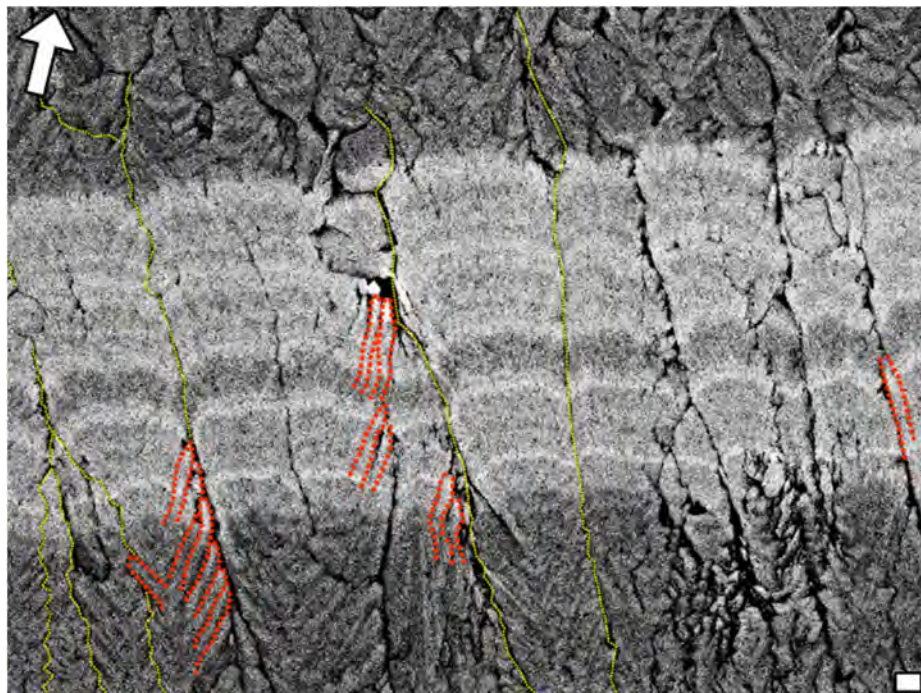


Supplementary Figure 2.3: SE-images of a *K. rhytiphora* shell broken radially. Blue arrows in (a) point to well preserved areas of the thin periostracum (about 1  $\mu\text{m}$  thick). The pink dashed line marks a ca. 100  $\mu\text{m}$  wide zone of spherulitic aragonite grains adjacent to the periostracum. The yellow dashed line marks the boundary between the compound composite prismatic (oOSL) and crossed-acicular (iOSL) ultrastructure. White arrow indicates the general growth direction of the shell. (b) magnification (red square in A) of the boundary between both layers shows spherulitic grains of up to 8  $\mu\text{m}$  in diameter. Scale bars are 100  $\mu\text{m}$  (a) and 10  $\mu\text{m}$  (b).

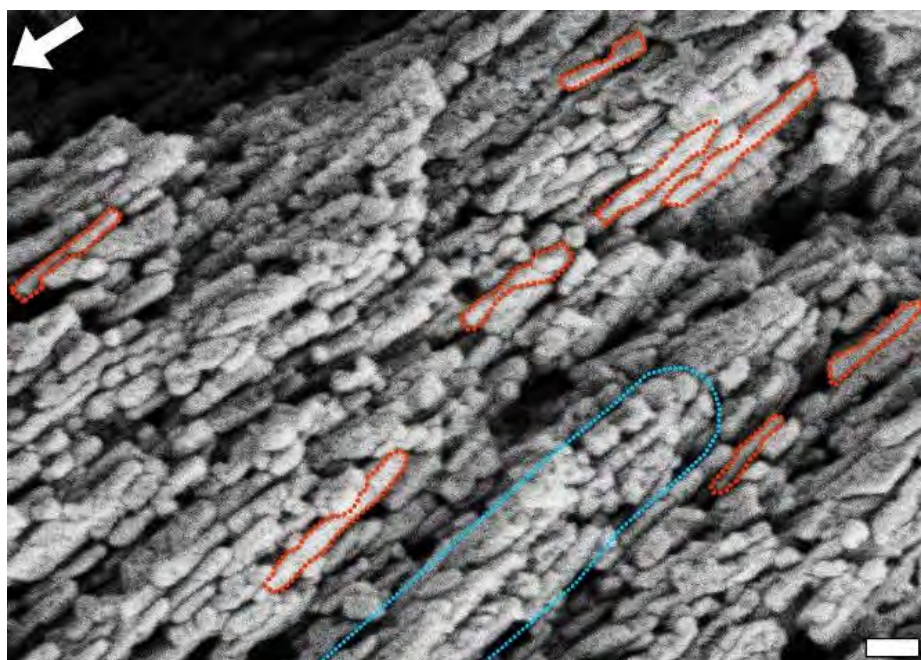


Supplementary Figure 2.4: BSE image of a polished longitudinal cross-section of a *K. rhytiphora* shell. This orientation allows to observe first-order prisms (oOSL) perpendicular to their length axis (see sectioning plane indicated by blue dashed line in inset) for thickness measurements that average  $17 \pm 5\text{ }\mu\text{m}$  ( $n=20$ ). Prism centres appear dark and patchy, which results from the angled, 3D radial arrangement of second-order prisms, some of which are removed during polishing. Scale bar is 10  $\mu\text{m}$ .



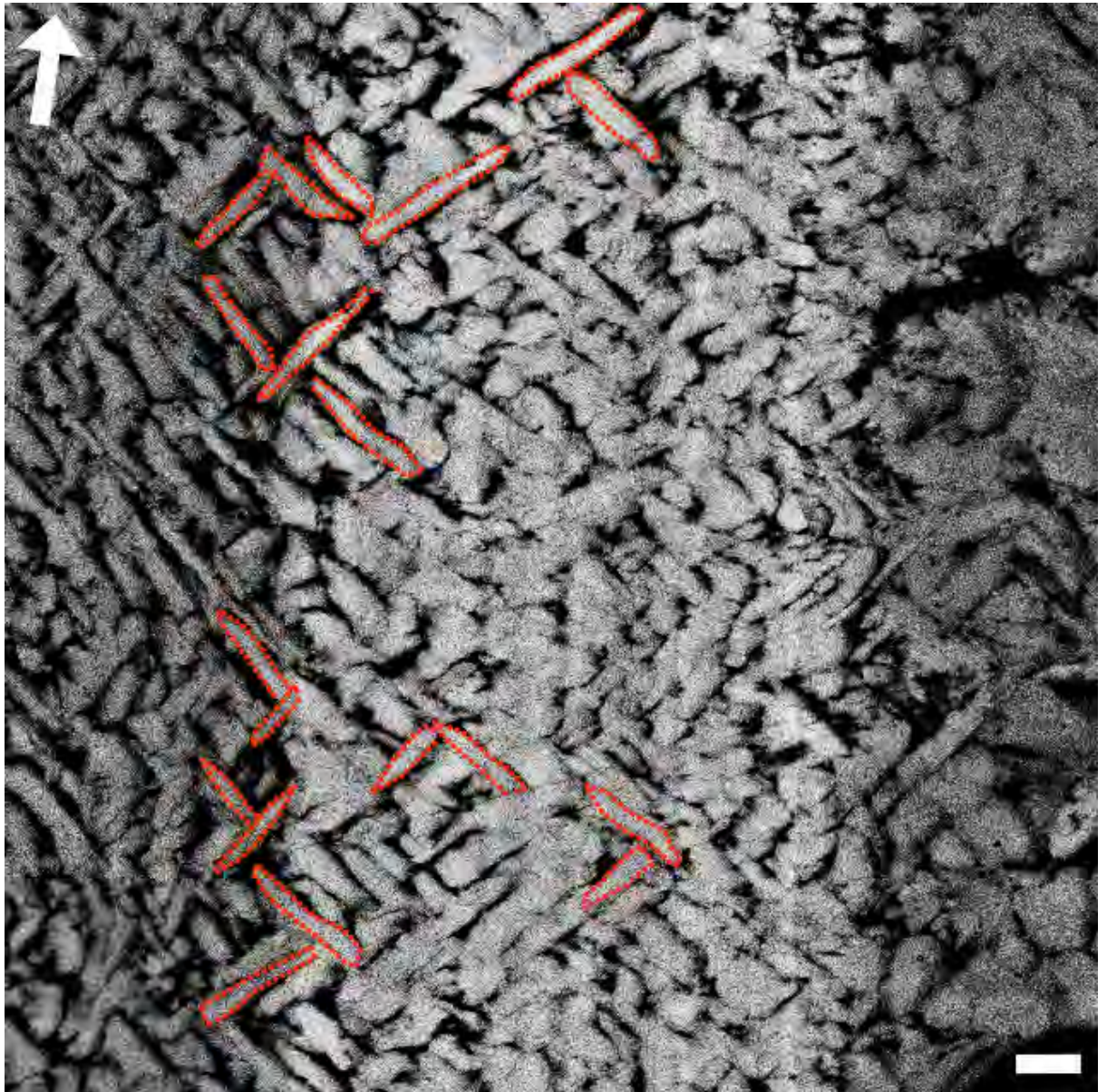


**Supplementary Figure 2.5:** BSE image showing a polished cross-section of the innermost (first) Sr label (LE1) in the compound composite prismatic ultrastructure oOSL (sample K2-04). The Sr label appears as bright grey due to a higher Z-contrast. First-order prisms (yellow dotted lines) are separated by organic sheaths visible as dark grey. Second-order prisms (outlined in red) radiate from the central axis of first-order prisms and are  $3 \pm 0.3 \mu\text{m}$  long and  $0.3 \pm 0.06 \mu\text{m}$  wide ( $n=8$ ). Note that these values are minimum values, since the base of each second-order prism is overlain by others. Maximum lengths can be up to twice those measured here. The angle between two second-order prisms facing each other is  $68^\circ$ . The thickness of the 6-day Sr label of  $14 \mu\text{m}$  and indicates that second-order prisms form over approx. 1.3 days during our experiments. A white arrow indicates the general growth direction of the shell, while the local growth direction is perpendicular to the Sr-labelled shell layer. Scale is  $1 \mu\text{m}$ .



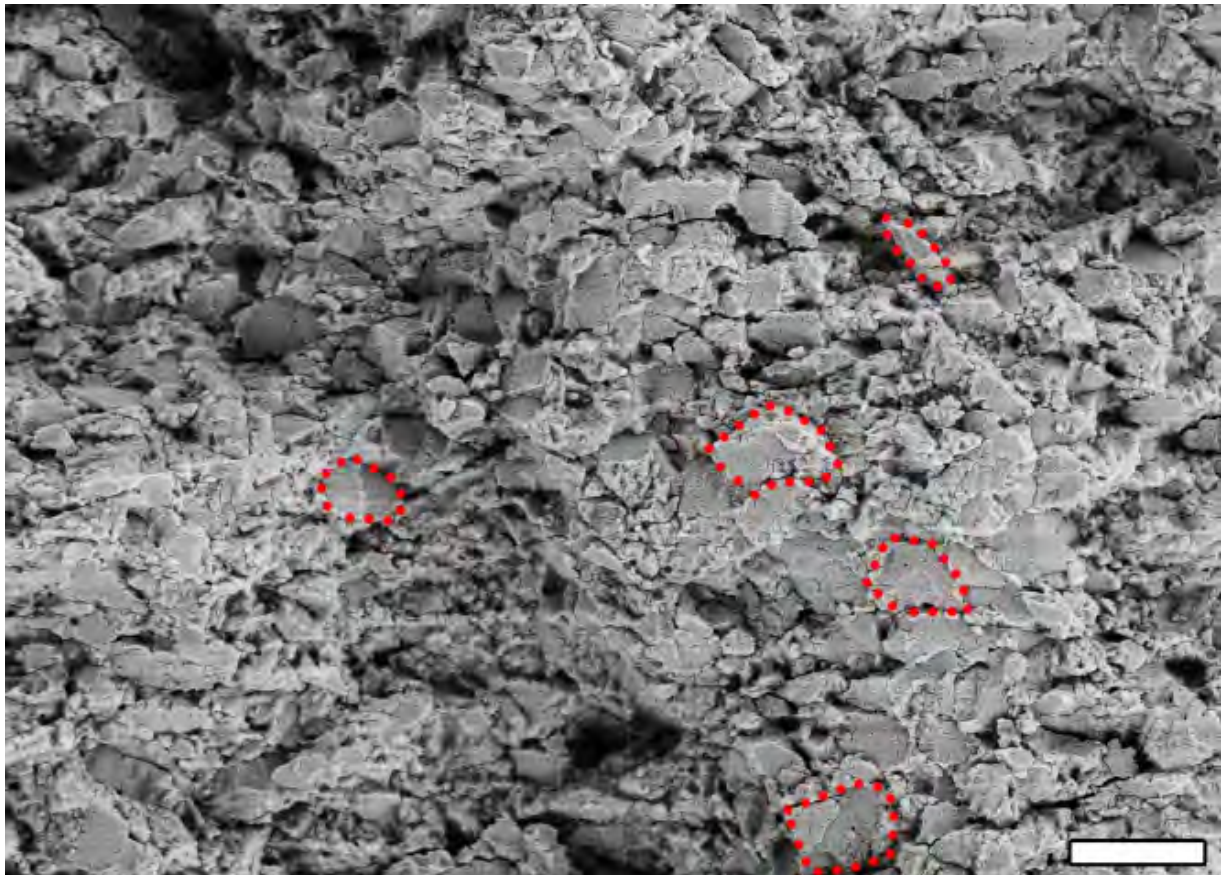
**Supplementary Figure 2.6:** SE image (magnification 100,000x) of a radially broken shell exposing detail in the compound composite prismatic ultrastructure (oOSL). Third-order prisms (outlined in red) are oriented parallel to each other within second-order prisms (outlined in blue). Fully exposed and unbroken third-order prisms were measured using ImageJ and are approx.  $496 \pm 129 \text{ nm}$  long and  $67 \pm 16 \text{ nm}$  wide ( $n=8$ ). These prismatic units are 28x shorter than the width of the Sr-labelled area of  $14 \mu\text{m}$ , resulting in a growth rate of five third-order prisms per day during our experiments. The white arrow indicates the general growth direction of the shell. Scale bar is  $200 \text{ nm}$ .



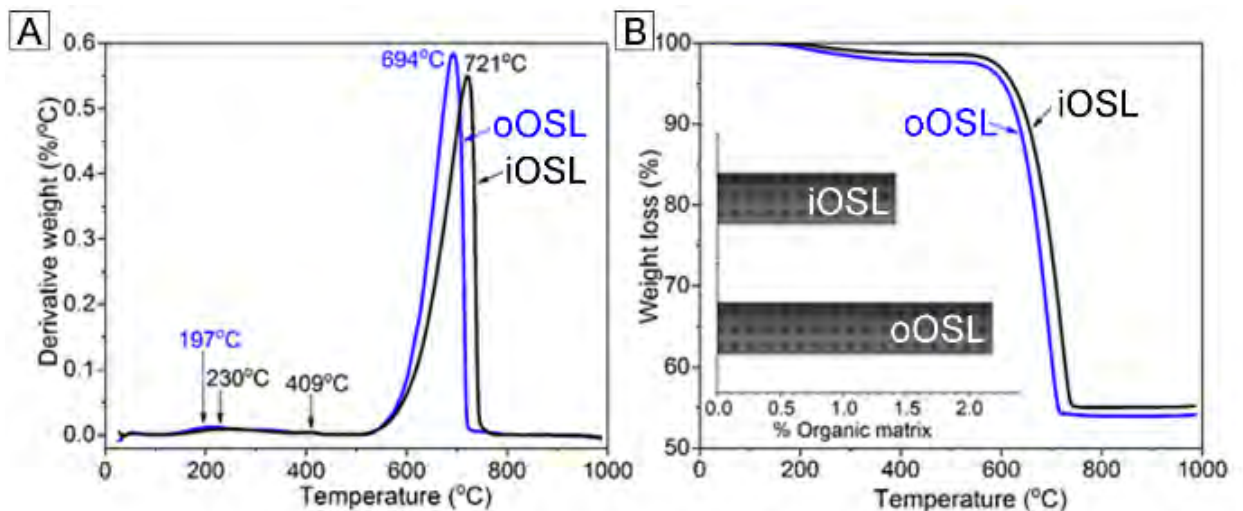


**Supplementary Figure 2.7:** BSE image showing a polished cross-section of Sr label LE1 within the crossed-acicular ultrastructure (iOSL, sample K2-04). This architecture consists of elongated lamellae (outlined in red) arranged into intersecting bundles. Lengths and widths are  $1.8 \pm 0.4 \mu\text{m}$  and  $0.22 \pm 0.05 \mu\text{m}$  ( $n=19$ ), with an angle of  $81^\circ \pm 8^\circ$  ( $n=6$ ). The projected length parallel to the general growth direction was calculated to be  $1.2 \mu\text{m}$ . Using the relationship between the projected length of  $1.2 \mu\text{m}$  and the width of the LE1 label in this area ( $\approx 9 \mu\text{m}$ ) acicular lamellae are deposited by constant rate of approximately 1 lamella/day during our experiments. The white arrow indicates the general growth direction of the shell, the local growth direction is perpendicular to the Sr label. Scale bar is  $1 \mu\text{m}$ .



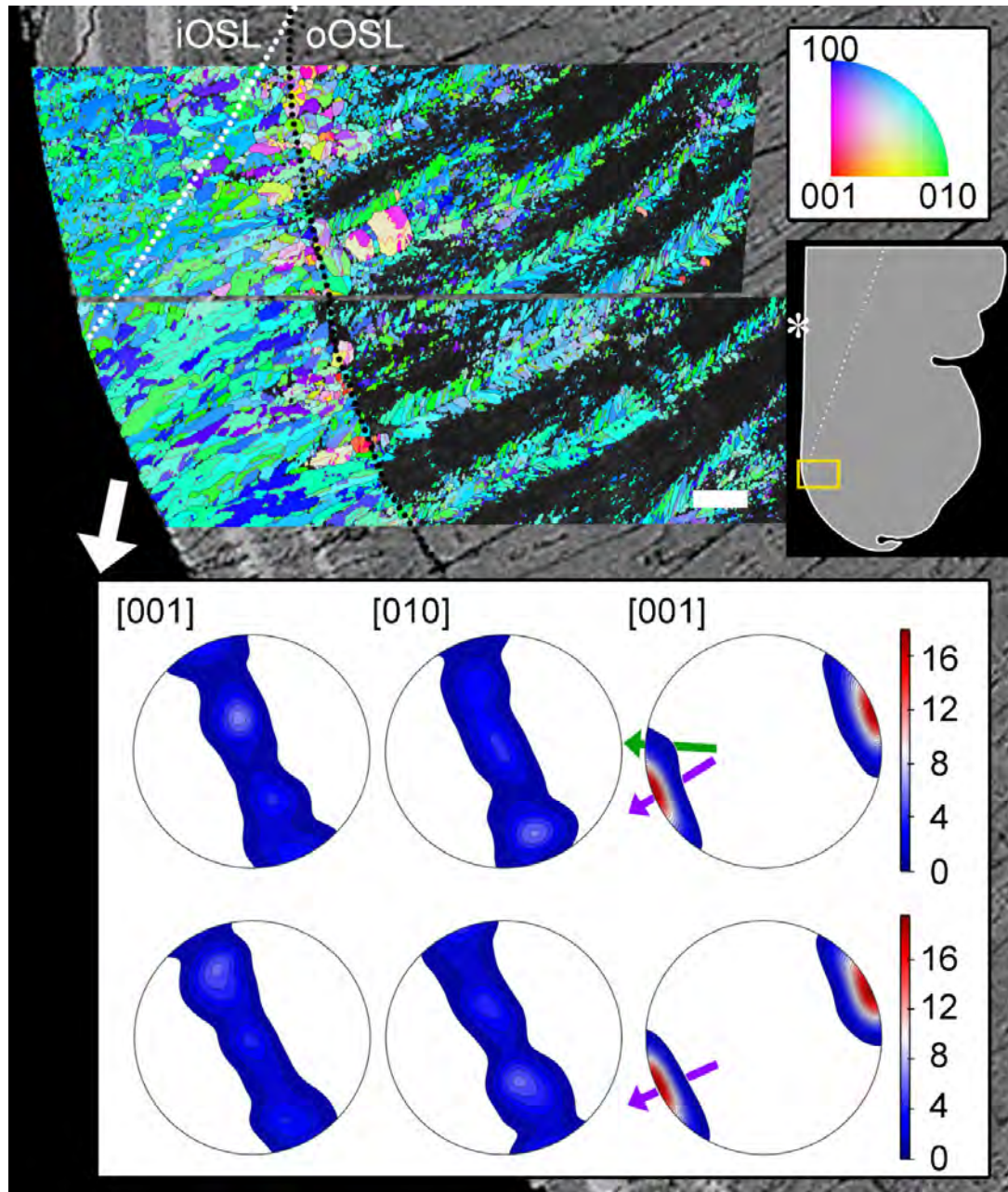


Supplementary Figure 2.8: SE image showing a radially broken surface of the crossed-acicular ultrastructure (iOSL). In contrast to the BSE images, the crossed-acicular units appear here as bundles of lamellae (red dashed lines), while individual lamellae cannot be identified, because SE fails to visualize the organic sheaths around individual lamellae seen in BSE images (Supplementary Figure 7). The bundles have sizes of around  $1.4 \times 0.8 \times 0.2 \mu\text{m}^3$ . The general growth direction of the shell is identical to that in Supplementary Figure 2.3. Scale bar is  $2 \mu\text{m}$ .

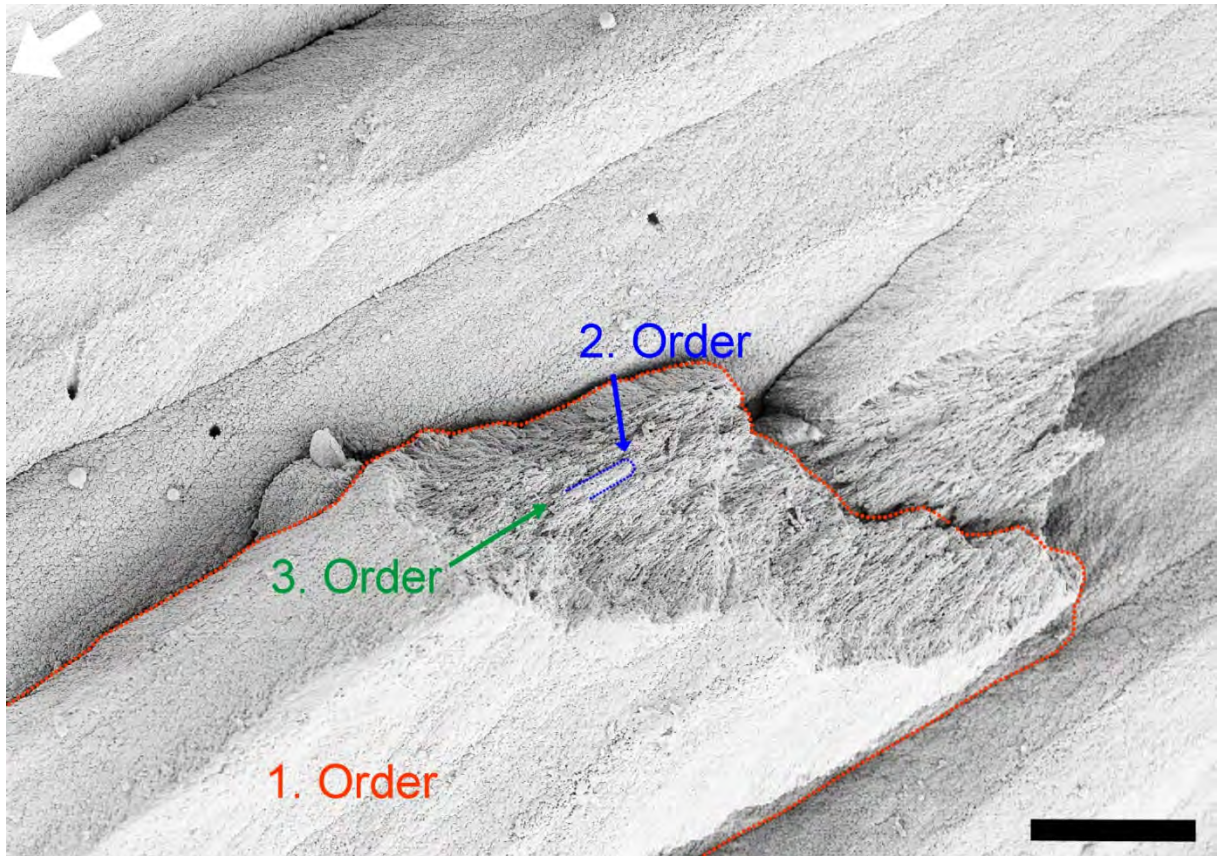


Supplementary Figure 2.9: Differential thermal analysis (a) and thermal gravimetric analysis (b) show thermal stability and total organic matrix contents of iOSL and oOSL. Taking the inorganic  $\text{CO}_2$  content of 42–43 wt.% into account the organic matrix amounts to 1.42 wt.% for the crossed-acicular ultrastructure (iOSL) and 2.19 wt.% for the compound composite prismatic oOSL (inset in (b)).



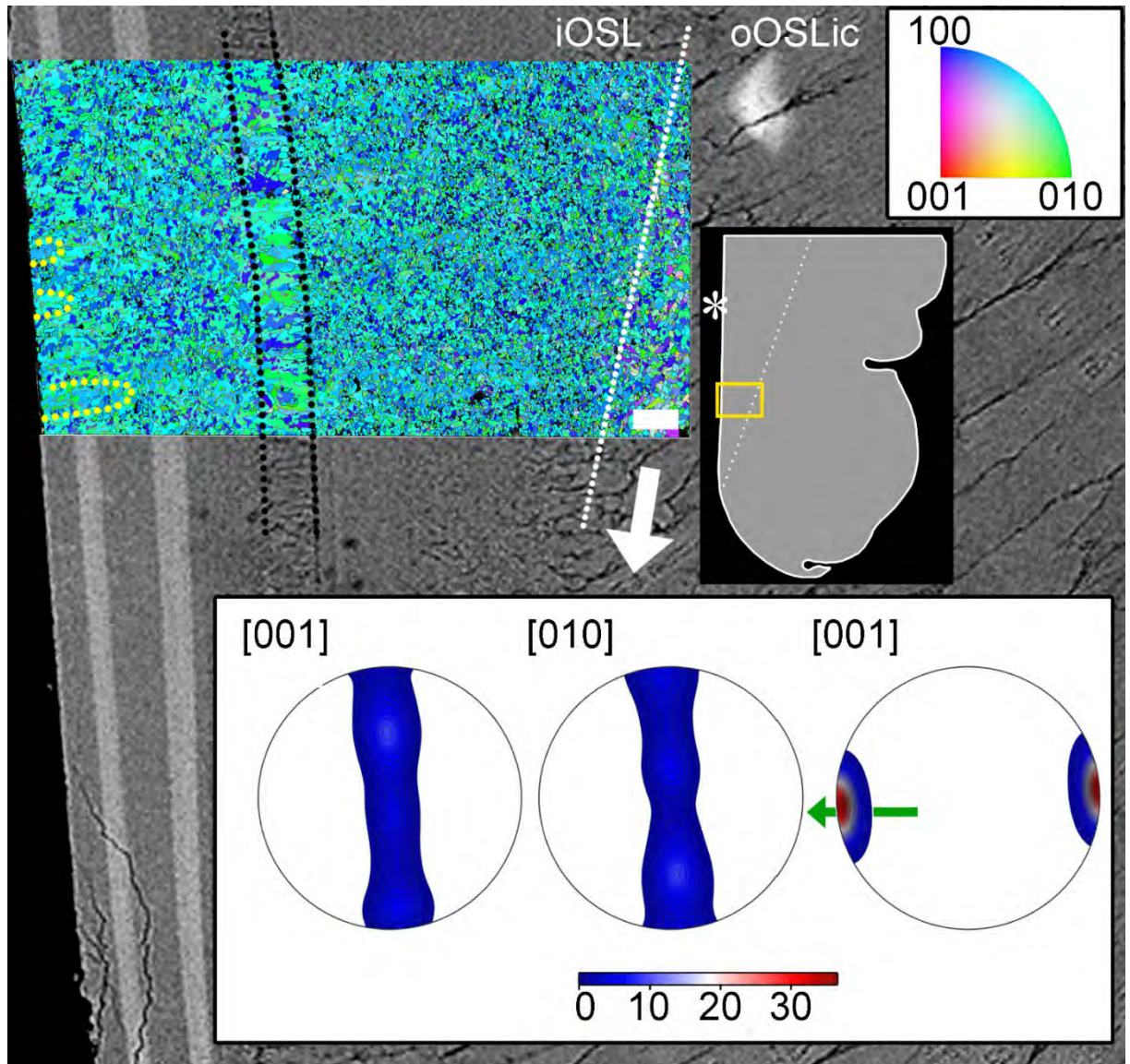


Supplementary Figure 2.10: Orientation maps for aragonite (A) of a pulsed Sr-labelled shell (specimen ID: K2-11) overlain on BSE images of the shell area. The map consists of two adjacent individual maps that are colour-coded according to the inverse pole figure colouring scheme for orthorhombic aragonite: Blue, green, and red indicate the alignment of crystallographic a- [100], b- [010], and c-axes [001], respectively. Further, the maps are color-coded to show the crystallographic orientation normal to the polished surface that vary randomly between the a-[100] and b-[010], while the c-axis [001] is aligned parallel with the local growth directions (i.e. perpendicular to the polished surface). Twinned grain boundaries are presented in red. The dotted white line outlines the boundary between oOSL and iOSL. Second-order prisms show a feathery arrangement within first-order prisms. Areas along the centres of first-order prisms in iOSL remain unindexed, which is likely an effect of damaging during sample polishing (see main text). The organic growth check in the oOSL that transitions as a thin prismatic layer into the iOSL is highlighted with light black dotted lines. Pole figures (lower hemisphere, equal area projection) show the mineral fabric for [100], [010] and [001] axes of aragonite. The local growth direction of the prismatic oOSL (purple arrow in B) coincides with the shell layers visualised by pulsed Sr labelling in the underlying BSE image and is angled to the general shell growth direction (white arrow). The crystallographic c-axes [001] form a strong maximum of 18.70 times uniform (see scale bar on the right), while the a- ([100]) and b- ([010]) axes form a girdle of random orientations around the c-axes. This girdle corresponds to the direction of the growth lines that run perpendicular to the general shell growth direction. Compared to the pole figures for the lower orientation map, those for the upper EBSD map, show a small contribution of the crossed-acicular ultrastructure (iOSL) to the maximum of the c-axes (green arrow in B). A schematic of the cross-sectioned shell tip shows the location of the orientation maps and the underlying BSE image. Asterisk marks the inner shell surface. Scale bar is 10  $\mu\text{m}$ .



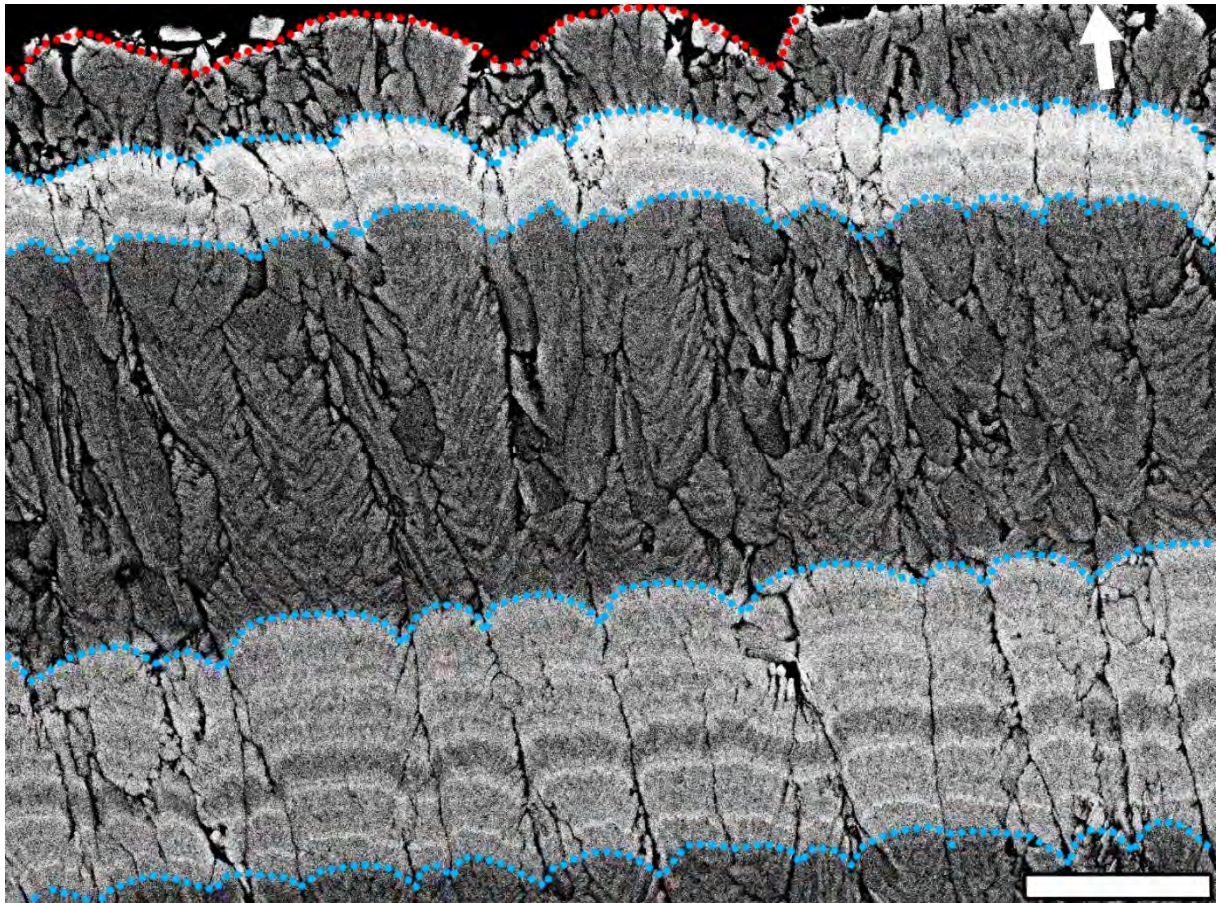
**Supplementary Figure 2.11: SE image showing a broken radial cross-section of the compound composite prismatic ultrastructure (oOSL). First-order prisms (outlined in red) have a compact internal architecture consisting of second-order prisms (outlined in blue) and third-order prisms (as fine-grained texture) are visible. The white arrow indicates the general growth direction of the shell. Scale bar is 10  $\mu\text{m}$ .**





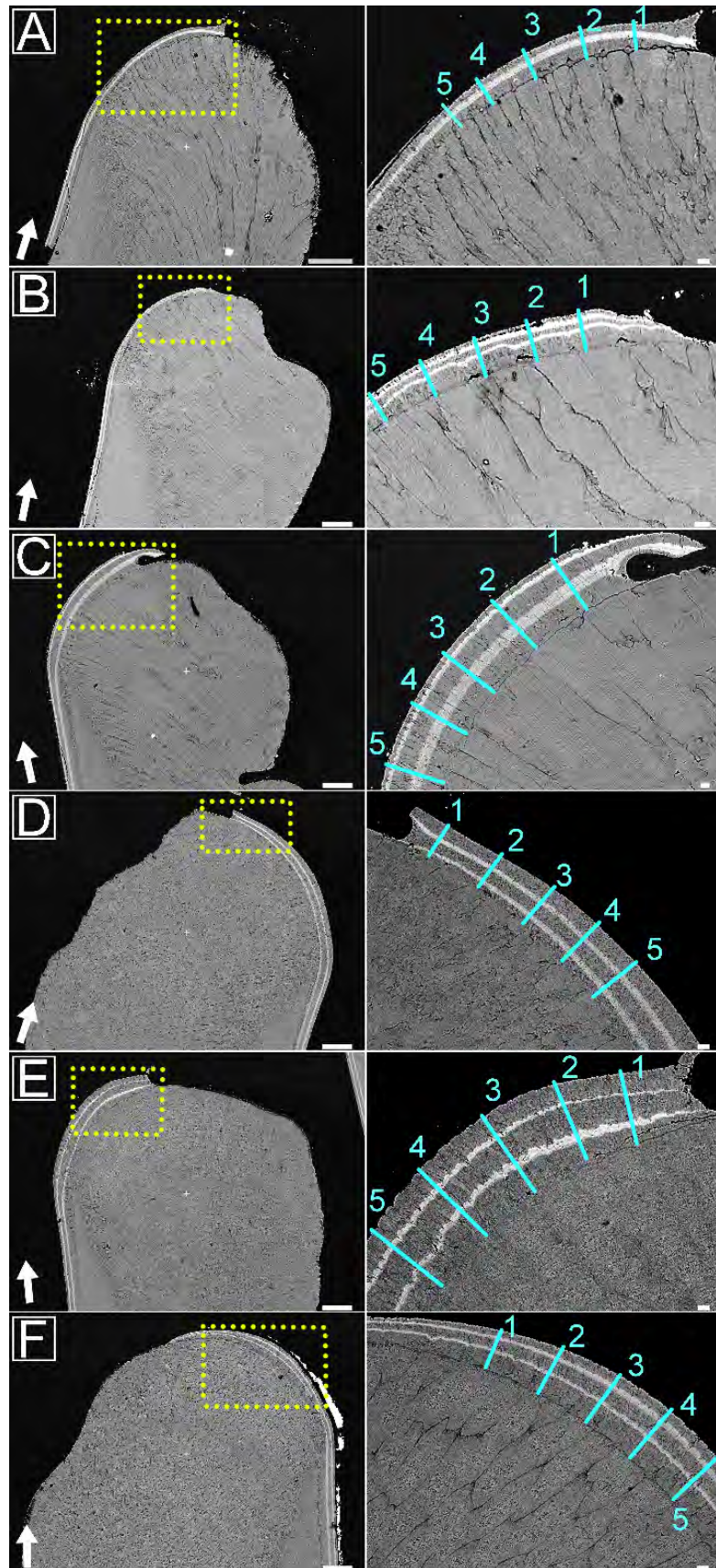
Supplementary Figure 2.12: Orientation map (A) of a pulse Sr-labelled shell (specimen ID: K2-11) overlain on a correlated BSE image. The map is color-coded to show the crystallographic orientation normal to the polished surface that vary randomly between the a-[100] and b-[010], while the c-axis [001] is aligned parallel with the local growth directions (i.e. perpendicular to the polished surface). Twinned grain boundaries are presented in red. The boundary between crossed-acicular (iOSL) and compound composite prismatic (oOSL) architectures is marked by a dashed white line. The dashed black lines highlight the mineralized growth check (a thin prismatic layer) that continues from the organic growth check in the oOSL. At the inner shell surface pseudo-prisms (co-orientated areas, outlined in yellow) can be seen (Pérez-Pérez-Huerta et al., 2014). Pole figures (lower hemisphere, equal area projection) show the alignment of the EBSD data with the [100], [010] and [001] axes of aragonite and exhibit a strong crystallographic preferred orientation (CPO) of the crystallographic c-axis of aragonite [001]. The local direction of growth for the crossed-acicular ultrastructure (green arrow in B) is perpendicular to the light grey Sr labels in the underlying BSE image and, at this specific locality in the shell, differs by ca. 90° from the general shell growth direction (white arrow). Similar to the oOSL in Supplementary Figure 2.10, the data forms a narrow girdle of random orientations for the [100] and [010] directions parallel to the growth lines running perpendicular to the general shell growth direction. Maximum density value for the [001] axes is 36.49 times uniform, thus exceeding significantly the value of the prismatic ultrastructure (oOSL, Supplementary Figure 2.10). A schematic of the shell tip shows the location of the orientation map and the BSE image. Asterisk marks the inner shell surface. Scale bar is 10  $\mu\text{m}$ .



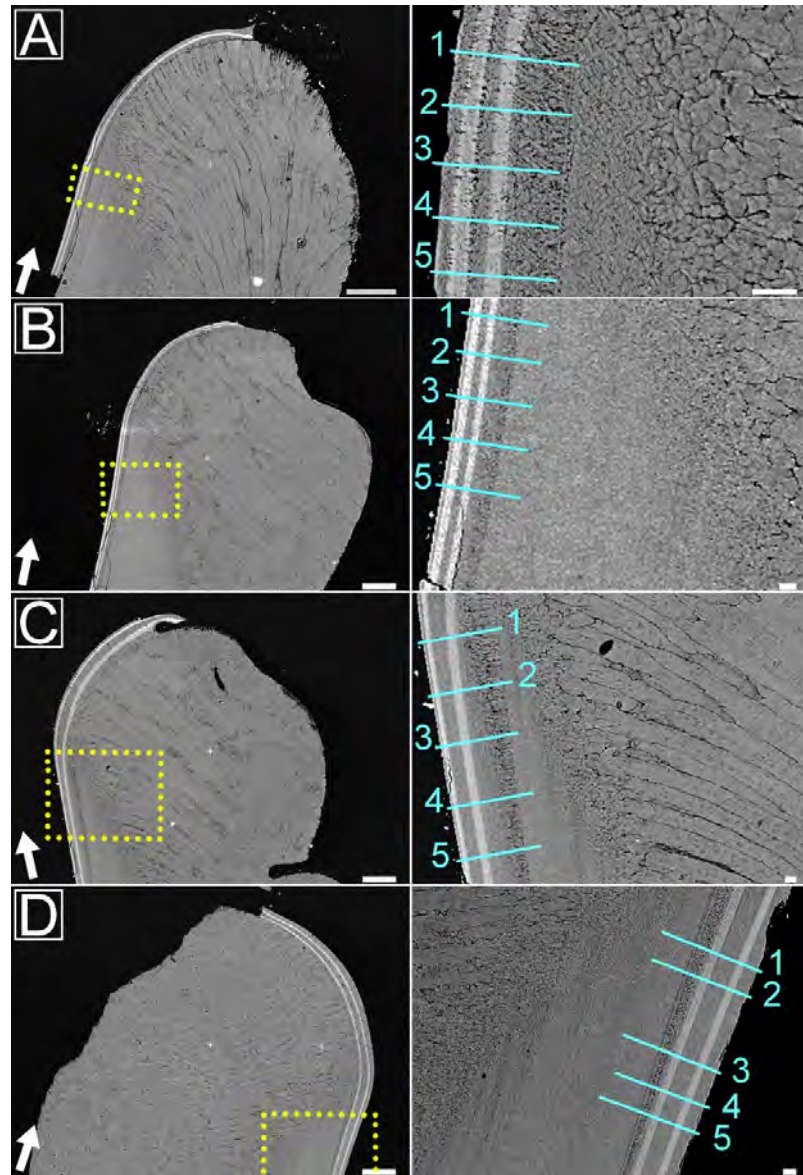


**Supplementary Figure 2.13:** First-order prisms (separated by organic sheaths) have undulated (red line follows inner shell surface, blue line shows same undulating pattern at beginning and end of Sr-label) growth fronts with the individual apex co-aligned with the centre of each prism. A white arrow indicates the general growth direction of the shell, while the local growth direction is perpendicular to the Sr-labelled shell layer. Scale bar is 10  $\mu\text{m}$ .



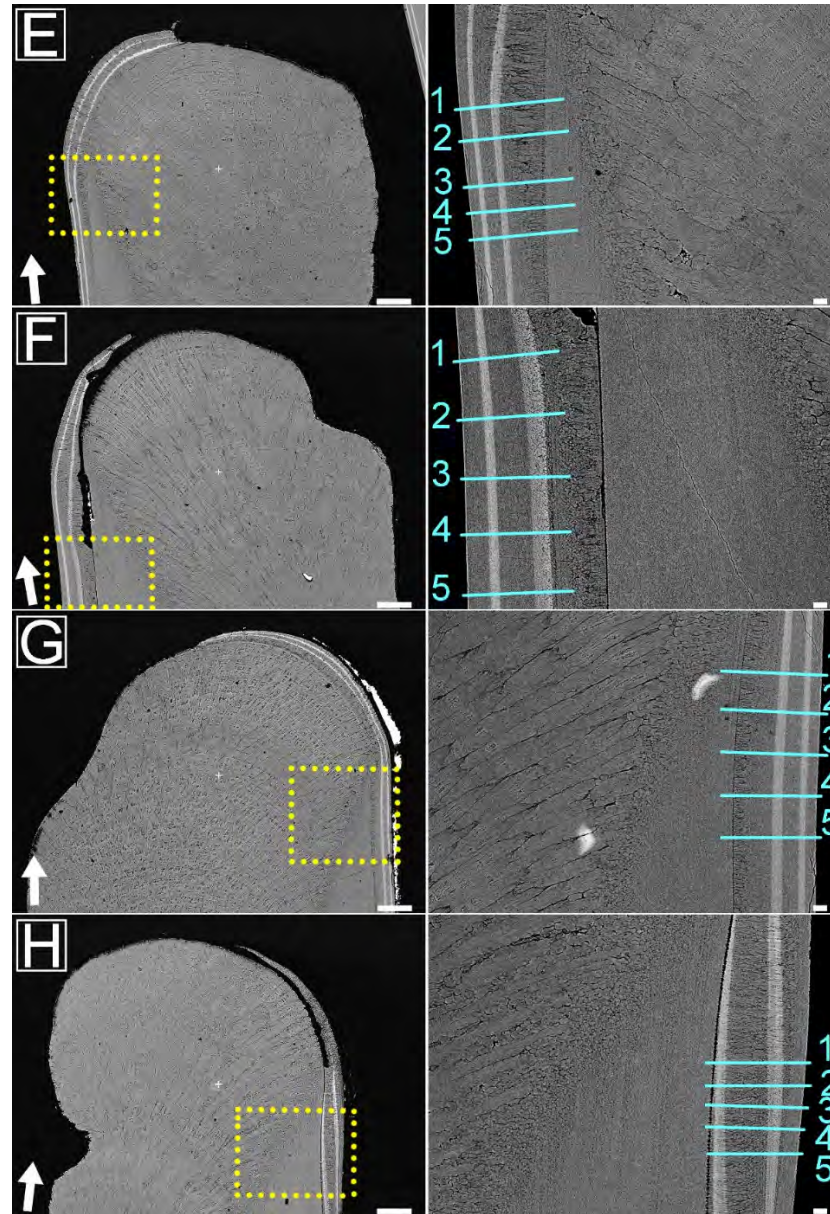


**Supplementary Figure 2.14: BSE images of polished cross-sections of compound composite prismatic shell at the growth front of the ventral margin. Overview images (left column) as well as higher magnification images of areas marked in yellow (right column). Blue numbered lines indicate where local growth rate measurements were obtained (all data see Supplementary Table 2.4, for averages see Table 2.2). Specimens used are K2-01 (a), K2-02 (b), K2-04 (c), K2-06 (d), K2-08 (e), and K2-11 (f). Specimens K2-10 and K2-14 are excluded here as they showed different perturbations at this growth front. White arrows indicate the general growth direction for each shell, while the individual local growth direction is perpendicular to the Sr-label in light grey. Scale bars: 100  $\mu$ m for left column and 10  $\mu$ m for right column images.**

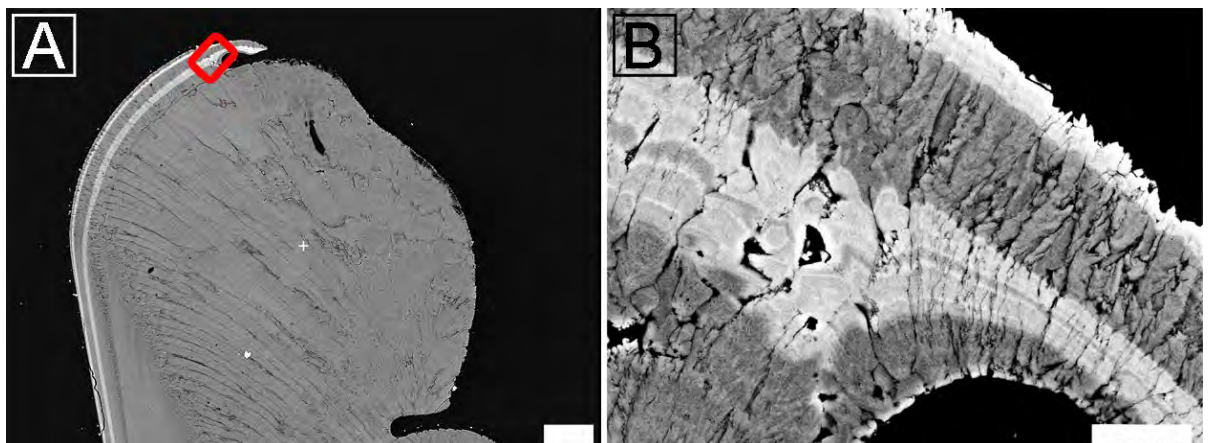


**Supplementary Figure 2.15: BSE images of polished cross-sections of crossed-acicular shell layers (iOSL) near the growth front of the ventral margin. Overview images (left column) as well as higher magnification images of areas marked in yellow (right column) show the Sr labels along the growth fronts in light grey. Blue numbered lines mark where growth measurements were obtained (for all data see Supplementary Table 2.5, for averages see Table 2.2). Specimens are K2-01 (a), K2-02 (b), K2-04 (c), K2-06 (d), K2-08 (e), K2-10 (f), K2-11 (g), and K2-14 (h). White arrows indicate the general growth directions for each shell, while the individual local growth direction is perpendicular to the Sr-label in light grey. Scale bars: 100  $\mu\text{m}$  for left column, 10  $\mu\text{m}$  for right column.**

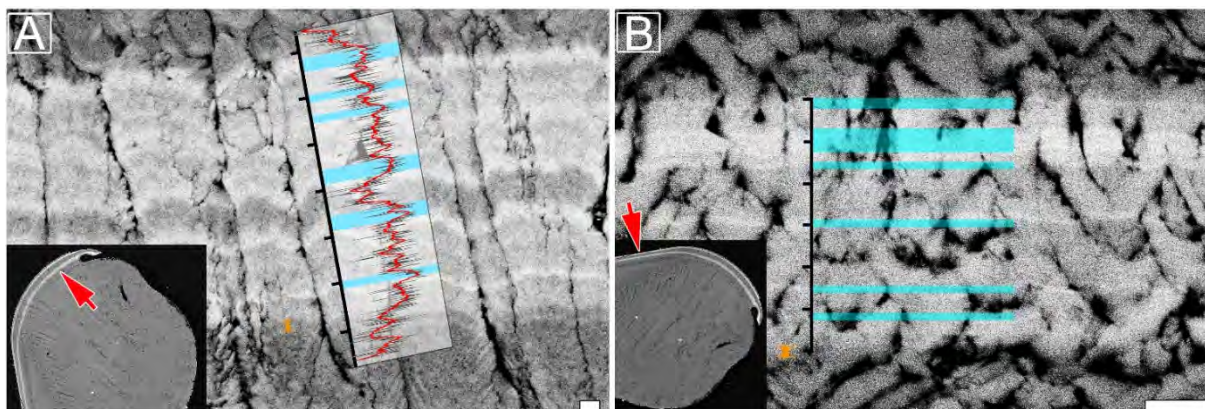




Supplementary Figure 2.15 Continued



Supplementary Figure 2.16: BSE images of a polished cross-section (sample K2-04) (a). (b) shows an enlarged area marked by the red box in (a). It can be clearly seen how the new ridge feature formed as a consequence of very high short-term local growth rate as the label is thicker here, likely, to stabilize the fragile new tip area. See Supplementary Figure 2.15C for general growth direction of the shell, while the individual local growth direction is perpendicular to the Sr-label in light grey. Scale bars are 100  $\mu\text{m}$  (a) and 10  $\mu\text{m}$  (b).



**Supplementary Figure 2.17:** BSE images of polished cross-sections of a Sr-labelled shell (sample K2-04). In the compound composite prismatic layer (oOSL), both Sr labels LE1 (a) and LE2 (b) consist of several narrow increments of varying bright greyscales. Similar patterns are observed in the crossed-acicular layer (iOSL) for LE1 (c) and LE2 (d) Comparison with micro-Raman maps (Figure 3) supports differences in Sr contents between these micro-increments of different grey scales. Line profile insets of BSE greyscale intensities for LE1 (a) reveal six distinct peaks. Generally, brighter greyscale areas correlating with the peaks in the line scans are significantly thinner than the darker areas between them. Differences in intensity and width of increments observed within the labels are suggested to result from metabolic activity, perhaps with higher growth rates incorporating higher amounts of Sr (as peaks) followed by wider intervals of lower Sr concentration, due to lower growth rates. The crossed-acicular ultrastructure (iOSL) shows similar patterns (b) that are highlighted by blue lines after visual examination. This approach was chosen since it is not possible to obtain line-profiles across these labels as the organic sheaths surrounding the lamellae distort the line profiles severely. A ca. 500 nm narrow greyscale transition in for the oOSL in (a) (ca. 150 nm in the iOSL (b)) is highlighted in orange and depicts shell growth in the range of 5 hours calculated by the local daily growth rates of Table 2.2. See Supplementary Figure 2.15C for general growth direction of the shell, while the Sr-labelled shell layers show the local growth directions at this particular site. Scale bars are 1 µm.

### *Supplementary tables*

**Supplementary Table 2.1: WDX Electron Probe Micro Analyser (EPMA) parameters.**

Routine:		"Biocarb" protocol:
Accelerating Voltage:		15 kV
Beam Current:		8 nA
Spot Size:	Scanning at 20000 magnification	
Elements and lines used:		11
- Na K $\alpha$		Albite
- Mg K $\alpha$		Dolomite
- P K $\alpha$		Apatite
- S K $\alpha$		BaSO <sub>4</sub>
- Cl K $\alpha$		Tugtupite
- K K $\alpha$		Orthoclase
- Ca K $\alpha$		CaCO <sub>3</sub>
- Mn K $\alpha$		Rhodochrosite
- Fe K $\alpha$		Fe <sub>2</sub> O <sub>3</sub>
- Sr L $\alpha$		SrSO <sub>4</sub>
- Ba L $\alpha$		BaSO <sub>4</sub>



**Supplementary Table 2.2: Geochemical composition of *K. rhytiphora* shells obtained from wavelength-dispersive X-ray spectrometry (WDS) electron probe micro analyser (EPMA) as wt.% (g·g<sup>-1</sup>) averages (Avg.) and standard deviations (Stdev.). Shell increments listed are those grown in the wild (“pre-aqua”), in aquaculture during pulsed Sr-labelling (“LE 1” and “LE 2”), and non-labelling (“pre-NE 1” and “NE 1”).**

			Na <sub>2</sub> O	MgO	SO <sub>3</sub>	Cl	CaO	SrO
Compound composite prismatic	Pre-Aqua	Avg.	0.72	0.03	0.10	0.04	54.38	0.12
	(n=5)	Stdev	0.06	0.02	0.04	0.01	0.20	0.03
	Pre-LE 1	Avg.	0.57	0.04	0.14	0.04	54.73	0.13
	(n=3)	Stdev	0.04	0.01	0.03	0.01	0.07	0.01
	LE 1	Avg.	0.56	0.04	0.12	0.03	52.86	2.36
	(n=3)	Stdev	0.04	0.01	0.02	0.01	0.09	0.07
	NE 1	Avg.	0.41	0.03	0.17	0.03	54.72	0.16
	(n=3)	Stdev	0.01	0.03	0.05	0.02	0.43	0.01
	LE 2	Avg.	0.65	0.04	0.12	0.02	53.80	2.29
	(n=3)	Stdev	0.04	0.01	0.03	0.01	0.15	0.02
Crossed Acicular	Pre-Aqua	Avg.	0.75	bdl	0.05	0.02	54.01	0.11
	(n=5)	Stdev	0.09	-	0.06	0.01	0.06	0.04
	Pre-LE 1	Avg.	0.77	bdl	0.05	0.02	53.76	0.10
	(n=3)	Stdev	0.09	-	0.03	0.02	0.07	0.04
	LE 1*	Avg.	0.75	bdl	0.13	0.03	53.18	>1.43
	(n=3)	Stdev	0.09	-	0.07	0.01	0.06	0.04
	NE 1*	Avg.	0.72	0.03	0.20	0.02	54.52	0.15
	(n=3)	Stdev	0.09	0.05	0.07	0.02	0.06	0.04
	Limits of Detection:		0.05	0.02	0.04	0.01	0.04	0.02

MnO (<0.025), BaO (<0.018), P<sub>2</sub>O<sub>5</sub> (<0.028), K<sub>2</sub>O (<0.017), and FeO (<0.020), were analysed and always below detection limits (provided in brackets as wt.%). \*LE2 and NE 2 in the crossed acicular ultrastructure (iOSL) were too close to the inner shell surface and are excluded, while LE1 is presented as a minimum value as the analysed area slightly exceeds the label width

**Supplementary Table 2.3: Raman band parameters of  $\nu_1[\text{CO}_3]$  as obtained from micro-Raman hyperspectral mapping of Sr labelled and unlabelled aragonite of the compound composite prismatic (oOSL) and crossed-acicular (iOSL) shell layers. FWHM distributions are shown in Figure 3, while Raman band positions shifts are shown in Supplementary Figure 3. Averages from spectra from labelled and unlabelled regions ( $\sim 25 \mu\text{m}^2$ ) are given ( $\emptyset$ ) together with minimum and maximum values of multiple spots (spot size  $2.25 \mu\text{m}^2$ ) and reflect subtle changes within respective layers. All FWHM values were corrected following the equation of Váczi (2014).**

Sample Area:		FWHM [ $\text{cm}^{-1}$ ]		Raman shift [ $\text{cm}^{-1}$ ]	
Compound composite prismatic	LE 1	$\emptyset$	1.9	$\emptyset$	1084.5
		Max:	2.7	Max:	1084.8
		Min:	1.7	Min:	1084.6
	NL 1	$\emptyset$	1.7	$\emptyset$	1084.8
		Max:	1.8	Max:	1084.9
		Min:	1.6	Min:	1084.7
	LE 2	$\emptyset$	2.1	$\emptyset$	1084.4
		Max:	2.2	Max:	1084.5
		Min:	2.0	Min:	1084.3
	NE 2*		n.a.		n.a.
	LE 1	$\emptyset$	1.8	$\emptyset$	1084.7
		Max:	1.9	Max:	1084.9
		Min:	1.7	Min:	1084.6
Crossed-acicular	NL 1	$\emptyset$	1.5	$\emptyset$	1085.3
		Max:	1.6	Max:	1085.4
		Min:	1.4	Min:	1085.2
	LE 2	$\emptyset$	2.3	$\emptyset$	1084.5
		Max:	2.4	Max:	1084.6
		Min:	2.2	Min:	1084.4
	NE 2	$\emptyset$	1.5	$\emptyset$	1085.3
		Max:	1.5	Max:	1085.4
		Min:	1.3	Min:	1085.2

\*NL 2 in the crossed-acicular ultrastructure map was too narrow for measuring.

**Supplementary Table 2.4: Local growth rates (three replicate measurements) under pulsed Sr-labelling aquaculture conditions for the compound composite prismatic (oOSL) layer. Line # refers to blue numbered lines in Supplementary Figure 13 where growth measurements were obtained. LE 1 and LE 2 (both 6 days), refer to the first and second labelling periods while NE 1 (12 days) denotes normal Sr conditions in-between LE 1, LE 2, and NE 2 (either 6 days or 12 days depending on specimen depicted as bold and normal font) describes growth at normal low Sr concentrations after the last labelling event. Specimens K2-06, K2-10 and K2-14 are excluded here as they showed different perturbations at the growth front.**

Sample ID:	Line #:	Rep.:	LE 1	NE 1	LE 2	NE 2
			[ $\mu\text{m}/6\text{d}$ ]	[ $\mu\text{m}/12\text{d}$ ]	[ $\mu\text{m}/6\text{d}$ ]	[ $\mu\text{m}/6\text{d}$ ] or [ $\mu\text{m}/12\text{d}$ ]
(A) K2-01	1	A	5.23	5.97	0	<b>0</b>
		B	5.33	5.97	0	<b>0</b>
		C	5.34	5.76	0	<b>0</b>
	2	A	5.07	5.69	0	<b>0</b>
		B	5.20	5.72	0	<b>0</b>
		C	5.00	5.51	0	<b>0</b>
	3	A	5.97	5.39	0	<b>0</b>
		B	6.07	5.25	0	<b>0</b>
		C	5.96	5.11	0	<b>0</b>
	4	A	4.87	6.57	0	<b>0</b>
		B	4.68	6.75	0	<b>0</b>
		C	4.65	6.55	0	<b>0</b>
	5	A	4.48	5.13	0	<b>0</b>
		B	4.31	4.77	0	<b>0</b>
		C	4.38	4.98	0	<b>0</b>
		Ave.	5.10	5.68	0	<b>0</b>
		Stdev.	0.55	0.58	0	<b>0</b>
(B) K2-02	1	A	2.52	3.44	3.49	<b>3.02</b>
		B	2.52	3.46	3.50	<b>3.08</b>
		C	2.64	3.32	3.30	<b>2.93</b>
	2	A	2.62	4.19	2.60	<b>3.03</b>
		B	2.65	4.12	2.67	<b>3.18</b>
		C	2.64	4.09	2.70	<b>3.05</b>
	3	A	2.02	4.40	2.38	<b>2.83</b>
		B	1.98	4.34	2.47	<b>2.78</b>
		C	1.91	4.33	2.34	<b>2.85</b>
	4	A	2.07	3.06	2.02	<b>3.01</b>
		B	2.19	2.83	2.27	<b>2.93</b>
		C	2.07	2.94	2.07	<b>2.91</b>
	5	A	1.68	3.70	2.34	<b>2.29</b>
		B	1.77	3.68	2.34	<b>2.18</b>
		C	1.72	3.64	2.28	<b>2.21</b>
		Ave.	2.20	3.70	2.58	<b>2.82</b>
		Stdev.	0.35	0.51	0.46	<b>0.31</b>
(C) K2-04	1	A	15.03	19.12	6.00	<b>5.00</b>
		B	14.92	19.17	6.16	<b>5.20</b>
		C	14.97	19.32	6.09	<b>5.14</b>
	2	A	12.44	20.21	4.69	<b>7.24</b>
		B	12.75	20.61	4.51	<b>7.24</b>
		C	12.95	20.23	4.65	<b>7.04</b>
	3	A	13.11	19.53	4.33	<b>5.93</b>
		B	13.00	19.62	4.42	<b>5.74</b>
		C	13.11	19.60	4.01	<b>5.73</b>
	4	A	12.94	19.99	4.80	<b>5.68</b>
		B	13.04	20.16	4.78	<b>5.62</b>
		C	13.49	19.94	4.65	<b>5.49</b>
	5	A	12.47	20.89	4.47	<b>5.34</b>
		B	12.41	20.80	4.39	<b>5.02</b>
		C	12.46	20.49	4.40	<b>5.15</b>
		Ave.	13.27	19.98	4.82	<b>5.77</b>
		Stdev.	0.90	0.56	0.66	<b>0.75</b>

**Supplementary Table 2.4 continued.**

Sample ID:	Line #:	Rep.:	LE 1	NE 1	LE 2	NE 2
			[ $\mu\text{m}/6\text{d}$ ]	[ $\mu\text{m}/12\text{d}$ ]	[ $\mu\text{m}/6\text{d}$ ]	[ $\mu\text{m}/6\text{d}$ ] or [ $\mu\text{m}/12\text{d}$ ]
(E) K2-08	1	A	5.76	21.47	2.17	16.59
		B	5.64	21.17	2.20	16.57
		C	5.65	21.15	2.12	16.45
	2	A	8.54	24.65	2.70	15.99
		B	8.52	24.53	2.77	16.21
		C	8.44	24.57	2.73	15.95
	3	A	8.89	22.21	4.16	17.30
		B	8.74	22.33	3.96	17.48
		C	8.03	22.30	4.11	17.12
	4	A	5.20	20.15	4.13	17.10
		B	5.13	20.07	4.43	17.32
		C	5.20	19.99	4.20	17.40
	5	A	4.30	23.46	4.21	17.33
		B	3.93	23.36	4.36	17.36
		C	4.12	23.58	4.28	17.51
		Ave.	6.40	22.33	3.50	16.91
		Stdev.	1.81	1.59	0.89	0.54
(F) K2-11	1	A	1.86	8.43	1.98	5.24
		B	1.80	8.53	2.06	5.40
		C	1.89	8.57	1.99	5.33
	2	A	3.28	10.30	2.99	7.59
		B	2.99	10.37	3.02	7.58
		C	3.27	10.30	3.04	7.52
	3	A	2.53	12.23	4.18	7.93
		B	2.55	12.13	4.16	7.93
		C	2.54	11.71	4.02	7.96
	4	A	3.59	12.11	4.41	8.40
		B	3.81	12.17	4.59	8.23
		C	4.18	11.87	4.34	8.39
	5	A	2.74	10.88	4.18	9.35
		B	2.74	10.95	4.19	9.28
		C	2.81	10.88	4.18	9.36
		Ave.	2.84	10.76	3.55	7.70
		Stdev.	0.68	1.31	0.92	1.33

**Supplementary Table 2.5: Local growth rates (three replicate measurements) under pulsed Sr-labelling aquaculture conditions for the crossed-acicular (iOSL) layer. Line # as above. LE 1 and LE 2 (both 6 days), refer to the first and second labelling periods while NE 1 (12 days) depicts normal Sr conditions between LE 1, LE 2, and NE 2 (either 6 days or 12 days depending on specimen) describes growth at normal conditions after the last labelling event.**

Sample ID:	Line #:	Rep.:	LE 1 [μm/6d]	NE 1 [μm/12d]	LE 2 [μm/6d]	NE 2 [μm/6d] or [μm/12d]
(A) K2-01	1	A	3.46	3.09	3.56	3.69
		B	3.44	3.13	3.50	3.59
		C	3.37	3.03	3.82	3.66
	2	A	3.23	3.80	4.06	3.23
		B	3.14	4.02	3.80	3.20
		C	3.29	3.80	3.92	3.10
	3	A	3.79	3.61	3.86	3.29
		B	3.73	3.67	3.86	3.26
		C	3.70	3.77	3.89	3.39
	4	A	3.64	3.99	4.08	3.23
		B	3.80	3.89	4.27	3.20
		C	3.61	4.05	4.27	3.16
	5	A	3.48	3.79	4.11	3.29
		B	3.38	3.86	4.24	3.36
		C	3.32	3.86	4.02	3.36
		Ave. Stdev.	3.49 0.20	3.69 0.33	3.95 0.23	3.33 0.17
(B) K2-02	1	A	4.26	4.08	3.61	2.46
		B	3.83	3.92	3.69	2.45
		C	3.91	3.82	3.77	2.47
	2	A	3.58	4.59	4.24	2.94
		B	3.32	4.73	4.10	3.20
		C	3.41	4.71	4.14	3.32
	3	A	3.92	3.92	3.74	2.43
		B	3.80	4.26	4.14	2.63
		C	3.43	3.99	3.72	2.33
	4	A	3.58	4.54	3.92	2.37
		B	3.48	4.40	4.03	3.02
		C	3.53	4.38	3.75	2.29
	5	A	3.29	4.40	4.03	2.34
		B	3.34	4.32	3.89	2.45
		C	3.28	4.27	4.07	2.39
		Ave. Stdev.	3.60 0.28	4.29 0.28	3.92 0.19	2.61 0.33
(C) K2-04	1	A	8.27	11.86	4.37	3.49
		B	8.17	12.19	4.59	3.46
		C	9.35	12.25	4.63	3.15
	2	A	3.49	9.89	4.47	2.68
		B	3.46	9.84	4.75	2.54
		C	3.15	9.59	4.75	2.80
	3	A	7.88	9.96	3.64	3.39
		B	7.82	9.87	3.64	3.46
		C	7.90	9.84	3.76	2.78
	4	A	7.50	9.77	4.23	1.93
		B	7.50	9.79	4.16	1.83
		C	7.86	9.78	4.35	1.95
	5	A	7.52	9.14	4.16	1.66
		B	7.50	9.49	4.25	1.69
		C	7.73	9.26	4.42	1.52
		Ave. Stdev.	7.01 1.88	10.17 0.99	4.28 0.35	2.55 0.71

**Supplementary Table 2.5 continued.**

Sample ID:	Line #:	Rep.:	LE 1	NE 1	LE 2	NE 2
			[μm/6d]	[μm/12d]	[μm/6d]	[μm/6d] or [μm/12d]
(D) K2-06	1	A	6.83	14.07	5.83	10.52
		B	6.71	14.35	5.98	10.48
		C	6.67	14.19	5.55	10.43
	2	A	6.52	14.19	5.40	10.40
		B	6.55	13.82	5.62	9.87
		C	6.56	14.18	5.42	9.73
	3	A	5.47	13.80	5.47	10.01
		B	5.49	13.80	5.50	10.11
		C	5.29	13.61	5.54	10.09
	4	A	5.87	13.06	5.79	10.52
		B	5.89	13.15	5.79	10.44
		C	5.88	12.99	5.27	10.09
	5	A	5.13	12.59	5.17	9.39
		B	5.42	12.72	5.22	9.35
		C	5.40	12.79	5.27	9.31
		Ave.	5.98	13.55	5.52	10.05
		Stdev.	0.58	0.59	0.24	0.42
(E) K2-08	1	A	5.99	11.10	4.11	7.56
		B	6.19	11.02	4.03	7.63
		C	6.06	11.09	4.04	7.62
	2	A	5.45	11.16	3.88	7.55
		B	5.40	11.03	3.82	7.56
		C	5.42	11.16	3.75	7.50
	3	A	5.04	10.79	3.30	7.48
		B	4.89	10.79	3.16	7.48
		C	4.88	10.72	3.32	7.41
	4	A	4.75	10.36	3.88	7.05
		B	4.89	10.20	3.95	7.19
		C	4.82	10.22	3.73	7.06
	5	A	4.76	10.44	3.31	6.91
		B	4.74	10.51	3.30	6.99
		C	4.89	10.44	3.45	6.98
		Ave.	5.21	10.74	3.67	7.33
		Stdev.	0.49	0.34	0.31	0.26
(F) K2-10	1	A	14.19	22.83	6.12	14.67
		B	13.86	22.75	6.12	14.75
		C	13.96	22.74	6.27	14.76
	2	A	13.29	24.30	6.34	16.13
		B	13.41	24.19	6.22	16.01
		C	13.49	24.31	6.32	16.03
	3	A	11.76	25.66	6.96	16.52
		B	11.74	25.88	7.07	16.53
		C	11.75	25.98	6.74	16.31
	4	A	12.72	25.66	6.41	16.85
		B	12.72	25.56	6.42	16.85
		C	12.62	25.44	6.52	16.86
	5	A	12.41	25.89	6.75	16.97
		B	12.40	25.89	6.75	17.07
		C	12.73	25.89	6.65	17.18
		Ave.	12.87	24.86	6.51	16.23
		Stdev.	0.78	1.20	0.29	0.83

**Supplementary Table 2.5 continued.**

Sample ID:	Line #:	Rep.:	LE 1	NE 1	LE 2	NE 2
			[ $\mu\text{m}/6\text{d}$ ]	[ $\mu\text{m}/12\text{d}$ ]	[ $\mu\text{m}/6\text{d}$ ]	[ $\mu\text{m}/6\text{d}$ ] or [ $\mu\text{m}/12\text{d}$ ]
(G) K2-11	1	A	6.64	11.23	4.66	8.05
		B	6.50	11.36	4.24	7.82
		C	6.49	11.36	4.52	7.97
	2	A	6.57	11.45	4.44	7.83
		B	6.71	11.51	4.38	7.83
		C	6.63	11.52	4.31	7.62
	3	A	6.21	11.86	4.59	7.41
		B	6.42	11.86	4.52	7.55
		C	6.23	11.85	4.45	7.62
	4	A	6.84	11.64	4.30	7.20
		B	6.91	11.57	4.30	7.13
		C	6.77	11.71	4.37	7.20
	5	A	7.20	11.99	4.16	7.41
		B	6.91	11.85	4.12	7.48
		C	6.91	11.78	4.16	7.55
	Ave.		6.66	11.64	4.37	7.58
	Stdev.		0.26	0.22	0.16	0.27
(H) K2-14	1	A	6.42	30.16	10.91	15.42
		B	6.06	29.80	11.05	15.40
		C	5.99	30.23	10.84	15.76
	2	A	5.92	30.16	9.42	15.20
		B	6.07	30.14	9.49	14.83
		C	6.21	30.16	9.27	15.05
	3	A	7.21	31.03	8.84	14.12
		B	7.35	30.96	8.84	14.19
		C	7.20	30.96	8.77	13.98
	4	A	8.35	29.95	7.70	13.90
		B	8.20	30.23	7.63	14.26
		C	8.56	29.95	7.70	14.05
	5	A	8.63	30.37	8.25	14.55
		B	8.84	30.02	8.27	14.40
		C	8.77	29.95	8.20	14.48
	Ave.		7.32	30.27	9.01	14.64
	Stdev.		1.11	0.38	1.12	0.58

# **3. MICRO- TO NANO-SCALE ARCHITECTURE AND GROWTH DYNAMICS OF BIVALVE SHELLS: CROSSED- LAMELLAR ARCHITECTURE OF *ANADARA TRAPEZIA* (MOLLUSCA, BIVALVIA)**

Laura M. Otter<sup>1\*</sup>, Patrick Trimby<sup>2</sup>, Hadrien Henry<sup>1</sup>, Robert Hovden<sup>3</sup>, Jiseok Gim<sup>3</sup>, Frédéric Marin<sup>4</sup>,  
Matt R. Kilburn<sup>5</sup>, Oluwatoosin B.A. Agbaje<sup>1</sup>, Matthew A Kosnik<sup>6</sup>, Dorrit E. Jacob<sup>1</sup>

<sup>1</sup>Department of Earth & Planetary Science, Macquarie University, NSW 2109, Australia

<sup>2</sup>Oxford Instruments NanoAnalysis, High Wycombe, HP12 3SE, United Kingdom

<sup>3</sup>Department of Materials Science & Engineering, University of Michigan, Ann Arbor, MI 48109, USA

<sup>4</sup>Biogéosciences UMR6282, CNRS, Université de Bourgogne Franche-Comté, Dijon, France

<sup>5</sup>Centre for Microscopy Characterisation and Analysis, University of Western Australia, WA 6009, Australia

<sup>6</sup>Department of Biological Sciences, Macquarie University, New South Wales 2109, Australia

\*Corresponding Author: [laura.otter@mq.edu.au](mailto:laura.otter@mq.edu.au)

This chapter is in preparation for Chemical Geology.

The author's contribution to the publication is as follows: LMO designed the study with the supervisor, acquired the bivalves and diet, conducted aquaculture experiments, sample preparation as well as performed optical microscopy, SEM, micro-Raman analysis and evaluated the data. Further, LMO supported NanoSIMS, EBSD EPMA and TGA analysis as well as data evaluation and drafted the manuscript.



## Abstract

The incorporation of Sr in the aragonitic shells of the bivalve *Anadara trapezia* has been investigated to forward our understanding of the formation mechanisms of shells to support geochemical proxy applications such as high-resolution (paleo-)environmental reconstructions. For this purpose, living shells were subjected to pulse Sr-labelling experiments in controlled aquaculture conditions at constant temperature using enriched seawater 18x (i.e. 144  $\mu\text{g/g}$ ) higher in Sr content than mean ocean water. NanoSIMS, EPMA, and micro-Raman mapping were used to characterize Sr incorporation and were correlated with SE/BSE imaging to investigate aspects of growth dynamics and architectural arrangements. Averaged daily growth rates from shell layers formed in Sr-labelled and unlabelled conditions follow a 1:1 trend suggesting that Sr concentration has no effect on growth rates. As shell layers grown in Sr-labelled and unlabelled conditions formed at constant temperature, it is likely that Sr incorporation into the shell is controlled by physiological effects. Distribution coefficients  $D_{\text{Sr/Ca}}$  obtained for unlabelled (0.14) and labelled shell (0.15) are lower than those for synthetic aragonite and indicate that Sr is actively excluded upon incorporation. Texture analysis using electron backscatter diffraction shows two main orientations of first order lamellae for the crystallographic b- and c-axes that are separated by a 60° rotation around the a-axis. Both orientations have a weaker sub-maximum consisting of at least 55 % twinned grain boundaries that share the same orientation with respect to their c-axis but differ by about 90° in their a- and b-axes.

## 3.1 Introduction

Bivalve shells are biocomposite materials consisting of a hierarchical arrangement of calcium carbonate (e.g. aragonite and/or calcite) and organic macromolecules (Weiner and Traub, 1980). These arrangements are expressed as different ultrastructures that have all evolved within the phylum Mollusca to enhance the mechanical properties of their exoskeleton (Boggild, 1930; Carter, 1989; Taylor, 1969; Weiner et al., 2000). Our main motivation to study shells is their ability to record climatic and environmental changes that are encoded as trace elemental and isotopic signatures within the growing biomineral (Weiner and Dove, 2003). These signatures are used empirically as high-resolution time-constrained proxies (e.g. Gillikin et al., 2006; Klein et al., 1996b; Schöne et al., 2004), but interpretation is often limited by the fundamental lack of knowledge of how trace elements are incorporated and how physiological processes influence shell growth. A good example demonstrating where we stand in this field of research is our understanding of how nacre forms: this has recently experienced a paradigm shift away from classical ion-by-ion crystallization and to crystallization via colloid attachment and transformation that involves amorphous calcium carbonate (ACC) nanoparticles as metastable precursor phases which transform into mature aragonite via processes of self-assembly and oriented attachment (Addadi et al., 2003; Cölfen, 2008; De Yoreo et al., 2015; De Yoreo and Vekilov, 2003; Jacob et al., 2008; Jacob et al., 2011; Levi-Kalishman et al., 2001; Weiss et al., 2002; Wolf et al., 2012; Wolf et al., 2016; Zhang and Xu, 2013). This concept is, however, not yet incorporated into paleoclimate proxy applications. Critical questions concerning the potential impact of this paradigm shift on trace element

partitioning and how sub-micron growth processes are influenced by the bivalve's physiology, need yet to be answered. Moreover, even less is known about the formation of non-nacreous bivalve shells, where ACC has also been found (Wolf et al., 2016), suggesting similar formation processes to nacreous shells.

The crossed-lamellar structure is the most common ultrastructure with the highest fracture toughness within the mollusca phylum (Almagro et al., 2016; Böhm et al., 2016; Dauphin and Denis, 2000). It is a complex architecture consisting of different hierarchical orders of lamellae (Boggild, 1930). First order lamellae are parallel arranged with thicknesses of ca. 20  $\mu\text{m}$  enveloped by organic membranes and show alternating orientations similar to plywood (Boggild, 1930; Dauphin and Denis, 2000; Kamat et al., 2000; Pokroy and Zolotoyabko, 2003; Taylor, 1973). They are polycrystalline bundles consisting of stacked second order lamellae (Almagro et al., 2016; Pokroy and Zolotoyabko, 2003). The latter consist of elongated fibres referred to as third order lamellae that show a granular surface roughness associated with nanometre sized fourth order lamellae (Almagro et al., 2016). Some studies described these fourth order units as crystallographic twins enveloped by thin organic membranes (Almagro et al., 2016; Dauphin and Denis, 2000; Kobayashi and Akai, 1994; Pokroy and Zolotoyabko, 2003; Uozumi et al., 1972). These arrangements vary in detail among different species and can be separated into groups with different crystallographic and architectural properties (Almagro et al., 2016; Böhm et al., 2016). Additionally, differences have been observed in the composition of the organic matrix (Agbaje et al., 2017a; Agbaje et al., 2018; Dauphin and Denis, 2000).

Marine bivalves of the genus *Anadara* occur worldwide and play an important role in paleoclimate reconstructions (e.g. Azzoug et al., 2012; Brockwell et al., 2016; Houk et al., 2003; Murillo De Nava et al., 1999; Reza Mirzaei et al., 2014). In most studied *Anadara* species, the outer and inner shell layer consist of crossed-lamellar and complex crossed-lamellar structures, respectively (Azzoug et al., 2012; Popov, 1986; Taylor, 1969).

In this study we use the semi-endobenthic Sydney cockle, *Anadara trapezia* (Deshayes), that occurs in intertidal mudflats along the Eastern and Southern coast of Australia (Azzoug et al., 2012), to visualize growth dynamics of the crossed-lamellar structure using pulsed strontium (Sr) labelling experiments in controlled aquaculture conditions at constant temperature. Pulse labelling combined with correlative micro- to nano-analysis is a relatively new variety of labelling that uses either elemental or enriched isotope spikes that allows for higher resolution imaging and trace elemental mapping of the calcareous exoskeletons at the micro to nano-scale (Brahmi et al., 2012; Domart-Coulon et al., 2014; Gorzelak et al., 2011; Nehrke et al., 2013; Otter et al., 2019) compared to other labelling techniques that aim at growth rate determination at lower spatial scales (Mouchi et al., 2013; Riascos et al., 2007; Zhao et al., 2017a).

## 3.2 Materials and methods

### 3.2.1 Aquaculture experiments

Twelve individuals of *Anadara trapezia* (Deshayes, 1839) measuring 7.4 to 8.2 cm in length were collected alive near Shoalhaven in New South Wales and were transferred to the Macquarie Seawater Facility, Sydney, where they were acclimated for four weeks prior to labelling experiments. They were maintained in 50 ltr polyethylene tanks at a density of six individuals/tank. All environmental parameters (salinity, pH and temperature) resembled local ocean values as the water was sourced directly from the ocean and a 12h/12h day/night light cycle was maintained throughout the experimental period. Bivalves were kept in sand-filled polyethylene boxes (20·40 cm<sup>2</sup> and 10 cm height) filled with beach sand up to 9.5 cm into which the bivalves burrowed. These sand-filled boxes were placed within the 50 ltr tanks. Bivalves were fed daily with a special bivalve diet (Shellfish Diet 1800, Reed Mariculture Inc., USA), a commercially available mix of six different microalgae species. See Otter et al. (2019) for more details.

After acclimatization, bivalves entered the experimental period of 21 days: First, they were transferred from normal seawater conditions with an ambient concentration of ca. 8 µg/g Sr, to labelling conditions with enriched Sr concentrations of 144 µg/g Sr (by dissolving 3.5 g SrCl<sub>2</sub>·6 H<sub>2</sub>O in 8 ltr seawater) for four days. Labelled seawater was constantly stirred by airstones and Sr-enriched seawater was fully renewed by emptying and refilling the designated labelling tank after 48h. As the bivalves were burrowing in sand-filled polyethylene boxes that were placed within the large 50 ltr tanks they were easily transferred between ambient and labelling conditions by simply transferring the smaller sand-filled boxes, which eliminates handling stress for the bivalves as repeated exhumation could be avoided (Otter et al., 2019). Post-labelling, the bivalves were transferred back to ambient conditions and sampled and deep-frozen at -20 °C in two batches after 9 and 16 days, respectively. After 48 hours all shells were defrosted, cleaned from adhesive tissues, rinsed in deionized water and air-dried.

### 3.2.2 Sample preparation

Left valves were sectioned along the maximum growth axis using an IsoMet low speed saw (Buehler, IL, USA), mounted in EpoFix epoxy resin (Struers, Australia) and cured at room temperature. Epoxy mounts were ground using sandpapers (250-2000 grit size) and polished with 3 and 1 µm diamond pastes. A suspension of 0.05 µm colloidal silica was used for final polishing before the mounts were carbon coated (20 nm thickness). Additional shell pieces were fractured and etched with EDTA using the method in Otter et al. (2019) and gold coated.

Electron transparent cross-sections for TEM and STEM imaging were prepared using the *ex situ* lift out method in a FEI FIB200 Focused Ion Beam (FIB) instrument at the German Research Centre For Geosciences (GFZ) in Potsdam, Germany, using the approach published in Jacob et al. (2017).

### 3.2.3 Optical microscopy

Specimens were imaged using a Zeiss Axio Imager M2m binocular stereomicroscope equipped with a motorized microscope platform. Images were acquired with a 10x long working distance objective and reflective light and later stitched, and contrast improved using the software package Zen2 Pro.

### 3.2.4 Scanning electron microscopy (SEM)

The Sr-label was visualized by acquiring Z-sensitive backscatter electron (BSE) images with a JEOL 7100F Field Emission Gun-Scanning Electron Microscope (FEG-SEM) from carbon coated epoxy mounts at Macquarie University, Australia. Images were acquired at 15 kV acceleration voltage, 8 nA beam current and 9 mm working distance. Etched shell pieces were imaged using secondary electron (SE) images acquired at 10 kV, 8 nA and 9 mm working distance.

### 3.2.5 Transmission electron microscopy (TEM) and scanning transmission electron microscopy (STEM)

Transmission Electron Microscopy (TEM) imaging was performed using a FEI Tecnai F20 field emission 200kV S/TEM equipped with an X-TWIN lens and a Gatan Tridiem imaging filter at the Helmholtz-Centre Potsdam, Germany. Imaging was performed following previously published procedures (Jacob et al., 2011).

For Scanning Transmission Electron Microscopy (STEM) imaging a JEOL 3100R05 microscope with double Cs aberration corrected STEM (300 keV, 22 mrad) together with a HAADF-STEM detector was used at the University of Michigan, Ann Arbor, MI-USA.

### 3.2.6 Electron backscatter diffraction (EBSD)

Electron backscatter diffraction (EBSD) maps (presented in Supplementary Figures 3.5 to 3.7) were collected using a Hitachi SU70 FEG-SEM equipped with a CMOS-based Symmetry EBSD detector at Oxford Instruments NanoAnalysis, United Kingdom. Maps were acquired using accelerating voltages of 15 and 20 kV, beam currents of 14 and 22 nA and step sizes of 350 and 150 nm for overview and detailed map, respectively. *A. trapezia* shells were found to be beam sensitive and different approaches of polishing were trialed to improve EBSD indexing. Best results were achieved using broad beam Argon ion polishing, which improved the electron beam scattering pattern quality, but created greater surface topography, especially around the microtubules in the shell (see auf Figure 3.5b)).

Post-acquisition data handling included noise reduction, wild spike removal and removal of all grains  $\leq 3$  pixels using the HKL software. EBSD maps, pole figures, and Young's modulus projections were generated with the MTEX toolbox in Matlab (Bachmann et al., 2010) following the protocol in Henry et al. (2017).

### 3.2.7 Electron probe micro analyser (EPMA)

Epoxy mounts were quantitatively analysed using wavelength-dispersive X-ray spectroscopy (WDS) analyses performed on a JEOL JXA 8200 Electron Probe Micro Analyser (EPMA) at the University of Mainz, Germany. Analysis was performed in scanning mode using a slightly defocused beam at 20,000x magnification and the analysed elements were: Na, Mg, P, S, Cl, K, Ca, Mn, Fe, Sr, and Ba. Mass fractions were calibrated against a set of minerals and synthetic reference materials (Otter et al., 2019), while data correction was performed using the ZAF protocol.

### 3.2.8 NanoSIMS analysis

Gold-coated epoxy mounts were pre-sputtered and analysed using a new generation CAMECA NanoSIMS 50L ion probe at the University of Western Australia. The instrument was equipped with a Hyperion RF plasma oxygen ion source that allowed for high-resolution data acquisition. The primary oxygen ion beam diameter was 100 nm and areas of  $100 \times 100 \mu\text{m}^2$  were acquired with a resolution of  $1024 \times 1024$  pixels (3.6 ms/pixel dwell time) for the isotopes  $^{24}\text{Mg}$ ,  $^{40}\text{Ca}$ , and  $^{88}\text{Sr}$  measured at a mass resolving power of 5000. Data processing involved detector dead time correction and the calculation of  $^{88}\text{Sr}/^{40}\text{Ca}$  ratios expressed as a Hue-Saturation-Intensity (HSI) colour scale (minima: blue = 10, maxima: magenta = 50) using the OpenMIMS plugin for ImageJ/FIJI.

### 3.2.9 Micro-Raman mapping

Raman spot measurements were collected in the  $150\text{--}1200 \text{ cm}^{-1}$  range, with a confocal Horiba Jobin Yvon LabRAM HR Evolution coupled to an Olympus optical microscope at Macquarie University, Australia. Spectra were recorded with 50x magnification at room temperature using a 473 nm excitation wavelength, a grating with 1800 grooves/mm, 12 s acquisition time and 4 accumulations. Spot measurements were normalized to the highest intensity peaks without further background subtraction.

A hyperspectral micro-Raman map was obtained from the shell tip area following the protocol of Otter et al. (2019). The map was acquired using a step size of  $0.6 \mu\text{m}$ , a confocal pinhole of 150, and 3 sec acquisition time per spot. Subtle changes of Raman band parameters of the aragonite peak centered at  $1084.8 \text{ cm}^{-1}$  were recorded and later interpreted qualitatively only. Maps were background subtracted and peak fitted using a Lorentzian-Gaussian (pseudo-Voigt) function. FWHM values were corrected for the instrumental apparatus function (Vácz, 2014).

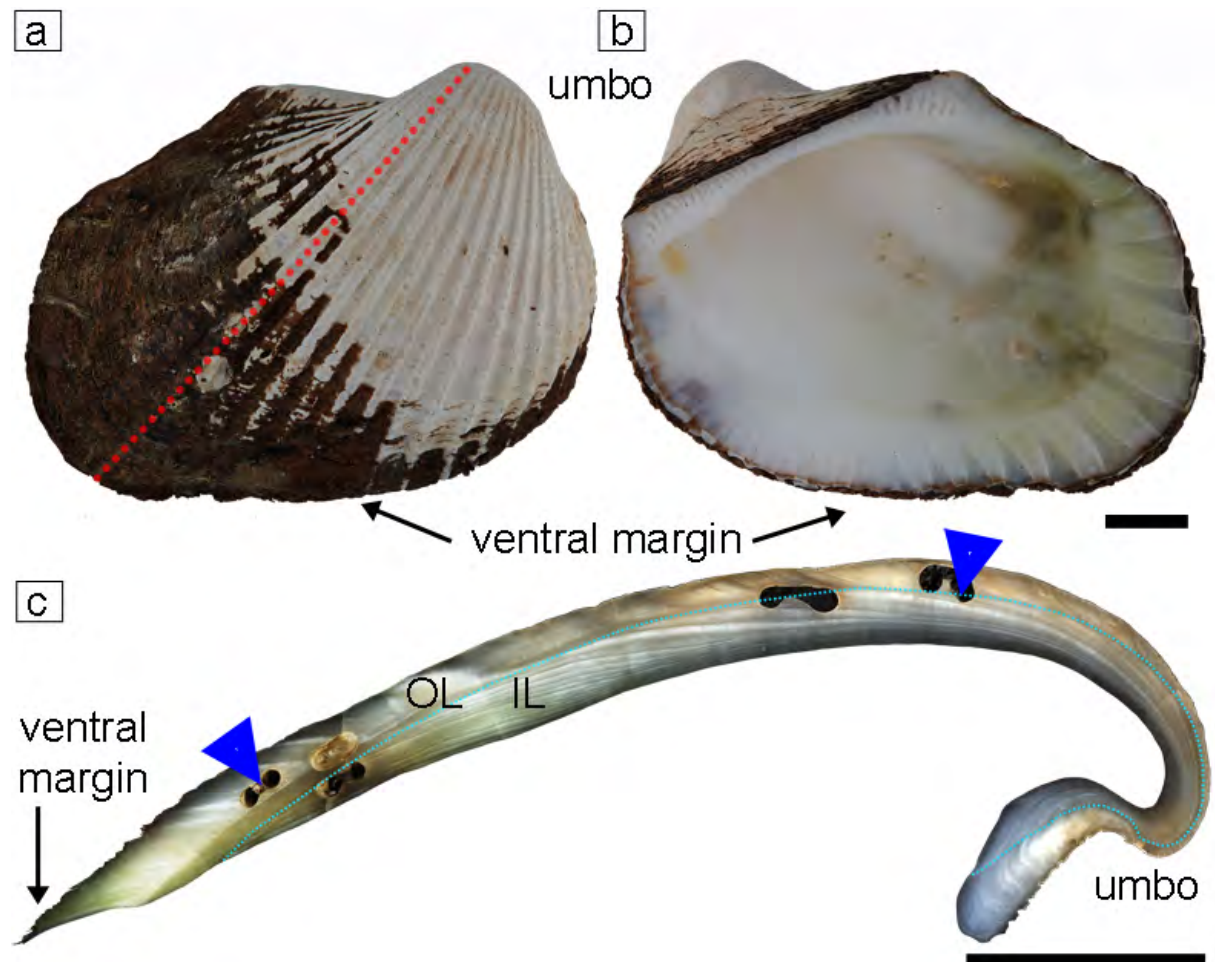
## 3.3 Results

### 3.3.1 General shell characteristics

The exterior of *A. trapezia* shells (Figure 3.1a) exhibit curved radial ribs and are covered by a thick, brown periostracum which is increasingly abraded towards the umbo (Sullivan, 1961). The interior of the shell is translucent white and shows along the ventral margin the negative imprints of the radial ribs (Figure 3.1b). This population of *A. trapezia* shows prominent signs of bioerosion as holes (i.e.  $800 \mu\text{m}$  in diameter, Figure 3.1c) that are characteristic for boring organisms e.g. sponges. They are a common

feature of siphon-less bivalves, such as *A. trapezia*, who are prone to this type of bioerosion, because they must keep their posterior end exposed to maintain filter-feeding and are therefore never entirely sediment-buried (Beesley et al., 1998; Taylor and Maher, 2012). The shell cross-section shows the two architecturally distinct layers in *A. trapezia* shells: An outer layer (OL) consisting of crossed-lamellar and an inner layer (IL) of complex crossed-lamellar ultrastructure. Growth lines within the crossed-lamellar ultrastructure have bent trajectories (Supplementary Figure 3.1).

*A. trapezia* shells are fully aragonitic (Supplementary Figure 3.2), as is characteristic for shells with these architectures (Popov, 1986). Shell surfaces at the adductor muscle scars as well as the pallial line are also aragonitic and not calcitic as in some other bivalves with the same shell architecture (e.g. Böhm et al., 2016). Raman bands for organic pigments were not detected consistent with the white colour of the shell (Supplementary Figure 3.2). This is different to nacreous shells and pearls that have distinct pigment-related Raman bands resulting from 3-5 wt.% total organic phases containing pigment molecules i.e. carotenoids that are accountable for the vibrant, iridescent colours of the natural material (Agbaje et al., 2017a; Hare, 1965; Otter et al., 2017; Soldati et al., 2008).



**Figure 3.1:** Shell of the bivalve *Anadara trapezia* (Deshayes, 1839). The shell exterior (a) shows curved radial ribs and is covered by a thick, brown periostracum along the ventral margin, while it is increasingly abraded towards the umbo. The red dashed line indicates where shells were cut. The interior (b) shows the negative imprints of the radial ribs along the ventral margin. The radial cross-section (c) prepared along the maximum growth axis depicts an inner layer (IL) and outer layer (OL) below and above the dashed blue line, respectively. Bioerosion is visible as holes in older shell parts (exemplarily highlighted by blue arrows). All scale bars are 1 cm.

### 3.3.2 Strontium enrichment and pulse labelled shell increments

EPMA-based WDS analyses of unlabelled *A. trapezia* shell areas were obtained from the crossed-lamellar structure at the ventral margin area for shell layers formed at natural conditions (i.e. “pre-aquaculture” in Table 3.1) and after pulsed Sr-labelling (i.e. “Unlabelled” in Table 3.1). The data show minor element concentrations with notable amounts of MgO and SrO, while MnO, is below detection limits (Table 3.1). “Pre-aquaculture” and “unlabelled” shell layers show very similar geochemical signatures within standard deviations. The section of Sr-labelled shell layer is clearly visible in the BSE images through brighter greyscale values as an effect of higher Z-contrast resulting from the increased incorporation of the heavier element Sr compared to Ca (Fig. 3.2).

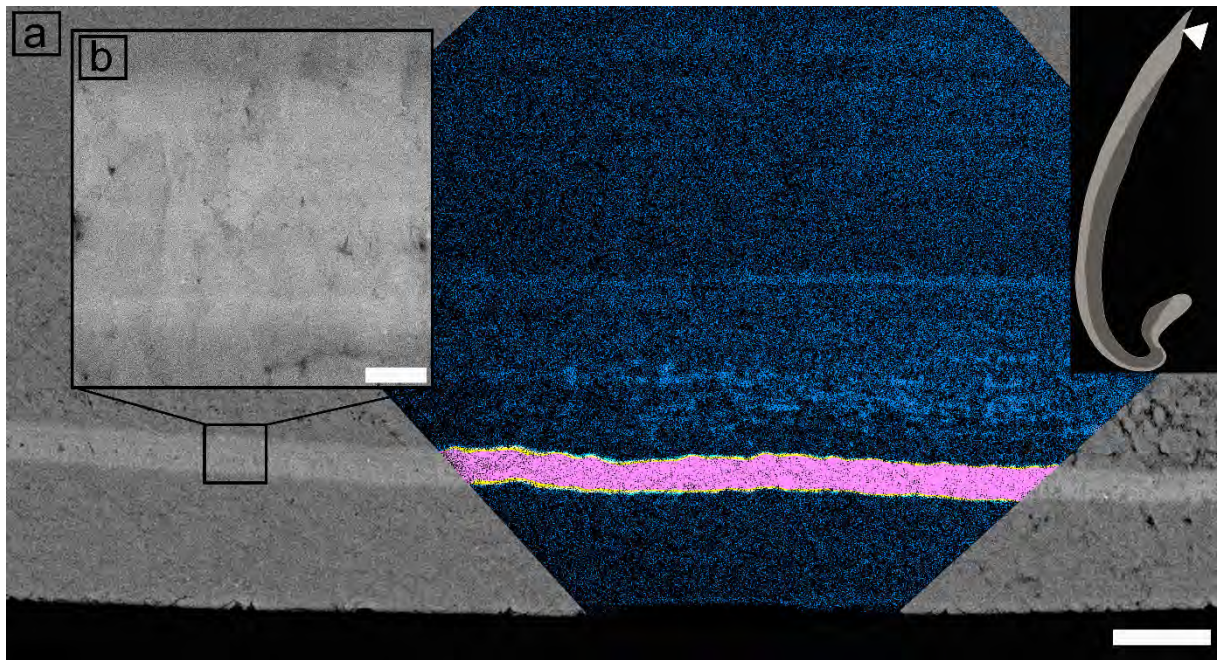
**Table 3.1: Major and minor element concentrations of unlabelled *A. trapezia* shell obtained from the crossed-lamellar ultrastructure at the ventral margin and acquired using wavelength-dispersive X-ray spectrometry (WDS) electron probe micro analysis (EPMA). All values are provided in wt.% (g:g-1) as averages (Av.) from n=12 and first standard deviation (StDev.) together with detection limits. The Sr-enriched label was too narrow for EPMA analysis. “Pre-Aquaculture Shell” averages were derived from shell layers grown prior to aquaculture experiments in the natural environment, while “unlabelled Shell” averages are obtained from aquaculture experiments after Sr pulse-labelling.**

	Na <sub>2</sub> O	MgO	P <sub>2</sub> O <sub>5</sub>	SO <sub>3</sub>	Cl	CaO	K <sub>2</sub> O	MnO	FeO	SrO	BaO
<b>Pre-Aquaculture Shell Av.:</b>	<b>0.68</b>	<b>0.03</b>	<b>0.19</b>	<b>0.11</b>	<b>0.02</b>	<b>55.34</b>	<b>b.d.l.</b>	<b>b.d.l.</b>	<b>b.d.l.</b>	<b>0.11</b>	<b>b.d.l.</b>
StDev.:	0.14	0.02	0.16	0.07	0.01	0.12	-	-	-	0.02	-
<b>Unlabeled Shell Av.:</b>	<b>0.68</b>	<b>0.02</b>	<b>0.03</b>	<b>0.13</b>	<b>0.03</b>	<b>55.03</b>	<b>b.d.l.</b>	<b>b.d.l.</b>	<b>b.d.l.</b>	<b>0.13</b>	<b>b.d.l.</b>
StDev.:	0.12	0.01	0.02	0.07	0.02	0.10	-	-	-	0.06	-
Detection Limits:	0.05	0.02	0.04	0.04	0.01	0.04	0.02	0.03	0.02	0.02	0.01

As the thickness of the Sr-label was less than the diameter of the analysis spots ( $> 3.6 \mu\text{m}$ ), EPMA-based WDS analyses could not be obtained for this area. However, we can calculate the Sr concentrations in the labelled shell areas using (i) the known Sr concentration measured in the unlabelled shell (Table 3.1), (ii) the mean BSE greyscale values from calibrated BSE images and (iii) relating these to measured Sr-labels for shells in a similar experiment (*K. rhytiphora* shells in Otter et al., 2019). This method gives us a close approximation of the Sr content within labelled shell areas as concentrations of all other elements within the seawater and environmental parameters (i.e. temperature, salinity, and food availability) were kept constant during the experiment – leaving the enrichment in Sr as the only major variable parameter. Using a linear correlation between greyscale ratio in *K. rhytiphora* between labelled to unlabelled shell areas of 1.49 and SrO-concentration, the greyscale ratio of 1.54 in *A. trapezia* translates to 2.37 wt.% SrO for the labelled shell part. This value was then subtracted from the CaO concentration of unlabelled shell and yields 52.66 wt.% CaO in labelled shell areas, which again agrees well to values obtained in a previous study (Otter et al., 2019).  $^{88}\text{Sr}/^{40}\text{Ca}$  NanoSIMS maps show the distinct Sr-labelled band in the crossed-lamellar shell layer obtained close to the ventral margin (Figure 3.2a). The NanoSIMS map is overlain on a BSE image acquired prior to NanoSIMS analysis from the same region of interest and demonstrates the excellent correlation between high  $^{88}\text{Sr}/^{40}\text{Ca}$  ratios (pink) in the NanoSIMS map with the brighter greyscale values of the BSE image within the labelled shell area (Figure 3.2a). In contrast, unlabelled, ambient shell parts show low  $^{88}\text{Sr}/^{40}\text{Ca}$  (blue) in the NanoSIMS map that correspond to darker greyscale values in the BSE image. A thin yellow to green zone at the beginning and the end of the Sr-labelled area is indicative of increasing and decreasing Sr-concentrations, respectively. Magnification of the pulse-chase labelled area shows alternating greyscale



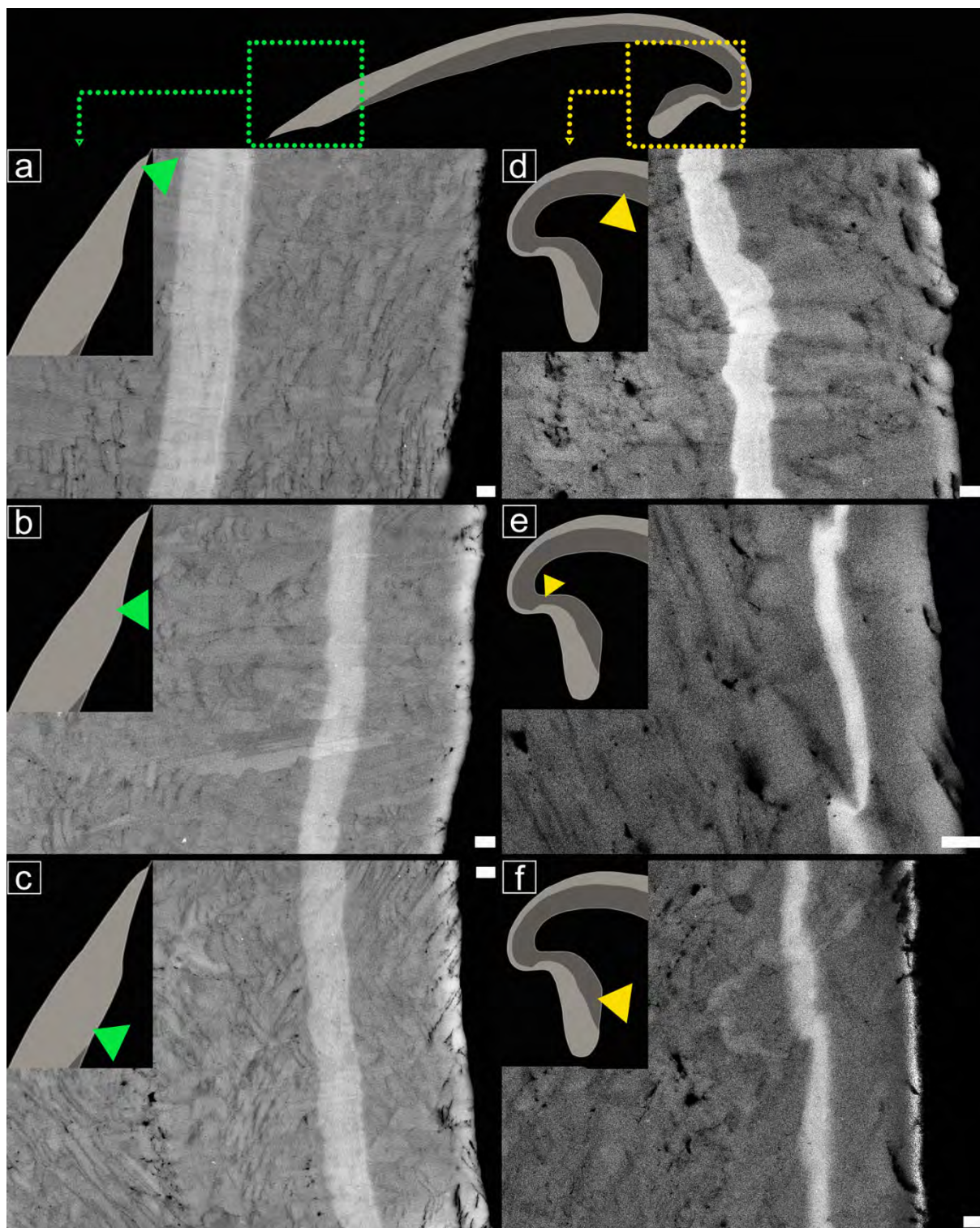
intensities within the label consisting of several narrow bright and broader darker increments (Figure 3.2b).



**Figure 3.2:** NanoSIMS  $^{88}\text{Sr}/^{40}\text{Ca}$  Hue-Saturation-Intensity (HSI) maps showing the polished cross-sections close to the ventral margin (see inset) of a Sr-labelled *A. trapezia* shell and overlaying a BSE image. Note the correlation between high  $^{88}\text{Sr}/^{40}\text{Ca}$  ratios (pink) in the NanoSIMS map and the bright greyscale values of the BSE image within labelled shell areas versus the low  $^{88}\text{Sr}/^{40}\text{Ca}$  ratios (blue) and the darker greyscale values in unlabelled ambient shell parts. Magnification of the Sr-label reveals distinct narrow increments of varying bright greyscales in BSE images. Scale bars are 10  $\mu\text{m}$  (a) and 1  $\mu\text{m}$  (b).

At a qualitative level, it is well known that local growth rates (i.e. the thickness of a growth increment at any shell part) of bivalve shells are highest at the ventral margin and decrease gradually towards the umbo (e.g. Schöne and Surge, 2012). This can be demonstrated using one representative shell with only minimal bioerosion that allows us to quantify relative local growth rates along the shell's cross-section. Local growth rates of the total growth period (i.e. labelled and unlabelled in  $\mu\text{m}$  per 19 days;  $n=5$  measurements see Supplementary Table 3.1) at the crossed-lamellar growth front are highest at the very tip of the ventral margin with  $15.55 \pm 0.16 \mu\text{m}$  on average (Figure 3.3a) and decreases to about  $51 \pm 1 \%$  ( $7.95 \pm 0.08 \mu\text{m}$ ) at a distance of about 5 mm from the tip (Figure 3.3b). At a distance of 10 mm from the tip, rates were found to be about  $52 \pm 1 \%$  ( $8.04 \pm 0.07 \mu\text{m}$ ) (Figure 3.3c). Another important growth front in bivalve shells is the hinge plate of the umbo. As the inner shell layer in *A. trapezia* consists of the complex crossed-lamellar ultrastructure (Figure 3.3) we also measured this growth front in order to compare it's local growth rates with those of the crossed-lamellar architecture: Shortly in front of the umbo, growth rates decreased to only about  $78 \pm 3 \%$  ( $12.16 \pm 0.40 \mu\text{m}$ ) compared to maximum growth at the tip (Figure 3.3d). At the innermost umbo growth is lowest with only around  $39 \pm 3 \%$  ( $6.06 \pm 0.43 \mu\text{m}$ ) relative to maximum growth at the tip (Figure 3.3e). A last measurement at the hinge plate yielded about  $42 \pm 2 \%$  ( $6.50 \pm 0.33 \mu\text{m}$ ), relative to maximum growth at the tip (Figure 3.3f). It should be noted that we do expect actual local growth rates to vary quantitatively across different individuals within bivalve populations (Otter et al., 2019), which is the reason why we choose to use relative local growth rates expressed as:  $\text{local growth rate}_{\text{Location x}} / \text{local growth rate}_{\text{ventral margin}} \times 100$ .





**Figure 3.3:** BSE images showing the growth fronts along the tip (a-c) and umbo (d-f) of the same specimen (sample ID: A1-8L) with crossed-lamellar and complex crossed-lamellar shell ultrastructure, respectively. Location of the BSE images are indicated in the schematic insets. Shell regions labelled with Sr show a brighter greyscale value compared to shell grown under ambient conditions. Scale bars are 1  $\mu\text{m}$ .

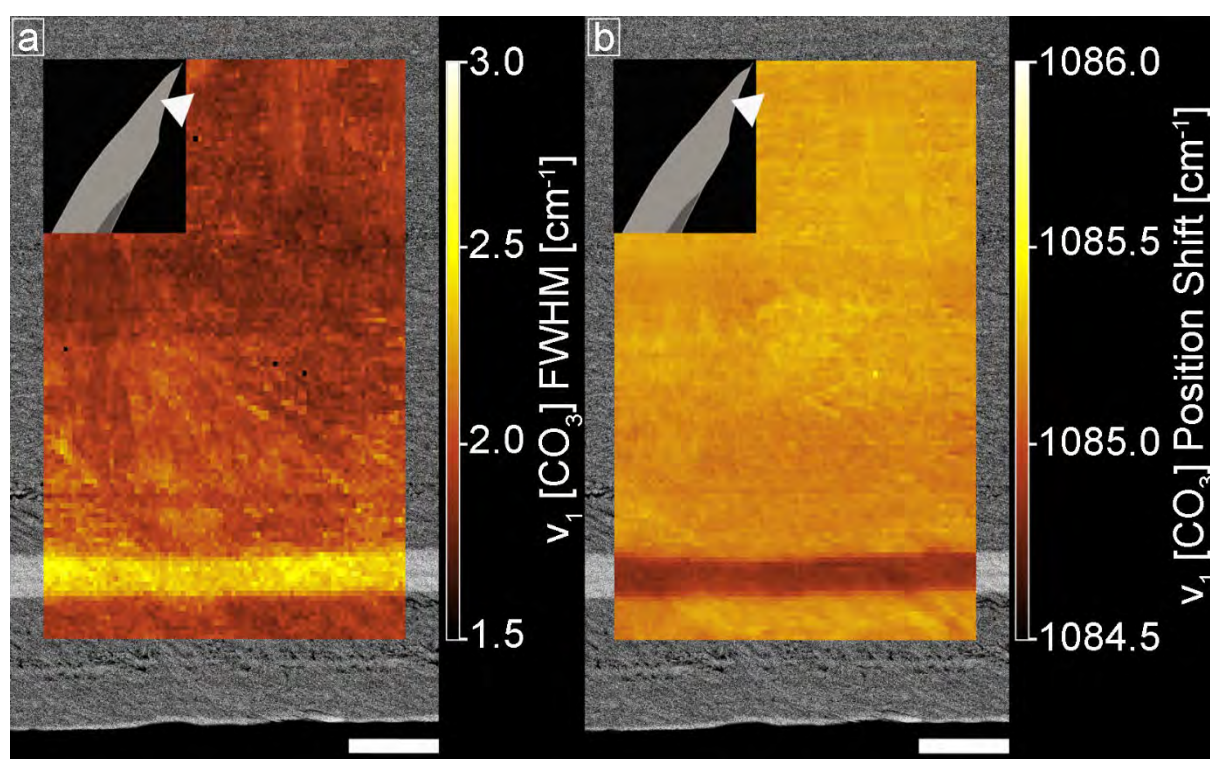
Along the growth front within the crossed-lamellar architecture, the Sr-label cuts through all structural units (first and second order lamellae) and does not follow the outline of any architectural units. This differs from the kinks and undulations observed in the complex crossed-lamellar layer (Figure 3.3d-f, Supplementary Table 3.1).

Micro-Raman maps of the crossed-lamellar ultrastructure depicting the intrinsic carbonate peak  $\nu_1$  located at  $1084.8\text{ cm}^{-1}$  show higher Sr concentrations of the pulsed labelling period to correlate

systematically with a peak broadening (FWHM increase) of about  $0.5 \text{ cm}^{-1}$  (Figure 3.4a, Table 3.2). In addition, the peak position is slightly shifted by about  $0.4 \text{ cm}^{-1}$  (Figure 3.4b, Table 3.2). The Sr-enriched labelled shell area is visible as lighter colour in the FWHM map and darker colour in the position shift map, respectively, and correlates to the bright shell areas of the underlying BSE image obtained from the same region of interest.

**Table 3.2: FWHM and position shifts of  $\nu_1[\text{CO}_3]$  obtained from micro-Raman hyperspectral mapping of Sr-labelled and unlabelled aragonite shell areas of *A. trapezia*. FWHM and Raman band positions shifts are shown in Figure 3.4. Averages with first standard deviations from within labelled and unlabelled shell areas were obtained from ca.  $2 \mu\text{m}^2$  spots and reflect subtle changes, which is why the observed effects on FWHM and position shift are interpreted only qualitatively within this study. All FWHM values were corrected for the instrumental apparatus function using the empirical correction from Váczi (2014).**

Sample Area:	$\nu_1[\text{CO}_3]$ FWHM:		$\nu_1[\text{CO}_3]$ Position Shift [ $\text{cm}^{-1}$ ]:	
	Average [ $\text{cm}^{-1}$ ] n=10	Stdev [ $\text{cm}^{-1}$ ] n=10	Average [ $\text{cm}^{-1}$ ] n=10	Stdev [ $\text{cm}^{-1}$ ] n=10
Pre-Labeling	1.9	0.07	1085.2	0.03
Labelling	2.4	0.06	1084.8	0.02
Post-Labeling	2.0	0.04	1085.2	0.02



**Figure 3.4: Micro-Raman maps obtained from a polished cross-section of a Sr-labelled *A. trapezia* (specimen 483 A1-6L) showing the effect of variable Sr concentrations on FWHM (a) and peak position (b) of the intrinsic carbonate peak  $\nu_1$  located at  $1084.8 \text{ cm}^{-1}$ . Both Raman maps are overlain on BSE image and show the outer crossed-lamellar microstructure. Higher Sr concentrations in the labelled shell areas cause peak broadening (FWHM increase) of  $0.4 \text{ cm}^{-1}$  and a peak position shifts to lower wavenumbers of  $0.4 \text{ cm}^{-1}$  on average (see Table 3.1). All FWHM values are corrected for the instrumental apparatus function using the empirical correction published in Váczi (2014). Scale bars are  $10 \mu\text{m}$ .**

### 3.3.3 Shell architecture and crystallographic preferred orientations

Fractured shell pieces show an outer crossed-lamellar (CL in Figure 3.5a) and inner complex crossed-lamellar (CCL in Figure 3.5a) ultrastructure. The first order lamellae in the outer crossed-lamellar structure (CL; Figure 3.5a) measure  $10 \pm 2 \mu\text{m}$  in thickness ( $n=30$ ) and are all arranged in bands with their long sides perpendicular to the inner shell surface and parallel to the ventral margin. These first order lamellae have alternating topographies and surface roughness visible as bands of alternating darker

and lighter greyscales (Figure 3.5b, yellow outlined in Figure 3.5a). Microtubule channels ( $3.1\ \mu\text{m} \pm 0.4\ \mu\text{m}$  ( $n=25$ ) in diameter) are abundant and are oriented parallel to each other and quasi-perpendicularly to the inner surface of the shell (Figure 3.5b, white arrows). An etched radial fracture surface (Figure 3.5c) oriented perpendicular to Figure 3.5a shows second order laths contained within the first order lamellae. Third order lamellae are arranged in bundles and contain organic material situated between these bundles of lamellae (Figure 3.5d, white arrows). These lamellae have increased porosity with spheroidal to oblate spheroidal pore-shapes in sizes of 1 to 5 nm ( $n=20$ ), with individuals measuring up to 15 nm (Figure 3.5e). Notably, these pores occur predominantly along the outer areas of the third order lamellae (Figure 3.5f, Supplementary Figure 3.3) and appear similarly distributed in other architectures such as the compound composite prismatic ultrastructure of *Katylisia rhytiphora* (Supplementary Figure 3.4). Fourth order lamellae can be seen as sub-units with different grey shades in the third order, which result from differences in diffraction contrast (Figure 3.5e). These subunits have sizes of  $250 \pm 60\ \text{nm}$  by  $50 \pm 17\ \text{nm}$ ;  $n=10$  as measured in this image).

A crystallographic orientation map situated close to the ventral margin for a Sr-labelled shell is shown in Supplementary Figure 3.5a. The Sr-label appears as a bright linear feature (Supplementary Figure 3.5b) that cannot be traced into the EBSD maps (Supplementary Figure 3.5a, c). The first order lamellae exhibit two different crystallographic orientations, namely green and yellow in Supplementary Figure 3.5a, c. The green orientation is significantly more beam sensitive and has a crystallographic orientation with the aragonite b-axis (i.e. [010]) oriented normal to the polished surface, while the yellow i.e. less beam sensitive orientation is between the aragonite b- and c-axis (i.e. [011]) (see Supplementary Figure 3.6c). See Supplementary section “Analytical challenges associated with EBSD” for additional information on how to interpret the provided EBSD figures and explanation of analytical challenges associated with them. Both EBSD maps show a high number of low angle grain boundaries ( $<10^\circ$ ; Supplementary Figure 3.5) as well as high amounts of twinning of aragonite (defined as  $63.8^\circ$  rotation along the c-axis): 37 % of the grains in the low resolution map (Supplementary Figure 3.5a) and 55 % of the grains in the high-resolution map (Supplementary Figure 3.5c) are twinned.

Pole figures (lower hemisphere, equal area projection) show two local maxima for the b- and c-axes corresponding to the two main orientations of first order lamellae (Supplementary Figure 3.5d). These maxima are separated by a ca.  $60^\circ$  rotation around the a-axis. Furthermore, both population of first order lamellae show a weaker sub-maximum made up by their twins that share the same orientation with respect to their c-axis but differ by about  $90^\circ$  in a- and b-axis (Supplementary Figure 3.5d). The c-axis parallels the overall shell growth direction (GD, Figure 3.5), while the a-axes are parallel to the growth lines (GL). Overall, the c-axis was found to achieve the highest maximum density and texture index (J-Index) with 17 and 8, respectively (Supplementary Figure 3.5d).



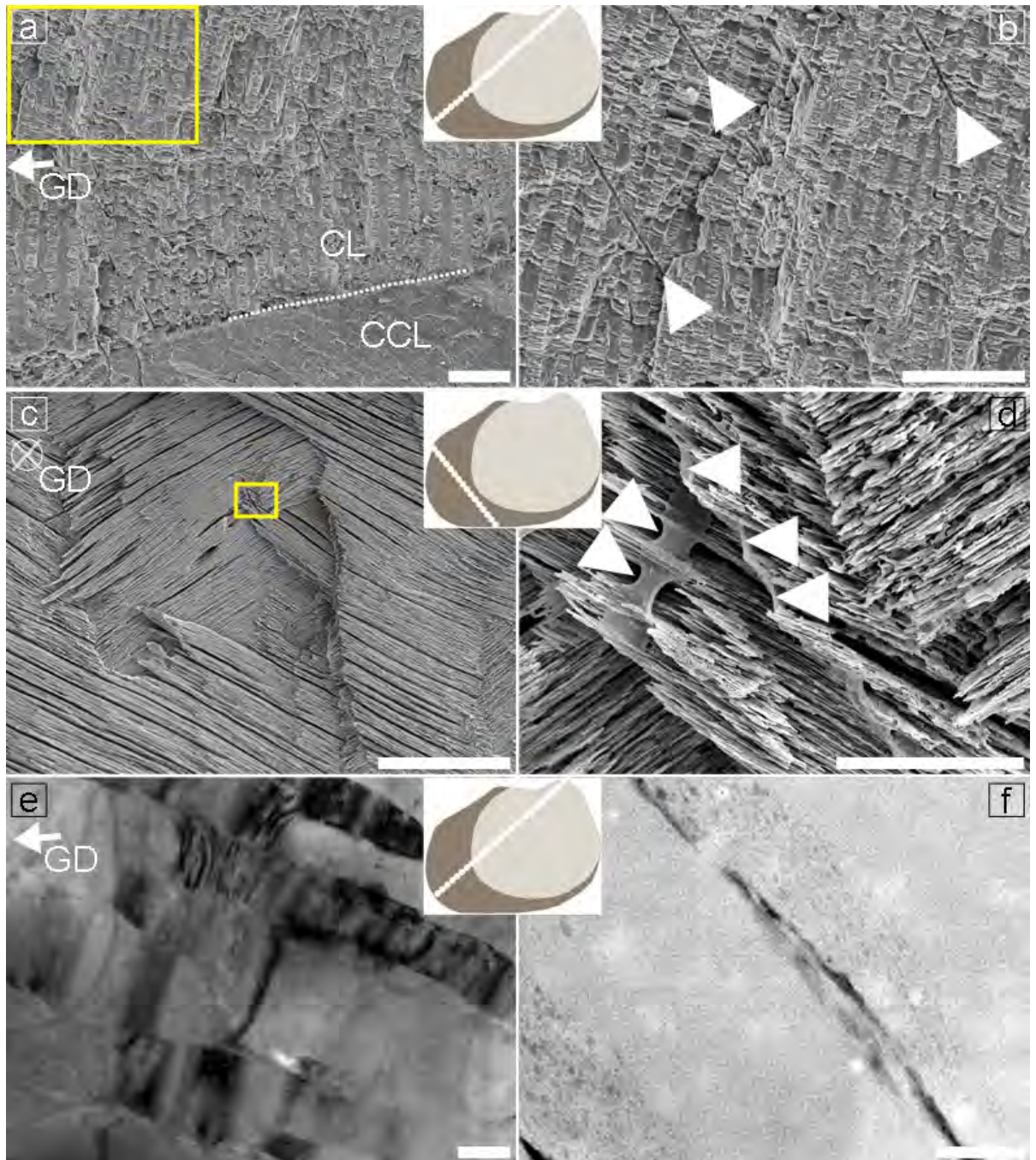


Figure 3.5: SE-SEM image depicting the fractured surface of the shell of an *A. trapezia* with the outer crossed-lamellar (CL) and inner complex crossed-lamellar (CCL) ultrastructure (a). First order lamellae of the CL structure consist of second order laths. Alternating darker and lighter greyscales of first orders are lastly caused by systematically alternating crystallographic orientations. Further magnification (b, yellow outlined in a) reveal cross-sections of microtubule channels (some highlighted with white arrowheads). The etched radial fracture surface (c, perpendicularly orientated to a) and shows the wide and flat aspects of first order lamellae with second order laths. Magnification (d, yellow outlined in c) reveals organic material (white arrowheads). Transmission electron micrograph (e) (bright-field) from a FIB-foil shows third order lamellae with different grey shades of aragonite sub-units, i.e. fourth order lamellae, via differences in diffraction contrast as well as numerous intragranular voids. Scanning transmission electron microscopy (f) (STEM, bright-field) shows third order lamellae have an area of higher organic inclusion abundance along their long axis. Both FIB foils were prepared adjacent to each other and with same orientation. Orientation of cross-sections is shown in schematic insets by white dashed line. Scale bars are 100  $\mu\text{m}$  (a, b, c), 10  $\mu\text{m}$  (d), 250 nm (e) and 100 nm (f).

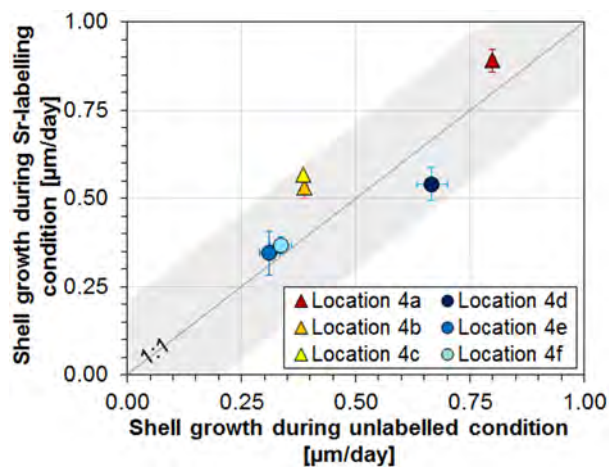
### 3.4 Discussion

#### 3.4.1 Shell geochemistry

Depending on their provenance, aragonite bivalve shells can have variable trace element concentrations: freshwater shells are generally characterized by higher Mn concentrations, while shells of marine origin yield higher Mg and Sr concentrations (Otter et al., 2019; Sturman et al., 2019; Wehrmeister et al., 2007). The major and trace element concentrations of “pre-aquaculture” and “unlabelled” shell layers in this study are both in the general range for marine bivalves (Table 3.1). The Sr-concentration of 2.37 wt.% SrO in labelled *A. trapezia* shell areas agree well with those previously published for *K. rhytiphora* maintained at an identical Sr enrichment (Otter et al., 2019). These identical conditions produced FWHM broadening and peak position shifts of the carbonate peak  $\nu_1$  (i.e. at  $1084.8\text{ cm}^{-1}$ ) indicating identical incorporation mechanisms of Sr into the aragonite crystal structure. In aragonite, Sr substitutes for Ca in the nine-fold coordinated Ca-sites, which results in changing interatomic distances and bond-lengths that produce the observed FWHM broadening effects and peak position shifts between labelled and unlabelled shell areas (Alia et al., 1997; Foster et al., 2009; Otter et al., 2019). The labelled areas with wider FWHM and lower peak position correlate well with the brighter greyscale intensities from the underlying BSE images and, in conjunction with correlative NanoSIMS maps, allow us to base investigations of Sr-labelled shell areas on these calibrated BSE images.

#### 3.4.2 Strontium incorporation

Average daily local growth rates from Figure 3.5 follow the 1:1 trend-line within the first standard deviation as they plot inside the grey shaded area in Figure 3.6. Within the context of our aquaculture experiments, this is interpreted such that high (i.e. 18x enriched) Sr concentrations did not negatively affect the vitality of the bivalves as this would have perhaps led to decreasing rates over the course of the experimental period especially in labelled shell layers, which is not observed (Figure 3.6). This is in accordance with observations on shells of *K. rhytiphora* (Otter et al., 2019).



**Figure 3.6:** Average daily local growth rates of labelled and unlabelled shell layers depicted in Figure 3.3. Growth along the ventral margin and thickening along the umbo are shown as triangles and circles, respectively. Each data point is presented with error bars derived from  $n=5$  measurements at each location (all values in Supplementary Table 3.1). Rates agree well between labelling and ambient conditions i.e. follow the 1:1 trend-line and plot within 1 $\sigma$  of the entire data set (grey shaded area).

Sr/Ca ratios of bivalve shells sourced from natural environments have been proposed as proxy for sea surface temperature (e.g. Dodd, 1965; Swan, 1956; Zhao et al., 2017a), while other studies argue that Sr/Ca ratios are mainly influenced by bivalve shell growth rate (e.g. Takesue and van Geen, 2004) and metabolic rate (e.g. Bailey and Lear, 2006; Foster et al., 2009; Gillikin et al., 2005; Purton et al., 1999). In other cases neither a temperature nor a growth or metabolic rate correlation could be found (e.g. Buchardt and Fritz, 1978).

Our experiments were carried out at constant temperature and yielded constant growth rates, both, in Sr-enriched and unlabelled conditions. From these experiments it could be speculated that the incorporation of Sr is intrinsically controlled by the physiology of the bivalve rather than through external stimuli such as specific temperature ranges or natural marine Sr-concentrations. Moreover, the distribution coefficient  $D_{\text{Sr/Ca}}$  calculated as  $(\text{Sr/Ca in unlabelled shell})/(\text{Sr/Ca in seawater})$  of 0.14 is very similar to that obtained from labelled shell of 0.15. Both  $D_{\text{Sr/Ca}}$  values are significantly below that for synthetic aragonite (1.19 at 20 °C: Gaetani and Cohen, 2006). While the reasons for the large difference between synthetic and biomineralised aragonite are yet unknown, they indicated that Sr is actively excluded, potentially, due to a multi-step fractionation process at play during mollusc shell biomineralisation (Addadi et al., 2003; Jacob et al., 2011; Wolf et al., 2016; Zhang and Xu, 2013).

### 3.4.3 Growth dynamics of *A. trapezia* shells

Bivalve shells grow fastest at the tip of the ventral margin, which is traditionally referred to as ‘shell extension’ and differs from the general thickening (e.g. Schöne and Surge, 2012). This study provides the first direct visualization of shell extension and thickening in the two most important regions – the ventral margin and the umbo (Figure 3.3 and 3.6, Supplementary Figure 3.8 and Supplementary Table 3.1). Highest rates were observed locally at the ventral margin (Figure 3.3a, Figure 3.6) and quickly decrease to between 50 and 60 % of maximum growth value, implying that trace elemental and isotopic transects can be obtained here at the highest possible resolution. Shell thickening in front of the umbo (Figure 3.3d, Figure 3.6, Supplementary Figure 3.8 and Supplementary Table 3.1) is in the same range as values obtained shortly behind the ventral margin (Figure 3.6b and 3.6c and Figure 3.6, Supplementary Figure 3.8 and Supplementary Table 3.1), while the innermost umbo has the lowest rates (i.e. 40 % compared to maximum growth) with highly condensed growth records that offer less potential for trace elemental and isotopic investigations.

Precisely defined pulse-chase labelling experiments (e.g. hours as opposed to days), such as those in this study, offer the opportunity to investigate aspects of growth dynamics that have not yet been investigated for crossed-lamellar shells. In similar experiments with *K. rhytiphora*, labelled shell areas were observed to start and end relatively abruptly, to grow evenly along the growth fronts and comprise several sub-layers that likely correlate with the number of days spent in pulse-labelling conditions (Otter et al., 2019). The reasons for larger areas of transition in the labelled shell areas in *A. trapezia* shells (Figure 3.3a) compared to *K. rhytiphora* are unclear. We speculate that these shells form either larger volumes of extrapallial fluid and slowly increase Sr-concentrations via mixing, or that this effect arises



from the more hierarchical ultrastructure of *A. trapezia* compared to that of *K. rhytiphora* and that yet unlabelled units and already labelled units create “mixed pixel” effects. The latter case could be confirmed via S/TEM investigations in the future. In comparison to testing this hypothesis, testing the existence of an extra pallial fluid with defined composition is much more difficult (Marin et al., 2012).

The crossed-lamellar ultrastructure of *A. trapezia* is sharply intersected by the labelled shell layer that cuts evenly across all hierarchical orders of the structure (Figure 3.3a-c), similar to findings for *K. rhytiphora* shells (Otter et al., 2019). We do not observe that specific orientations of lamellae grow before others nor that specific hierarchical orders grow sequentially, as this would have produced patterns of labelled lamellae protruding into unlabelled areas. Instead, all hierarchical structures within the labelled shell layer appear to grow simultaneously along this growth front. This observation should not be confused with conclusion drawn for growth rates perpendicular to the growth front, which can be quite variable (Otter et al., 2019). These growth patterns have been inferred from shells formed in natural environments in the past, however, interpretations were hampered by lack of direct evidence via growth visualization by rigorous time-resolved labelling as that presented in this study.

In contrast to the crossed-lamellar ultrastructure, the complex crossed-lamellar layer in *A. trapezia* shows kinks and undulations of the labelled shell layers (Figure 3.3d-f). We suggest that this is caused by a sectioning effect of the highly hierarchical architecture of this layer that is characterised by lamellae being arranged in several radial directions with inclined orientations of adjacent lamellae (Chateigner et al., 2000; Taylor, 1969). Distinct brighter and darker increments within the Sr pulse-labelled shell layer (Figure 3.3b) are unfortunately too narrow to be resolved in the NanoSIMS map, but likely reflect changing Sr-concentrations in the shell as only this element was artificially increased during labelling and all other trace elements and factors such as food availability, temperature, and salinity remained unchanged. As these factors can be excluded, it is speculated that these changes in Sr concentration reflect the metabolic activity of the bivalve and thus support findings in the literature (e.g. Bailey and Lear, 2006; Foster et al., 2009; Gillikin et al., 2005; Purton et al., 1999).

#### 3.4.4 Macro- to micro-scale properties of crossed-lamellar shells

First order lamellae of *A. trapezia* have wide, flat aspects with thicknesses of about 10  $\mu\text{m}$  that compare well to thicknesses reported for other bivalve species with the same shell architecture from Böhm et al. (2016) and Chateigner et al. (2000), while Agbaje et al. (2017b) report greater thicknesses of 20–50  $\mu\text{m}$  for the Southern giant clam *Tridacna derasa*. These greater thicknesses result from varying thicknesses of first orders of *T. derasa* (Agbaje et al., 2017b) that differ from the regular thicknesses in *A. trapezia* (Figure 3.5a, b). The orientations of second order laths within each first order lamella seem identical from the EBSD maps (Supplementary Figure 3.5a, c). Thicknesses of first order lamellae (i.e. about 10  $\mu\text{m}$ ) correspond to widths of second order laths. Thicknesses of second order laths are estimated to be about 1  $\mu\text{m}$  in thickness (Figure 3.5d), which agrees well with previous studies (Chateigner et al., 2000).

High amounts of crystallographic twinning are a universal characteristic of aragonitic bivalve shells (Agbaje et al., 2017b; Almagro et al., 2016; Kobayashi and Akai, 1994). In *A. trapezia*, the amount of

twinning varies with the spatial resolution of the EBSD map, namely between 37 % in the low-resolution map (Supplementary Figure 3.5a) and 55 % in the high-resolution map (Supplementary Figure 3.5c). This resolution-based dependency supports earlier observations (Agbaje et al., 2017b) and highlights the importance of appropriate choice of analytical conditions. Hence, the observed amount of 55 % is a minimum value resulting from the resolving power of the instrumentation and is in the same range as reported for other compound composite prismatic (46 %, Otter et al., 2019), crossed-acicular (56 %, Otter et al., 2019) and the nacreous (60-70 %, Chateigner et al., 2000) ultrastructures. Moreover, these values are in accordance with taxonomically unrelated marine calcifiers such as bryozoa that have at least 45 % twin grain boundaries in the aragonitic part of their bimineralic skeletons, which emphasizes that twinning at the micro-nanoscale is a common motif in aragonitic biominerals (Jacob et al., 2019).

#### 3.4.5 Nanoscale properties of crossed-lamellar shells

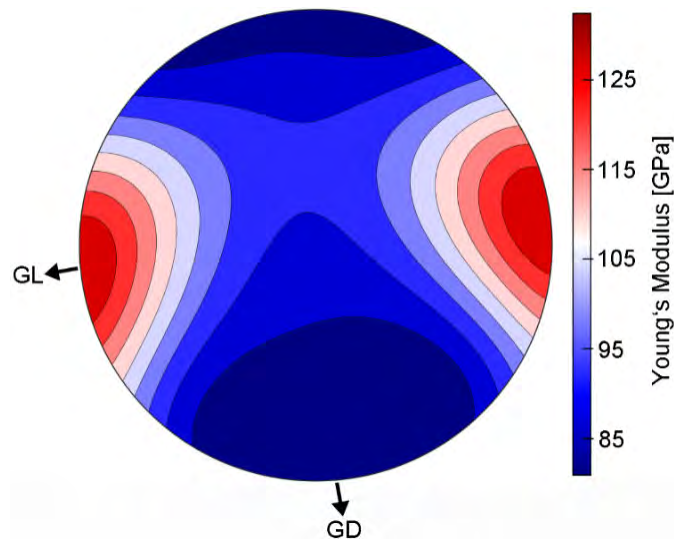
An increased abundance of smaller voids (potentially organic inclusions) around the outer layers of third order lamellae are similar to observations for *T. derasa*. Moreover, a similar distribution of voids is observed for the compound composite prismatic ultrastructure of *K. rhytiphora* (Supplementary Figure 3.4) and suggests to be a common characteristic of non-nacreous shells instead of a species specific feature (Agbaje et al., 2017b). An increased abundance of voids or organic inclusions along the outer layers in crossed-lamellar shells differs significantly from the nacreous structure, where each nacre tablet has a zone of depleted organic inclusion abundance around its outer layer (Eder et al., 2019; Younis et al., 2012b). As the formation of organic inclusions is likely directly linked to growth processes of the shell this finding may point towards distinct biomineralisation processes between nacreous and non-nacreous shells.

#### 3.4.6 Aspects of shell mechanical properties

Shells have mechanical properties (e.g. strength and toughness) that are several magnitudes higher as geological monolithic aragonite (Jackson et al., 1988; Katti et al., 2006; Meyers et al., 2008; Wang et al., 2001). The key to these improved properties lie in a variety of strengthening strategies that monolithic aragonite lacks: their inorganic-organic composite material nature, nano-granularity, three dimensional and hierarchical architecture, and high amounts of twinned grain boundaries (Barthelat et al., 2006; Fratzl et al., 2007; Gao et al., 2003; Kamat et al., 2000; Li et al., 2004; Smith et al., 1999). These adaptations are associated with higher rigidity and fracture-resistance that pose significant evolutionary advantages crucial for the organism's survival (Kamat et al., 2000; Weiner et al., 2000), while the mechanical performance of brittle monolithic aragonite on the other side is compromised by its high anisotropic elasticity (De Villiers, 1971). Amongst all mollusc shell architectures, the crossed-lamellar ultrastructure is known to have the highest fracture toughness (Kamat et al., 2000).

The Young's modulus is an important measure for the mechanical performance of materials as it describes the materials response to stress and strain (Hashin, 1962). Here, this parameter is calculated from EBSD maps via Voigt–Reuss–Hill scheme averaging using the elastic constants of the mechanical performance of aragonite single crystals (Pavese et al., 1992). The Young's modulus of *A. trapezia*

shells show a maximum (132 GPa) oriented parallel to the shell's growth lines, while a direction of lower resistance (i.e. 81 GPa) is oriented parallel to the shell's growth direction (Figure 3.7). The maximum (Figure 3.8, 132 GPa) is even higher than that reported for other crossed-lamellar shells from *T. derasa*, while the values for lowest resistance are virtually identical (Agbaje et al., 2017b). Other non-nacreous shells yield lower maximum values with 111 GPa and 105 GPa for the crossed-acicular and compound composite prismatic ultrastructure, respectively (Otter et al., 2019). Commonly, the Young's modulus in shells show a girdle-like orientation of [100] and [010] around [001] in the pole figures, thus creating a plane of quasi-isotropy, which minimizes the natural elastic anisotropy of aragonite and strengthens the shell (Agbaje et al., 2017b; Ouhenia et al., 2008; Weiner et al., 2000). A girdle-like arrangement of an elastically stiffer plane is not observed in this study. Instead, the Young modulus pole figure shows a defined maxima (Figure 3.7). However, it should be noted that in order to calculate the Young's modulus, the shell's beam sensitivity required reduction of EBSD maps to smaller subsets located along the inner shell surface of the EBSD maps (e.g. bracket in Supplementary Figure 3.5) to allow for accurate sampling of both first order lamellae orientations. As these selected areas consist of only the youngest shell layers and, hence, do not reflect larger transect across the shell as in previous studies (Agbaje et al., 2017b; Otter et al., 2019) this areal restriction may explain the absence of a girdle-like structure in this shell in our study. Other strengthening strategies of shells involve the presence of bent trajectories that are also present in *A. trapezia* (Supplementary Figure 3.1) within the outer shell layers of crossed-lamellar shells thought to deflect and reduce crack propagation towards the soft body of the bivalve (Böhm et al., 2016).



**Figure 3.7:** Young's modulus (upper hemisphere and equal area projection) calculated after EBSD data for the crossed-lamellar ultrastructure of *A. trapezia*. Calculation were performed using Voigt–Reuss–Hill scheme averaging using the single crystal elastic constants of aragonite from Pavese et al. (1992). EBSD maps were reduced to smaller subsets located along the inner shell surface in order to sample, more accurately, both orientations of first order lamellae (see bracket in Figure 3.3c indicating a representative area). The shell shows a maxima (i.e. 132 GPa) paralleling the growth line. A direction of lower resistance (i.e. 81 GPa) is oriented parallel to the shell's growth direction.

### 3.5 Conclusion

Pulsed Sr-labelling experiments consisting of 4 days spent in 18x enriched seawater followed by 15 days in ambient conditions were combined with stepwise correlated spatially downscaled analysis. We show here, that this approach is a powerful tool to visualize micron-scale aspects of shell ultrastructure and dynamic shell growth processes. BSE images obtained from pulsed Sr-labelled shell areas serve as a basis to quantify the relative growth rates at the main growth fronts of the shell – ventral margin and umbo. We draw the following conclusions from Sr-labelling experiments and architectural investigations:

1. The pulse Sr-labelled shell layer cuts sharply across all hierarchical orders of the crossed-lamellar ultrastructure, which is interpreted as sign that all hierarchical units within the labelled shell layer appear to grow simultaneously along this growth front. In the complex crossed-lamellar layer, the labelled shell layer shows kinks and undulations that are most likely due to a sectioning effect cutting across lamellae that are arranged in different radial directions with inclined orientations.
2. Average daily growth rates in Sr-enriched and ambient conditions follow a 1:1 trend. Since the experiments were carried out in controlled aquaculture conditions at constant temperatures it is concluded that Sr incorporation is intrinsically controlled by the bivalve's physiology rather than by external stimuli such as specific temperature ranges or natural marine Sr-concentrations.
3. Distribution coefficients  $D_{\text{Sr/Ca}}$  for unlabelled and labelled shell portions (0.14 and 0.15, respectively) are well below the equilibrium  $D_{\text{Sr/Ca}}$  for synthetic aragonite, suggesting that Sr is actively excluded during multi-step fractionation processes during mollusc shell biomineralisation.
4. We observe high amounts of crystallographic twinning of at least 55 %.
5. Nano-scale voids along the outer layers of third order lamellae with sizes between mainly 1 to 5 nm are likely organic inclusions. This distribution contrasts with the nacreous ultrastructure that shows a reduction of organic inclusions around the outer layer of nacre tablets. We postulate that this distribution of voids along only the outer layers is a characteristic of non-nacreous shells. More research is needed e.g. using Atom Probe Tomography or TEM-based techniques to better understand the composition of these inclusions and their role during shell biomineralisation and their influence on mechanical properties.

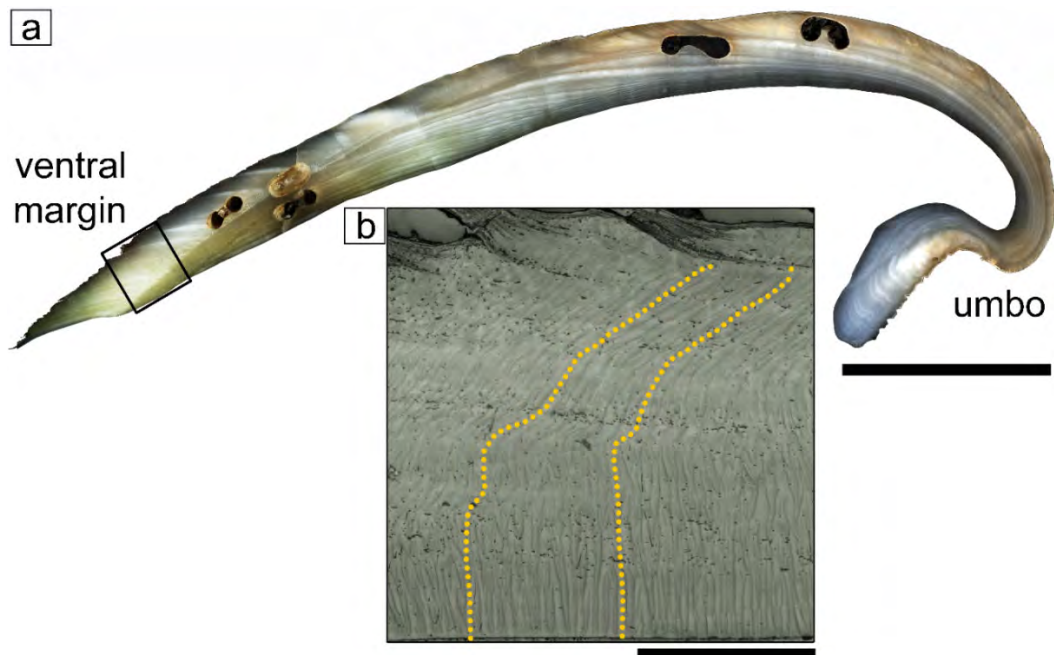
### Acknowledgements

We kindly acknowledge Stephan Buhre for calibrating the EPMA system. We thank the Macquarie University Faculty of Science and Engineering Microscope Facility (MQFoSE MF) for access to its instrumentation and thank its staff members Sue Lindsay and Chao Shen for their support. We acknowledge the Michigan Centre for Materials Characterization for use of their instrumentation. Jane Williamson and Josh Aldridge are thanked for access and assistance at the Macquarie Seawater Facility and are grateful for Wayne O'Connor's (Port Stephens Fisheries Centre, NSW Department of Primary

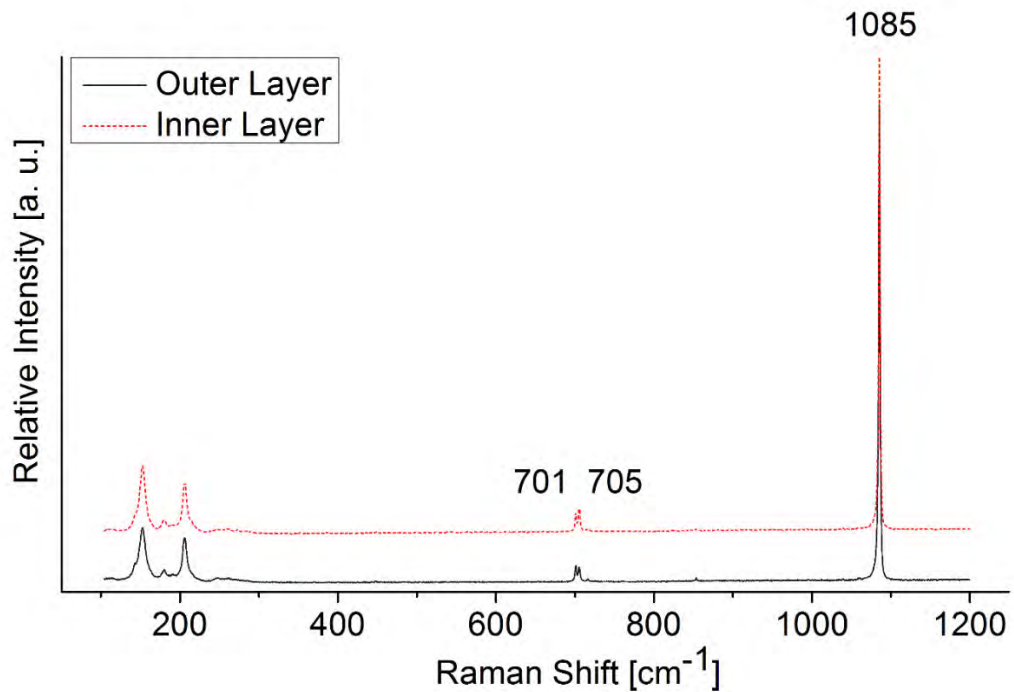
Industries) for advice on husbandry protocols. The authors are grateful to Richard Wirth for assistance with TEM data collection. The authors received financial support through an Australian Government International Postgraduate Research Scholarship (IPRS) and a Macquarie University Postgraduate Research Fund (PGRF) awarded to LMO, while DEJ is supported through an ARC Discovery Grant (DP160102081). The analytical data were obtained using instrumentation funded by DEST Systemic Infrastructure Grants, ARC LIEF, NCRIS/AuScope, industry partners and Macquarie University. Lastly, the authors acknowledge Microscopy Australia, the Science and Industry Endowment Fund, and the State Government of Western Australian for contributing to the Ion Probe Facility at the University of Western Australia.

## Supporting material

### Supplementary figures

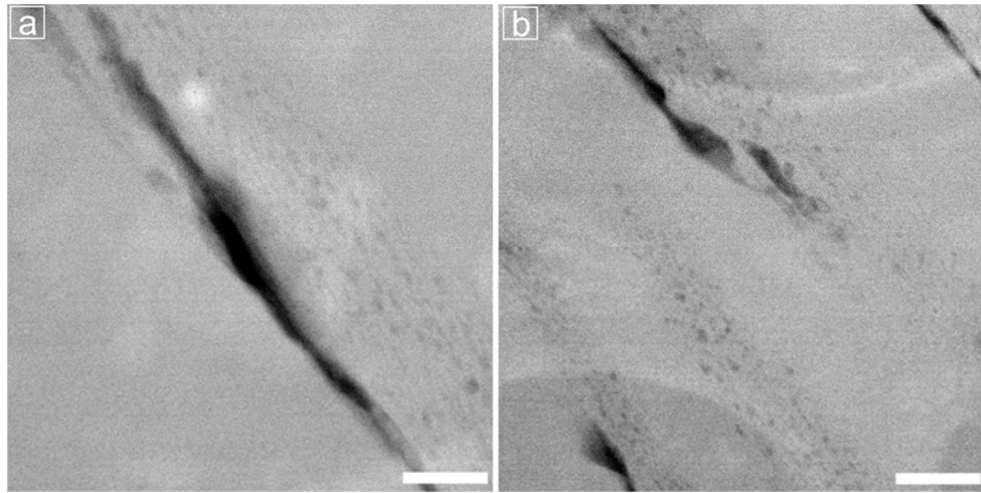


Supplementary Figure 3.1: Polished cross-section of an *Anadara trapezia* shell (a) and light microscopic close up (b) of area marked with black square in (a). The magnified region shows the layer of first order lamellae of the crossed-lamellar ultrastructure with bent and kinked trajectories of growth lines (yellow dashed lines). Scale bars are 1 cm (a) and 500  $\mu\text{m}$  (b).

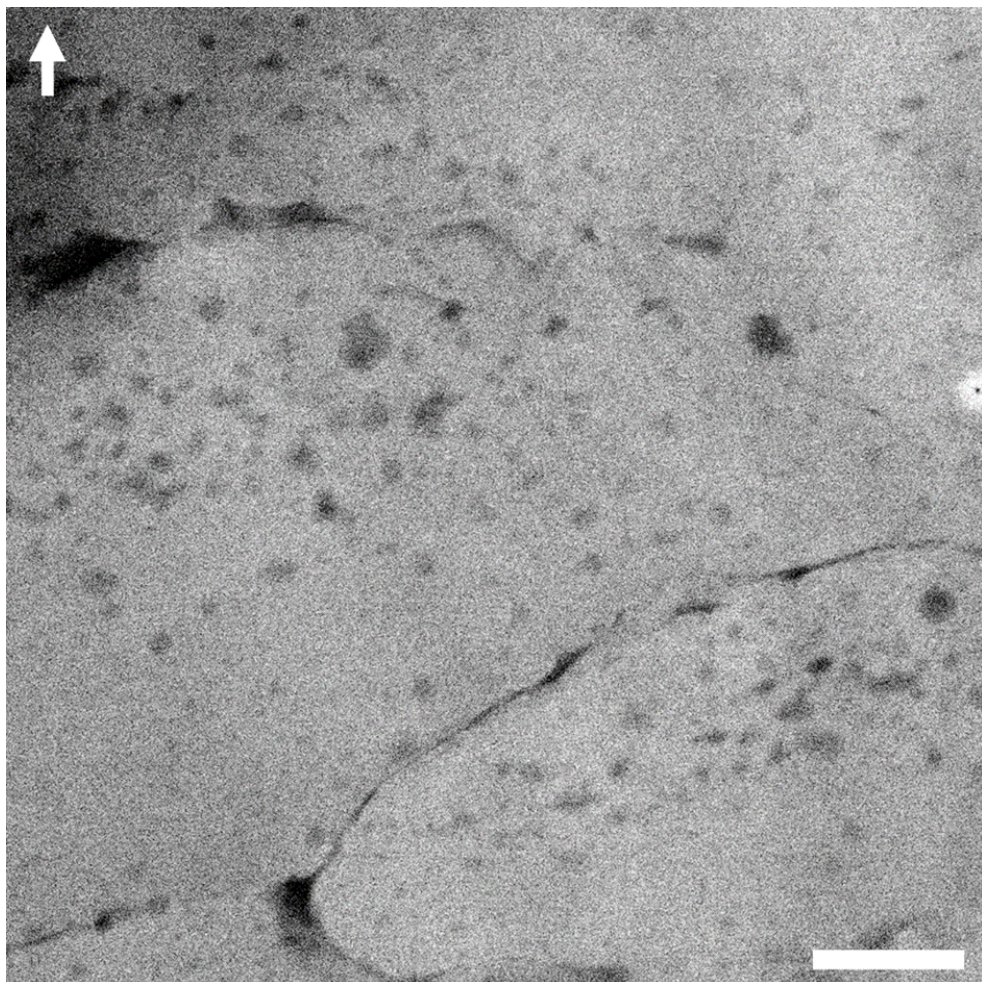


Supplementary Figure 3.2: Representative micro-Raman spectra of the inner and outer layer of an *A. trapezia* shell cross-section. Relative Raman intensities are normalized to the highest intensity peak at 1085  $\text{cm}^{-1}$  (no baseline correction applied).



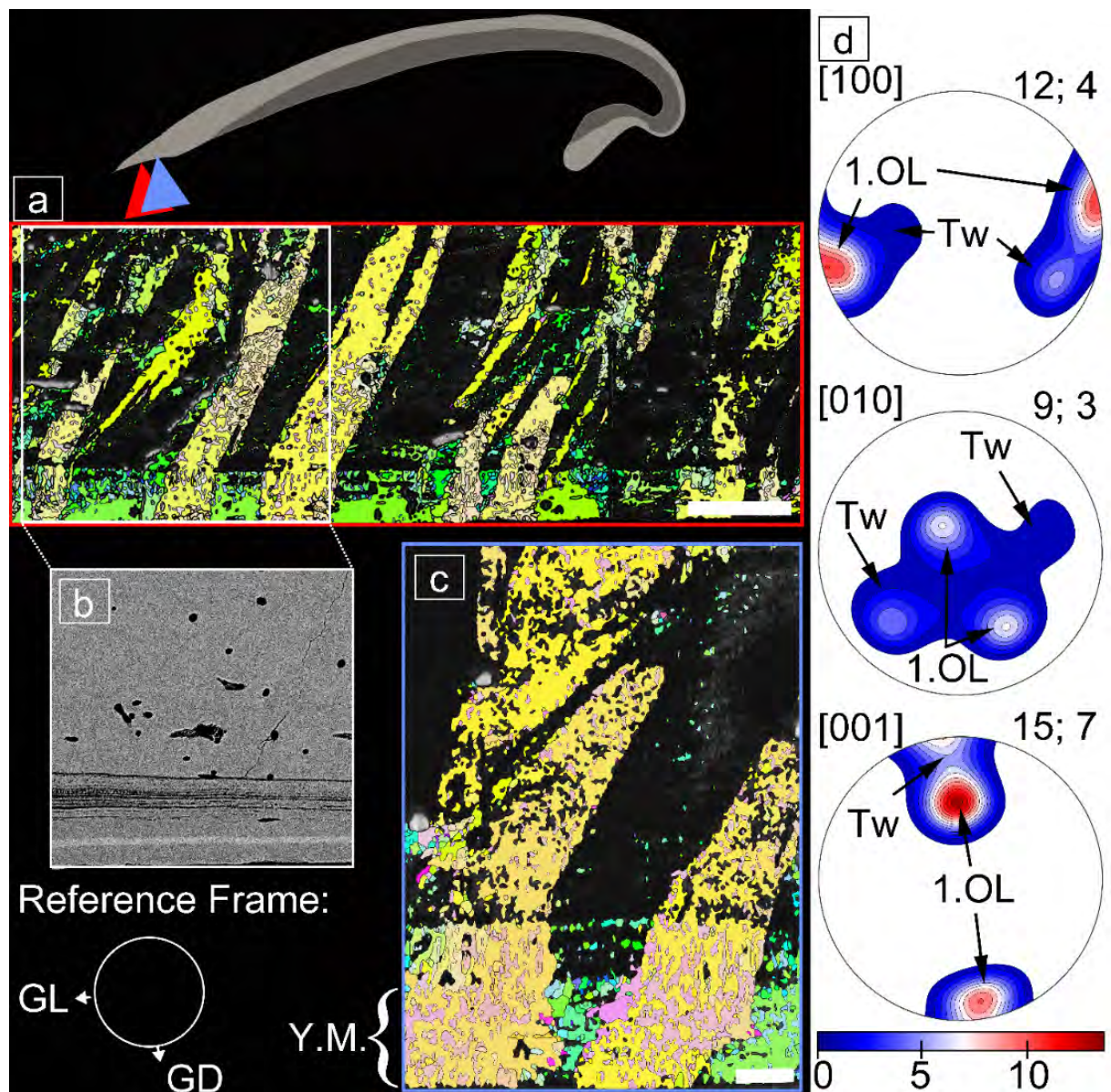


**Supplementary Figure 3.3:** Scanning transmission electron microscopy (STEM, bright-field) images showing that nanometre sizes voids (likely organic inclusions) predominantly distributed along the outer layers of third order lamellae parallel with the dark organic sheaths. Both images are oriented identically to Figure 3.5f in the main text. Scale bars are 100 nm.

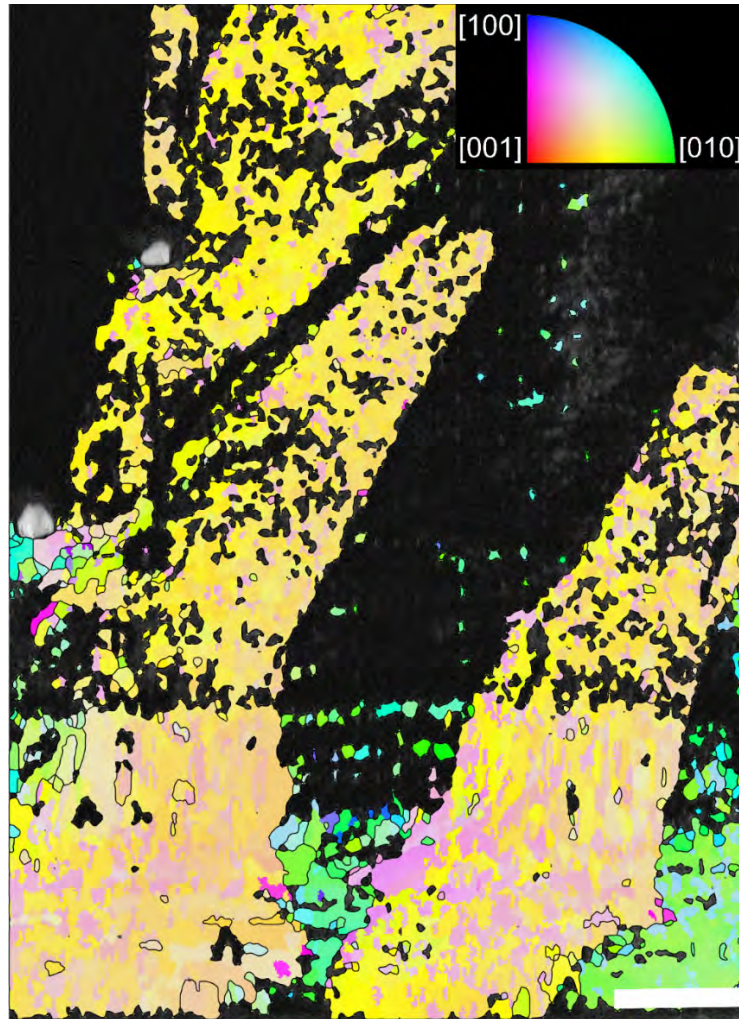


**Supplementary Figure 3.4:** Scanning transmission electron microscopy (STEM, bright-field) images showing the compound composite prismatic ultrastructure in the outer shell layer of the venerid bivalve *Katelysia rhytiphora*. Details on this architecture are presented in Otter et al. (2019). The sample was prepared and analysed using FIB and STEM using the same protocols as presented for *A. trapezia* in the main text. This image is included to show that nanometre sized voids (likely organic inclusions) are similarly distributed in *K. rhytiphora* (namely along the outer layers of third order prisms) and *A. trapezia* and suggests that this is rather a general feature of non-nacreous shells than a species-specific effect. The image is oriented identically to Figure 3.5f in the main text. Scale bars are 100 nm.



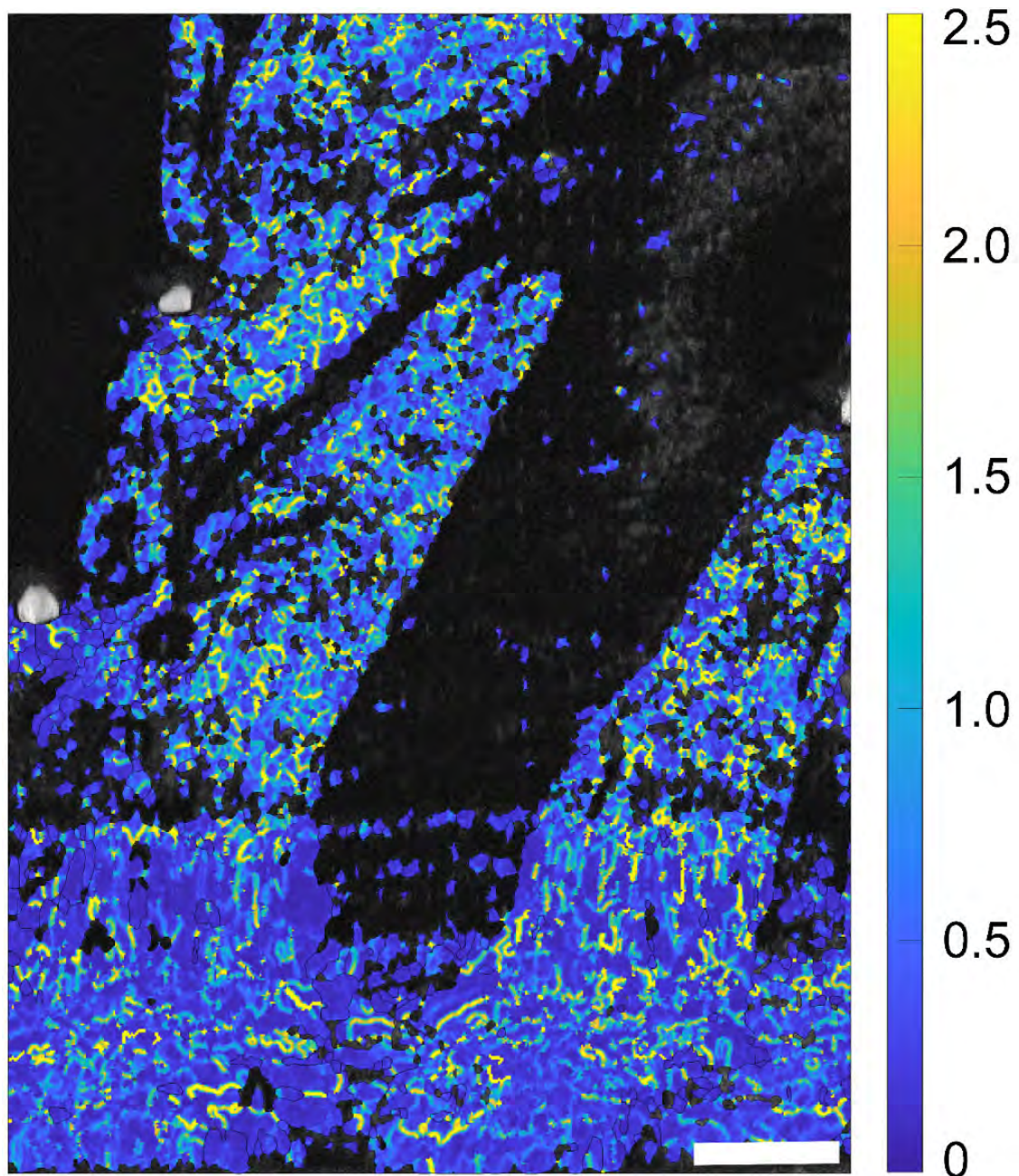


Supplementary Figure 3.5: Crystallographic orientation map for aragonite with crossed-lamellar structure (a) obtained from close to the ventral margin (see schematic, red arrow) of a labelled *A. trapezia* shell. The map is coloured according to the mean orientation of grains whereby similar colour denote similar crystallographic orientation. Two main orientations (green and yellow as main colour) of first order lamellae are visible at the youngest shell layers along the bottom of the map, while mainly one orientation is preserved in older shell areas. A BSE image obtained from the same area (b) shows the youngest shell layer to be separated by darker greyscales bands likely resulting from higher amounts of organics marking a new growth scale. The Sr-label appears as bright linear feature, while black round to elliptical holes result from microtubules. A smaller EBSD map with higher resolution (see schematic, blue arrow) shows high amounts of twinning in both orientations of first order lamellae. The bracket indicates exemplarily the area used for Young Modulus (“Y.M.”) calculations. Pole figures (lower hemisphere, equal area projection) of the a-axis [100], b-axis [010] and c-axis [001] of aragonite (d). The data shows two local maxima with relatively stronger crystallographic preferred orientations for the b- and c-axes corresponding to the orientations of both populations of first order lamellae. These maxima are ca. 60° apart and parallel the overall shell growth direction (GD, see lower left for reference frame). Both orientations of first order lamellae are rotated around the a-axis and show secondary maxima corresponding to crystallographic twins. The c-axis was found to achieve the highest maximum density and texture index with 17 and 8, respectively (see value in PF). Scale bars are 50 µm (a, b) and 10 µm (c).



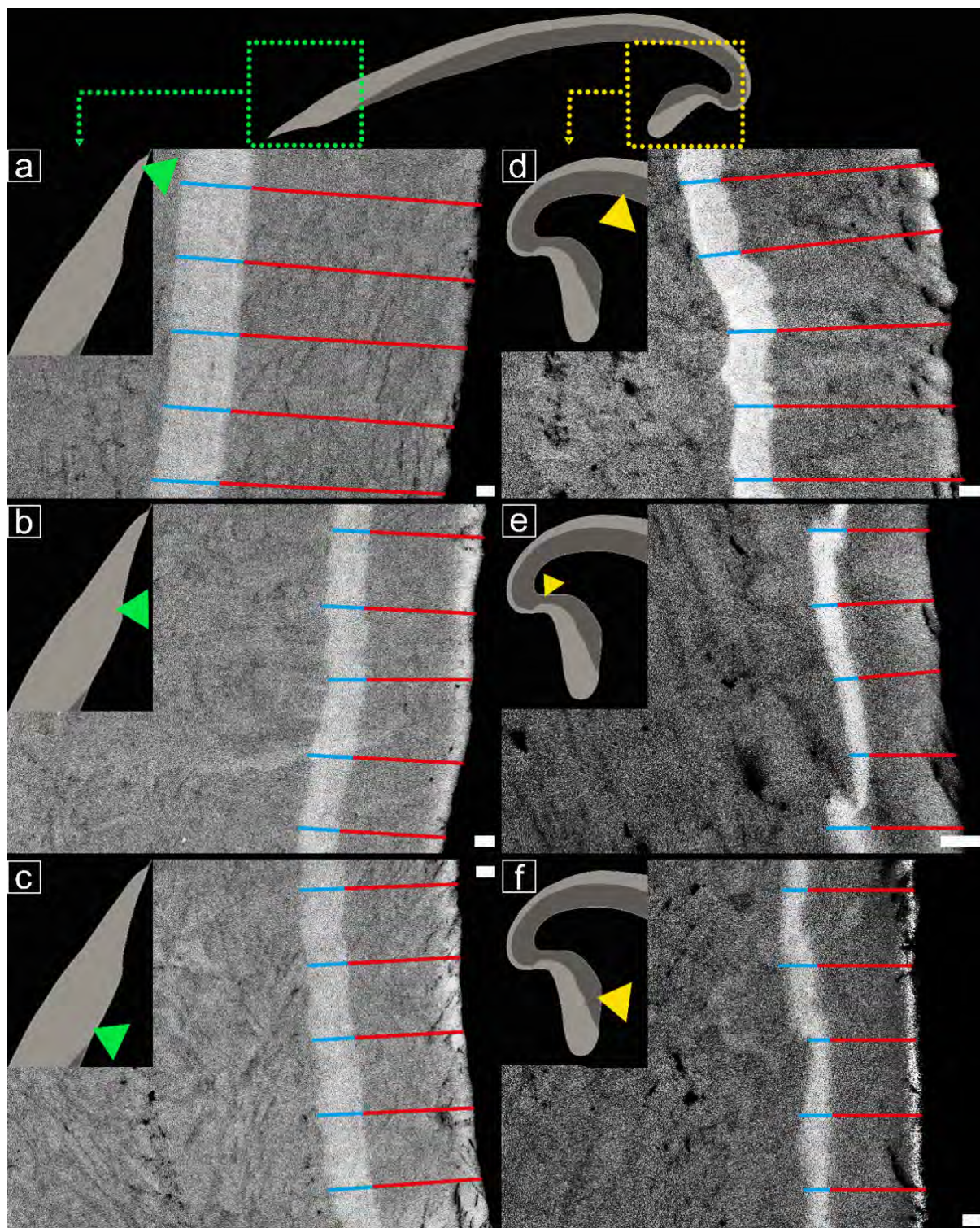
**Supplementary Figure 3.6:** Crystallographic orientation map for aragonite with crossed-lamellar structure obtained from close to the ventral margin of a Sr-labelled *A. trapezia* shell. Blue, green, and red represent the crystallographic a- [100], b- [010], and c-axes [001] of aragonite, respectively (see colour scheme). The map is colour-coded to show the crystallographic orientation normal to the polished surface. This map shows that the more beam sensitive orientation of first order lamellae (green) has a crystallographic orientation parallel with the aragonite b-axis (i.e. [010]), while the less beam sensitive orientation (yellow to pink) is oriented approximately midway between the aragonite b- and c-axis (i.e. [011]). See Supplementary Figure 3.5 for schematic and reference frame. Scale bar is 10  $\mu\text{m}$ .





**Supplementary Figure 3.7: Kernel average misorientation EBSD map colour coded to reveal the intergranular average misorientation angle per orientation calculated on a first order kernel and reflects the high number of low angle grain boundaries i.e. sub-grains in the crossed-lamellar structure of *A. trapezia*. See Supplementary Figure 3.5 for schematic and reference frame. Scale bar is 10  $\mu\text{m}$ .**





**Supplementary Figure 3.8: BSE image compilation as shown in the main text of this study with the addition of blue and red lines referring to growth rate measurements in Sr-labelled and ambient (non-labelled) conditions, respectively. Scale bars are 1  $\mu\text{m}$ .**

### *Analytical challenges associated with EBSD*

The map is coloured according to the mean orientation of the grains i.e. similar colours represent similar crystallographic orientations. Pattern quality is best at the youngest i.e. innermost 30-40  $\mu\text{m}$  of each of the shell layers and shows two main crystal orientations for the first order lamellae (green and yellow in Supplementary Figure 3.5a) with a layered texture paralleling the inner shell surface, also visible in a BSE image of the same area (Supplementary Figure 3.5b). The quality of the EBSD pattern decreases rapidly towards older shell areas, to the extent that one of the first order lamella orientations is almost completely lost (black areas in Supplementary Figure 3.5a, c). This is also visible in a smaller EBSD map (Supplementary Figure 3.5c) obtained at higher resolution than Supplementary Figure 3.5a. Such strong and orientation-selective beam sensitivity in biominerals are very unusual in our experience (e.g. Agbaje et al., 2017b; Jacob et al., 2019; Otter et al., 2019). The difference in beam sensitivity and fracture surface most likely results from the anisotropic material properties of aragonite (Agbaje et al., 2017b; De Villiers, 1971).

Supplementary table

**Supplementary Table 3.1: Growth rates of an *A. trapezia* shell, formed during aquaculture experiments with ambient and enriched Sr-concentrations, measured at the ventral margin (crossed lamellar) and the umbo (complex crossed lamellar). Line # refers to the numbered lines in Supplementary Figure 3.6 and demonstrate where growth measurements were obtained.**

BSE image from Figure:	Line #:	Shell Growth Increments:		Total growth (labelled and ambient) in $\mu\text{m}/19$ days	Daily Growth Rates:	
		Sr-labelled $[\mu\text{m}/4$ days]	Ambient post labelling $[\mu\text{m}/15$ days]		Sr-labelled $[\mu\text{m}/\text{day}]$	Ambient post labelling $[\mu\text{m}/\text{day}]$
3.6A	1	3.80	12.01	15.81	0.95	0.80
	2	3.51	12.12	15.63	0.88	0.81
	3	3.45	12.06	15.51	0.86	0.80
	4	3.48	11.85	15.33	0.87	0.79
	5	3.56	11.92	15.48	0.89	0.79
	AV $\pm$ STDEV	3.56 $\pm$ 0.13	11.99 $\pm$ 0.10	15.55 $\pm$ 0.16	0.89 $\pm$ 0.03	0.80 $\pm$ 0.01
3.6B	1	2.04	5.98	8.02	0.51	0.40
	2	2.04	5.82	7.86	0.51	0.39
	3	2.06	5.78	7.84	0.52	0.39
	4	2.34	5.71	8.05	0.59	0.38
	5	2.11	5.85	7.96	0.53	0.39
	AV $\pm$ STDEV	2.12 $\pm$ 0.11	5.83 $\pm$ 0.09	7.95 $\pm$ 0.08	0.53 $\pm$ 0.03	0.39 $\pm$ 0.01
3.6C	1	2.29	5.87	8.16	0.57	0.39
	2	2.26	5.76	8.02	0.57	0.38
	3	2.23	5.77	8.00	0.56	0.38
	4	2.27	5.69	7.96	0.57	0.38
	5	2.28	5.79	8.07	0.57	0.39
	AV $\pm$ STDEV	2.27 $\pm$ 0.02	5.78 $\pm$ 0.06	8.04 $\pm$ 0.07	0.57 $\pm$ 0.01	0.39 $\pm$ 0.01
3.6D	1	2.08	10.92	12.70	0.52	0.71
	2	2.10	10.69	12.49	0.53	0.69
	3	2.53	9.28	11.81	0.63	0.62
	4	2.07	9.55	11.62	0.52	0.64
	5	2.03	10.15	12.18	0.51	0.68
	AV $\pm$ STDEV	2.16 $\pm$ 0.19	10.12 $\pm$ 0.63	12.16 $\pm$ 0.40	0.54 $\pm$ 0.05	0.67 $\pm$ 0.03
3.6E	1	1.68	4.32	6.00	0.42	0.29
	2	1.28	5.02	6.30	0.32	0.33
	3	1.27	4.38	5.65	0.32	0.29
	4	1.03	4.56	5.59	0.26	0.30
	5	1.65	5.09	6.74	0.41	0.34
	AV $\pm$ STDEV	1.38 $\pm$ 0.25	4.67 $\pm$ 0.32	6.06 $\pm$ 0.43	0.35 $\pm$ 0.06	0.31 $\pm$ 0.02
3.6F	1	1.38	5.65	7.03	0.35	0.38
	2	1.58	5.09	6.67	0.40	0.34
	3	1.60	4.66	6.08	0.36	0.31
	4	1.40	4.72	6.32	0.40	0.31
	5	1.36	5.03	6.39	0.34	0.34
	AV $\pm$ STDEV	1.47 $\pm$ 0.10	5.03 $\pm$ 0.35	6.50 $\pm$ 0.33	0.37 $\pm$ 0.03	0.34 $\pm$ 0.02



## 4. OVERCOMING CHALLENGES ASSOCIATED WITH THE ANALYSIS OF NACRE IN THE ATOM PROBE

Katja Eder<sup>1\*</sup>, Laura M. Otter<sup>2</sup>, Limei Yang<sup>1</sup>, Dorrit E. Jacob<sup>2</sup>, Julie M. Cairney<sup>1</sup>

<sup>1</sup>Australian Centre for Microscopy and Microanalysis, the University of Sydney, NSW 2006, Australia

<sup>2</sup>Department of Earth & Planetary Science, Macquarie University, Sydney, NSW 2109, Australia

\*Corresponding Author: [katja.eder@sydney.edu.au](mailto:katja.eder@sydney.edu.au)

This chapter has been published in *Geostandards and Geoanalytical Review* as:

K. Eder, **L.M. Otter**, L. Yang, D. E. Jacob, J. M. Cairney (2019): Overcoming challenges associated with the analysis of nacre by atom probe tomography, *Geostandards and Geoanalytical Research*, Vol. 43, No. 3, pp. 385–395. Doi: 10.1111/ggr.12279.

The author's contribution to the publication is as follows: LMO designed the study with the supervisor and the Atom probe specialists (KE and JMC). LMO acquired the bivalves, conducted aquaculture experiments and sample preparation and performed analysis to evaluate the successful incorporation of strontium prior to atom probe experiments. Further, LMO wrote parts of the manuscript and participated actively prior to submission and in the peer-review process.

Chapter 4 of this thesis has been removed due to copyright reasons

## 5. A PEARL IDENTIFICATION CHALLENGE

Nicholas Sturman<sup>1\*</sup>, Laura M. Otter<sup>2</sup>, Artitaya Homkrajae<sup>3</sup>, Areeya Manustrong<sup>3</sup>, Nanthaporn Nilpetploy<sup>1</sup>, Kwanreun Lawanwong<sup>1</sup>, Promlikit Kessrapong<sup>1</sup>, Klaus Peter Jochum<sup>4</sup>, Brigitte Stoll<sup>4</sup>, Hermann Götz<sup>5</sup>, Dorrit E. Jacob<sup>2</sup>

<sup>1</sup>Gemological Institute of America Laboratory, Bangkok, 10500 Thailand

<sup>2</sup>Department of Earth and Planetary Sciences, Macquarie University, Sydney NSW 2109 Australia

<sup>3</sup>Gemological Institute of America Laboratory, Carlsbad, CA 92008, USA

<sup>4</sup>Biogeochemistry and Climate Geochemistry Departments, Max Planck Institute for Chemistry, 55128 Mainz, Germany

<sup>5</sup>Platform Biomaterials, University Medical Centre of the Johannes Gutenberg University, 55131 Mainz, Germany

\*Corresponding Author: [nsturman@gia.edu](mailto:nsturman@gia.edu)

This chapter has been published in *Gems & Gemology* as:

N. Sturman, **L.M. Otter**, A. Homkrajae, A. Manustrong, N. Nilpetploy, K. Lawanwong, P. Kessrapong, K.P. Jochum, B. Stoll, H. Götz, D.E. Jacob (2019): A Pearl Identification Challenge, *Gems & Gemology*, Vol. 54, No. 2, 229–243. Doi: 10.5741/GEMS.55.2.229. Open Access at: <https://www.gia.edu/gems-gemology/summer-2019-pearl-identification-challenge>

The author's contribution to the publication is as follows: LMO performed LA-ICP-MS data acquisition and evaluation at the MPIC, participated in writing the final draft and preparing the revised version of the manuscript.

## Abstract

Nacreous pearls are usually found in saltwater (SW) or freshwater (FW) environments yet there are some reports of pearls originating from a brackish environment. Likewise, nacreous pearls may form naturally or by human manipulation (bead and non-bead-cultured) yet there are pearls where the origin is hard to prove, and agreement is not unanimous between all gemmologists testing them. Two pearls examined by the authors were unique, in their opinions, as their origins (natural or cultured) as well as their environment (FW versus SW) proved to be challenging to determine. This in turn had a direct impact on deciding on which mollusc produced the pearls, a factor that would have helped answer the two former questions. It is very rare to find pearls where all these criteria are in doubt as usually it is straightforward to determine at least two of them without concern. The results of the work on the pearls are included in this article for readers to see the challenges that laboratories sometimes face when testing pearls.

### 5.1 Introduction

When a laboratory receives pearls for examination, they undergo a series of tests to reach a conclusion on their identification (natural, cultured, imitation, assembled), the environment they formed within (SW or FW), and whether any treatments have been applied (colour modification, filling or coating). When possible, some laboratories, such as GIA, also provide an opinion on the likely mollusc that produced the pearls. The two pearls described in this work (Figure 5.1) were submitted to GIA's Bangkok laboratory at different times by different clients and were subsequently purchased later for further analysis, after their identity (natural/cultured), their environment (FW/SW), and consequently, also the mollusc in which they formed were found to remain challenging to determine. The trace element geochemistry is an important factor to consider when identifying the environment in which a pearl-producing mollusc lived (Wehrmeister et al., 2007). A clear answer to this question in turn yields potential information about the cultured versus natural origin of pearls produced and may assist with mollusc identification (Hänni, 2012).



**Figure 5.1:** The two challenging pearls discussed in this report. Pearl A is sitting on a freshwater shell (top) and pearl B on an iridescent saltwater shell (bottom).

The initial results from the work carried out by GIA revealed internal structures that were neither typical of natural pearls nor of non-bead-cultured pearls. Bead cultured pearls were quickly ruled out as were assembled and imitation pearls. However, the most unusual initial findings related to the pearls' chemistry and their optical X-ray fluorescence reactions (see relevant sections). In fact, the questions that arose from the initial work carried out on the pearls led to discussions with other colleagues in the industry which in turn led to the lead author seeking additional tests on the pearls using different equipment at the Max Planck Institute for Chemistry and the Johannes Gutenberg University, Mainz, Germany, in order to compare the results with those obtained by GIA. It was felt that taking this approach would produce helpful data and discussions which indeed turned out to be the case.

## **5.2 Materials and methods**

Two pearls weighing 8.52 carats (sample A) and 10.66 carats (sample B) and measuring 11.81 x 10.45 x 9.21 mm and 13.77 x 11.82 x 8.67 mm, respectively, were examined with a variety of equipment. The analysis of the pearls' surfaces was carried out with gemological microscopes (magnification ranges between 10x and 60x) and documented by photomicrographs using a Nikon SMZ18 microscope (various magnifications up to 176x) incorporating NIS-Elements photomicrography software and a Canon G16 camera. The pearls' ultra-violet fluorescence reactions were observed under an 8-watt UV lamp with both longwave (LWUV) and short-wave (SWUV) at 365 and 254 nm excitation wavelengths, respectively. A DiamondView unit also provided deep-ultraviolet (<230 nm) luminescence reactions.

The two main X-ray techniques used by gemologists to identify pearls today are real-time microradiography (RTX) (Karampelas et al., 2017), film usage is mainly obsolete now, and X-ray computed microtomography ( $\mu$ -CT) (Karampelas et al., 2010; Krzemnicki et al., 2010; Otter et al., 2014). The former allows the tester to obtain results on the whole volume of the sample while the latter permits the user to obtain an idea on a pearl's structure from micron thin slices as well as reconstructing a three-dimensional volume of the sample. While the vast majority of pearls submitted undergo only RTX investigation, as this technique is significantly faster and cost-efficient, a smaller number of pearls still require more in-depth  $\mu$ -CT analysis. This technique allows finer structural detail through its higher sensitivity for finer density-based compositional differences to be discerned within pearls as a result of its high-resolution capability to resolve material down to the order of few microns per voxel (3D pixel) depending on the overall size of the sample volume (Karampelas et al., 2010; Otter et al., 2014; Wehrmeister et al., 2004).

The internal structures were examined using a Faxitron CS-100 2D real-time (RTX) microradiography unit (90 kV and 100  $\mu$ A excitation), and a Procon CT-Mini model X-ray computed microtomography ( $\mu$ -CT) unit fitted with a Thermo Fisher 8W/90 kV X-ray tube and a Hamamatsu flat-panel sensor detector. Additional X-ray computed microtomography scans were obtained using a SCANCO  $\mu$ -CT-40 unit (Scanco Medical AG, Bassersdorf, Switzerland) with an acceleration voltage of 70 kV together with 114  $\mu$ A target current at the Medical Centre of the Johannes Gutenberg University, Mainz, Germany. The resulting images were processed using the open source visualization software OsiriX.



A custom modified FocalSpot Verifier (model FSX-PF100) optical X-ray fluorescence unit (voltage 100 kV and current 3.2 mA) incorporating a Canon EOS Rebel T4i camera was subsequently used to check whether the pearls originated from a saltwater (SW) or freshwater (FW) environment as pearls from each react differently when exposed to X-rays (Hänni et al., 2005; Nilpetploy et al., 2018). The results of EDXRF analysis provided further data to be used in conjunction with the optical fluorescence results.

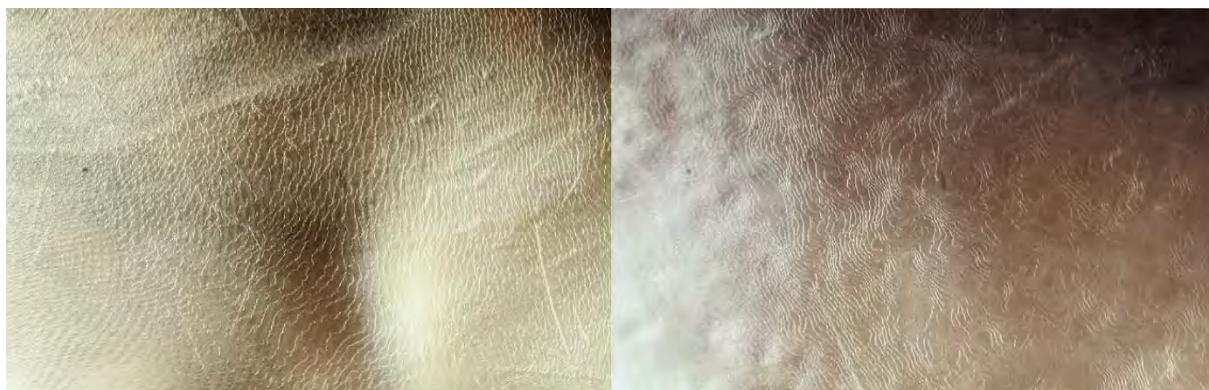
The pearls' chemical composition was initially analysed using a Thermo Scientific ARL QUANT'X energy dispersive X-ray fluorescence (EDXRF) spectrometer. However, since the results appeared very unusual compared to all previously analysed pearls, more thorough investigations were obtained by means of laser ablation–inductively coupled plasma–mass spectrometry (LA-ICP-MS) carried out in different laboratories: Firstly, the pearls were analysed for spot analyses using a Thermo X Series II LA-ICP-MS system in combination with a New Wave Research (NWR) UP-213 laser ablation system at both GIA laboratories in Bangkok, Thailand, and New York, USA. The microanalytical carbonate reference materials MACS-1 and MACS-3 from the United States Geological Survey (USGS) were used as matrix-matched calibration materials. A pulse repetition rate of 7 Hz, energy density of 10 J/cm<sup>2</sup>, and spot diameter of 40 µm were applied. Later, the pearls were further investigated with depth profiles obtained using a ThermoFisher Element 2 single-collector sector-field ICP-MS with the same LA system as before. A pulse repetition rate of 10 Hz, energy density of 8 J/cm<sup>2</sup>, and spot diameter of 80 µm were applied. Here, both pearls were measured by analysing nine locations evenly distributed over the surface of the pearls, whereby each location consisted of three groups of three adjacent spots to monitor the reproducibility of the trace-element pattern in every location. Data reduction and elimination of obvious outliers were performed following a programmed routine in Microsoft Excel described in Jochum et al. (2007) and the calibration followed the method for accurate trace element analysis of biogenic calcium carbonates published in Jochum et al. (2012), where refractory lithophile elements are calibrated with NIST glasses (SRM610 and 612), while chalcophile and siderophile elements with low boiling points were matrix-matched calibrated with USGS MACS-1 and -3. A Leica DMRX incident light microscope with well-defined zoom steps for each grid on its focusing adjustment screw was used to measure the depth of the ablation spots left in the pearls after analysis.

## 5.3 Results

### 5.3.1 External appearance

In most cases, gemologists and those in the pearl trade with sufficient pearl handling experience, are able to visually identify pearls based on their external characteristics (lustre, colour, shape, etc.). However, these two pearls did not exhibit either typical SW or FW features and hence their outward appearances did not look particularly natural or cultured. Based on the authors' experiences handling countless pearls of all types the form of the platy overlapping nacreous structures (size of platelets, their spacing and the shape/appearance of the platelet edges – see Figure 5.2) could be considered more towards FW than SW and the flat surfaces on one side of each pearl could also have been taken as

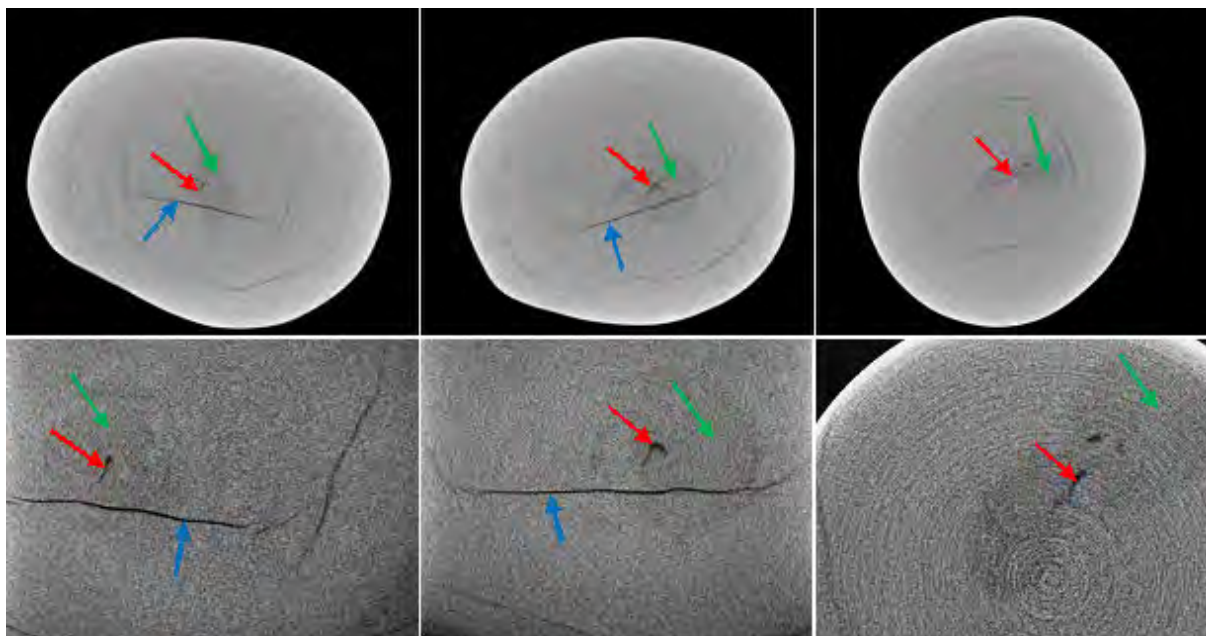
indicators of freshwater origin. The pearls certainly did not display enough characteristic features to sway the decision one way or the other.



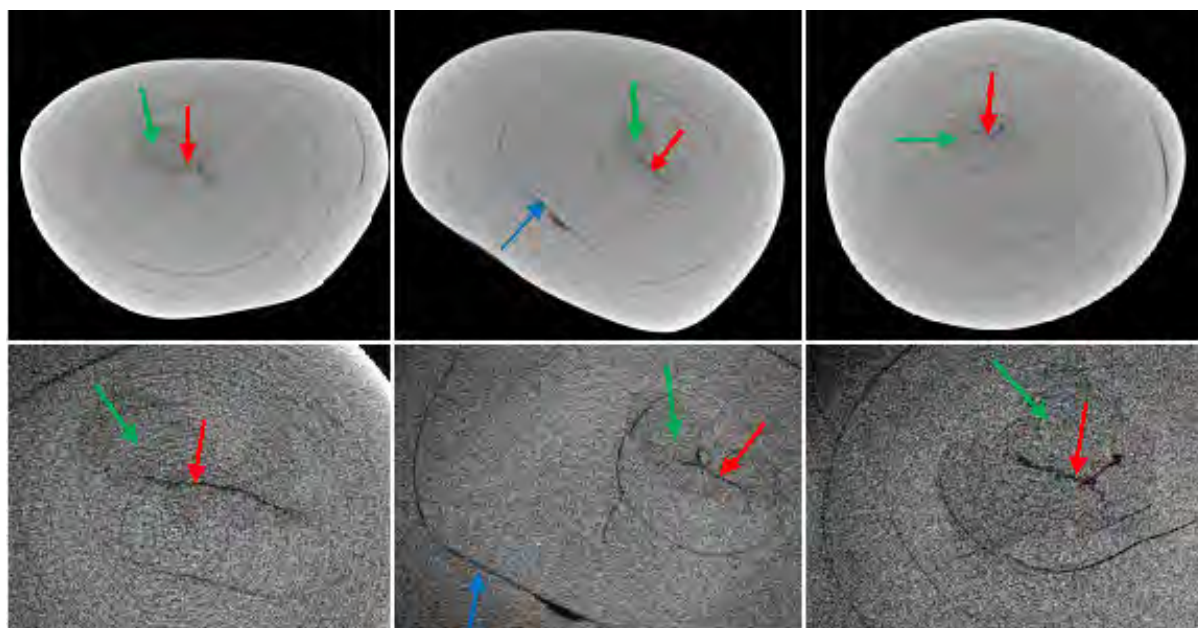
**Figure 5.2:** Platy structure typical of nacreous pearls was evident on both pearls (A left, FOV 2.34 mm and B right, FOV 1.76 mm). The platelets of both were finely to moderately spaced, while areas of pearl B also showed some “distortions” in the patterns of the platelets similar to those seen on some freshwater pearls by the authors. However, the nature of the platelets was not specific enough to indicate whether the pearls formed in a freshwater or a saltwater environment. Photomicrographs by Artitaya Homkrajae.

### *5.3.2 Real-time microradiography (RTX) and $\mu$ -computed tomography ( $\mu$ -CT) analysis*

Both pearls in this study showed structures that were not straightforward when examined by the RTX units in Bangkok. Similarities in the darker organic-rich arcs extending from near the centre to the outer surfaces of the pearls and small organic-rich areas adjacent to the centres were revealed. A straight organic-rich feature (Figure 5.3 and Figure 5.4) was observed in each pearl relating to the flat surfaces visible on the exterior of the pearls was also evident. Such structures are not conclusive of any particular type of pearl and do not match the usual SW or FW structures usually associated (see box A) with non-bead cultured pearls, so the chances they were natural remained a possibility. In order to try and identify the true origin more work was considered necessary and so both pearls were further examined by  $\mu$ -CT. The resulting  $\mu$ -CT work provided more detail but did not resolve the origin to the complete satisfaction of all those who examined the data. As can be seen from the sample RTX and  $\mu$ -CT images in Figure 5.3 and Figure 5.4, the structures were inconclusive either way although the majority of opinions favoured a cultured origin based on experience when testing previous pearls. However, an idea of their chemistry was also needed before reaching any conclusions as linking the internal structures to pearls of a known environment is an important part of pearl identification.



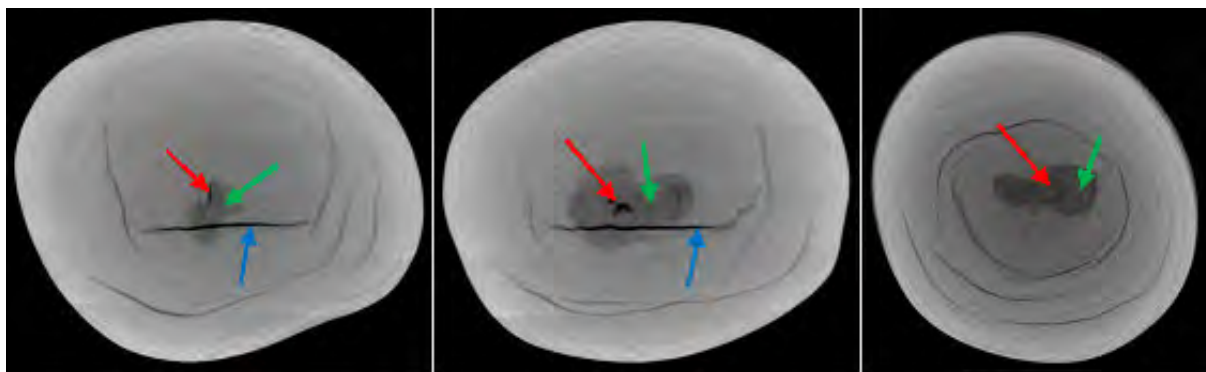
**Figure 5.3:** Three  $\mu$ -CT slices obtained during the analysis of pearl A in Bangkok (top row show the whole pearl, lower row magnified areas). All show the suspect small dark linear-appearing void feature (red arrows) within a dark grey organic-rich area (around the green arrows). The linear structure relating to the flat surface area is indicated by the blue arrow, although it does not show on both end images owing to the pearl's orientation. Note the similarity to the features observed in pearl B. Note: The weak white rings on the lower right image are artifacts and not pearl related structures.



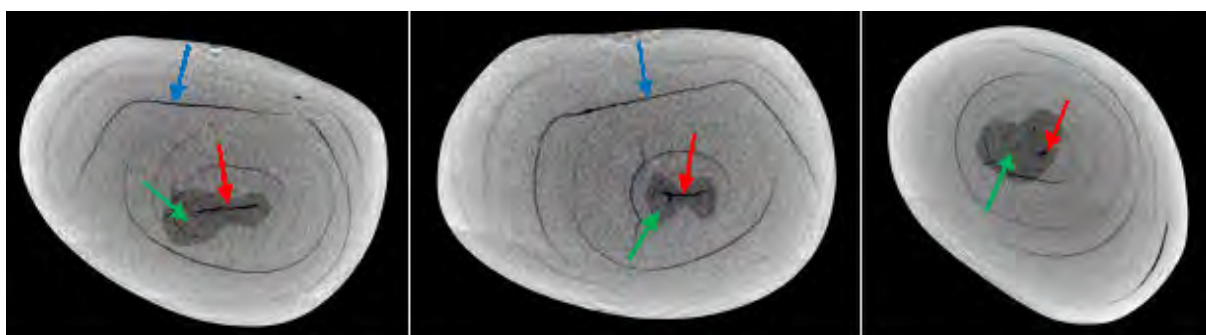
**Figure 5.4:** Three  $\mu$ -CT slices obtained during the analysis of pearl B in Bangkok. (top row show the whole pearl, lower row magnified areas) All show the suspect small dark linear-appearing void feature (red arrows) within a dark grey organic-rich area (around the green arrows).

Complementary  $\mu$ -CT and trace element characterization were performed at Mainz University (MU) and the Max Planck Institute for Chemistry (MPIC), respectively. The additional findings matched those of GIA's as can be seen in Figure 5.5 and Figure 5.6. However, GIA's analysis time was sixteen minutes compared with 5.4 hours at MU which motivated another analytical run in which the pearls were positioned closer to the tube to increase magnification. The acquisition time difference is due to the equipment used and the software/parameters applied, which is why a second opinion was sought, since

the lengthier analysis usually yields sharper features. Following the  $\mu$ -CT results the trace element results were considered even more important for the identification of these particular pearls.

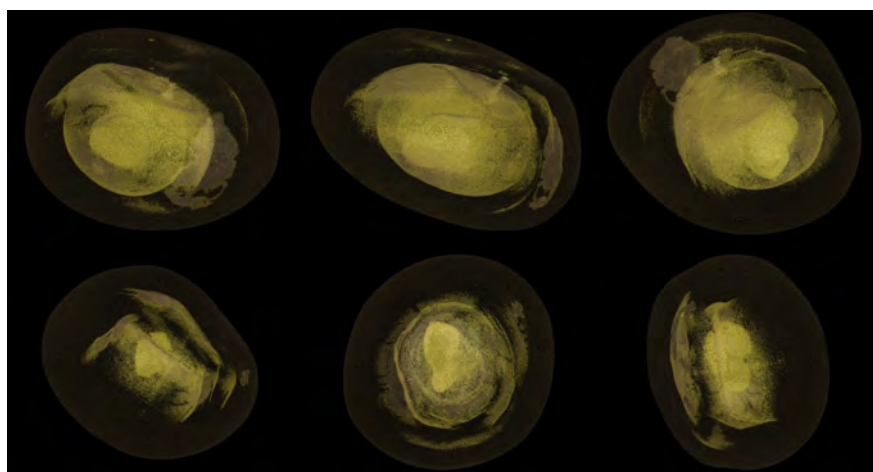


**Figure 5.5:** Three  $\mu$ -CT slices obtained during the analysis of pearl A in Germany. All show the suspect small dark linear-appearing void feature (red arrows) within a dark grey organic-rich area (around the green arrows). Note the similarity to the features observed in the other pearl.



**Figure 5.6:** Three  $\mu$ -CT slices obtained during the analysis of pearl B in Germany. All show the suspect small dark linear-appearing void feature (red arrows) within a dark grey organic “rich” area (around the green arrows). Note the similarity to the features observed in the other pearl.

Further specialist software analysis in Germany (Figure 5.7) indicated that the composition of the layers varied significantly in density with four internal layers showing a different unenclosed profile – visible as yellow structures in the figure - to the main body of the pearl. The introduction of such software in pearl identification has been used to provide more detail in cases worthy of the extra work (Otter et al., 2014; Zhou et al., 2016). The yellow areas in question did not appear to reach the surface so it is unlikely that they related to the trace element characteristics although the only way to verify this would require cutting the pearls in half and analysing their trace element results in more detail.



**Figure 5.7:** Additional software analysis revealed four layers of different density (yellow structures) within the pearls that did not appear to reach the surface. Pearl A upper row and Pearl B lower row.



### 5.3.3 Energy dispersive X-ray fluorescence (EDXRF)

Since the interpretation of the RTX and  $\mu$ -CT data failed in reaching a conclusive identity on the pearls other useful tests had to be considered in order to help in providing more data by which to assist in supporting either a natural or cultured origin. One of the main supporting techniques available to pearl gemologists is trace element analysis. By confirming whether a pearl is SW or FW and linking the environment to the RTX and/or  $\mu$ -CT structure the decision on a pearl's identity can often be made easier.

In order to see in which environment, the pearls in question formed they were each tested in an EDXRF spectrometer. While lower manganese (Mn) levels (below detection levels of around  $40 \mu\text{g}\cdot\text{g}^{-1}$  usually indicate a SW origin, higher values (most often  $150 \mu\text{g}\cdot\text{g}^{-1}$  into the low to mid thousands) identify a FW origin (Wada and Fujinuki, 1988; Wehrmeister et al., 2007). The opinions of some gemologists who looked at the pearls favored a FW origin more than a SW one based on the internal structures observed via the X-ray work. Therefore, further EDXRF analysis was carried out in more positions on the pearls to provide further data (Table 5.1). This produced very interesting and conflicting results that the GIA has not encountered on any pearls tested in the past and, hence, led to more extensive research on these pearls. Owing to the EDXRF results it was decided to check the reactions of the pearls under optical X-ray fluorescence conditions. Pearls that fluoresce strongly when checked by this method tend to originate in FW environments as the Mn content is higher and is thought to cause the strong visible reaction, while in SW pearls Mn is low or absent and hence no reaction is observed (Hänni et al., 2005; Nilpetploy et al., 2018). Strontium, on the other hand, is known to reach high concentrations for biogenic calcium carbonates i.e. pearls and shells from SW environments, while low values are characteristic for FW origins (Wehrmeister et al., 2007). Together, for Mn and Sr concentrations, combined with those of other elements, are useful tools to determine the habitat of the pearl forming mollusc (saltwater or freshwater).

**Table 5.1: EDXRF results in  $\mu\text{g}\cdot\text{g}^{-1}$  obtained from the pearls in six different positions. The two highlighted rows for pearl B reveal freshwater signatures while the remaining results for both pearls indicate saltwater origin. Note the correlation of high Mn with low Sr that is indicative for FW environments, while low Mn coupled with high Sr point towards marine origins.**

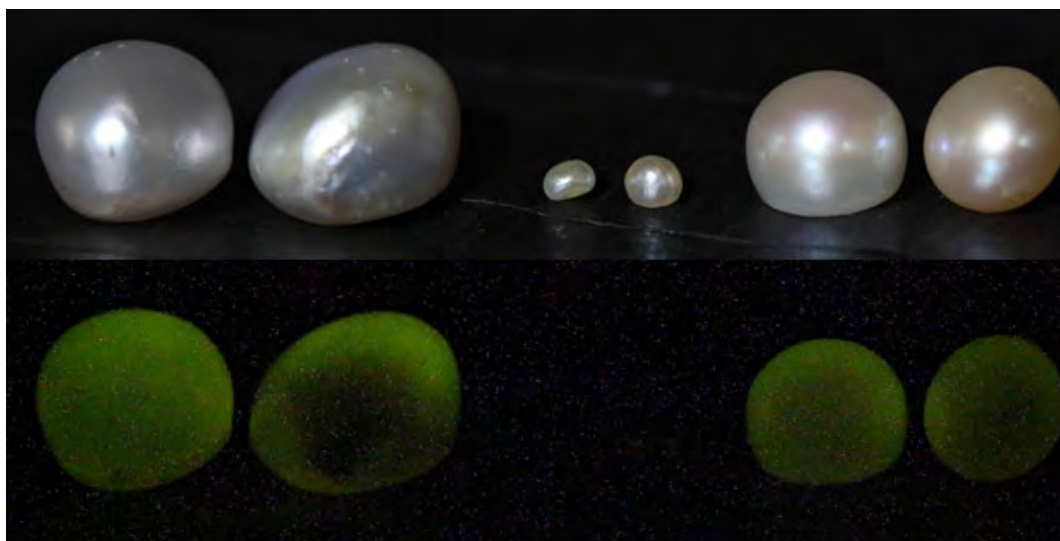
Pearl ID	Mn	Sr
A_Position 1	<5	1364
A_Position 2	<5	1284
A_Position 3	<5	2073
A_Position 4	<5	1524
A_Position 5	<5	1261
A_Position 6	<5	1497
B_Position 1	<5	1293
B_Position 2	<5	1128
B_Position 3	1006	588
B_Position 4	<5	1422
B_Position 5	1501	538
B_Position 6	66	1107
Detection Limit (DL)	5	6



### 5.3.4 Optical X-ray fluorescence

According to the results obtained by the EDXRF analysis the 8.52 carat pearl (A) should in theory be of saltwater origin as the consistent results from the six different positions tested did not find detectable amounts of Mn. On the other hand, the 10.66 carat pearl (B) seemed to be a mixture of saltwater and freshwater origin which came as rather a surprise since this is the first time GIA has encountered such mixed trace element signatures in a pearl and to our knowledge there are no other recorded cases of such test results in the literature.

In order to examine the pearls more and see how the data from the EDXRF results would be reflected in the visual reactions of the elemental distributions throughout the pearls we turned to the simple but effective method of optical X-ray fluorescence. A pearl with mixed trace element signatures should in theory show an inhomogeneous reaction relating to the areas of freshwater and saltwater composition detected while the saltwater pearl, in keeping with known saltwater pearl reactions, should show no reaction or at best a very weak reaction. The results obtained are shown in Figure 5.8.



**Figure 5.8:** The optical X-ray fluorescence reactions of the two pearls in question (left) shown together with two known non-bead cultured freshwater pearls from China to the right and two natural saltwater pearls from Venezuela in the centre. Pearl A (far left) should not be showing any reaction when its trace element characteristics are taken into account while that of pearl B (2nd left) shows a predominantly freshwater reaction which again does not conform entirely to the trace element observations. The camera settings used to record the luminescence were ISO speed 12800, F-stop of 5 and exposure time of 5 seconds. Photos by Chunhui Zhou.

The reactions were completely at odds to those predicted and did not correlate to the expected results already described. Instead of an inhomogeneous reaction the 10.66 carat pearl exhibited a fairly homogenous moderate to strong greenish yellow reaction while the apparent SW pearl revealed a very similar reaction that should not be present given the trace element data. This added to the identification challenges already existing with the pearls since now not only was the nature of their origin (natural or cultured) in doubt but also the environment in which they formed. On top of this the question about Mn and its role in fluorescence immediately came into focus, which is to date not yet fully understood, so it was decided that even more work than is normally applied to pearl identification was needed for these two examples.

### 5.3.5 Laser ablation-inductively coupled plasma-mass spectrometry (LA-ICP-MS) analyses

Since the EDXRF results and subsequent optical X-ray fluorescence analysis produced unusual results, both pearls were examined by LA-ICP-MS to obtain more accurate comparison trace element data. In routine pearl testing LA-ICP-MS analysis is not usually applied since the EDXRF and optical X-ray fluorescence techniques provide sufficiently accurate and distinct data to reach a conclusion on their exact environmental origin. When combined with their external appearance, the form of their platy structure and their internal structures, the identity of the environment becomes even more accurate; however, with the two pearls under discussion their external appearances, platelet form, internal structure, chemistry results and optical X-ray fluorescence reactions were all inconsistent with regards to any particular type of pearl, environment or mollusc.

The initial ICP work was carried out in Bangkok after their acquisition, two preliminary spots for pearl A and six spots for pearl B, and the results obtained are shown at the top of Table 5.2.

Surprisingly the results from the BKK unit on pearl A still fell within those expected from SW pearls so it was decided to keep the pearl back until the results of pearl B were known.

Since the results from two spots on pearl B agreed with two of the areas tested by the EDXRF spectrometer it was decided to check the pearl in question even more carefully, so it was subsequently sent to GIA NY for examination on their LA-ICP-MS unit to check for consistency. The results proved to be very similar and are shown in Table 5.2 for comparison.

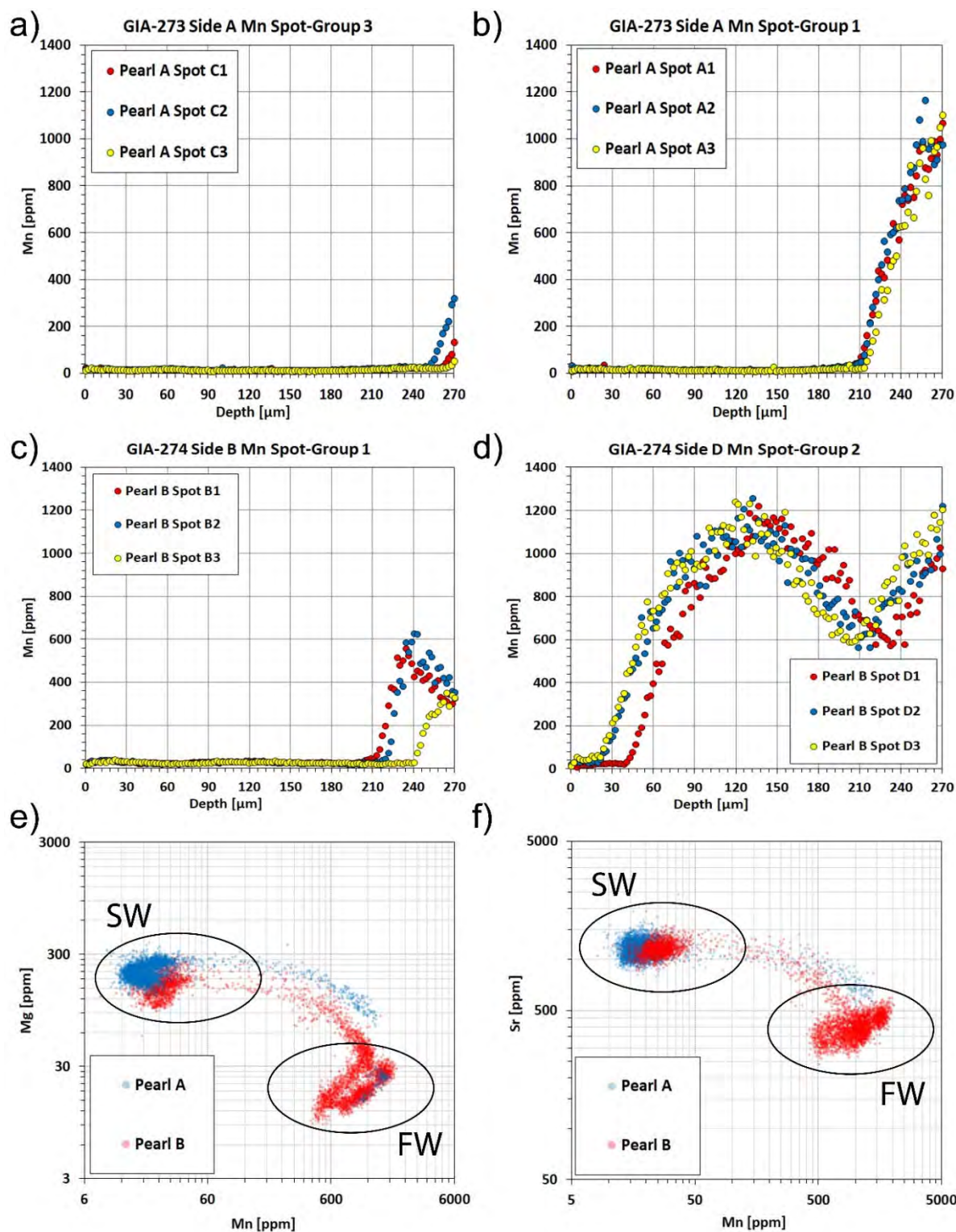
As the chemistry of the pearls and their fluorescent reactions were so intriguing, we also sent the pearls to one of the co-authors (LMO) for more detailed chemical analysis in Mainz. In order to obtain a good set of results with which to perform their calculations the team in Mainz tested 33 spots in four different positions on pearl A and 36 spots in four different positions on pearl B. The estimated depth of these ablation spots was around 270  $\mu\text{m}$ . The results of the analysis on both pearls reflected the findings of GIA for both pearls (lower part of Table 5.2).

The greater number of spots evaluated as depth profiles over a greater surface area revealed deeper Mn-rich areas (Figure 5.9a, b). Pearl B showed a higher concentration of Mn closer to the surface in several spots (Figure 5.9c, d). The patterns start for both pearls at low Mn values of around 20  $\mu\text{g}\cdot\text{g}^{-1}$  that are characteristic for marine (SW) conditions and rise steadily to high values of over 1000  $\mu\text{g}\cdot\text{g}^{-1}$ , which are characteristic for FW conditions. These high Mn values are found generally closer to the surface in Pearl B on average at about 100  $\mu\text{m}$  depth, whereby the depth of the Mn-rich areas was found to be very heterogeneously distributed over the surface of the pearl, ranging from its presence directly at the surface to its absence within the profile. Pearl A showed the Mn-rich area at around 240  $\mu\text{m}$  depths on average. In addition, bivariate double-logarithmic plots showing the full data-sets of both pearls for Mn *versus* Mg (Figure 5.9e) as well as Mn *versus* Sr (Figure 5.9f) reveal further mixed FW (high Mn and low Mg/Sr) and SW-like (low Mn and high Mg/Sr) compositions and the heterogeneity observed in Mg and Sr shows that the concentration of these elements changes similarly within the depth profiles. Thus, it

is clear to see that while both pearls appear to contain areas of both saltwater and freshwater trace element characteristics, pearl A trends generally more towards saltwater than pearl B, even if the chemistry of both is not specific to a defined environment.

**Table 5.2: LA-ICP-MS data in  $\mu\text{g}\cdot\text{g}^{-1}$  obtained in three different laboratories for both pearls. The highlighted spots mark freshwater-like trace element compositions. Values from Germany are expressed as averages of three spots each.**

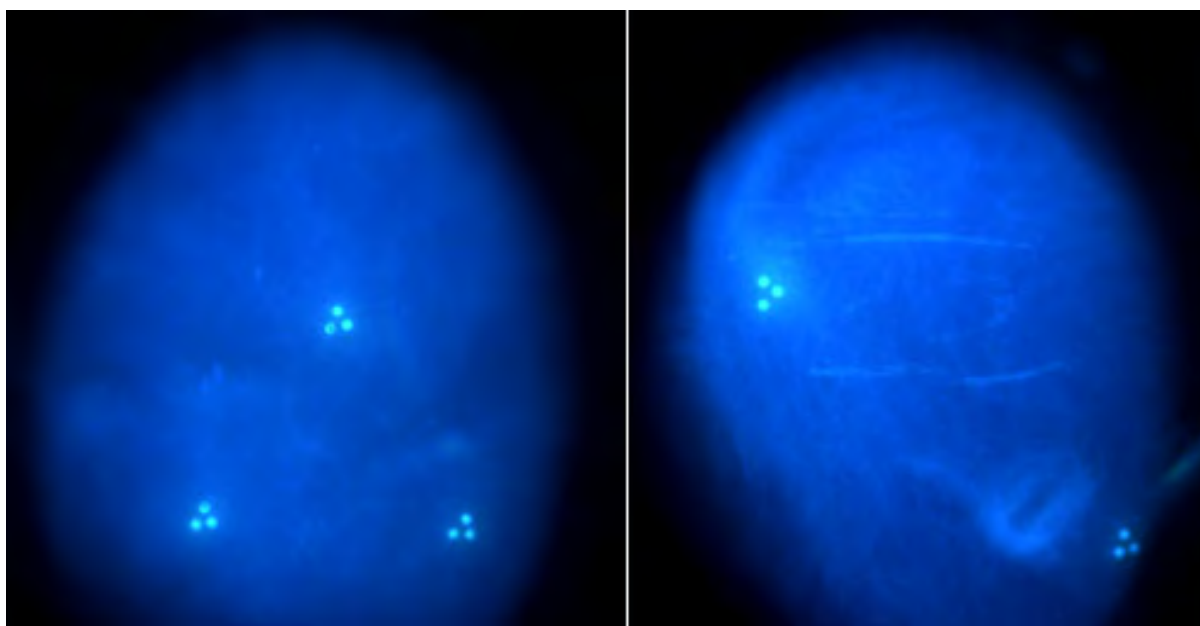
Laboratory:	Pearl ID	B	Mg	Mn	Fe	Sr	Ba
<b>GIA Bangkok:</b>							
	A_Position 1	12	210	16	238	1561	1
	A_Position 2	11	180	21	186	1287	1.5
	B_Position 1	16	127	45	130	1119	0.6
	B_Position 2	15	195	44	236	1373	2
	B_Position 3	BDL	39	1672	287	438	57
	B_Position 4	11	145	19	168	1137	0.7
	B_Position 5	BDL	35	2307	152	523	77
	B_Position 6	16	204	21	194	1261	BDL
	Bangkok Detection Limit	3	0.5	2	50	0.1	0.5
<b>GIA USA:</b>							
	B_Position 1	19	208	47	209	1570	2.5
	B_Position 2	16	149	50	216	1290	0.6
	B_Position 3	BDL	39	1672	287	438	57
	B_Position 4	14	174	27	180	0.3	0.1
	B_Position 5	BDL	35	2307	152	523	78
	B_Position 6	18	187	26	179	1455	BDL
	USA Detection Limit	3	1	1	60	0.3	0.1
<b>MPIC:</b>							
	A_Position 1	10	207	156	51	1026	5.5
	A_Position 2	10	204	236	51	1003	9
	A_Position 3	11	213	23	48	1064	0.7
	A_Position 4	12	181	22	38	1115	0.5
	A_Position 5	12	213	21	36	1129	0.5
	A_Position 6	11	213	20	35	1144	0.5
	A_Position 7	7	147	476	53	1010	16
	A_Position 8	11	212	16	49	1218	0.6
	A_Position 9	7	147	476	53	1010	16
	A_Position 10	10	211	19	62	1281	0.7
	A_Position 11	11	221	20	61	1211	0.5
	B_Position 1	3	51	768	52	480	29
	B_Position 2	3	58	783	54	481	28
	B_Position 3	1.5	36	885	54	388	38
	B_Position 4	12	172	87	38	1127	8
	B_Position 5	12	162	29	38	1170	0.5
	B_Position 6	1	24	1252	58	464	49
	B_Position 7	1	22	1371	58	445	48
	B_Position 8	0.8	20	1071	57	424	44
	B_Position 9	12	131	39	67	1157	1
	B_Position 10	3.6	62	746	68	578	31
	B_Position 11	0.9	17	939	69	377	63
	MPIC Detection Limit	0.1	0.3	0.1	4	0.9	0.1



**Figure 5.9:** Depth profiles obtained by LA-ICP-MS show significant fluctuations for Mn with depth for both Pearl A (a and b) as well as Pearl B (c and d). Each figure a)-d) shows one of the exemplary depth profile groups consisting of three spots ablated adjacent to each other. Bivariate double-logarithmic plots showing Mn versus Mg (e) and Mn versus Sr (f) show a mixture of saltwater and freshwater environments with high Mn together with low Sr or Mg values indicating a freshwater (FW)-origin whereas low Mn in combination with high Mg or Sr point towards a marine (SW) origin. Generally, pearl B exhibits a higher proportion of Mn when compared to the results obtained from pearl A which definitely fall more within a saltwater environment. The fine trace of data points connecting the SW-like and FW-like composition (black circles) have not been observed in any pearls so far. Altogether, the trace-element patterns of both pearls proved to be atypical of pearls tested by GIA over the years.

### 5.3.6 UV radiation and DiamondView reactions

The majority of white to cream nacreous pearls exhibit a weak to strong, chalky yellow to bluish (depending in part on the producing mollusc species) fluorescence under SW and LW UV radiation. These reactions may be further influenced by various processes, including treatments (Strack, 2006). Such treatments may also provide some indications about the nature of the pearls. For example, bleaching is commonly applied to cultured freshwater and akoya pearls and may show as a stronger bluish reaction in some examples. Both subject pearls fluoresced a weak chalky yellow under SWUV, while pearl A reacted with a moderate chalky yellow under LWUV and pearl B showed a similar reaction but with more of a blue component. The reactions were not those more commonly associated with cultured FW pearls or akoya pearls that have undergone bleaching. The DiamondView unit, although not always useful in assisting in the identification of natural from cultured or saltwater from freshwater origins, may aid in determining treatments in pearls. However, since these are white pearls which usually show a marked blue reaction within the DiamondView, we did not expect to see anything unusual and that turned out to be the case when both pearls exhibited a characteristic blue reaction (Figure 5.10) as expected.



**Figure 5.10:** The DiamondView results for pearl A (left) and pearl (B) right show the characteristic blue reaction of untreated pearls. The small triangular groups of dots each consist of three laser ablation holes that react with a stronger bluish white fluorescence which from GIA's experience is typical of pearls where the underlying surface structure has been exposed by different means (e.g. LA-ICP-MS analyses, drilling, working, heavy polishing). This reaction is not only seen by exposure to the DiamondView but also from SW and LWUV radiation too.

## 5.4 Discussion

The results obtained from the analysis described so far led to two main questions: Firstly, did the pearls form naturally in a mollusc without any human intervention? Secondly, did the molluscs in which the pearls formed live in a SW or FW environment? In most cases submitted to labs on a daily basis these questions are relatively straightforward to answer but, in this case, both answers proved to be uncertain after examining these two pearls.



The first method of identification employed was that of RTX analysis and the results showed suspect structures, although not enough to prove they were non-bead cultured. It was possible that the pearls could still be natural, and many pearls examined by GIA over its history have shown odd natural structures. The results led to the next identification method being employed and so  $\mu$ -CT analysis was performed. Again, the results revealed structures that could be considered either natural or non-bead-cultured and were not definitive.

The chemistry was considered next and as the results above reveal, in this case the exact environment in which the pearls formed (saltwater or freshwater) also proved to be challenging: EDXRF data obtained from both pearls in six different areas showed conflicting results regarding their possible formation environment: Pearl A yielded  $<5$   $\mu\text{g/g}$  Mn in every spot and an average concentration of 1500  $\mu\text{g/g}$  for Sr. Both trace elements are considered environmental indicators, since a combination of  $<20$   $\mu\text{g/g}$  Mn and  $>1300$   $\mu\text{g/g}$  Sr is associated with marine environments, while the reverse relation of  $>20$   $\mu\text{g/g}$  Mn and  $<1300$   $\mu\text{g/g}$  are indicative of freshwater origins (Wehrmeister et al., 2007). However, the EDXRF analysis employed covered a 6.0 mm area (dependent on the collimator applied) of the surface and the penetration depth was in the order of a few microns, so it could not determine the chemistry deeper within the samples. LA-ICP-MS is better suited to determine the elements deeper within a sample, although still limited to micron depths, yet in contrast to the EDXRF method the surface area tested is significantly smaller (Li et al., 2011).

LA-ICP-MS performed at GIA laboratories in Bangkok and New York showed similar results as the EDXRF and identified both FW and SW-like signatures in different average spot compositions for both pearls. The LA-ICP-MS depth profiles, obtained at the MPIC in Germany, revealed a very atypical trace-element composition so far not observed for pearls: Several environmental indicative elements, namely B, Mg, Mn, Sr and Ba, were found to vary in concentration forming discrete layers of alternating FW-like and SW-like composition. In all spots, the patterns start at low Mn values of around  $20 \mu\text{g}\cdot\text{g}^{-1}$  that likely correspond to marine (SW) conditions and rise steadily to high values of over  $1000 \mu\text{g}\cdot\text{g}^{-1}$  for both pearls. These fresh-water (FW) conditions are found closer to the surface along the depth profile of Pearl B at ca.  $100 \mu\text{m}$  compared to ca.  $240 \mu\text{m}$  for Pearl A. Peak concentrations decrease and rise in Pearl B for two times, creating a steady, alternating trend. These steady alternating patterns imply that the pearls grew uninterruptedly within a mollusc and not in two separate molluscs first within FW and later SW environments, which would have produced abrupt changes from SW to FW trace element characteristics. The LA-ICP-MS craters were “only” drilled to a depth of around  $270 \mu\text{m}$  since increasing depths at some point hinder the rising evaporate and also increases the chance of element fractionation, however, it can be expected that the concentrations of Mn, Sr and Mg continue to alternate towards the centre of the pearl. The alternating patterns between FW-like and SW-like compositions could result from growth in a river dominated estuary where the predominant water input is freshwater with only occasional season-dependent saltwater input when the river carries little water i.e. during summers in warm climates. While there are no confirmed farms that operate in brackish waters, of which the authors are aware, reports of shells originating from around islands within the Mississippi delta in

North America exist (Moore, 1961) and farms are known to operate in river deltas in Vietnam (Huong pers. Comm.), both possibly underlining this possibility. However, this does not aid in determining the natural or cultured nature of the pearls and although this hypothetical setting favours an overall FW-related origin it does not satisfyingly answer the question of the bivalve species that produced these pearls, since little is known about the environmental tolerances of the Unionidae and Pteriidae families. These changes in trace element composition are, however, too low to affect the major element composition of the pearls and are therefore not enough to discriminate between marine and freshwater nacre in the  $\mu$ -CT datasets. Instead, the  $\mu$ -CT datasets show the density changes between organic material and nacre. The not fully enclosed appearance of the organic layers are possibly “pseudoannuli” growth rings (Jacob et al., 2011), which are characteristic of continuous growth within a mollusc, whereas the use of beads as nuclei for further pearl growth would likely produce a prominent concentric layer of organic material as often observed for bead cultured pearls (Karampelas et al., 2010; Krzemnicki et al., 2010; Otter et al., 2014). These inner unenclosed growth rings also lead to questions about the intensity of the pearls’ optical X-ray fluorescence, since most SW layers that cover freshwater layers/components (i.e. freshwater nuclei in most bead cultured pearls) mask the effects producing weak to moderate fluorescence. This was not the case with these two samples and the fluorescence was quite marked (see Figure 5.8).

Average nacre deposition rates for marine environments range between 0.5 to 2.0 mm/year for akoya cultured pearls from the temperate climates in e.g. Eastern Australia produced by *Pinctada imbricata fucata* to tropical climates in the South Sea produced by *Pinctada maxima* (Otter et al., 2017; Strack, 2006). Lower values of the akoya pearls are likely an effect of the colder climate compared to the warmer, near-equatorial distribution of *Pinctada maxima* (Strack, 2006). Freshwater species such as *Hyriopsis schlegelii* and *Hyriopsis cumingii* or their hybrids are known to have higher growth rates and can deposit up to 10 mm of nacre within six years that account to ca. 1.5 mm/year (Akamatsu et al., 2001). Using the mean diameter of 10.5 mm for Pearl A it can be assumed that it could have grown for 7 (FW growth rate) or between 5 and 21 years (for tropic and temperate marine growth rates, respectively) depending on the mollusc species and environment used (numbers for Pearl B are in the same range). The shorter FW-growth period of seven years would, therefore, still be in the timeframe of FW NBCPs from China (Akamatsu et al., 2001). On the other hand, slower growth rates from marine environment would point towards a natural origin as the estimated SW growth period exceeds the timeframe for cultured pearls by up to ten times. Since species of the *Pinctada* genus can reach ages of up to 40 years (Strack, 2006) a growth period of around 20 years does not seem impossible.

## 5.5 Conclusion

The identification of these two pearls presented challenges on many fronts. While the authors believe that their internal structures are more likely NBC it is by no means definite. Hence, there is a chance they could be natural pearls with unusual structures. Pearl testing is relatively straightforward in most cases yet there are plenty of pearls in existence where identification is subjective and one gemmologist

may have a different opinion to that of another gemmologist, even if the two gemmologists work in the same organization, let alone separate unrelated ones! Likewise, determination of the environment in which pearls form is almost always straightforward, yet the pearls in this report prove that on very rare occasions it is possible to encounter cases where anomalies in trace elements exist thus leading to questions about the true environmental origin of samples. The clear fluorescence observed under X-rays as well as the general appearance of the pearls lead the authors to believe that they are more likely FW pearls yet there is no clear explanation why a predominantly SW pearl, based on chemistry, such as example B should have reacted the way it did under such stimulation. Even if there are zones of freshwater material within the saltwater material the freshwater reaction should in theory be masked to a greater extent, just as the reactions of freshwater bead nuclei in almost all commercial bead cultured pearls are when subjected to the same test.

As a consequence of these two factors it also calls into question the identity of the producing mollusc for laboratories such as GIA that routinely attempt to identify the species of mollusc in which a pearl formed. If either of the pearls could be identified as SW they would likely have formed in a species from the Pteriidae family, however if they were FW they would have formed within a mussel species belonging to the Unionidae family that inhabit the rivers and lakes worldwide. The location would in many ways be influenced by whether they formed naturally or with the assistance of humans, so again we come full circle to the subjectivity involved in all three factors that resulted from the data obtained during their examination.

Although the final conclusions were not unanimous and questions still exist about the true identification, environment, and the producing mollusc in which the pearls formed the results obtained prove that there is always something new to discover when it comes to the analysis of gem materials, especially organic ones such as pearls. Further destructive work on the pearls, specifically cutting each in half to study their internal chemistry in greater detail, and conducting deoxyribonucleic (DNA) analysis on powder samples extracted (Meyer et al., 2013; Saruwatari et al., 2018), may have to be considered in order to provide more data with which to reach a possible conclusion.

## **Acknowledgements**

We thank Dr. Ursula Wehrmeister and other GIA pearl team members in New York, Carlsbad and Bangkok for enriching discussions. The authors also appreciate the feedback received from Elisabeth Strack and Lore Kiefert as well as the third anonymous peer-reviewer who provided fruitful discussions on this work.

## 6. AKOYA CULTURED PEARL FARMING IN EASTERN AUSTRALIA

Laura M. Otter<sup>1\*</sup>, Oluwatoosin B. A. Agbaje<sup>1</sup>, Le Thi-Thu Huong<sup>2</sup>, Tobias Häger<sup>3</sup>, Dorrit E. Jacob<sup>1,4</sup>

<sup>1</sup>Department of Earth & Planetary Science, Macquarie University, Sydney, NSW 2109, Australia

<sup>2</sup>Institute of Earth Sciences, Karl Franzens University, Graz, Austria

<sup>3</sup>Centre for Gemstone Research, Institute for Geosciences, Johannes Gutenberg University Mainz, Germany

<sup>4</sup>Australian Research Council Centre of Excellence for Core to Crust Fluid System (CCFS) / GEMOC

\*Corresponding Author: [laura.otter@mq.edu.au](mailto:laura.otter@mq.edu.au)

This chapter has been published in *Gems & Gemology* as:

**L.M. Otter**, O.B. Agbaje, L.T.T. Huong, T. Häger, D.E. Jacob (2017): Akoya Cultured Pearl Farming in Eastern Australia, *Gems & Gemology*, Vol. 53, No. 4, pp. 423–437. Doi: 10.5741/GEMS.53.4.423. Open Access available at <https://www.gia.edu/gems-gemology/winter-2017-akoya-cultured-pearl-farming-eastern-australia>

The author's contribution to the publication is as follows: LMO visited the pearl farm, interviewed their staff, acquired samples, and took photographs. LMO weighted, measured and characterized the colour of the pearls, performed Raman and photoluminescence spectroscopy and evaluated the data. Further, LMO supported FTIR and UV-Vis spectroscopy and corresponding data analysis and drafted the first version of the manuscript. All co-authors participated in editing the draft and gave final approval for publication.

## Abstract

Akoya cultured pearls have been produced on the eastern shoreline of Australia since approximately 1999 using *Pinctada imbricata fucata* molluscs native to New South Wales. Unlike many of their Japanese counterparts, Australian akoya cultured pearls are harvested after 18 months of growth and marketed without any post-harvest treatments involving dyes or bleaches. This study presents the first gemological and mineralogical characterization of Australian akoya cultured pearls using Raman, photoluminescence, FTIR, and UV-Vis specular reflectance spectroscopy. Raman and FTIR spectroscopy identified the major mineral phase aragonite as well as some organic compounds. While Raman spectroscopy revealed polyene-related pigments with bands occurring at 1134 and 1532  $\text{cm}^{-1}$ , FTIR spectroscopy showed sulfate- and polysaccharide-associated groups occurring at around 1200 and 1115  $\text{cm}^{-1}$ , respectively. UV-Vis spectroscopy revealed broad spectral features that provide insight into the distinct bodycolours and enable discrimination from some non-akoya saltwater cultured pearls from *P. margaritifera*, *P. maxima*, and *P. mazatlanica* bivalves, while separation from other untreated akoya pearls is not possible. Production processes are examined to better understand the modern, sustainable, and environmentally friendly pearl farming operations in Australia.

## 6.1 Introduction

The *Pinctada imbricata fucata* mollusc has long been used to produce akoya cultured pearls, dating back to the pioneering work in the early 1900s by Japanese entrepreneur Kokichi Mikimoto (Strack, 2006). This bivalve is distributed widely across Asia and also occurs on the eastern coast of Australia (Gifford et al., 2004), where it is used to produce untreated and sometimes vibrantly coloured cultured pearls (Figure 6.1).



**Figure 6.1: A bracelet showing naturally coloured blue, cream, yellow, and silver akoya cultured pearls from Broken Bay Pearls.**

With *Pinctada imbricata fucata* populations readily available on New South Wales's Central Coast region between Sydney and the city of Lake Macquarie, a local enterprise called Broken Bay Pearls with expertise in farming of edible Sydney rock oysters (*Saccostrea glomerata*) has been culturing akoya



pearls since 2003 (Figure 6.2). The climate in New South Wales is ideally suited for pearl culturing using *Pinctada imbricata fucata*. It is located approximately the same distance from the equator as the southern Japanese pearl farms, and its very similar seasonal variations of water temperature optimize nacre quality during the cultivation process (Gilbert et al., 2017; Strack, 2006).



**Figure 6.2:** The map of Australia (A) indicates the location of the Broken Bay Pearls farm near Woy Woy in New South Wales, on the south-eastern shoreline (B). The akoya pearl farming operation near Woy Woy (C) and some of the long-line systems for juvenile *Pinctada imbricata fucata* that are held nearby (D). For scale, the wooden jetty shown in C and D is 1.5 metres wide.

Australia was originally known for its large-scale production of silver- and gold-coloured natural and cultured South Sea pearls from *Pinctada maxima* (Scarratt et al., 2012 and references therein), which are valued for their large sizes of up to 20 mm in diameter (Strack, 2006). Australian akoya cultured pearls have yet to receive comparable attention in the gemmological community. This study aims to characterize the occurrence of akoya cultured pearls in eastern Australia and presents what is believed to be the first thorough gemmological and mineralogical characterization through Raman, photoluminescence (PL), ultraviolet-visible (UV-Vis), and fouriertransform infrared (FTIR) spectroscopic analysis.

### 6.1.1 Hatchery and spat production

For about a decade, the hatchery facilities located at NSW Fisheries, Port Stephens Fisheries Institute (PSFI) have supplied Broken Bay Pearls with young *Pinctada imbricata fucata*. Broodstock are collected from both the farm and in the wild and selected based on nacre colour and shell shape. Priority

is given to stock with more convex shells, which allow for larger nuclei to be implanted during seeding. These parents are brought to the hatchery, where spawning is induced by increasing water temperatures by about 4°C. Eggs and sperm are mixed in 1,000-liter tanks. They are kept at 24–26°C until they develop into larvae (Figure 6.3a and 6.3b) after 20–24 hours; water temperature, feeding protocols, and stock density are regulated as needed (O'Connor et al., 2003). The larval cycle takes approximately three weeks before they are ready to settle from the water column and attach to a substrate such as mesh screens or bags.

After settlement, these spat are retained until reaching approximately 1.5 mm in size, whereupon they are transferred from the hatchery in Port Stephens to the pearl farm near Woy Woy (Figure 6.2). Here, they are placed in 0.5 mm mesh bags (Figure 6.3c) attached to several parallel long-line systems about 200 metres in length and situated at a depth of 4 meters below the low tide water level. As the juvenile *Pinctada imbricata fucata* bivalves grow, they are progressively transferred to larger mesh bags or cages that are cleaned regularly to ensure good water flow. Broken Bay Pearls is currently the only akoya pearl farm on the New South Wales coastline. Several small islands act as a barrier between the open ocean and the farm, creating a well-protected bay that is ideally suited for pearl farming. This area within the estuary provides stable salinity, nutrient availability, and high levels of dissolved oxygen, which are key factors for the long-term development and cultivation of a healthy stock.



**Figure 6.3:** Australian *Pinctada imbricata fucata* larvae, shown here at an age of about 25 hours (A) with approximately 200 µm shell size, are reared in 1,000-liter polyethylene tanks at the nursery (B). After 24 days, the larvae mature to spat with approximately 1.5 mm shell lengths. They are transferred to longline systems and kept in 0.5 mm nylon mesh bags (C).

#### 6.1.2 Seeding and maintaining of Australian akoya pearl oysters

The juvenile pearl oysters are maintained on the farm until they are approximately two years old with shell heights of about 7 cm. Similar to other farms, the molluscs are cleaned with high-pressure cleaners every two to four weeks (Gifford et al., 2004). It is common practice to condition the pearl oysters for several weeks before seeding by reducing their physiological fitness. At Broken Bay this is achieved by

stocking the molluscs at high density within barnacle- overgrown wicker baskets that restrict water flow and food availability. Other farms, such as those in Southeast Asia, cover the molluscs with fabric to achieve the same effect (Hänni, 2007). Either way, they respond to food shortage by ceasing gamete production that would otherwise interfere with the seeding process (Hänni, 2007). This conditioning strategy allows the seeders at Broken Bay Pearls to process the animals without having to apply relaxant drugs to immobilize them (Acosta-Salmón et al., 2005). The bivalves are seeded in the austral summer month of February using only shells of suitable size (shell height larger than 7 cm) and fitness. This ensures acceptance of the bead, fast recovery from surgery, and a greater chance for successful pearl growth. The production of cultured pearls requires two types of mollusc broodstock. Donor molluscs are selected for nacre colour and quality and are sacrificed in the seeding process to extract the mantle tissue graft that is later inserted with the bead. The host animals, on the other hand, are selected for fitness and health to enable optimal proliferation of the tissue graft into a nacre-producing pearl sac (Hänni, 2012). The two Australian seeders at Broken Bay Pearls were trained by Japanese specialists who also visit regularly during harvests. Each year they insert several thousand beads-exact numbers remain confidential-together with tissue grafts. Two beads are inserted per mollusc. Tissue grafts are prepared following the Japanese method. First, the outermost part of the mantle lobe is removed from the donor (Figure 6.4a) and the outer epithelial tissue is carefully separated from the darker marginal mantle tissue (Figure 6.4b). Then the outer epithelial tissue is cut into approximately  $2 \times 2$  mm pieces, known as the saibo or graft (Figure 6.4c). The gonad in the donor mollusc is opened (Figure 6.4d), and each tissue graft is carefully inserted into the mollusc together with a 6 mm bead manufactured from American freshwater mussel shells (Figure 6.4e). Graft and bead are carefully placed in contact with each other (Figure 6.4f). Since the gonad tissue itself is unable to produce pearls, the bead must be accompanied by the mantle tissue graft. Following the seeding process, the graft proliferates to form a pearl sac, fully enclosing the bead (Hänni, 2012) and producing calcium carbonate, causing the deposition of nacre onto the bead (Jacob et al., 2011). Hence, the relative position between tissue graft and bead as well as the position within the pearl sac determine the eventual shape of the pearl: In the ideal case, when tissue graft and bead are in tight contact, a round pearl is formed. Near-round, semi-baroque, or baroque pearls are formed by an irregular contact between bead and graft that results in cavities or even loose beads (Hänni, 2012; Otter et al., 2014).





**Figure 6.4:** These photos show the steps involved in the seeding of Australian akoya pearls. **A:** The outermost part of the mantle lobe is cut from a donor mollusc. **B:** The outer epithelial tissue is separated from the darker marginal mantle part using a scalpel. **C:** The outer epithelial tissue is cut into small, approximately  $2 \times 2$  mm tissue grafts (saibo). **D:** An incision is carefully made in the gonad, while the bivalve is affixed to an oyster stand. **E:** The 6 mm beads are manufactured from American freshwater mussel shells. **F:** Tissue and bead are inserted into the gonad.

### *6.1.3 Harvesting and general farming procedures of Australian akoya cultured pearls*














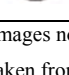
After seeding, the *Pinctada* bivalves are returned to the long-line systems in bags or cages, where their food supply is no longer restricted. Their metabolic activity increases, and the production of nacre needed for shell growth and pearl development returns to normal. Hence, the bulk of pearl growth occurs during the austral summer months (December to February), when the animals have an increased metabolism and food is abundant. In contrast, a finer and therefore more lustrous outermost layer of nacre is deposited in austral winter (June to August), when colder temperatures slow down metabolic and biomineralising processes (Gilbert et al., 2017). Bead rejection rates are approximately 10 %, which is relatively low compared to farms in the Federated States of Micronesia (28 %) or southwest India (14 %), while recent rejection rates from Japan were not available in the literature (Cartier et al., 2012; Kripa et al., 2007 and references therein). Broken Bay Pearls generally allows a longer cultivation time of 18 months to achieve a thicker nacre, compared to the standard 6–12 months in Japan (Strack, 2006). The longer cultivation time results in a nacre layer around the bead measuring approximately 0.8 mm, estimated from pearls used in this study (see bead sizes and diameter measurements in Table 6.1) as well as verification measurements on a cross section of a low-quality pearl. This is high compared to Japanese akoya, whose nacre thickness averages only 0.2 mm in the northern islands and rarely exceeds 0.3 mm in the warmer waters of the southern islands (Strack, 2006). The pearls are harvested in the austral winter months of June and July. Following the Japanese akoya culturing tradition, pearl oysters at Broken Bay Pearls are generally not seeded a second time but are removed from their cages (Figure 6.5a) and sacrificed by cutting through the adductor muscle. A motorized separator (Figure 6.5b) reduces the soft tissues to small pieces while the relatively heavy pearls collect at the bottom of the machine and are extracted by opening a valve (Figure 6.5c). Adhesive organic remains are removed by using a suspension of salt in freshwater (Figure 6.5d), while walnut shells are used to buff the pearls, a common practice in Japan. The pearls are spread out on cloth for air drying in sunlight (Figure 6.5e), which could be understood as a minimal maeshori<sup>1</sup> lustre enhancement, depending on how strictly this is defined. However, it is emphasized here that no colour- or lustre-improving substances or processes are otherwise applied-e.g., dyes, bleaches, or alcohol, which are traditionally used for Japanese akoya (Gervis and Sims, 1992). After drying, the pearls are graded for quality, colour, lustre, shape, and size.

---

<sup>1</sup>Maeshori treatment aims to enhance a pearl's luster. This can involve different chemical (e.g., alcohol or salty solutions) or physical (e.g., heating and cooling) treatments. It is traditionally applied to Japanese akoya cultured pearls, often in combination with dyes or bleaches.



**Table 6.1: Characteristics of natural-colour cultured pearls from *Pinctada imbricata fucata* bivalves from eastern Australia.**

Photo:	Sample ID:	Diameter [mm]:	Carat Weight:	Bodycolour:	Overtone:
	BBP01	7.3	3.01	Light yellow	Gold with slight green tinge
	BBP02	6.7	2.20	Light yellow	Gold
	BBP03	7.0	2.51	Dark-yellow	Greenish
	BBP04	6.9	2.48	Dark-yellow	Gold, Pink
	BBP05	6.9	2.50	Pink	Pink
	BBP06	7.5	3.03	Pink	Pink, green, brown
	BBP07	7.4	2.90	Silver	Blue
	BBP08	6.8	2.31	Silver cream	Rose to light pink
	BBP09	7.2	2.66	Silver white	Pink
	BBP10	7.0	2.49	White	Cream, light-blue
	BBP13	7.9	3.56	Silver-green	Brownish, pink
	BBP14	7.7 x 8.2	3.65	Silver-green	Cooler green
	BBP11	6.7	2.00	Dark-blue*	Silver (strong, almost metallic lustre)
	BBP12	7.2	2.48	Brownish blue	Pink to olive brown

Images not to scale. \*Colour was found to vary from dark-blue on one side and silver-blue on the other, however, all measurements were taken from the dark side.



**Figure 6.5:** The steps involved in the process of harvesting Australian akoya pearls. A: Bivalves are removed from their cages. B: The separator cleans the pearls from the tissues. C: Separated pearls are collected by opening a valve at the bottom of the machine. D: Wooden revolving drums are used to wash the pearls in a saltwater solution. E: A selection of the day's harvest with the range of colours displayed at the front.

The farm in Broken Bay produces several thousand pearls per year, and about 50 % are of gem quality. The average size ranges from 6.5 to 8 mm and in very rare cases up to 10 mm. Keshi pearls also occur as a result of the seeding process, as the fragile epithelial cells of the mantle tissue can be injured or separated and develop into small pearl sacs that produce an additional though unintended small pearl (Hänni, 2006). Broken Bay pearls are cultured in a wide range of colours. Bodycolours include the traditional akoya silver and white (Figure 6.6 and 6.7, respectively), though light and dark yellows appear almost as frequently, and blues are also occasionally seen (Figure 6.1). Intense orange bodycolours (as in BBP05 and BBP06, Table 6.1) occur very rarely. Overtones range from orange, pink,

silver, white, silvergreen, and cream through yellow to gold. The two seeders at Broken Bay have noticed a difference in the respective proportions of silver to white, yellow, and blue bodycolours they produced (Figure 6.8). After tracing back and comparing their individually seeded bivalves, which had been colour coded on their cages, the seeders concluded that while cutting and preparing the tissue grafts, they each favored slightly different coloured tissue pieces, thus influencing the harvested colours.



**Figure 6.6:** This silver pendant features a round 7.5 mm silver akoya pearl from Broken Bay. The silver disk is etched with a pattern resembling the reflection of the moon on the rippling ocean.

It is understood that modern pearl farming yields many positive consequences for the local ecosystem. The exceptionally high filtering capabilities of the *Pinctada* species, up to 25 liters per gram of dried tissue each day, effectively remove heavy metals, organic pollutants, and nutrient overloads from coastal environments (Gifford et al., 2004). Hence, pearl farming reduces turbidity and eutrophication-i.e., the excess supply of nutrients coupled with high biomass loads.



**Figure 6.7:** Naturally white cultured pearls from Broken Bay: two necklaces, a pair of stud earrings, and three loose pearls. Photo courtesy of Percy Marks Jewellers.



Turbidity is reduced by the long-line systems, with their many large cages that act as a barrier for nearsurface currents. Eutrophication is reduced by the high filter-feeding capacities of the bivalves. Furthermore, the timber-free long-line systems prevent entanglement of dolphins and other marine species. Following these environmentally friendly principles, Broken Bay Pearls has been successful in supplying a wide range of Australian wholesalers and jewellers each year.



**Figure 6.8:** Broken Bay’s two seeders tag their own cages of freshly seeded bivalves to track the proportions of bodycolours produced. The proportion of white, yellow, and blue bodycolours is seen to vary between the seeders, and this is attributed to slight variations in the selection of appropriate tissue graft. The red line shows the overall abundance of each bodycolour as an average of both seeders.

## 6.2 Materials and methods

The lead author attended Broken Bay’s annual pearl harvest in June 2016 to obtain pearls for this study. The molluscs were brought to the farm by boat and taken from the nets and opened by hand. After extraction from the separator, the pearls were spread out on a cloth and examined. The author visually determined a wide range of bodycolours, including yellow, silver, white, cream, orange, blue, and light silver-green of various shades and intensities (Figure 6.5e). A total of 14 saltwater cultured pearls were selected as representative of each bodycolour group for the present study. The pearls were found to be mostly round (samples BBP01 to BBP13) to semi-round (BBP14) in shape. They measured 6.7–8.2 mm in diameter with an average of 7.2 mm, while their weight varied from 2.0 to 3.7 ct (Table 6.1).

Raman spectra of each pearl were collected at room temperature using a Horiba Jobin Yvon LabRAM HR Evolution confocal spectrometer with 473 nm laser excitation. All Raman spectra were recorded in the 100–2000  $\text{cm}^{-1}$  range using a spectral acquisition time of 12 seconds and four accumulations. A grating with 1800 grooves/mm was used with a slit width of 100  $\mu\text{m}$  to ensure a high spectral resolution of approximately 0.8  $\text{cm}^{-1}$ . PL spectra were collected using the same instrument, although measurement conditions were adjusted to a spectral acquisition time of eight seconds and five accumulations per cycle,

with 532 nm excitation wavelength. Data were collected in the 537–710 nm range using a grating with 600 grooves/mm to achieve higher intensities at a spectral resolution of approximately 2 cm<sup>-1</sup>.

Mid-FTIR spectra were recorded with a Thermo Scientific Nicolet iN10 infrared microscope using a 149 × 149 μm aperture and an acquisition time of five seconds per spectrum. All data were collected with 16 scans per spectrum in the range of 675–3970 cm<sup>-1</sup> using a liquid-nitrogen-cooled MCT-A detector system and a spectral resolution of 4 cm<sup>-1</sup>. A background spectrum was collected in air before each sample spectrum. Raman, PL, and FTIR data were collected at Macquarie University's Department of Earth and Planetary Sciences in Sydney.

UV-Vis spectra were recorded 16 times per sample in the 380–800 nm range using a Leica Orthoplan microscope in combination with a Leica MPV-SP UV Vis spectrophotometer at Johannes Gutenberg University in Mainz, Germany. Microscope-based UV-Vis data acquisition is generally performed without the use of an integrated sphere accessory, which made it necessary to collect all spectra in specular reflection mode with well-defined incident and reflected light angles (2° in this study). Specular reflection mode uses a thin plate of polished aluminium as reference material, since it has higher reflectance properties than BaSO<sub>4</sub> or Spectralon, which are only used when data collection is performed in diffuse reflection mode. All spectra were collected using 32× magnification by focusing on the surface of each pearl. Some individual samples (namely BBP05, BBP07, BBP11, and BBP12) yielded reflectance values greater than 100 %, which made it necessary to focus slightly subsurface.

## 6.3 Results and discussion

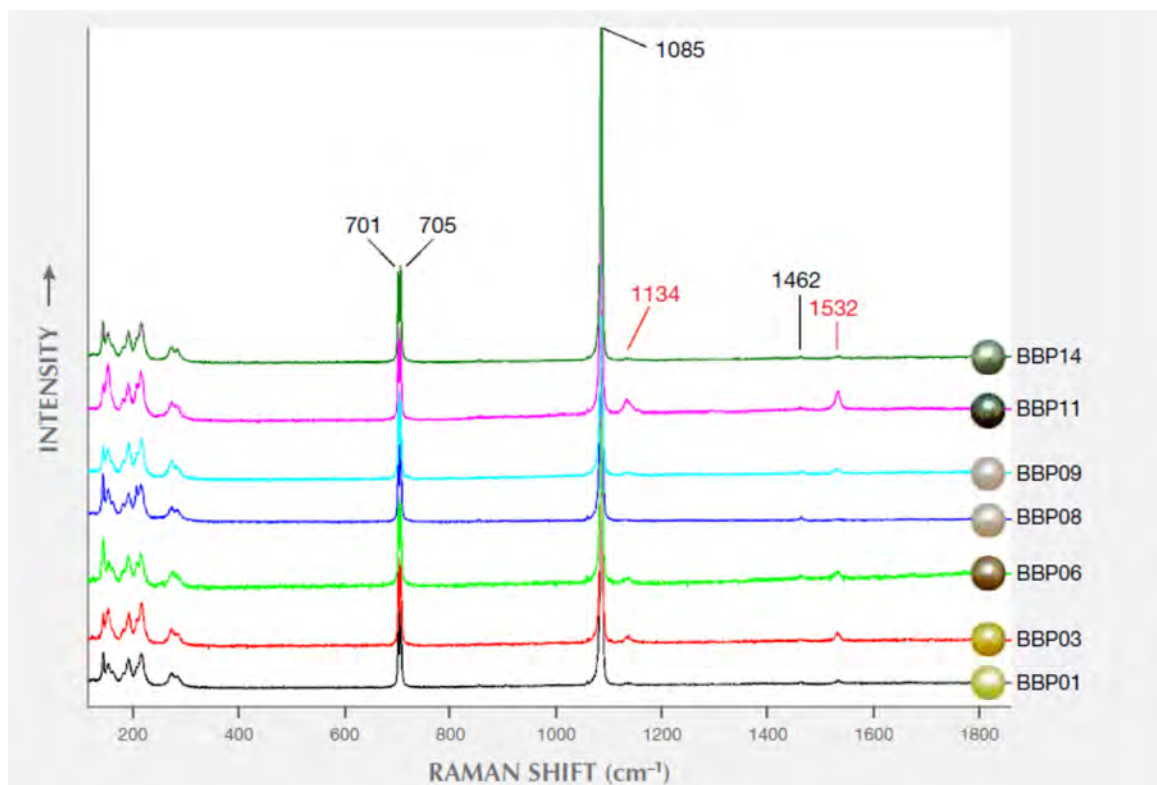
### 6.3.1 Raman spectrometry

Figure 6.9 presents seven representative Raman spectra of Australian akoya cultured pearls across the range of bodycolours as outlined in Table 6.1 (yellow, orange, silver, white, green, and blue). The most prominent peaks are assigned to aragonite (black lines), the crystalline calcium carbonate polymorph generally associated with lustrous pearls of the Pteriidae family (e.g., Hänni, 2012; Jacob et al., 2011; Wehrmeister et al., 2011). Among these, the highest intensity band was observed at 1085 cm<sup>-1</sup>, as well as a doublet with peak centres at 701 and 705 cm<sup>-1</sup>, which are assigned to  $\nu_1$  (symmetric stretching) and  $\nu_4$  (in-plane bending) modes of the carbonate anion (CO<sub>3</sub><sup>2-</sup>) in aragonite (e.g., Urmos et al., 1991). The small peak at 1462 cm<sup>-1</sup> is identified as  $\nu_3$  (in-plane asymmetric stretching); due to its low intensity, this peak is not observed equally well in all pearls. In addition, aragonite lattice modes were observed between 170 and 300 cm<sup>-1</sup> (Urmos et al., 1991). All pearls showed virtually identical peak centres, intensities, and backgrounds except for the darkest one (BBP11), which had a slightly increased background (Figure 6.9). This is due to a stronger contribution of luminescence in the background signal, possibly related to pigments contributing to the pearl's dark blue colour.

Peaks of weaker intensity (Figure 6.9, red lines) corresponded to distinct bands of pigments (polyenes) consistent with previously published values (Bersani and Lottici, 2010; Karampelas et al., 2007; Karampelas et al., 2009; Soldati et al., 2008). These include peaks at 1134 and 1532 cm<sup>-1</sup> that belong to



the stretching modes of the C-C single bond ( $\nu_2$ ) and C=C double bond ( $\nu_1$ ) in the polyene chain biomolecule, respectively. Samples with darker bodycolours such as dark blue (BBP11), orange (BBP06), and dark yellow (BBP03) displayed the highest intensities for both pigment-related peaks, while green (BBP14), white (BBP09), and light yellow and yellow (BBP01) pearls exhibited much lower intensities. For the white specimen BBP08, the peaks were undetectable.

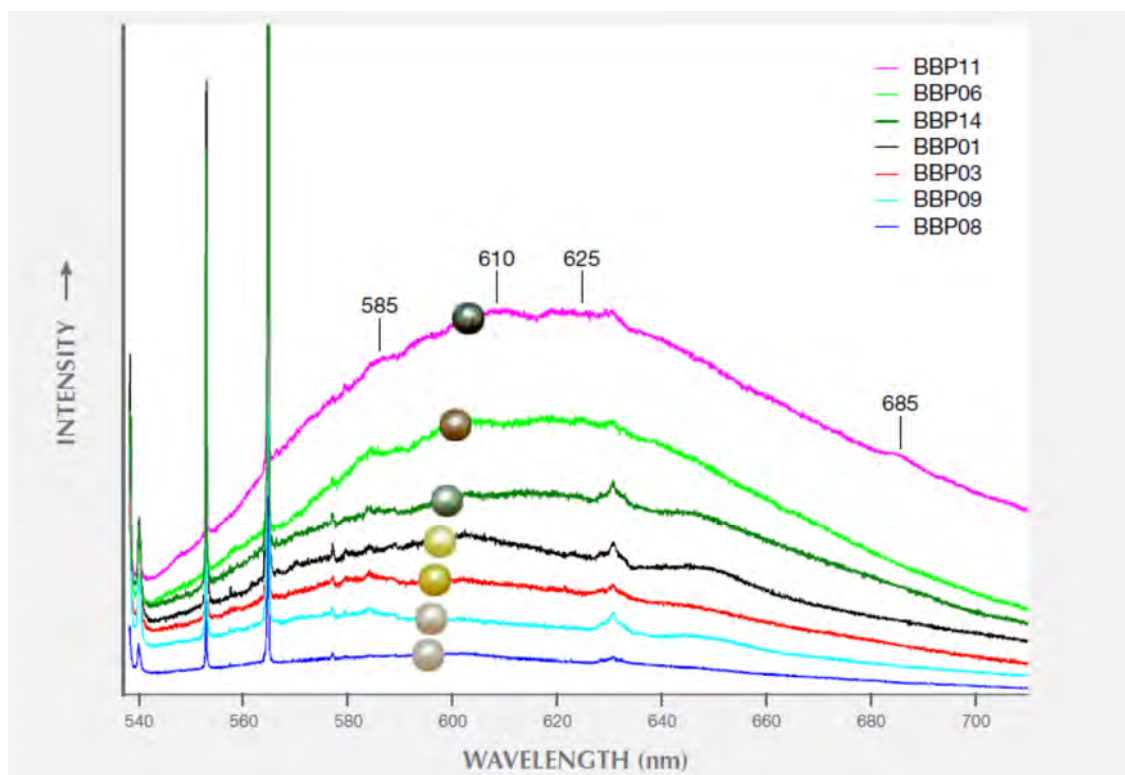


**Figure 6.9:** Raman spectra of seven Broken Bay akoya cultured pearls from *Pinctada imbricate fucata* normalized to the highest-intensity peak at  $1085\text{ cm}^{-1}$  and offset for clarity. The selection shows a cross section of bodycolours ranging from light yellow (BBP01, BBP03), orange (BBP06), white (BBP08), silver (BBP09), and dark blue (BBP11) to green (BBP14). The spectra show identical bands for aragonite (black lines), while two remaining peaks are attributed to pigments (red lines).

### 6.3.2 Photoluminescence spectrometry

All PL spectra showed virtually identical features in the yellow to red region at 585, 610, 625, and 685 nm (Figure 6.10). Sharp peaks in the spectra resulted from the Raman effect and occurred independently of the PL bands. These included features in the 538–540 nm region (vibrational properties of the aragonite lattice modes), as well as discrete peaks, caused by vibrational modes of the carbonate ion, at 552 nm (in-plane bending,  $\nu_4$ ), 565 nm (symmetric stretching,  $\nu_1$ ), 577 nm (in-plane asymmetric stretching,  $\nu_3$ ), and 630 nm (caused by  $\nu_1 + \nu_3$ ; Xu and Poduska, 2014). The four PL bands had positions similar to those previously published for cultured pearls from *Pinctada maxima*, *Pinctada margaritifera*, *Pinctada mazatlanica*, and *Pteria sterna*, at 620, 650, and 680 nm; however, the weak band at 585 nm has not been described for these species (Karampelas, 2012; Kiefert et al., 2004; Miyoshi et al., 1987). It should be noted that all bands appear less defined for the akoya pearls than for those produced by *Pinctada maxima*, *Pinctada margaritifera*, and *Pteria sterna*. PL features in pearls are generally thought to result from organic compounds within the nacre composite material (Karampelas et al., 2007). This

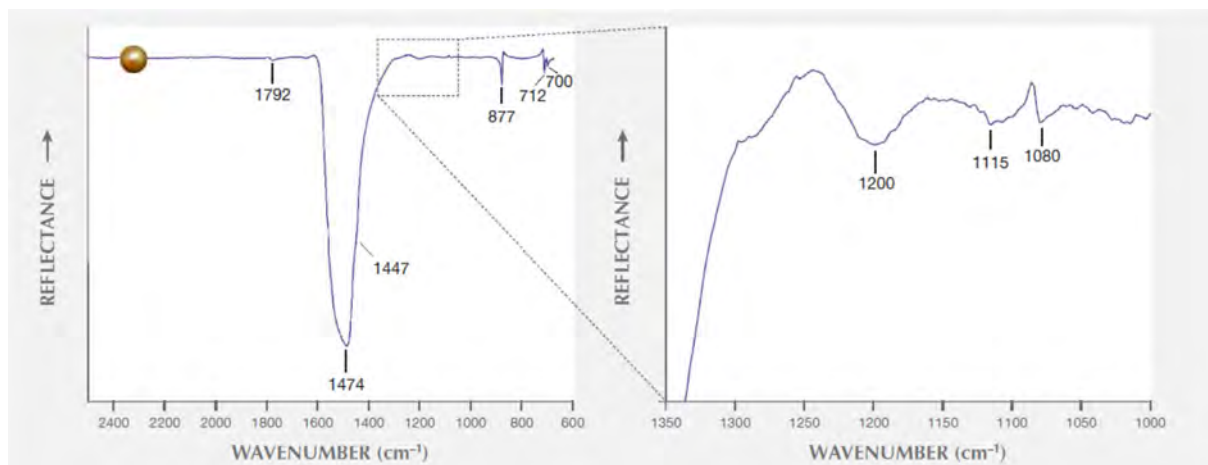
is consistent with our observation that the relative PL intensity correlated with colour intensity in the specimens and stronger pigment-related Raman bands (Figure 6.9).



**Figure 6.10:** Uncorrected photoluminescence (PL) spectra of the seven akoya cultured pearls whose Raman spectra are shown in Figure 6.9. Spectra are offset for clarity while maintaining their original order of relative PL intensities. All spectra show identical features at 585, 610, 625, and 685 nm, with varying amounts of luminescence that correlate with the colour intensity of the samples. Peaks in the 538–540 nm region as well as at 552, 565, 577, and 630 nm originate from the Raman effect of aragonite.

### 6.3.3 Mid-FTIR spectrometry

The most prominent features observed in the spectra of cultured pearls from Australian *Pinctada imbricata fucata* were caused by the intrinsic vibrational modes of the aragonite crystal lattice (Figure 6.11, left), namely  $\nu_{4b}$  and  $\nu_{4a}$  at 700 and 712  $\text{cm}^{-1}$  (internal modes),  $\nu_2$  at 877  $\text{cm}^{-1}$  (out-of-plane bending mode), and  $\nu_3$  at 1447  $\text{cm}^{-1}$  (in-plane asymmetric stretching). Strong absorption bands in the 1600–1400  $\text{cm}^{-1}$  range resulted from several closely spaced peaks at 1570, 1525, 1488, 1474, and 1440  $\text{cm}^{-1}$  (Andersen and Brecevic, 1991; Xu and Poduska, 2014). The highest-intensity band at 1474  $\text{cm}^{-1}$  was previously found to result from a combination of the lattice mode peaks at 220, 263, 290, and 700  $\text{cm}^{-1}$  (Andersen and Brecevic, 1991; Xu and Poduska, 2014). A weak band at 1792  $\text{cm}^{-1}$  was caused by a combination of the  $\nu_1$  and  $\nu_{4a}$  modes, while  $\nu_1$  (symmetric stretching vibration) was observed in Figure 6.11, right (an enlargement of the red box in Figure 6.11, left). Three other bands in Figure 6.11 (right) can be attributed to different organic compounds in nacre: Broad bands at around 1200 and 1115  $\text{cm}^{-1}$  likely resulted from S-O of sulfate and C-O of polysaccharide groups, respectively (Marxen et al., 1998). The peak at 1080  $\text{cm}^{-1}$  is assigned to the symmetric stretching vibration ( $\nu_1$ ) of  $\text{CO}_3^{2-}$ .

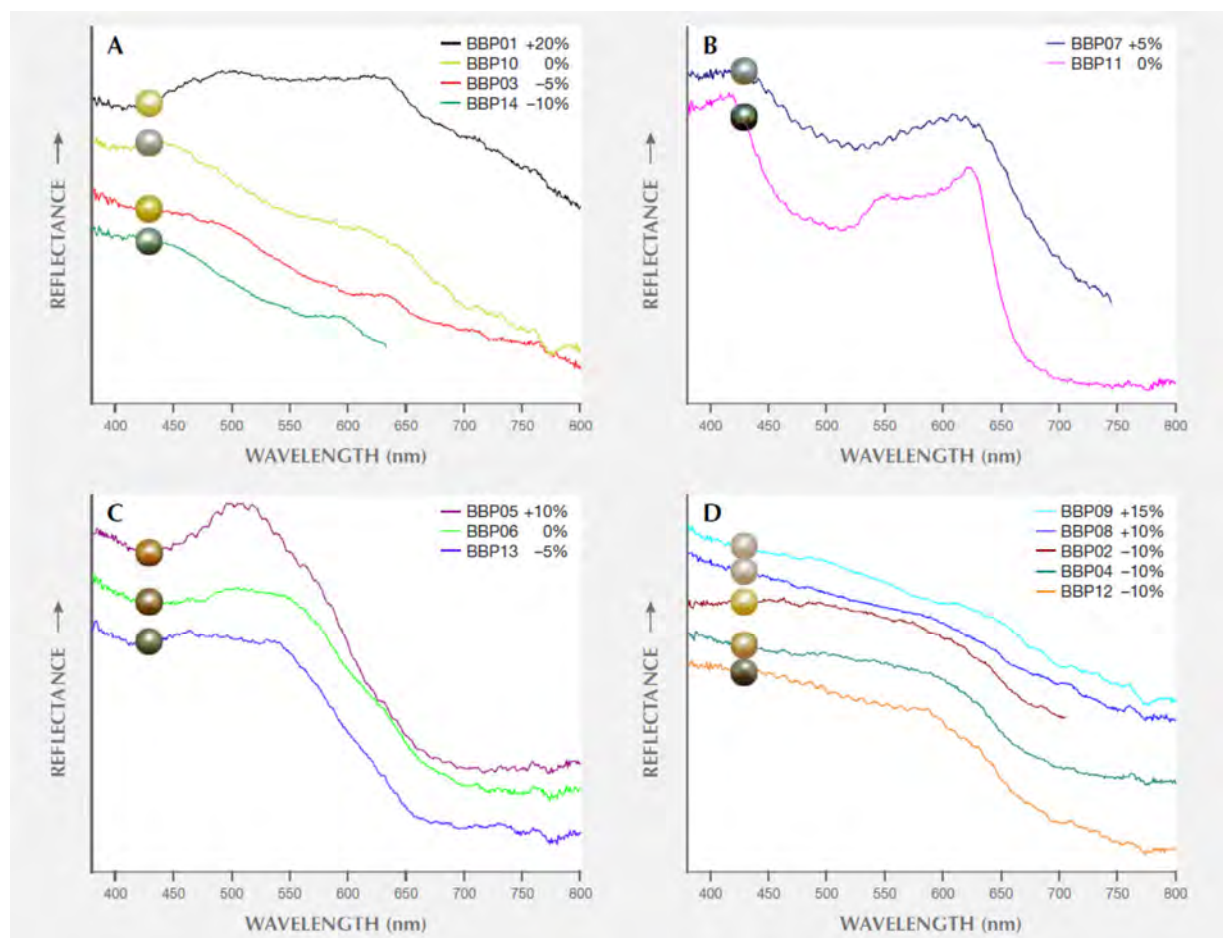


**Figure 6.11:** Left: The mid-FTIR spectrum of an orange sample from Broken Bay Pearls (BBP05) shows bands at 700, 712, 877, 1447, 1474, and 1792  $\text{cm}^{-1}$  that are characteristic for aragonite and were found in all other samples. However, this sample also shows several weak peaks in the 1000–1350  $\text{cm}^{-1}$  region (red box in A). Right: Enlargement of this region reveals several small peaks at around 1200 and 1115  $\text{cm}^{-1}$  that are assigned to sulfate and polysaccharide groups of the organic component. The weak band at 1080  $\text{cm}^{-1}$  results from stretching vibrations of the carbonate.

### 6.3.4 UV-Vis spectrometry

The pearls were grouped into different UV-Vis spectra with similar characteristics. For better readability, overlapping spectra were offset by adding or subtracting each measured intensity value with a fixed offset value expressed as a percentage relative to the original measured intensity (Figure 6.12). The specimens shown in Figure 6.12a consist of two pearls of a rather cooler shade of yellow, which might result from green hues and/or overtones (BBP01 and BBP03), plus silver (BBP10) and green (BBP14) samples. They are characterized by a slight spectral trough in the blue-green to yellow region between 450 and 600 nm (except for BBP01) and have a sharp drop in relative intensity from approximately 645 nm onward. The light-yellow specimen BBP01 (Table 6.1) has the brightest bodycolour, which correlates with the highest relative intensity. Of the two pearls in Figure 6.12b, one has a light silver bodycolour with a blue hue and overtone (BBP07) and the other a dark blue (BBP11) bodycolour with green, blue, and silver hues and overtones (hues and overtones determined by visual observation). The spectrum of the dark blue pearl (BBP11) shows two distinct troughs at 425–530 nm (blue to green region) and 550–625 nm (green to orange region), while the silver specimen (BBP07) has a trough at 425–625 nm. Both pearls display a sharp drop in reflectance at 625 nm. A lower intensity over the full spectral range is responsible for the dark colour of BBP11; specimen BBP07 shows a similar pattern, but at an overall higher relative intensity that corresponds to its brighter colour. Figure 6.12c shows spectra for the pearls with orange bodycolour (BBP05 and BBP06) as well as for a green specimen with warm pink and silver hues and overtones (BBP13). These specimens exhibit distinct absorption features between 400 and 475 nm and between 600 and 800 nm that correspond to the blue region and the orange to red region, respectively. At 800 nm, relative intensities drop to below 55 %. Lastly, Figure 6.12d shows spectra for pearls that exhibit white (BBP08 and BBP09), dark silver (BBP12), and yellow bodycolours (BBP02 and BBP04). Note that the pearls with yellow bodycolour from Figure 6.12d have orange and golden hues and overtones, while the other yellow specimens in

Figure 6.12a show green and yellow hues and overtones. Their spectra lack distinct absorption features and differ only in relative intensity.



**Figure 6.12: UV-Vis specular reflectance spectra of 14 Australian akoya samples normalized to the reflectance yield of a polished aluminum plate. Some spectra are offset for clarity, with offset values provided in the legends.**

Altogether, each pearl's bodycolour is strongly dependent on its specific absorption features and relative intensities, which are produced by different combinations of pigments present in the organic compound of the nacre (Karampelas et al., 2009; Karampelas, 2012; Soldati et al., 2008). The bodycolour was found to correlate with the overall relative intensity of the PL spectra (Figure 6.10), where the dark blue specimen (BBP11) exhibited the highest relative PL intensity, while the yellow, white, and silver samples had the lowest.

Although the pearls from this study show a wide variety of spectral features, they can be differentiated from untreated pearls of some other species: Grey, yellow, and black pearls from *Pinctada margaritifera* as well as grey, yellow, and green pearls from *Pinctada mazatlanica* show a distinct trough at 700 nm that is not present in any of the akoya pearls from this study. In those pearls, the feature is associated with the presence of pigments (Cartier et al., 2012; Elen, 2002; Miyoshi et al., 1987). Further, dark grey pearls from both *Pinctada margaritifera* and *Pinctada mazatlanica* show an absorption feature at 405 nm that is known to result from uroporphyrin pigments (Homkrajae, 2016 and references therein). Yellow pearls from *Pinctada maxima* show a broad trough from 310 to 510 nm, with individual absorption features centered at 360 and 430 nm. This distinguishes them from the *Pinctada imbricata*

*fucata* pearls from this study, which also show various absorption features at higher and lower wavelengths (Table 6.2). While discrimination between naturally coloured pearls across different saltwater species appears promising, naturally coloured white akoya pearls remain indistinguishable from untreated white pearls produced by other molluscs, due to the absence of characteristic spectral features. Also, the discrimination of naturally coloured akoya cultured pearls produced in eastern Australia from others of different geographic origin is considered beyond the capability of this method.

**Table 6.2: Summary of colour and corresponding absorption centres of untreated cultured pearls from *P. fucata*, *P. margaritifera*, and *P. maxima*.**

Bivalve species	Pearl bodycolour:	Absorption centres in specific range [nm]:				References
		380 - 450	450 - 550	550 - 650	650 - 800	
<i>P. fucata</i>	White	407	no	554, 585	775	This study
	Yellow (greenish)	407	no	554, 605	c.a.	
	Yellow (reddish)	no	478	no	c.a.	
	Silver/Crème	no	no	no	c.a.	
	Pink	428	no	no	718	
	Silver-Green	407, 428	no	554	718	
	Silver-Blue	no	513	no	c.a.	
	Dark-blue	no	510, 544	579	750	
<i>P. margaritifera</i>	White	no	no	no	no	Elen, 2002
	Grey	no	460, 495	no	700	Karampelas et al., 2012,
	Yellow	no	no	no	700	Elen, 2002
	Black	405	495	no	700	Elen, 2002
<i>P. maxima</i>	Yellow	no	495	no	no	Karampelas et al., 2012
	Grey	no	460, 495	no	no	

c.a. = continued absorption

## 6.4 Conclusion

We have presented a description and characterization of akoya cultured pearls from the Central Coast region of New South Wales in eastern Australia. Apart from the absence of bleaching or dyeing procedures, the pearls are cultured following the Japanese tradition. Their natural variety of bodycolours ranges from lighter and darker golden yellows to different shades and intensities of orange and blue to the classic silver and white. These colourful akoya pearls can be used to create modern, nature-inspired jewellery (Figure 6.1 and 6.6) as well as classic pieces (Figure 6.7).

Raman and FTIR spectroscopy verified the main mineral phase as aragonite (Figure 6.9 and 6.11), and pigment-related Raman bands were observed at 1135 and 1530  $\text{cm}^{-1}$ . These belong to stretching modes of the C-C single bond and C=C double bond of the polyene chain biomolecules. These peaks were found to have the highest intensities for samples with darker bodycolours, such as dark blue, orange, and yellow (Figure 6.9, red lines). The pearls showed four rather indistinct PL bands in the yellow to red region of the electromagnetic spectrum (Figure 6.10), which were similar to the band positions observed for *Pinctada maxima*, *Pinctada margaritifera*, *Pinctada mazatlanica*, and *Pteria sterna* bivalves (though not as prominent). FTIR spectroscopy of an intense orange pearl revealed the presence of sulfates and polysaccharides representative of organic compounds (Figure 6.11). Lastly, UV-Vis specular reflectance spectroscopy showed several absorption features in the visible range that result from the pearls' different bodycolours, hues, and overtones (Figure 6.12a–d). This technique was found



to be useful in discriminating between diverse colourful akoya pearls from this study and cultured pearls from *Pinctada margaritifera*, *Pinctada mazatlanica*, and *Pinctada maxima* bivalves (Table 6.2), while akoya pearls from other locations as well as white specimens from various species are likely not distinguishable.

## **Acknowledgements**

We gratefully acknowledge Ian and Rose Crisp as well as Peter Clift from Broken Bay Pearls Pty Ltd for the opportunity to visit their pearl farm during seeding and harvest season, and for providing all the pearls shown in this study and answering all our questions. Dr. Jennifer Rowland is kindly thanked for skilful editing of the final manuscript. We thank Ursula Wehrmeister, Dilmi Herath, Michael Förster, Christoph Lenz, and Matthew A. Kosnik for many enriching discussions. Dr. Wayne O'Connor, centre director for aquaculture at the Port Stephens Fisheries Centre, NSW Department of Primary Industries, is kindly acknowledged for insightful comments on an earlier draft. Furthermore, we thank Celeste Boonaerts from AngelRock Jewellers, Cameron Marks from Percy Marks Jewellers, and Wayne O'Connor for providing photographs. The lead author is supported by an Australian Government International Postgraduate Research Scholarship (IPRS). Mr. Agbaje is supported by a Macquarie University Research Excellence Scholarship, and Dr. Jacob is financially supported by the Australian Research Council via a Future Fellowship and a Discovery Grant. Lastly, we thank three anonymous reviewers for providing very constructive and valuable comments.

## 7. GENERAL CONCLUSIONS OF THE THESIS

### 7.1 Aspects of trace element incorporation and pulse Sr-labelling

This thesis set out to “Evaluate the feasibility and potential of pulse-chase labelling as a tool to further our understanding of growth dynamics in different bivalve ultrastructures” (see primary goal 1, 1.7 Motivation and aim of the thesis). This goal has been reached by clearly demonstrating that shells of *Katelysia rhytiphora* (Chapter 2), *Anadara trapezia* (Chapter 3), and *Mytilus galloprovincialis* (Chapter 4) could successfully be Sr-labelled. Moreover, a new non-invasive approach was developed for burrowing species that does not (I) significantly stress the bivalves, and (II) negatively interfere with biomineralisation processes. For both burrowing and non-burrowing species it is shown in this thesis that pulse Sr-labelled shell portions allow correlation of data from a wide range of analytical cutting-edge instruments such as FEG-SEM, EPMA, NanoSIMS, Micro-Raman, and Atom Probe Tomography (see Chapters 2, 3, and 4). Although ‘labelling’ methods have been around for many years providing visualisations of shell growth at much smaller spatial scales, this thesis is the first application of pulse Sr-labelling experiments on bivalves to observe architectural growth processes at the micro- to nano-scale in a rigorously time-resolved manner.

Primary goal 2 of this thesis was to achieve a “Better understanding of architectural growth processes and sub-micron growth dynamics of bivalve shells, through direct study and comparison studies with bryozoa skeletons”. This thesis shows that high resolution Sr-labelling experiments in conjunction with architectural observations provide more valuable information than studying the architecture alone, which I see as the actual novelty of this body of work.

The following new insights into the architectural growth processes and sub-micron growth dynamics of non-nacreous shells have been made:

- (1) The label is observed to grow evenly along the growth fronts in both *A. trapezia* and *K. rhytiphora*, thus, evenly cutting across all hierarchical units, demonstrating that units of all hierarchical structures grow simultaneously along this growth front (Chapter 2 and 3). However, perpendicular to the growth front growth rates are more variable.
- (2) Labelled shell layers comprise distinct brighter and darker sub-layers that may yield additional insights into the interplay between physiology and shell growth and may warrant more labelling experiments of shorter pulse duration in the future.
- (3) Areas at the start and end of the labelled shell layer appear to have a transition between unlabelled and labelled shell areas in both species. This may either suggest a larger volume of extrapallial fluid (if this exists) that slowly increases in Sr-concentrations via mixing, or this effect arises from sectioning effects across the hierarchical architectures.

(4) I show that Sr substitutes randomly for Ca in shell aragonite, thereby excluding the formation of a clustered Sr-carbonate phase that would have produced a significant peak position shift away from the  $\nu_1[\text{CO}_3]$  Raman band position at  $1084.8\text{ cm}^{-1}$  to that of strontianite ( $\text{SrCO}_3$ ) at  $1073\text{ cm}^{-1}$  – which was not observed.

(5) This thesis also shows that non-nacreous bivalve species (*A. trapezia* and *K. rhytiphora*) do not show an influence of Sr abundance on growth rate at constant temperatures. In addition, distribution coefficients  $D_{\text{Sr/Ca}}$  of labelled and unlabelled shell layers are virtually identical, namely: 0.15 for labelled *A. trapezia*, 0.15 for the labelled compound prismatic ultrastructure of *K. rhytiphora* shells, 0.14 for unlabelled *A. trapezia*, and 0.14 for the unlabelled compound prismatic ultrastructure of *K. rhytiphora* shells, 0.14 for the unlabelled crossed-acicular ultrastructure of *K. rhytiphora* shells. These values are all dramatically smaller than the  $D_{\text{Sr/Ca}}$  in synthetic aragonite of 1.19, suggesting that Sr is actively excluded during a potentially multi-step fractionation processes during biomineralisation. This implies that Sr incorporation is mainly controlled by the bivalve's physiology rather than specific temperature ranges or natural marine Sr-concentrations. These findings will have implications for real-world applications such as a better determination of pearl provenances.

## **7.2 Aspects of shell architecture and crystallographic orientations of marine calcifiers**

Apart from the many insights gained through pulse Sr-labelling, further insights into the investigated architectures are gained to further fulfil primary goal 2: The non-nacreous architectures of *K. rhytiphora*, namely the compound composite prismatic and the crossed-acicular ultrastructure have been investigated for the first time at high resolution in this thesis (Chapter 2). The compound composite prismatic architecture consists of a similar complex hierarchy (3 orders) as crossed-lamellar shells (4 orders in *A. trapezia*, Chapter 3). The crossed-acicular architecture appears less hierarchical in BSE images, however, SE images and EBSD maps suggest at least two hierarchical orders in which the acicular units are arranged into co-oriented bundles, which again are grouped to pseudo-prisms. These complex hierarchical architectures suggest strong biological control on biomineralisation and differ significantly from that of other marine calcifiers, such as the cheilostome bryozoan *A. latirostris* that has a less pronounced hierarchy, suggesting a lower degree of biological control over its calcification processes (Chapter 9). In addition, this thesis presents for the first time the total organic content of these two structures of 2.2 wt.% (compound composite prismatic) and 1.4 wt.% (crossed-acicular) which are intermediate between nacre and crossed-lamellar shells. A proportion of these organic phases are pigments that are well detectable in Raman and FTIR spectra of untreated nacreous pearls from *P. imbricata fucata*. They are derived from sulphate- and polysaccharide-associated groups (Chapter 6) and are, thus, similar to the spectra obtained from yellow-purple shells of *K. rhytiphora* (Chapter 2).

In keeping with general characteristics of mollusc shells, the smallest mineralized unit in the compound composite prismatic, crossed-lamellar, and crossed-acicular ultrastructures are nanogranules with sizes

of tens of nanometres. A prominent commonality of the studied bivalve shell ultrastructures are their high abundances of twinned grain boundaries, namely: 56 % crossed-acicular (Chapter 2), 55 % crossed-lamellar (Chapter 3), and 46 % compound composite prismatic (Chapter 2), that compare well with values derived from the taxonomically unrelated marine bryozoan *A. latirostris* (> 45 %, Chapter 9)).

Architectural investigations at the sub-nano scale using S/TEM (Chapter 3 and 8) and Atom Probe Tomography (Chapter 4) are in line with primary goal 3, which is to “Further our understanding regarding the role of sub-micron organic inclusions that are abundant in bivalve shells with different architectures”: (1) this thesis presents the first ever Atom Probe data of organic inclusion in nacre (Chapter 4). These organic-rich phases are shown to play a crucial role in the mechanical properties of the shell (see 7.3). (2) it is demonstrated that organic inclusions are oriented preferably along only the outer layers of higher order units for the compound composite prismatic and crossed-acicular ultrastructure of *K. rhytiphora*. For the crossed-lamellar ultrastructure of *A. trapezia*, similar inclusions with sizes mainly between 1 to 5 nm have been observed and follow the same pattern as in *K. rhytiphora* (Chapter 3). The distribution pattern of these non-nacreous shells differs from that of nacre that shows a reduction of organic inclusions along all outer rims of tablets (Younis et al., 2012a). This difference in inclusion distribution may likely result from differences in the biomineralisation processes between nacreous and non-nacreous shells. However, findings of this thesis suggest that organic inclusions are a common motif in non-nacreous shells as their sizes and distinct distribution patterns have only been observed previously in one earlier study (Agbaje et al., 2017b).

Secondary goal 4. of this thesis is to “Provide a basis for future pearl provenance investigations by applying the results from this thesis on shell growth processes”. Analysis of bivalve shell architectures allowed the study of untreated nacreous pearls in the case of Australian Akoya cultured pearls (Chapter 6) and pearls of unknown origin (Chapter 5). It is demonstrated that Australian akoya pearls are currently the only source of colourful akoya cultured pearls and highlight the organic pigment phases of the material that are not compromised through bleaching or dying. Moreover, UV-Vis-NIR spectroscopy shows potential to discriminate these pearls from some other pearl types. Another important method in determining a pearls origin is trace element characterisation as has been demonstrated by the case of pearls from unknown origin. Therefore, more research focussing on the trace element characteristics of Australian akoya cultured pearls is under way to work towards more rigorous provenance identification.

### **7.3 Aspects of mechanical properties of marine calcifiers**

Secondary goal 5 of this thesis was to “Compare mechanical properties of shells and other marine calcifiers”. This goal has been realised for nacre in Chapter 8 and for non-nacreous shells and bryozoa in Chapters 2, 3, and 9. Chapter 8 presents cutting-edge nanoindentation experiments performed in s TEM that are captured on movies in real time. Here it is demonstrated that the hierarchical architectural arrangements of bivalve shells namely organic membranes, crystallographically preferred orientations (i.e. texture), organic inclusions, and nanogranules explain excellently the higher toughness and resilience compared to its geological/synthetic counterparts. The mechanical properties of non-nacreous

shells and those of other marine calcifiers such as bryozoa are still at the stage of bulk characterizations, which need to be understood before these investigations can be taken to the nano-scale as achieved for nacre. This thesis contributes to our understanding of non-nacreous shells by presenting their Young's moduli in quantitative numbers and stereographic visualisation. The latter are explained in context of ultrastructure and shell geometry. From Chapter 2 it is understood that the strongly controlled crystallographic orientations within the non-nacreous bivalve shell ultrastructures of *K. rhytiphora* create a girdle-like quasi-isotropic planes perpendicular to the growth directions. In comparison, the Young's modulus of biimineralic cheilostome bryozoa *A. latirostris* differs significantly from bivalves, as the weaker mechanical direction is oriented perpendicularly to the colony's upper surface, which is speculated to facilitate this organism's strategy of clonal reproduction via fragmentation.

## 7.4 Future directions

Observations of shell growth processes at the micron scale can serve as a starting point for research that could take the architectural and geochemical investigations of non-nacreous shell architectures further into the nano-scale to investigate Sr-labelled shell areas at even higher resolution by means of S/TEM imaging.

The successful outcome of Sr pulse-labelling experiments of nacreous and non-nacreous shells presented in this thesis warrant also further developments of the experimental approach. I suggest taking the experimental approach one step further and to conduct two-stage pulse-chase labelling experiments using Sr alongside a second geochemical label that will only be incorporated into the organic constituents. This innovative approach would allow us to study both the growth dynamics of the mineral and organic phases and would, thus, provide *in situ* insights into the co-orientation of mineral and organic phases as well as a more in depth understanding of the shell growth sequence.

Further, this thesis presents the first analytical protocol for best practice APT data for nacre that allows for a correlative investigation of organic membranes and organic inclusions within the mineral phase by significantly reducing artefacts in the mass spectrum. As this method has now been successfully established, I aim to carry out further APT experiments to accurately compare aspects of Sr-incorporation at sub-nanometre resolution from inside the Sr-label and unlabelled shell areas. These results will be used in conjunction with NanoSIMS maps and together these methods can potentially shed light on growth processes in nacre by characterising Sr-labelled mineral bridge structures. As APT is sensitive for the element compositions of the mineral and the organic phase, this method may even refine the two-step formation process in nacre by looking at how individual nacre tablets were "filled" with Sr-enriched aragonite. Moreover, the composition, shape, size and distribution of organic inclusions can finally be investigated at high-resolution in both nacreous and non-nacreous shells. As the inclusions are distributed differently within these two architectures this may yield new insights into the shell formation processes at the nano-scale – which are yet unknown today.



Other aspects that require further investigation are investigations of Sr pulse labelled *P. imbricata fucata* shells that were labelled within this PhD project and still require more data collection and evaluation. *Pinctada* shells have complex growth scale patterns that can be better understood using the Sr-labelled shell areas. Also, growth dynamics of aragonitic nacre and calcitic prisms in *Mytilus* and *Pinctada* specimens will be further compared and investigated.

Lastly, more investigations of untreated cultured pearls are in progress with the aim to better understand the formation of non-bead cultured pearls, the development of circle structures on pearl surfaces and achieving better tools for provenance determination.

## REFERENCES

- Acosta-Salmón, H., Martínez-Fernández, E., Southgate, P.C., 2005. Use of relaxants to obtain saibo tissue from the blacklip pearl oyster (*Pinctada margaritifera*) and the Akoya pearl oyster (*Pinctada fucata*). *Aquaculture* 246 (1), 167–172.
- Addadi, L., Joester, D., Nudelman, F., Weiner, S., 2006. Mollusk shell formation: a source of new concepts for understanding biomineralization processes. *Chemistry—A European Journal* 12 (4), 980–987.
- Addadi, L., Moradian, J., Shay, E., Maroudas, N.G., Weiner, S., 1987. A chemical model for the cooperation of sulfates and carboxylates in calcite crystal nucleation: Relevance to biomineralization. *Proceedings of the National Academy of Sciences* 84 (9), 2732–2736.
- Addadi, L., Raz, S., Weiner, S., 2003. Taking advantage of disorder: Amorphous calcium carbonate and its roles in biomineralization. *Advanced Materials* 15 (12), 959–970.
- Agbaje, O.B.A., Shir, I.B., Zax, D.B., Schmidt, A., Jacob, D.E., 2018. Biomacromolecules within bivalve shells: Is chitin abundant? *Acta Biomaterialia* (80), 176–187.
- Agbaje, O.B.A., Thomas, D.E., McInerney, B.V., Molloy, M.P., Jacob, D.E., 2017a. Organic macromolecules in shells of *Arctica islandica*: Comparison with nacreoprismatic bivalve shells. *Marine Biology* 164 (208), 1–13.
- Agbaje, O.B.A., Wirth, R., Morales, L.F.G., Shirai, K., Kosnik, M., Watanabe, T., Jacob, D.E., 2017b. Architecture of crossed-lamellar bivalve shells: The southern giant clam (*Tridacna derasa*, Röding, 1798). *Royal Society Open Science* 4 (9), 1–15.
- Akamatsu, S., Zansheng, L.T., Moses, T.M., Scarratt, K., 2001. The current status of Chinese freshwater cultured pearls. *Gems & Gemology* 37 (2), 96–113.
- Alia, J.M., Mera, Y.D. de, Edwards, H.G.M., Martín, P.G., Andres, S.L., 1997. FT-Raman and infrared spectroscopic study of aragonite-strontianite ( $\text{CaSr}_{1-x}\text{CO}_3$ ) solid solution. *Spectrochimica Acta Part A: Molecular and Biomolecular Spectroscopy* 53 (13), 2347–2362.
- Allison, N., Cohen, I., Finch, A.A., Erez, J., 2011. Controls on Sr/Ca and Mg/Ca in scleractinian corals: The effects of Ca-ATPase and transcellular Ca channels on skeletal chemistry. *Geochimica et Cosmochimica Acta* 75 (21), 6350–6360.
- Almagro, I., Drzymala, P., Berent, K., Sainz-Díaz, C.I., Willinger, M.G., Bonarski, J., Checa, A.G., 2016. New crystallographic relationships in biogenic aragonite: The crossed-lamellar microstructures of mollusks. *Crystal Growth & Design* 16 (4), 2083–2093.
- Andersen, F.A., Brecevic, L., 1991. Infrared spectra of amorphous and crystalline calcium carbonate. *Acta Chemica Scandinavica* 45 (10), 1018–1024.
- Auzoux-Bordenave, S., Badou, A., Gaume, B., Berland, S., Helléouet, M.-N., Milet, C., Huchette, S., 2010. Ultrastructure, chemistry and mineralogy of the growing shell of the European abalone *Haliotis tuberculata*. *Journal of Structural Biology* 171 (3), 277–290.
- Azzoug, M., Carré, M., Schauer, A.J., 2012. Reconstructing the duration of the West African Monsoon season from growth patterns and isotopic signals of shells of *Anadara senilis* (Saloum Delta, Senegal). *Palaeogeography, Palaeoclimatology, Palaeoecology* 346–347, 145–152.
- Babinsky, K., Kloe, R. de, Clemens, H., Primig, S., 2014. A novel approach for site-specific atom probe specimen preparation by focused ion beam and transmission electron backscatter diffraction. *Ultramicroscopy* 144, 9–18.

- Bachmann, F., Hielscher, R., Jupp, P.E., Pantleon, W., Schaeben, H., Wegert, E., 2010. Inferential statistics of electron backscatter diffraction data from within individual crystalline grains. *Journal of Applied Crystallography* 43 (6), 1338–1355.
- Bailey, T.R., Lear, C.H., 2006. Testing the effect of carbonate saturation on the Sr/Ca of biogenic aragonite: A case study from the River Ehen, Cumbria, UK. *Geochemistry, Geophysics, Geosystems* 7 (3), 1–6.
- Bandel, K., 1977. Die Herausbildung der Schraubenschicht der Pteropoden. *Biom mineralisation* 9, 73–85.
- Barthelat, F., Espinosa, H.D., 2007. An experimental investigation of deformation and fracture of nacre–mother of pearl. *Experimental mechanics* 47 (3), 311–324.
- Barthelat, F., Li, C.-M., Comi, C., Espinosa, H.D., 2006. Mechanical properties of nacre constituents and their impact on mechanical performance. *Journal of Materials Research* 21 (8), 1977–1986.
- Barthelat, F., Tang, H., Zavattieri, P.D., Li, C.-M., Espinosa, H.D., 2007. On the mechanics of mother-of-pearl: A key feature in the material hierarchical structure. *Journal of the Mechanics and Physics of Solids* 55 (2), 306–337.
- Beesley, P.L., Ross, G.J.B., Wells, A., 1998. *Mollusca: The southern synthesis*. CSIRO, 1250 pp.
- Belcher, A.M., Wu, X.H., Christensen, R.J., Hansma, P.K., Stucky, G.D., Morse, D.E., 1996. Control of crystal phase switching and orientation by soluble mollusc-shell proteins. *Nature* 381 (6577), 56–58.
- Benedix, G., Jacob, D.E., Taylor, P.D., 2014. Bimineralic bryozoan skeletons: A comparison of three modern genera. *Facies* 60 (2), 389–403.
- Beniash, E., Addadi, L., Weiner, S., 1999. Cellular control over spicule formation in sea urchin embryos: A structural approach. *Journal of Structural Biology* 125 (1), 50–62.
- Bergström, L., Sturm, E.V., Salazar-Alvarez, G., Cölfen, H., 2015. Mesocrystals in biominerals and colloidal arrays. *Accounts of chemical research* 48 (5), 1391–1402.
- Bers, A.V., D'Souza, F., Klijnsma, J.W., Willemsen, P.R., Wahl, M., 2006. Chemical defence in mussels: Antifouling effect of crude extracts of the periostracum of the blue mussel *Mytilus edulis*. *Biofouling* 22 (4), 251–259.
- Bersani, D., Lottici, P.P., 2010. Applications of Raman spectroscopy to gemology. *Analytical and bioanalytical chemistry* 397 (7), 2631–2646.
- Bevelander, G., Nakahara, H., 1969. An electron microscope study of the formation of the nacreous layer in the shell of certain bivalve molluscs. *Calcified Tissue Research* 3 (1), 84–92.
- Bhowmick, S., Espinosa, H., Jungjohann, K., Pardo, T., Pierron, O., 2019. Advanced microelectromechanical systems-based nanomechanical testing: Beyond stress and strain measurements. *MRS Bulletin* 44 (6), 487–493.
- Bischoff, W.D., Sharma, S.K., MacKenzie, F.T., 1985. Carbonate ion disorder in synthetic and biogenic magnesian calcites: A Raman spectral study. *American Mineralogist* 70 (5-6), 581–589.
- Blank, S., Arnoldi, M., Khoshnavaz, S., Treccani, L., Kuntz, M., Mann, K., Grathwohl, G., Fritz, M., 2003. The nacre protein perlucin nucleates growth of calcium carbonate crystals. *Journal of Microscopy* 212 (3), 280–291.
- Bock, P.E., Gordon, D.P., 2013. Phylum Bryozoa Ehrenberg, 1831. *Zootaxa* 3703 (1), 67–74.
- Boggild, O.B., 1930. The shell structure of the mollusks. *Det Kongelige Danske Videnskabernes Selskabs Skrifter, Natruvidenskabelig og Mathematisk, Afdeling, Ser. 9* 2, 231–326.
- Böhm, C.F., Demmert, B., Harris, J., Fey, T., Marin, F., Wolf, S.E., 2016. Structural commonalities and deviations in the hierarchical organization of crossed-lamellar shells: A case study on the shell of the bivalve *Glycymeris glycymeris*. *Journal of Materials Research* 31 (5), 536–546.

- Borowitzka, M.A., 1982. Morphological and cytological aspects of algal calcification. *International Review of Cytology* 74, 127–162.
- Bourrat, X., Francke, L., Lopez, E., Rousseau, M., Stempflé, P., Angellier, M., Albéric, P., 2007. Nacre biocrystal thermal behaviour. *CrystEngComm* 9 (12), 1205–1208.
- Brahmi, C., Domart-Coulon, I., Rougée, L., Pyle, D.G., Stolarski, J., Mahoney, J.J., Richmond, R.H., Ostrander, G.K., Meibom, A., 2012. Pulsed  $^{86}\text{Sr}$ -labeling and NanoSIMS imaging to study coral biomineralization at ultra-structural length scales. *Coral Reefs* 31 (3), 741–752.
- Branson, O., Bonnin, E.A., Perea, D.E., Spero, H.J., Zhu, Z., Winters, M., Hönlisch, B., Russell, A.D., Fehrenbacher, J.S., Gagnon, A.C., 2016. Nanometer-scale chemistry of a calcite biomineralization template: Implications for skeletal composition and nucleation. *Proceedings of the National Academy of Sciences* 113 (46), 12934–12939.
- Brockwell, S., Marwick, B., Bourke, P., Faulkner, P., Willan, R., 2016. Late Holocene Climate Change And Human Behavioural Variability In The Coastal Wet-Dry Tropics Of Northern Australia: Evidence from a pilot study of oxygen isotopes in marine bivalve shells from archaeological sites. *Australian Archaeology* 76 (1), 21–33.
- Buchardt, B., Fritz, P., 1978. Strontium uptake in shell aragonite from the freshwater gastropod *Limnaea stagnalis*. *Science* 199 (4326), 291–292.
- Bunge, H.-J., 2013. *Texture analysis in materials science: Mathematical methods*. Elsevier, 614 pp.
- Cann, J.H., Deckker, P. de, Murray-Wallace, C.V., 1991. Coastal aboriginal shell middens and their palaeoenvironmental significance, Robe Range, South Australia. *Transactions of the Royal Society of South Australia* 115 (4), 161–175.
- Canu, F., Bassler, R.S., 1927. *Classification of the cheilostomatous Bryozoa*, 44 pp.
- Carré, M., Bentaleb, I., Blamart, D., Ogle, N., Cardenas, F., Zevallos, S., Kalin, R.M., Ortlieb, L., Fontugne, M., 2005. Stable isotopes and sclerochronology of the bivalve *Mesodesma donacium*: Potential application to Peruvian paleoceanographic reconstructions. *Palaeogeography, Palaeoclimatology, Palaeoecology* 228 (1-2), 4–25.
- Carré, M., Bentaleb, I., Bruguier, O., Ordinola, E., Barrett, N.T., Fontugne, M., 2006. Calcification rate influence on trace element concentrations in aragonitic bivalve shells: Evidences and mechanisms. *Geochimica et Cosmochimica Acta* 70 (19), 4906–4920.
- Carter, J.G., 1989. *Skeletal biomineralization: patterns, processes and evolutionary trends*. American Geophysical Union, 700 pp.
- Carteret, C., La Pierre, M. de, Dossot, M., Pascale, F., Erba, A., Dovesi, R., 2013. The vibrational spectrum of  $\text{CaCO}_3$  aragonite: A combined experimental and quantum-mechanical investigation. *The Journal of Chemical Physics* 138 (014201), 1–12.
- Cartier, L.E., Krzemnicki, M.S., Ito, M., 2012. Cultured pearl farming and production in the Federated States of Micronesia. *Gems & Gemology* 48 (2), 108–122.
- Cartwright, J.H.E., Checa, A.G., 2007. The dynamics of nacre self-assembly. *Journal of The Royal Society Interface* 4 (14), 491–504.
- Chateigner, D., Hedegaard, C., Wenk, H.-R., 2000. Mollusc shell microstructures and crystallographic textures. *Journal of Structural Geology* 22 (11-12), 1723–1735.
- Checa, A., 2000. A new model for periostracum and shell formation in Unionidae (Bivalvia, Mollusca). *Tissue and Cell* 32 (5), 405–416.

- Checa, A.G., Cartwright, J.H.E., Willinger, M.-G., 2011. Mineral bridges in nacre. *Journal of Structural Biology* 176 (3), 330–339.
- Checa, A.G., Mutvei, H., Osuna-Mascaró, A.J., Bonarski, J.T., Faryna, M., Berent, K., Pina, C.M., Rousseau, M., Macías-Sánchez, E., 2013. Crystallographic control on the substructure of nacre tablets. *Journal of Structural Biology* 183 (3), 368–376.
- Checa, A.G., Okamoto, T., Ramírez, J., 2006. Organization pattern of nacre in Pteriidae (Bivalvia: Mollusca) explained by crystal competition. *Proceedings of the Royal Society of London B: Biological Sciences* 273 (1592), 1329–1337.
- Checa, A.G., Ramírez-Rico, J., González-Segura, A., Sánchez-Navas, A., 2009. Nacre and false nacre (foliated aragonite) in extant monoplacophorans (= Tryblidiida: Mollusca). *Naturwissenschaften* 96 (1), 111–122.
- Checa, A.G., Rodríguez-Navarro, A.B., Esteban-Delgado, F.J., 2005. The nature and formation of calcitic columnar prismatic shell layers in pteriomorphian bivalves. *Biomaterials* 26 (32), 6404–6414.
- Cheetham, A.H., Rucker, J.B., Carver, R.E., 1969. Wall structure and mineralogy of the cheilostome bryozoan *Metrarabdotos*. *Journal of Paleontology* 43 (1), 129–135.
- Chen, C.-C., Lin, C.-C., Liu, L.-G., Sinogeikin, S.V., Bass, J.D., 2001. Elasticity of single-crystal calcite and rhodochrosite by Brillouin spectroscopy. *American Mineralogist* 86 (11-12), 1525–1529.
- Cölfen, H., 2008. Single crystals with complex form via amorphous precursors. *Angewandte Chemie International Edition* 47 (13), 2351–2353.
- Cölfen, H., Mann, S., 2003. Higher-order organization by mesoscale self-assembly and transformation of hybrid nanostructures. *Angewandte Chemie International Edition* 42 (21), 2350–2365.
- Cook, P.L., Chimonides, P.J., 1983. A short history of the lunulite Bryozoa. *Bulletin of Marine Science* 33 (3), 566–581.
- Cook, P.L., Chimonides, P.J., 1994. Notes on the genus *Anoteropora* (Bryozoa, Cheilostatida). *Zoologica Scripta* 23 (1), 51–59.
- Crenshaw, M.A., Ristedt, H., 1976. The histochemical localization of reactive groups in septal nacre from *Nautilus pompilius* L. *The Mechanisms of Mineralization in the Invertebrates and Plants* 5, 355–367.
- Cueva, P., Hovden, R., Mundy, J.A., Xin, H.L., Muller, D.A., 2012. Data processing for atomic resolution electron energy loss spectroscopy. *Microscopy and Microanalysis* 18 (4), 667–675.
- Cuif, J.-P., Dauphin, Y., Howard, L., Nouet, J., Rouzière, S., Salomé, M., 2011. Is the pearl layer a reversed shell? A re-examination of the theory of pearl formation through physical characterizations of pearl and shell developmental stages in *Pinctada margaritifera*. *Aquatic Living Resources* 24 (4), 411–424.
- Cuif, J.-P., Dauphin, Y., Sorauf, J.E., 2010. *Biomaterials and fossils through time*. Cambridge University Press, 503 pp.
- Currey, J.D., 1977. Mechanical properties of mother of pearl in tension. *Proceedings of the Royal Society London* 196 (1125), 443–463.
- Currey, J.D., Kohn, A.J., 1976. Fracture in the crossed-lamellar structure of *Conus* shells. *Journal of Materials Science* 11 (9), 1615–1623.
- Currey, J.D., Taylor, J.D., 1974. The mechanical behaviour of some molluscan hard tissues. *Journal of Zoology* 173 (3), 395–406.
- Cusack, M., Parkinson, D., Freer, A., Perez-Huerta, A., Fallick, A.E., Curry, G.B., 2008. Oxygen isotope composition in *Modiolus modiolus* aragonite in the context of biological and crystallographic control. *Journal of Mineral Science* 72 (2), 569–577.



- Dauphin, Y., 2001. Nanostructures de la nacre des tests de céphalopodes actuels. *Paläontologische Zeitschrift* 75 (1), 113–122.
- Dauphin, Y., Brunelle, A., Medjoubi, K., Somogyi, A., Cuif, J.-P., 2018. The Prismatic Layer of Pinna: A Showcase of Methodological Problems and Preconceived Hypotheses. *Minerals* 8 (365), 1–19.
- Dauphin, Y., Cuif, J.-P., Massard, P., 2006. Persistent organic components in heated coral aragonitic skeletons—implications for palaeoenvironmental reconstructions. *Chemical Geology* 231 (1-2), 26–37.
- Dauphin, Y., Denis, A., 2000. Structure and composition of the aragonitic crossed lamellar layers in six species of Bivalvia and Gastropoda. *Comparative Biochemistry and Physiology Part A: Molecular & Integrative Physiology* 126 (3), 367–377.
- Dauphin, Y., Zolotoyabko, E., Berner, A., Lakin, E., Rollion-Bard, C., Cuif, J.P., Fratzl, P., 2019. Breaking the long-standing morphological paradigm: Individual prisms in the pearl oyster shell grow perpendicular to the c-axis of calcite. *Journal of Structural Biology* 205 (2), 121–132.
- De Villiers, J.P.R., 1971. The Crystal Structures of Aragonite, Strontianite, and Witherite. *American Mineralogist* 56 (5-6), 758–767.
- De Yoreo, J.J., Gilbert, P.U.P.A., Sommerdijk, N.A., Penn, R.L., Whitlam, S., Joester, D., Zhang, H., Rimer, J.D., Navrotsky, A., Banfield, J.F., 2015. Crystallization by particle attachment in synthetic, biogenic, and geologic environments. *Science* 349 (6247), 1-9.
- De Yoreo, J.J., Vekilov, P.G., 2003. Principles of crystal nucleation and growth. *Reviews in Mineralogy and Geochemistry* 54 (1), 57–93.
- Dimasi, E., Sarikaya, M., 2004. Synchrotron X-ray microbeam diffraction from abalone shell. *Journal of Materials Research* 19 (5), 1471–1476.
- Dodd, J.R., 1965. Environmental control of strontium and magnesium in *Mytilus*. *Geochimica et Cosmochimica Acta* 29 (5), 385–398.
- Domart-Coulon, I., Stolarski, J., Brahmi, C., Gutner-Hoch, E., Janiszewska, K., Shemesh, A., Meibom, A., 2014. Simultaneous extension of both basic microstructural components in scleractinian coral skeleton during night and daytime, visualized by in situ <sup>86</sup>Sr pulse labeling. *Journal of Structural Biology* 185 (1), 79–88.
- Durrant, H.M.S., Clark, G.F., Dworjanyn, S.A., Byrne, M., Johnston, E.L., 2013. Seasonal variation in the effects of ocean warming and acidification on a native bryozoan, *Celleporaria nodulosa*. *Marine Biology* 160 (8), 1903–1911.
- Eder, K., Otter, L.M., Yang, L., Jacob, D.E., Cairney, J.M., 2019. Overcoming Challenges Associated with the Analysis of Nacre by Atom Probe Tomography. *Geostandards and Geoanalytical Research* 43 (3), 385–395.
- Edgar, G.J., 2000. Australian marine life: The plants and animals of temperate waters, Rev. ed. ed. Reed New Holland, Frenchs Forest, N.S.W., London, 544 pp.
- Edwards, T., Yu, S., Dodson, P., 2018. Lustre: Pearling & Australia. Western Australian Museum, Welshpool DC, W.A., 127 pp.
- Egerton, R.F., 2011. Electron energy-loss spectroscopy in the electron microscope. Springer Science & Business Media, 491 pp.
- Elen, S., 2002. Identification of yellow cultured pearls from the black-lipped oyster *Pinctada margaritifera*. *Gems & Gemology* 38, 66–72.
- Epstein, S., Buchsbaum, R., Lowenstam, H., Urey, H.C., 1951. Carbonate-water isotopic temperature scale. *Geological Society of America Bulletin* 62 (4), 417–426.

- Espinosa, H.D., Juster, A.L., Latourte, F.J., Loh, O.Y., Gregoire, D., Zavattieri, P.D., 2011. Tablet-level origin of toughening in abalone shells and translation to synthetic composite materials. *Nature Communications* 2 (173), 1–9.
- Espinosa, H.D., Prorok, B.C., Peng, B., 2004. Plasticity size effects in free-standing submicron polycrystalline FCC films subjected to pure tension. *Journal of the Mechanics and Physics of Solids* 52 (3), 667–689.
- Espinosa, H.D., Rim, J.E., Barthelat, F., Buehler, M.J., 2009. Merger of structure and material in nacre and bone—Perspectives on de novo biomimetic materials. *Progress in Materials Science* 54 (8), 1059–1100.
- Evans, A.G., Charles, E.A., 1976. Fracture toughness determinations by indentation. *Journal of the American Ceramic Society* 59 (7-8), 371–372.
- Evans, A.G., Suo, Z., Wang, R.Z., Aksay, I.A., He, M.Y., Hutchinson, J.W., 2001. Model for the robust mechanical behavior of nacre. *Journal of Materials Research* 16 (9), 2475–2484.
- Evans, J.W., 1972. Tidal growth increments in the cockle *Clinocardium nuttalli*. *Science* 176 (4033), 416–417.
- Falini, G., Albeck, S., Weiner, S., Addadi, L., 1996. Control of aragonite or calcite polymorphism by mollusk shell macromolecules. *Science* 271 (5245), 67–69.
- Fantner, G.E., Hassenkam, T., Kindt, J.H., Weaver, J.C., Birkedal, H., Pechenik, L., Cutroni, J.A., Cidade, G.A.G., Stucky, G.D., Morse, D.E., 2005. Sacrificial bonds and hidden length dissipate energy as mineralized fibrils separate during bone fracture. *Nature Materials* 4 (8), 612–616.
- Fischer, A.M., Wei, Y.O., Ponce, F.A., Moseley, M., Gunning, B., Doolittle, W.A., 2013. Highly luminescent, high-indium-content InGaN film with uniform composition and full misfit-strain relaxation. *Applied Physics Letters* 103 (131101), 1–4.
- Fitzer, S.C., Zhu, W., Tanner, K.E., Phoenix, V.R., Kamenos, N.A., Cusack, M., 2015. Ocean acidification alters the material properties of *Mytilus edulis* shells. *Journal of The Royal Society Interface* 12 (103), 1–8.
- Forsythe, G.T.W., Scourse, J.D., Harris, I., Richardson, C.A., Jones, P., Briffa, K., Heinemeier, J. (Eds.), 2003. Towards an absolute chronology for the marine environment: The development of a 1000-year record from *Arctica islandica*.
- Foster, L.C., Allison, N., Finch, A.A., Andersson, C., 2009. Strontium distribution in the shell of the aragonite bivalve *Arctica islandica*. *Geochemistry, Geophysics, Geosystems* 10 (3), 1–14.
- Frankel, R.B., Bazylnski, D.A., 2003. Biologically induced mineralization by bacteria. *Reviews in Mineralogy and Geochemistry* 54 (1), 95–114.
- Fratzl, P., Gupta, H.S., Fischer, F.D., Kolednik, O., 2007. Hindered Crack Propagation in Materials with Periodically Varying Young's Modulus—Lessons from Biological Materials. *Advanced Materials* 19 (18), 2657–2661.
- Gaetani, G.A., Cohen, A.L., 2006. Element partitioning during precipitation of aragonite from seawater: A framework for understanding paleoproxies. *Geochimica et Cosmochimica Acta* 70 (18), 4617–4634.
- Gao, H., Ji, B., Jäger, I.L., Arzt, E., Fratzl, P., 2003. Materials become insensitive to flaws at nanoscale: Lessons from nature. *Proceedings of the National Academy of Sciences of the United States of America* 100 (10), 5597–5600.
- Gault, B., Moody, M.P., Cairney, J.M., Ringer, S.P., 2012. Atom probe microscopy. Springer Science & Business Media, 396 pp.
- Gervis, M.H., Sims, N.A., 1992. The biology and culture of pearl oysters (*Bivalvia pteriidae*). *WorldFish*, 49 pp.
- Gibbs, J.W., 1879. On the equilibrium of heterogeneous substances.
- Gifford, S., Dunstan, R.H., O'Connor, W., Roberts, T., Toia, R., 2004. Pearl aquaculture—profitable environmental remediation? *Science of the Total Environment* 319 (1), 27–37.

- Gilbert, P.U.P.A., Abrecht, M., Frazer, B.H., 2005. The organic-mineral interface in biominerals. *Reviews in Mineralogy and Geochemistry* 59 (1), 157–185.
- Gilbert, P.U.P.A., Bergmann, K.D., Myers, C.E., Marcus, M.A., DeVol, R.T., Sun, C.-Y., Blonsky, A.Z., Tamre, E., Zhao, J., Karan, E.A., 2017. Nacre tablet thickness records formation temperature in modern and fossil shells. *Earth and Planetary Science Letters* 460, 281–292.
- Gilbert, P.U.P.A., Metzler, R.A., Zhou, D., Scholl, A., Doran, A., Young, A., Kunz, M., Tamura, N., Coppersmith, S.N., 2008. Gradual ordering in red abalone nacre. *Journal of the American Chemical Society* 130 (51), 17519–17527.
- Gillikin, D.P., Lorrain, A., Bouillon, S., Willenz, P., Dehairs, F., 2006. Stable carbon isotopic composition of *Mytilus edulis* shells: Relation to metabolism, salinity,  $\delta^{13}\text{CDIC}$  and phytoplankton. *Organic Geochemistry* 37 (10), 1371–1382.
- Gillikin, D.P., Lorrain, A., Navez, J., Taylor, J.W., André, L., Keppens, E., Baeyens, W., Dehairs, F., 2005. Strong biological controls on Sr/Ca ratios in aragonitic marine bivalve shells. *Geochemistry, Geophysics, Geosystems* 6 (5), 1–16.
- Gillikin, D.P., Lorrain, A., Paulet, Y.-M., André, L., Dehairs, F., 2008. Synchronous barium peaks in high-resolution profiles of calcite and aragonite marine bivalve shells. *Geo-Marine Letters* 28 (5-6), 351–358.
- Goldstein, J.I., Newbury, D.E., Michael, J.R., Ritchie, N.W.M., Scott, J.H.J., Joy, D.C., 2017. Scanning electron microscopy and X-ray microanalysis. Springer.
- Gordon, L.M., Joester, D., 2011. Nanoscale chemical tomography of buried organic–inorganic interfaces in the chiton tooth. *Nature* 469 (7329), 194–197.
- Gordon, L.M., Tran, L., Joester, D., 2012. Atom probe tomography of apatites and bone-type mineralized tissues. *ACS nano* 6 (12), 10667–10675.
- Gorzela, P., Stolarski, J., Dery, A., Dubois, P., Escrig, S., Meibom, A., 2014. Ultrascale and microscale growth dynamics of the cidaroid spine of *Phyllacanthus imperialis* revealed by  $^{26}\text{Mg}$  labeling and NanoSIMS isotopic imaging. *Journal of Morphology* 275 (7), 788–796.
- Gorzela, P., Stolarski, J., Dubois, P., Kopp, C., Meibom, A., 2011.  $^{26}\text{Mg}$  labeling of the sea urchin regenerating spine: Insights into echinoderm biomineralization process. *Journal of Structural Biology* 176 (1), 119–126.
- Gower, L.B., 2008. Biomimetic model systems for investigating the amorphous precursor pathway and its role in biomineralization. *Chemical Reviews* 108 (11), 4551–4627.
- Gries, K., Kröger, R., Kübel, C., Fritz, M., Rosenauer, A., 2009a. Investigations of voids in the aragonite platelets of nacre. *Acta Biomaterialia* 5 (8), 3038–3044.
- Gries, K., Kröger, R., Kübel, C., Schowalter, M., Fritz, M., Rosenauer, A., 2009b. Correlation of the orientation of stacked aragonite platelets in nacre and their connection via mineral bridges. *Ultramicroscopy* 109 (3), 230–236.
- Gröcke, D.R., Gillikin, D.P., 2008. Advances in mollusc sclerochronology and sclerochemistry: Tools for understanding climate and environment 28 (5-6), 265–268.
- Gu, G.X., Libonati, F., Wettermark, S.D., Buehler, M.J., 2017. Printing nature: Unraveling the role of nacre's mineral bridges. *Journal of the mechanical behavior of biomedical materials* 76, 135–144.
- Gutner-Hoch, E., Schneider, K., Stolarski, J., Domart-Coulon, I., Yam, R., Meibom, A., Shemesh, A., Levy, O., 2016. Evidence for Rhythmicity Pacemaker in the Calcification Process of Scleractinian Coral. *Scientific Reports* 6 (20191), 1–8.
- Håkansson, E., 1973. Mode of growth of the Cupuladriidae (Bryozoa, Cheilostomata). *Living and Fossil Bryozoa: Recent Advances in Research*, 287–298.

- Hall, E.O., 1951. The deformation and ageing of mild steel: III discussion of results. *Proceedings of the Physical Society. Section B* 64 (9), 747–753.
- Hallmann, N., Burchell, M., Schöne, B.R., Irvine, G.V., Maxwell, D., 2009. High-resolution sclerochronological analysis of the bivalve mollusk *Saxidomus gigantea* from Alaska and British Columbia: Techniques for revealing environmental archives and archaeological seasonality. *Journal of Archaeological Science* 36 (10), 2353–2364.
- Handschuh, S., Baeumler, N., Schwaha, T., Ruthensteiner, B., 2013. A correlative approach for combining microCT, light and transmission electron microscopy in a single 3D scenario. *Frontiers in zoology* 10 (44), 1–16.
- Hänni, H.A., 2006. A short review of the use of 'keshi' as a term to describe pearls. *Journal of Gemmology* 30 (1/2), 52–58.
- Hänni, H.A., 2007. A description of pearl farming with *Pinctada maxima* in South East Asia. *Journal of Gemmology* 30 (7/8), 357–365.
- Hänni, H.A., 2012. Natural pearls and cultured pearls: a basic concept and its variations. *The Australian Gemmologist* 24 (11), 256–266.
- Hänni, H.A., Kiefert, L., Giese, P., 2005. X-ray luminescence, a valuable test in pearl identification. *Journal of Gemmology* 29 (5-6), 325–329.
- Hare, P.E., 1965. Amino acid composition of some calcified proteins. *Carnegie Institution for Science Washington Yearbook* 64, 223–232.
- Harmer, S.F., 1957. J The Polyzoa of the Siboga Expedition; part. IV: Cheilostomata Ascophora (Ascophora except Reteporidae, with additions to part II, Anasca). *Siboga Expeditie*, 19–118.
- Hashin, Z., 1962. The elastic moduli of heterogeneous materials. *Journal of Applied Mechanics* 29 (1), 143–150.
- Hasse, B., Ehrenberg, H., Marxen, J.C., Becker, W., Epple, M., 2000. Calcium carbonate modifications in the mineralized shell of the freshwater snail *Biomphalaria glabrata*. *Chemistry—A European Journal* 6 (20), 3679–3685.
- Henry, H., Tilhac, R., Griffin, W.L., O'Reilly, S.Y., Satsukawa, T., Kaczmarek, M.-A., Grégoire, M., Ceuleneer, G., 2017. Deformation of mantle pyroxenites provides clues to geodynamic processes in subduction zones: Case study of the Cabo Ortegal Complex, Spain. *Earth and Planetary Science Letters* 472, 174–185.
- Hielscher, R., Schaeben, H., 2008. A novel pole figure inversion method: Specification of the MTEX algorithm. *Journal of Applied Crystallography* 41 (6), 1024–1037.
- Hillion, F., Kilburn, M.R., Hoppe, P., Messenger, S., Weber, P.K., 2008. The effect of QSA on S, C, O and Si isotopic ratio measurements. *Geochimica et Cosmochimica Acta* 72, A377.
- Hofmann, D.C., Suh, J.-Y., Wiest, A., Duan, G., Lind, M.-L., Demetriou, M.D., Johnson, W.L., 2008. Designing metallic glass matrix composites with high toughness and tensile ductility. *Nature* 451 (7182), 1085–1089.
- Homkrajac, A., 2016. Spectral characteristics of *Pinctada mazatlanica* and *Pinctada margaritifera* pearl oyster species. *Gemmological Institute of America*, 5345 Armada Dr, Carlsbad, CA 92008 USA.
- Hoppe, P., Cohen, S., Meibom, A., 2013. NanoSIMS: Technical aspects and applications in cosmochemistry and biological geochemistry. *Geostandards and Geoanalytical Research* 37, 111–154.
- Houk, S.D., Maasch, K.A., Sandweiss, D.H. (Eds.), 2003. Marine bivalves as high-temporal-resolution paleoclimate proxies: A study in the northern Peruvian littoral.
- Hovden, R., Muller, D.A., 2012. Efficient elastic imaging of single atoms on ultrathin supports in a scanning transmission electron microscope. *Ultramicroscopy* 123, 59–65.

- Hovden, R., Wolf, S.E., Holtz, M.E., Marin, F., Muller, D.A., Estroff, L.A., 2015. Nanoscale assembly processes revealed in the nacreprismatic transition zone of *Pinna nobilis* mollusc shells. *Nature Communications* 6 (10097), 1–7.
- Hüning, A.K., Lange, S.M., Ramesh, K., Jacob, D.E., Jackson, D.J., Panknin, U., Gutowska, M.A., Philipp, E.E.R., Rosenstiel, P., Lucassen, M., 2016. A shell regeneration assay to identify biomineralization candidate genes in mytilid mussels. *Marine Genomics* 27, 57–67.
- Huxley, T.H. (Ed.), 1852. Upon animal individuality. Royal Institution of Great Britain.
- Jackson, A.P., Vincent, J.F.V., Turner, R.M., 1988. The mechanical design of nacre. *Proceedings of the Royal Society of London B: Biological Sciences* 234 (1277), 415–440.
- Jackson, A.P., Vincent, J.F.V., Turner, R.M., 1990. Comparison of nacre with other ceramic composites. *Journal of Materials Science* 25 (7), 3173–3178.
- Jackson, D.J., McDougall, C., Woodcroft, B., Moase, P., Rose, R.A., Kube, M., Reinhardt, R., Rokhsar, D.S., Montagnani, C., Joubert, C., 2009. Parallel evolution of nacre building gene sets in molluscs. *Molecular Biology and Evolution* 27 (3), 591–608.
- Jacob, D.E., Ruthensteiner, B., Trimby, P., Henry, H., Martha, S.O., Leitner, J., Otter, L.M., Scholz, J., 2019. Architecture and biomineralization of *Anoteropora latirostris* (Bryozoa, Cheilostomata). *Scientific Reports* 9 (11439), 1–13.
- Jacob, D.E., Soldati, A.L., Wirth, R., Huth, J., Wehrmeister, U., Hofmeister, W., 2008. Nanostructure, composition and mechanisms of bivalve shell growth. *Geochimica et Cosmochimica Acta* 72 (22), 5401–5415.
- Jacob, D.E., Wirth, R., Agbaje, O.B.A., Branson, O., Eggins, S.M., 2017. Planktic foraminifera form their shells via metastable carbonate phases. *Nature Communications* 8 (1265), 1–9.
- Jacob, D.E., Wirth, R., Soldati, A.L., Wehrmeister, U., Schreiber, A., 2011. Amorphous calcium carbonate in the shells of adult Unionoida. *Journal of Structural Biology* 173 (2), 241–249.
- Jochum, K.P., Scholz, D., Stoll, B., Weis, U., Wilson, S.A., Yang, Q., Schwalb, A., Börner, N., Jacob, D.E., Andreae, M.O., 2012. Accurate trace element analysis of speleothems and biogenic calcium carbonates by LA-ICP-MS. *Chemical Geology* 318, 31–44.
- Jochum, K.P., Stoll, B., Herwig, K., Willbold, M., 2007. Validation of LA-ICP-MS trace element analysis of geological glasses using a new solid-state 193 nm Nd: YAG laser and matrix-matched calibration. *Journal of Analytical Atomic Spectrometry* 22 (2), 112–121.
- Kamat, S., Su, X., Ballarini, R., Heuer, A.H., 2000. Structural basis for the fracture toughness of the shell of the conch *Strombus gigas*. *Nature* 405 (6790), 1036–1040.
- Karampelas, S., 2012. Spectral Characteristics of Natural-Color Saltwater Cultured Pearls from *Pinctada Maxima*. *Gems & Gemology* 48 (3), 193–197.
- Karampelas, S., Al-Alawi, A.T., Al-Attawi, A., 2017. Real-Time Microradiography of Pearls: A Comparison Between Detectors. *Gems & Gemology* 53 (4), 452–456.
- Karampelas, S., Fritsch, E., Mevellec, J.-Y., Sklavounos, S., Soldatos, T., 2009. Role of polyenes in the coloration of cultured freshwater pearls. *European Journal of Mineralogy* 21 (1), 85–97.
- Karampelas, S., Fritsch, E., Mevellec, J.-Y., Gauthier, J.-P., Sklavounos, S., Soldatos, T., 2007. Determination by Raman scattering of the nature of pigments in cultured freshwater pearls from the mollusk *Hyriopsis cumingi*. *Journal of Raman Spectroscopy* 38 (2), 217–230.
- Karampelas, S., Michel, J., Zheng-Cui, M., Schwarz, J.-O., Enzmann, F., Fritsch, E., Leu, L., Krzemnicki, M.S., 2010. X-Ray Computed Microtomography Applied to Pearls: Methodology, Advantages, and Limitations. *Gems & Gemology* 46 (2), 122–127.



- Katti, K.S., Mohanty, B., Katti, D.R., 2006. Nanomechanical properties of nacre. *Journal of Materials Research* 21 (5), 1237–1242.
- Kawakami, I.K., 1952. Studies on pearl sac formation. 1. On the regeneration and transplantation of the mantle piece in the pearl oyster. *Memoirs Faculty Science Kyushu University Ser E (Biol)* 1, 83–88.
- Kearney, C., Zhao, Z., Bruet, B.J.F., Radovitzky, R., Boyce, M.C., Ortiz, C., 2006. Nanoscale anisotropic plastic deformation in single crystal aragonite. *Physical Review Letters* 96 (255505), 1–4.
- Keith, J., Stockwell, S., Ball, D., Remillard, K., Kaplan, D., Thannhauser, T., Sherwood, R., 1993. Comparative analysis of macromolecules in mollusc shells. *Comparative Biochemistry and Physiology* 105 (3-4), 487–496.
- Keller, R.R., Geiss, R.H., 2012. Transmission EBSD from 10 nm domains in a scanning electron microscope. *Journal of Microscopy* 245 (3), 245–251.
- Kelly, T.F., Miller, M.K., 2007. Atom probe tomography. *Review of Scientific Instruments* 78 (031101), 1–20.
- Key, M.M., Zágoršek, K., Patterson, W.P., 2013. Paleoenvironmental reconstruction of the Early to Middle Miocene Central Paratethys using stable isotopes from bryozoan skeletons. *International Journal of Earth Sciences* 102 (1), 305–318.
- Kiefert, L., Moreno, D.M., Arizmendi, E., Hanni, H.A., Elen, S., 2004. Cultured pearls from the Gulf of California, Mexico. *Gems & Gemology* 40 (1), 26–38.
- Klein, R.T., Lohmann, K.C., Thayer, C.W., 1996a. Bivalve skeletons record sea-surface temperature and  $\delta^{18}\text{O}$  via Mg/Ca and  $^{18}\text{O}/^{16}\text{O}$  ratios. *Geology* 24 (5), 415–418.
- Klein, R.T., Lohmann, K.C., Thayer, C.W., 1996b. Sr/Ca and  $^{13}\text{C}/^{12}\text{C}$  ratios in skeletal calcite of *Mytilus trossulus*: Covariation with metabolic rate, salinity, and carbon isotopic composition of seawater. *Geochimica et Cosmochimica Acta* 60 (21), 4207–4221.
- Kobayashi, I., 1971. Internal shell micro-structure of Recent bivalvian molluscs. *Sci. Re., Niigata Univ.,(E)* 2, 27–50.
- Kobayashi, I., Akai, J., 1994. Twinned aragonite crystals found in the bivalvian crossed lamellar shell structure. *The Journal of the Geological Society of Japan* 100 (2), 177–180.
- Kobayashi, I., Samata, T., 2006. Bivalve shell structure and organic matrix. *Materials Science and Engineering: C* 26 (4), 692–698.
- Kripa, V., Abraham, K.J., Libini, C.L., Velayudhan, T.S., Radhakrishnan, P., Mohamed, K.S., Modayil, M.J., 2008. Production of designer mabe pearls in the black-lipped pearl oyster, *Pinctada margaritifera*, and the winged pearl oyster, *Pteria penguin*, from Andaman and Nicobar Islands, India. *Journal of the World Aquaculture Society* 39 (1), 131–137.
- Kripa, V., Mohamed, K.S., Appukuttan, K.K., Velayudhan, T.S., 2007. Production of Akoya pearls from the Southwest coast of India. *Aquaculture* 262 (2), 347–354.
- Krzemnicki, M.S., Friess, S.D., Chalus, P., Hänni, H.A., Karampelas, S., 2010. X-Ray Computed Microtomography: Distinguishing Natural Pearls from Beaded and Non-Beaded Cultured Pearls. *Gems & Gemology* 46 (2), 128–134.
- Kunitake, M.E., Mangano, L.M., Peloquin, J.M., Baker, S.P., Estroff, L.A., 2013. Evaluation of strengthening mechanisms in calcite single crystals from mollusk shells. *Acta Biomaterialia* 9 (2), 5353–5359.
- La Fontaine, A., Zavgorodniy, A., Liu, H., Zheng, R., Swain, M., Cairney, J., 2016. Atomic-scale compositional mapping reveals Mg-rich amorphous calcium phosphate in human dental enamel. *Science Advances* 2 (9), 1–6.
- Landman, N.H., Mikkelsen, P.M., Bieler, R., Bronson, B., 2001. Pearls: A natural history. Harry N. Abrams New York, 232 pp.

- Langelier, B., Wang, X., Grandfield, K., 2017. Atomic scale chemical tomography of human bone. *Scientific Reports* 7 (39958), 1–9.
- Larson, D.J., Prosa, T., Ulfig, R.M., Geiser, B.P., Kelly, T.F., 2013. Local electrode atom probe tomography. Springer, 328 pp.
- Levi-Kalishman, Y., Falini, G., Addadi, L., Weiner, S., 2001. Structure of the nacreous organic matrix of a bivalve mollusk shell examined in the hydrated state using cryo-TEM. *Journal of Structural Biology* 135 (1), 8–17.
- Li, H., Xin, H.L., Kunitake, M.E., Keene, E.C., Muller, D.A., Estroff, L.A., 2011. Calcite prisms from mollusk shells (*Atrina Rigida*): Swiss-cheese-like organic–inorganic single-crystal composites. *Advanced Functional Materials* 21 (11), 2028–2034.
- Li, X., Chang, W.-C., Chao, Y.J., Wang, R., Chang, M., 2004. Nanoscale Structural and Mechanical Characterization of a Natural Nanocomposite Material: The Shell of Red Abalone. *Nano Letters* 4 (4), 613–617.
- Li, X., Xu, Z.-H., Wang, R., 2006. In situ observation of nanograin rotation and deformation in nacre. *Nano Letters* 6 (10), 2301–2304.
- Lin, A.Y.-M., 2008. Structural and functional biological materials: Abalone nacre, sharp materials, and abalone foot adhesion. UC San Diego.
- Lin, A.Y.-M., Chen, P.-Y., Meyers, M.A., 2008. The growth of nacre in the abalone shell. *Acta Biomaterialia* 4 (1), 131–138.
- Liu, L.-G., Chen, C.-C., Lin, C.-C., Yang, Y.-J., 2005. Elasticity of single-crystal aragonite by Brillouin spectroscopy. *Physics and Chemistry of Minerals* 32 (2), 97–102.
- Lombardi, C., Cocito, S., Gambi, M.C., Cisterna, B., Flach, F., Taylor, P.D., Keltie, K., Freer, A., Cusack, M., 2011. Effects of ocean acidification on growth, organic tissue and protein profile of the Mediterranean bryozoan *Myriapora truncata*. *Aquatic Biology* 13 (3), 251–262.
- Lombardi, C., Cocito, S., Hiscock, K., Occhipinti-Ambrogi, A., Setti, M., Taylor, P.D., 2008. Influence of seawater temperature on growth bands, mineralogy and carbonate production in a bioconstructional bryozoan. *Facies* 54 (3), 333–342.
- Lowenstam, H.A., 1981. Minerals formed by organisms. *Science* 211 (4487), 1126–1131.
- Lowenstam, H.A., Weiner, S., 1989. On biomineralization. Oxford University Press on Demand, 395 pp.
- MacDonald, G.J.F., 1956. Experimental determination of calcite-aragonite equilibrium relations at elevated temperatures and pressures. *American Mineralogist: Journal of Earth and Planetary Materials* 41 (9-10), 744–756.
- Mainprice, D., Hielscher, R., Schaebe, H., 2011. Calculating anisotropic physical properties from texture data using the MTEX open-source package. Geological Society, London, Special Publications 360 (1), 175–192.
- Mann, S., 2001. Biomineralization: Principles and concepts in bioinorganic materials chemistry. Oxford University Press on Demand, 220 pp.
- Marie, B., Joubert, C., Tayalé, A., Zanella-Cléon, I., Belliard, C., Piquemal, D., Cochennec-Laureau, N., Marin, F., Gueguen, Y., Montagnani, C., 2012. Different secretory repertoires control the biomineralization processes of prism and nacre deposition of the pearl oyster shell. *Proceedings of the National Academy of Sciences* 109 (51), 20986–20991.
- Marie, B., Luquet, G., Barros, J.-P.P. de, Guichard, N., Morel, S., Alcaraz, G., Bollache, L., Marin, F., 2007. The shell matrix of the freshwater mussel *Unio pictorum* (Paleoheterodonta, Unionoida). *The FEBS Journal* 274 (11), 2933–2945.

- Marin, F., Le Roy, N., Marie, B., 2012. The formation and mineralization of mollusk shell. *Frontiers in Bioscience* 4, 1099–1125.
- Marin, F., Luquet, G., 2004. Molluscan shell proteins. *Comptes Rendus Palevol* 3 (6-7), 469–492.
- Marxen, J.C., Hammer, M., Gehrke, T., Becker, W., 1998. Carbohydrates of the organic shell matrix and the shell-forming tissue of the snail *Biomphalaria glabrata* (Say). *The Biological Bulletin* 194 (2), 231–240.
- McKinney, F.K., Jackson, J.B.C., 1991. *Bryozoan evolution*. University of Chicago Press.
- Menig, R., Meyers, M.H., Meyers, M.A., Vecchio, K.S., 2000. Quasi-static and dynamic mechanical response of *Haliotis rufescens* (abalone) shells. *Acta Materialia* 48 (9), 2383–2398.
- Merkel, C., Deuschle, J., Griesshaber, E., Enders, S., Steinhauser, E., Hochleitner, R., Brand, U., Schmahl, W.W., 2009. Mechanical properties of modern calcite-(*Mergerlia truncata*) and phosphate-shelled brachiopods (*Discradisca stella* and *Lingula anatina*) determined by nanoindentation. *Journal of Structural Biology* 168 (3), 396–408.
- Metzler, R.A., Abrecht, M., Olabisi, R.M., Ariosa, D., Johnson, C.J., Frazer, B.H., Coppersmith, S.N., Gilbert, P.U.P.A., 2007. Architecture of columnar nacre, and implications for its formation mechanism. *Physical Review Letters* 98 (268102), 1–4.
- Metzler, R.A., Evans, J.S., Killian, C.E., Zhou, D., Churchill, T.H., Appathurai, N.P., Coppersmith, S.N., Gilbert, P.U.P.A., 2010. Nacre protein fragment templates lamellar aragonite growth. *Journal of the American Chemical Society* 132 (18), 6329–6334.
- Metzler, R.A., Zhou, D., Abrecht, M., Chiou, J.-W., Guo, J., Ariosa, D., Coppersmith, S.N., Gilbert, P.U.P.A., 2008. Polarization-dependent imaging contrast in abalone shells. *Physical Review B* 77 (064110), 1–9.
- Meyer, J.B., Cartier, L.E., Pinto-Figueroa, E.A., Krzemnicki, M.S., Hänni, H.A., McDonald, B.A., 2013. DNA fingerprinting of pearls to determine their origins. *PloS one* 8 (10), 1–11.
- Meyers, M.A., Chen, P.-Y., Lin, A.Y.-M., Seki, Y., 2008. Biological materials: Structure and mechanical properties. *Progress in Materials Science* 53 (1), 1–206.
- Meyers, M.A., McKittrick, J., Chen, P.-Y., 2013. Structural biological materials: Critical mechanics-materials connections. *Science* 339 (6121), 773–779.
- Miller, M.K., 2000. The development of atom probe field-ion microscopy. *Materials Characterization* 44 (1-2), 11–27.
- Minor, A.M., Asif, S.S., Shan, Z., Stach, E.A., Cyrankowski, E., Wyrobek, T.J., Warren, O.L., 2006. A new view of the onset of plasticity during the nanoindentation of aluminium. *Nature Materials* 5 (9), 697–702.
- Minor, A.M., Dehm, G., 2019. Advances in in situ nanomechanical testing. *MRS Bulletin* 44 (6), 438–442.
- Mitchell, P.R., Phakey, P.P., Smillie, A.C., Wise, S.W., 1995. Notes on the microstructure of the Nautilus shell. Discussion. *Scanning Microscopy* 9 (1), 215–230.
- Miyoshi, T., Matsuda, Y., Komatsu, H., 1987. Fluorescence from pearls to distinguish mother oysters used in pearl culture. *Japanese Journal of Applied Physics* 26, 578–581.
- Moore, D.R., 1961. The marine and brackish water Mollusca of the State of Mississippi. *Gulf and Caribbean Research* 1 (1), 1–58.
- Mouchi, V., Rafélis, M. de, Lartaud, F., Fialin, M., Verrecchia, E., 2013. Chemical labelling of oyster shells used for time-calibrated high-resolution Mg/Ca ratios: A tool for estimation of past seasonal temperature variations. *Palaeogeography, Palaeoclimatology, Palaeoecology* 373, 66–74.
- Munch, E., Launey, M.E., Alsem, D.H., Saiz, E., Tomsia, A.P., Ritchie, R.O., 2008. Tough, bio-inspired hybrid materials. *Science* 322 (5907), 1516–1520.

- Murillo De Nava, J.M., Gorsline, D.S., Goodfriend, G.A., Vlasov, V.K., Cruz-Orozco, R., 1999. Evidence of Holocene climatic changes from Aeolian deposits in Baja California Sur, México. *Quaternary International* 56 (1), 141–154.
- Mutvei, H., 1979. On the internal structures of the nacreous tablets in molluscan shells. *Scanning Electron Microscopy* 1979 (2), 457–462.
- Mutvei, H., Dunca, E., 2010. Crystalline structure, orientation and nucleation of the nacreous tablets in the cephalopod *Nautilus*. *Paläontologische Zeitschrift* 84 (4), 457–465.
- Nakahara, H., Bevelander, G., 1971. The formation and growth of the prismatic layer of *Pinctada radiata*. *Calcified Tissue Research* 7 (1), 31–45.
- Nalla, R.K., Kinney, J.H., Ritchie, R.O., 2003. Effect of orientation on the in vitro fracture toughness of dentin: The role of toughening mechanisms. *Biomaterials* 24 (22), 3955–3968.
- Nehrke, G., Keul, N., Langer, G., Nooijer, L.J. de, Bijma, J., Meibom, A., 2013. A new model for biomineralization and trace-element signatures of Foraminifera tests. *Biogeosciences* 10 (10), 6759–6767.
- Nell, J.A., O'Connor, W.A., Heasman, M.P., Goard, L.J., 1994. Hatchery production for the venerid clam *Katelysia rhytiphora* (Lamy) and the Sydney cockle *Anadara trapezia* (Deshayes). *Aquaculture* 119 (2-3), 149–156.
- Nell, J.A., Paterson, K.J., 1997. Salinity studies on the clams *Katelysia rhytiphora* (Lamy) and *Tapes dorsatus* (Lamarck). *Aquaculture Research* 28 (2), 115–119.
- Nellen, W., 1996. MINDIK : Reise Nr. 5, 2. Januar 1987 - 24. September 1987. Leitstelle METEOR, Hamburg, 287 pp.
- Nilpetploy, N., Lawanwong, K., Kessrapong, P., 2018. The Gemological Characteristics of Pipi Pearls Reportedly from *Pinctada maculata* 54 (4), 418–427.
- Nudelman, F., 2015. Nacre biomineralisation: A review on the mechanisms of crystal nucleation. *Seminars in Cell & Developmental Biology* 46, 2–10.
- Nudelman, F., Gotliv, B.A., Addadi, L., Weiner, S., 2006. Mollusk shell formation: Mapping the distribution of organic matrix components underlying a single aragonitic tablet in nacre. *Journal of Structural Biology* 153 (2), 176–187.
- Nudelman, F., Shimoni, E., Klein, E., Rousseau, M., Bourrat, X., Lopez, E., Addadi, L., Weiner, S., 2008. Forming nacreous layer of the shells of the bivalves *Atrina rigida* and *Pinctada margaritifera*: An environmental-and cryo-scanning electron microscopy study. *Journal of Structural Biology* 162 (2), 290–300.
- Nukala, P.K., Simunovic, S., 2005. A continuous damage random thresholds model for simulating the fracture behavior of nacre. *Biomaterials* 26 (30), 6087–6098.
- O'Donnell, M.D., Fredholm, Y., Rouffignac, A. de, Hill, R.G., 2008. Structural analysis of a series of strontium-substituted apatites. *Acta Biomaterialia* 4 (5), 1455–1464.
- O'Connor, W.A., Lawler, N.F., Heasman, M.P., 2003. Trial Farming the Akoya Pearl Oyster, *Pinctada imbricata*, in Port Stephens, NSW: Final Report to Australian Radiata Pty Ltd., 1440–3544.
- O'Dea, A., Jackson, J.B.C., Taylor, P.D., Rodriguez, F., 2008. Modes of reproduction in recent and fossil cupuladriid bryozoans. *Palaeontology* 51 (4), 847–864.
- O'Dea, A., Okamura, B., 1999. Influence of seasonal variation in temperature, salinity and food availability on module size and colony growth of the estuarine bryozoan *Conopeum seurati*. *Marine Biology* 135 (4), 581–588.
- Okumura, K., Gennes, P.-G. de, 2001. Why is nacre strong? Elastic theory and fracture mechanics for biocomposites with stratified structures. *The European Physical Journal E* 4 (1), 121–127.

- Olson, I.C., Blonsky, A.Z., Tamura, N., Kunz, M., Pokroy, B., Romao, C.P., White, M.A., Gilbert, P.U.P.A., 2013a. Crystal nucleation and near-epitaxial growth in nacre. *Journal of Structural Biology* 184 (3), 454–463.
- Olson, I.C., Metzler, R.A., Tamura, N., Kunz, M., Killian, C.E., Gilbert, P.U.P.A., 2013b. Crystal lattice tilting in prismatic calcite. *Journal of Structural Biology* 183 (2), 180–190.
- Ostwald, W., 1897. Studien über die Bildung und Umwandlung fester Körper. *Zeitschrift für Physikalische Chemie* 22 (1), 289–330.
- Otter, L.M., Agbaje, O., Le Huong, T.-T., Häger, T., Jacob, D.E., 2017. Akoya Cultured Pearl Farming in Eastern Australia. *Gems & Gemology* 53 (4), 423–437.
- Otter, L.M., Agbaje, O.B.A., Kilburn, M.R., Lenz, C., Henry, H., Trimby, P., Hoppe, P., Jacob, D.E., 2019. Insights into architecture, growth dynamics, and biomineralization from pulsed Sr-labelled *Katelysia rhytiphora* shells (Mollusca, Bivalvia). *Biogeosciences* 16 (17), 3439–3455.
- Otter, L.M., Wehrmeister, U., Enzmann, F., Wolf, M., Jacob, D.E., 2014. A Look Inside A Remarkably Large Beaded South Sea Cultured Pearl. *Gems & Gemology* 50 (1), 58–62.
- Ouhenia, S., Chateigner, D., Belkhir, M.A., Guilmeau, E., 2008. Microstructure and crystallographic texture of *Charonia lampas lampas* shell. *Journal of Structural Biology* 163 (2), 175–184.
- Pannella, G., MacClintock, C., 1968. Biological and environmental rhythms reflected in molluscan shell growth. *Journal of Paleontology* 42 (S2), 64–80.
- Pavese, A., Catti, M., Price, G.D., Jackson, R.A., 1992. Interatomic potentials for CaCO<sub>3</sub> polymorphs (calcite and aragonite), fitted to elastic and vibrational data. *Physics and Chemistry of Minerals* 19 (2), 80–87.
- Pedrazzini, S., London, A.J., Gault, B., Saxey, D., Speller, S., Grovenor, C.R.M., Danaie, M., Moody, M.P., Edmondson, P.D., Bagot, P.A.J., 2017. Nanoscale stoichiometric analysis of a high-temperature superconductor by atom probe tomography. *Microscopy and Microanalysis* 23 (2), 414–424.
- Peng, B., Locascio, M., Zapol, P., Li, S., Mielke, S.L., Schatz, G.C., Espinosa, H.D., 2008. Measurements of near-ultimate strength for multiwalled carbon nanotubes and irradiation-induced crosslinking improvements. *Nature nanotechnology* 3 (10), 626–631.
- Pérez-Huerta, A., Cuif, J.-P., Dauphin, Y., Cusack, M., 2014. Crystallography of calcite in pearls. *European Journal of Mineralogy* 26 (4), 507–516.
- Pérez-Huerta, A., Laiginhas, F., 2018. Preliminary Data on the Nanoscale Chemical Characterization of the Inter-Crystalline Organic Matrix of a Calcium Carbonate Biomineral. *Minerals* 8 (6), 223.
- Petch, N.J., 1953. The cleavage strength of polycrystals. *Journal of the Iron and Steel Institute* 174, 25–28.
- Peters, W., 1972. Occurrence of chitin in Mollusca. *Comparative Biochemistry and Physiology* 41 (3), 541–550.
- Pokroy, B., Fitch, A.N., Marin, F., Kapon, M., Adir, N., Zolotoyabko, E., 2006. Anisotropic lattice distortions in biogenic calcite induced by intra-crystalline organic molecules. *Journal of Structural Biology* 155 (1), 96–103.
- Pokroy, B., Zolotoyabko, E., 2003. Microstructure of natural plywood-like ceramics: A study by high-resolution electron microscopy and energy-variable X-ray diffraction. *Journal of Materials Chemistry* 13 (4), 682–688.
- Politi, Y., Arad, T., Klein, E., Weiner, S., Addadi, L., 2004. Sea urchin spine calcite forms via a transient amorphous calcium carbonate phase. *Science* 306 (5699), 1161–1164.
- Popov, S.V., 1986. Composite prismatic structure in bivalve shell. *Acta Palaeontologica Polonica* 31 (1-2), 3–26.
- Purton, L.M.A., Shields, G.A., Brasier, M.D., Grime, G.W., 1999. Metabolism controls Sr/Ca ratios in fossil aragonitic mollusks. *Geology* 27 (12), 1083–1086.
- Radermacher, P., Schöne, B.R., Gischler, E., Oschmann, W., Thébault, J., Fiebig, J., 2009. Sclerochronology—a highly versatile tool for mariculture and reconstruction of life history traits of the queen conch, *Strombus gigas* (Gastropoda). *Aquatic Living Resources* 22 (3), 307–318.



- Reza Mirzaei, M., Yasin, Z., Shau Hwai, A.T., 2014. Periodicity and shell microgrowth pattern formation in intertidal and subtidal areas using shell cross sections of the blood cockle, *Anadara granosa*. *The Egyptian Journal of Aquatic Research* 40 (4), 459–468.
- Rhoads, D.C., Lutz, R.A., 1980. *Skeletal Growth of Aquatic Organisms: Biological records of environmental change*. Plenum Press, 750 pp.
- Riascos, J., Guzman, N., Laudien, J., Heilmayer, O., Oliva, M., 2007. Suitability of three stains to mark shells of *Concholepas concholepas* (Gastropoda) and *Mesodesma donacium* (Bivalvia). *Journal of Shellfish Research* 26 (1), 43–50.
- Ritchie, R.O., 2011. The conflicts between strength and toughness. *Nature Materials* 10 (11), 817–822.
- Rodriguez-Navarro, A.B., Checa, A., Willinger, M.-G., Bolmaro, R., Bonarski, J., 2012. Crystallographic relationships in the crossed lamellar microstructure of the shell of the gastropod *Conus marmoreus*. *Acta Biomaterialia* 8 (2), 830–835.
- Ropes, J.W., Jones, D.S., Murawski, S.A., Serchuk, F.M., Jearld, A., 1984. Documentation of annual growth lines in ocean quahogs, *Arctica islandica* Linne. *Fishery Bulletin* 82 (1), 1–19.
- Rousseau, M., Meibom, A., Gèze, M., Bourrat, X., Angellier, M., Lopez, E., 2009. Dynamics of sheet nacre formation in bivalves. *Journal of Structural Biology* 165 (3), 190–195.
- Rucker, J.B., Carver, R.E., 1969. A survey of the carbonate mineralogy of cheilostome Bryozoa. *Journal of Paleontology* 43 (3), 791–799.
- Ruschel, K., Nasdala, L., Kronz, A., Hanchar, J.M., Többsen, D.M., Škoda, R., Finger, F., Möller, A., 2012. A Raman spectroscopic study on the structural disorder of monazite–(Ce). *Mineralogy and Petrology* 105 (1-2), 41–55.
- Russell, M.P., Urbaniak, L.M. (Eds.), 2004. *Does calcein affect estimates of growth rates in sea urchins?* CRC Press, 53 pp.
- Ryland, J.S. (Ed.), 1979. *Structural and physiological aspects of coloniality in Bryozoa*, 589 pp.
- Sand, K.K., Pedersen, C.S., Matthiesen, J., Dobberschütz, S., Stipp, S.L.S., 2017. Controlling biomineralisation with cations. *Nanoscale* 9 (35), 12925–12933.
- Saruwatari, K., Matsui, T., Mukai, H., Nagasawa, H., Kogure, T., 2009. Nucleation and growth of aragonite crystals at the growth front of nacre in pearl oyster, *Pinctada fucata*. *Biomaterials* 30 (16), 3028–3034.
- Saruwatari, K., Suzuki, M., Zhou, C., Kessrapong, P., Sturman, N., 2018. DNA Techniques Applied to the Identification of *Pinctada Fucata* Pearls from Uwajima, Ehime Prefecture, Japan. *Gems & Gemology* 54 (1), 40–50.
- Scarratt, K., Bracher, P., Bracher, M., Attawi, A., Safar, A., Saeseaw, S., Homkrajae, A., Sturman, N., 2012. Natural pearls from Australian *Pinctada maxima*. *Gems & Gemology* 48 (4), 236–261.
- Schäffer, T.E., Ionescu-Zanetti, C., Proksch, R., Fritz, M., Walters, D.A., Almqvist, N., Zaremba, C.M., Belcher, A.M., Smith, B.L., Stucky, G.D., 1997. Does abalone nacre form by heteroepitaxial nucleation or by growth through mineral bridges? *Chemistry of Materials* 9 (8), 1731–1740.
- Schindelin, J., Rueden, C.T., Hiner, M.C., Eliceiri, K.W., 2015. The ImageJ ecosystem: An open platform for biomedical image analysis. *Molecular Reproduction and Development* 82 (7-8), 518–529.
- Schmidt, W.J., 1924. Bau und Bildung der Perlmuttermasse. *Zoologische Jahrbucher, Abteilung für Anatomie und Ontogenie der Tiere* 45, 1–148.
- Schoeppler, V., Gránásy, L., Reich, E., Poulsen, N., Kloe, R. de, Cook, P., Rack, A., Pusztai, T., Zlotnikov, I., 2018. Biomineralization as a Paradigm of Directional Solidification: A Physical Model for Molluscan Shell Ultrastructural Morphogenesis. *Advanced Materials* 30 (45), 1–8.

- Schöne, B., Surge, D.M., 2012. Treatise Online no. 46: Part N, Revised, Volume 1, Chapter 14: Bivalve sclerochronology and geochemistry. Treatise Online.
- Schöne, B.R., 2008. The curse of physiology—challenges and opportunities in the interpretation of geochemical data from mollusk shells. *Geo-Marine Letters* 28 (5-6), 269–285.
- Schöne, B.R., Castro, A.D.F., Fiebig, J., Houk, S.D., Oschmann, W., Kröncke, I., 2004. Sea surface water temperatures over the period 1884–1983 reconstructed from oxygen isotope ratios of a bivalve mollusk shell (*Arctica islandica*, southern North Sea). *Palaeogeography, Palaeoclimatology, Palaeoecology* 212 (3-4), 215–232.
- Schöne, B.R., Fiebig, J., Pfeiffer, M., Gleß, R., Hickson, J., La Johnson, A., Dreyer, W., Oschmann, W., 2005. Climate records from a bivalved *Methuselah* (*Arctica islandica*, Mollusca; Iceland). *Palaeogeography, Palaeoclimatology, Palaeoecology* 228 (1-2), 130–148.
- Schöne, B.R., Goodwin, D.H., Flessa, K.W., Dettman, D.L., 2002. Sclerochronology and Growth of the Bivalve Mollusks *Chione* (*Chionista*) *fluctifraga* and *C.(Chionista) cortezi*. *the Veliger* 45 (1), 45–54.
- Schöne, B.R., Zhang, Z., Radermacher, P., Thébault, J., Jacob, D.E., Nunn, E.V., Maurer, A.-F., 2011. Sr/Ca and Mg/Ca ratios of ontogenetically old, long-lived bivalve shells (*Arctica islandica*) and their function as paleotemperature proxies. *Palaeogeography, Palaeoclimatology, Palaeoecology* 302 (1-2), 52–64.
- Sethmann, I., Hinrichs, R., Wörheide, G., Putnis, A., 2006. Nano-cluster composite structure of calcitic sponge spicules—a case study of basic characteristics of biominerals. *Journal of Inorganic Biochemistry* 100 (1), 88–96.
- Shen, X., Belcher, A.M., Hansma, P.K., Stucky, G.D., Morse, D.E., 1997. Molecular cloning and characterization of lustrin A, a matrix protein from shell and pearl nacre of *Haliotis rufescens*. *Journal of Biological Chemistry* 272 (51), 32472–32481.
- Shimamoto, M., 1986. Shell microstructure of the Veneridae (*Bivalvia*) and its phylogenetic implications. 東北大學理科報告. 地質學 56 (1), 1-40.
- Shirai, K., Sowa, K., Watanabe, T., Sano, Y., Nakamura, T., Clode, P., 2012. Visualization of sub-daily skeletal growth patterns in massive *Porites* corals grown in Sr-enriched seawater. *Journal of Structural Biology* 180 (1), 47–56.
- Silén, L., 1947. Conescharrellinidae (Bryozoa Gymnolaemata) collected by Prof Dr. Sixten Bock's expedition to Japan and the Bonin Islands 1914. *Arkiv för Zoologi*, 1–59.
- Simkiss, K., 1965. The organic matrix of the oyster shell. *Comparative Biochemistry and Physiology* 16 (4), 427–435.
- Skemer, P., Katayama, I., Jiang, Z., Karato, S.-i., 2005. The misorientation index: Development of a new method for calculating the strength of lattice-preferred orientation. *Tectonophysics* 411 (1-4), 157–167.
- Slodzian, G., Hillion, F., Stadermann, F.J., Zinner, E., 2004. QSA influences on isotopic ratio measurements. *Applied Surface Science* 231, 874–877.
- Smith, A.M., 2014. Growth and calcification of marine bryozoans in a changing ocean. *The Biological Bulletin* 226 (3), 203–210.
- Smith, A.M., Key, M.M., 2004. Controls, variation, and a record of climate change in detailed stable isotope record in a single bryozoan skeleton☆. *Quaternary Research* 61 (2), 123–133.
- Smith, B.L., Schäffer, T.E., Viani, M., Thompson, J.B., Frederick, N.A., Kindt, J., Belcher, A., Stucky, G.D., Morse, D.E., Hansma, P.K., 1999. Molecular mechanistic origin of the toughness of natural adhesives, fibres and composites. *Nature* 399 (6738), 761–763.

- Soldati, A.L., Jacob, D.E., Wehrmeister, U., Häger, T., Hofmeister, W., 2008. Micro-Raman spectroscopy of pigments contained in different calcium carbonate polymorphs from freshwater cultured pearls. *Journal of Raman Spectroscopy* 39 (4), 525–536.
- Song, F., Soh, A.K., Bai, Y.L., 2003. Structural and mechanical properties of the organic matrix layers of nacre. *Biomaterials* 24 (20), 3623–3631.
- Stach, E.A., Freeman, T., Minor, A.M., Owen, D.K., Cumings, J., Wall, M.A., Chraska, T., Hull, R., Morris, J.W., Zettl, A., 2001. Development of a nanoindenter for in situ transmission electron microscopy. *Microscopy and Microanalysis* 7 (6), 507–517.
- Stempflé, P.H., Pantalé, O., Rousseau, M., Lopez, E., Bourrat, X., 2010. Mechanical properties of the elemental nanocomponents of nacre structure. *Materials Science and Engineering: C* 30 (5), 715–721.
- Stephenson, A.E., DeYoreo, J.J., Wu, L., Wu, K.J., Hoyer, J., Dove, P.M., 2008. Peptides enhance magnesium signature in calcite: Insights into origins of vital effects. *Science* 322 (5902), 724–727.
- Strack, E., 2006. Pearls. Rühle-Diebener, Stuttgart, Germany, 696 pp.
- Sturman, N., Otter, L.M., Homkrajae, A., Manustrong, A., Nilpetploy, N., Lawanwong, K., Kessrapong, P., Jochum, K.P., Stoll, B., Götz, H., Jacob, D.E., 2019. A Pearl Identification Challenge. *Gems & Gemology* 55 (2), 229–243.
- Sudo, S., Fujikawa, T., Nagakura, T., Ohkubo, T., Sakaguchi, K., Tanaka, M., Nakashima, K., Takahashi, T., 1997. Structures of mollusc shell framework proteins. *Nature* 387 (6633), 563–564.
- Sullivan, G.E., 1961. Functional Morphology, Micro-anatomy, and histology of the Sydney Cockle *Anadara trapezia* (Deshayes) (Lamellibranchia: Arcidae). *Australian Journal of Zoology* 9 (2), 219–257.
- Sun, J., Bhushan, B., 2012. Hierarchical structure and mechanical properties of nacre: A review. *Royal Society of Chemistry Advances* 2 (20), 7617–7632.
- Sun, J.-y., Tong, J., 2007. Fracture toughness properties of three different biomaterials measured by nanoindentation. *Journal of Bionic Engineering* 4 (1), 11–17.
- Suzuki, M., Nagasawa, H., 2013. Mollusk shell structures and their formation mechanism. *Canadian Journal of Zoology* 91 (6), 349–366.
- Suzuki, M., Saruwatari, K., Kogure, T., Yamamoto, Y., Nishimura, T., Kato, T., Nagasawa, H., 2009. An acidic matrix protein, Pif, is a key macromolecule for nacre formation. *Science* 325 (5946), 1388–1390.
- Swan, E.F., 1956. The meaning of strontium-calcium ratios. *Deep-Sea Research* 4, 71.
- Takesue, R.K., van Geen, A., 2004. Mg/Ca, Sr/Ca, and stable isotopes in modern and Holocene *Protothaca staminea* shells from a northern California coastal upwelling region. *Geochimica et Cosmochimica Acta* 68 (19), 3845–3861.
- Tavener-Smith, R., Williams, A., 1972. The secretion and structure of the skeleton of living and fossil Bryozoa. *Philosophical Transactions of the Royal Society of London B: Biological Sciences* 264 (859), 97–160.
- Taylor, A.M., Maher, W.A., 2012. Exposure-dose-response of *Anadara trapezia* to metal contaminated estuarine sediments. 2. Lead spiked sediments. *Aquatic Toxicology* 116–117, 79–89.
- Taylor, J., Strack, E., 2008. Pearl production. Elsevier: Amsterdam, The Netherlands, 589 pp.
- Taylor, J.D., 1969. The shell structure and mineralogy of the Bivalvia. Introduction. *Nuculacea-Trigonacea. Bulletin of the British Museum (Natural History). Zoology* 3, 1–125.
- Taylor, J.D., 1973. The shell structure and mineralogy of the Bivalvia. II. *Kucinacea-Clavagellacea* conclusions. *Bulletin of the British Museum (Natural History). Zoology* 22, 253–294.
- Taylor, P.D., James, N.P., Bone, Y., Kuklinski, P., Kyser, T.K., 2009. Evolving mineralogy of cheilostome bryozoans. *Palaios* 24 (7), 440–452.

- Taylor, P.D., Kudryavtsev, A.B., Schopf, J.W., 2008. Calcite and aragonite distributions in the skeletons of bimineralic bryozoans as revealed by Raman spectroscopy. *Invertebrate Biology* 127 (1), 87–97.
- Taylor, P.D., Lombardi, C., Cocito, S., 2015. Biomineralization in bryozoans: Present, past and future. *Biological Reviews* 90 (4), 1118–1150.
- Taylor, P.D., Sendino, C., 2010. Latitudinal distribution of bryozoan-rich sediments in the Ordovician. *Bulletin of Geosciences* 85 (4), 565–572.
- Tebo, B.M., 1997. Bacterially mediated mineral formation: Insights into manganese (II) oxidation from molecular genetic and biochemical studies. *Geomicrobiology: Interactions between Microbes and Minerals*, 225–266.
- Tesch, P., Smith, N., Martin, N., Kinion, D., 2008. High current focused ion beam instrument for destructive physical analysis applications, In: *Thirty-fourth International Symposium for Testing and Failure Analysis*. ASM International, 528 pp.
- Thébault, J., Chauvaud, L., Clavier, J., Fichez, R., Morize, E., 2006. Evidence of a 2-day periodicity of striae formation in the tropical scallop *Comptopallium radula* using calcein marking. *Marine Biology* 149 (2), 257–267.
- Trimby, P.W., Cao, Y., Chen, Z., Han, S., Hemker, K.J., Lian, J., Liao, X., Rottmann, P., Samudrala, S., Sun, J., 2014. Characterizing deformed ultrafine-grained and nanocrystalline materials using transmission Kikuchi diffraction in a scanning electron microscope. *Acta Materialia* 62, 69–80.
- Turnbull, D., Fisher, J.C., 1949. Rate of nucleation in condensed systems. *The Journal of Chemical Physics* 17 (1), 71–73.
- Uozumi, S., Iwata, K., Togo, Y., 1972. The ultrastructure of the mineral in and the construction of the crossed-lamellar layer in molluscan shell. *Journal of the Faculty of Science, Hokkaido University. Series 4, Geology and Mineralogy*= 北海道大學理學部紀要 15 (3-4), 447–477.
- Urey, H.C., Lowenstam, H.A., Epstein, S., McKinney, C.R., 1951. Measurement of paleotemperatures and temperatures of the Upper Cretaceous of England, Denmark, and the southeastern United States. *Geological Society of America Bulletin* 62 (4), 399–416.
- Urmos, J., Sharma, S.K., Mackenzie, F.T., 1991. Characterization of some biogenic carbonates with Raman spectroscopy. *American Mineralogist* 76 (3-4), 641–646.
- Vácz, T., 2014. A new, simple approximation for the deconvolution of instrumental broadening in spectroscopic band profiles. *Applied Spectroscopy* 68 (11), 1274–1278.
- Valiev, R., 2004. Nanostructuring of metals by severe plastic deformation for advanced properties. *Nature Materials* 3 (8), 511–516.
- Volmer, M., Weber, A., 1926. Keimbildung in übersättigten Gebilden. *Zeitschrift für Physikalische Chemie* 119 (1), 277–301.
- Wada, K., Fujinuki, T., 1988. Factors controlling amounts of minor elements in pearls. *Journal of the Gemmological Society of Japan* 13 (1-4), 3–12.
- Wang, D., Wallace, A.F., Yoreo, J.J. de, Dove, P.M., 2009. Carboxylated molecules regulate magnesium content of amorphous calcium carbonates during calcification. *Proceedings of the National Academy of Sciences* 106 (51), 21511–21516.
- Wang, J., Cheng, Q., Tang, Z., 2012. Layered nanocomposites inspired by the structure and mechanical properties of nacre. *Chemical Society Reviews* 41 (3), 1111–1129.
- Wang, R.Z., Suo, Z., Evans, A.G., Yao, N., Aksay, I.A., 2001. Deformation mechanisms in nacre. *Journal of Materials Research* 16 (9), 2485–2493.

- Watabe, N., Wilbur, K.M., 1960. Influence of the organic matrix on crystal type in molluscs. *Nature* 188 (4747), 334.
- Wegst, U.G.K., Ashby, M.F., 2004. The mechanical efficiency of natural materials. *Philosophical Magazine* 84 (21), 2167–2186.
- Wegst, U.G.K., Bai, H., Saiz, E., Tomsia, A.P., Ritchie, R.O., 2015. Bioinspired structural materials. *Nature Materials* 14 (1), 23–36.
- Wehrmeister, U., Götz, H., Jacob, D.E., Soldati, A., Xu, W., Duschner, H., Hofmeister, W., 2004. Visualization of the internal structures of cultured pearls by computerized X-ray microtomography. *Gemmology* 31 (1/2), 15–21.
- Wehrmeister, U., Jacob, D.E., Soldati, A.L., Häger, T., Hofmeister, W., 2007. Vaterite in freshwater cultured pearls from China and Japan. *Journal of Gemmology* 30 (7/8), 269–276.
- Wehrmeister, U., Jacob, D.E., Soldati, A.L., Loges, N., Häger, T., Hofmeister, W., 2011. Amorphous, nanocrystalline and crystalline calcium carbonates in biological materials. *Journal of Raman Spectroscopy* 42 (5), 926–935.
- Wehrmeister, U., Soldati, A.L., Jacob, D.E., Häger, T., Hofmeister, W., 2010. Raman spectroscopy of synthetic, geological and biological vaterite: a Raman spectroscopic study. *Journal of Raman Spectroscopy* 41 (2), 193–201.
- Weiner, S., Addadi, L., Wagner, H.D., 2000. Materials design in biology. *Materials Science and Engineering: C* 11 (1), 1–8.
- Weiner, S., Dove, P.M., 2003. An overview of biomineralization processes and the problem of the vital effect. *Reviews in Mineralogy and Geochemistry* 54 (1), 1–29.
- Weiner, S., Hood, L., 1975. Soluble protein of the organic matrix of mollusk shells: A potential template for shell formation. *Science* 190 (4218), 987–989.
- Weiner, S., Lowenstam, H.A., 1986. Organization of Extracellularly Mineralized Tissues: A Comparative Study of Biological Crystal Growth. *Critical Reviews in Biochemistry* 20 (4), 365–408.
- Weiner, S., Talmon, Y., Traub, W., 1983. Electron diffraction of mollusc shell organic matrices and their relationship to the mineral phase. *International Journal of Biological Macromolecules* 5 (6), 325–328.
- Weiner, S., Traub, W., 1980. X-ray diffraction study of the insoluble organic matrix of mollusk shells. *FEBS Letters* 111 (2), 311–316.
- Weiner, S., Traub, W., Parker, S.B., 1984. Macromolecules in mollusc shells and their functions in biomineralization [and Discussion]. *Philosophical Transactions of the Royal Society of London B: Biological Sciences* 304 (1121), 425–434.
- Weiss, I.M., Tuross, N., Addadi, L., Weiner, S., 2002. Mollusc larval shell formation: Amorphous calcium carbonate is a precursor phase for aragonite. *Journal of Experimental Zoology* 293 (5), 478–491.
- Wolf, S.E., Böhm, C.F., Harris, J., Demmert, B., Jacob, D.E., Mondeshki, M., Ruiz-Agudo, E., Rodriguez-Navarro, C., 2016. Nonclassical Crystallization in vivo et in vitro (I): Process-Structure-Property relationships of nanogranular biominerals. *Journal of Structural Biology* 196 (2), 244–259.
- Wolf, S.E., Lieberwirth, I., Natalio, F., Bardeau, J.-F., Delorme, N., Emmerling, F., Barrea, R., Kappl, M., Marin, F., 2012. Merging models of biomineralisation with concepts of nonclassical crystallisation: Is a liquid amorphous precursor involved in the formation of the prismatic layer of the Mediterranean Fan Mussel *Pinna nobilis*? *Faraday Discussions* 159 (1), 433–448.
- Wu, B., Heidelberg, A., Boland, J.J., 2005. Mechanical properties of ultrahigh-strength gold nanowires. *Nature Materials* 4 (7), 525–529.



- Xu, B., Poduska, K.M., 2014. Linking crystal structure with temperature-sensitive vibrational modes in calcium carbonate minerals. *Physical Chemistry Chemical Physics* 16 (33), 17634–17639.
- Yang, L., Killian, C.E., Kunz, M., Tamura, N., Gilbert, P., 2011. Biomineral nanoparticles are space-filling. *Nanoscale* 3 (2), 603–609.
- Younis, S., Kauffmann, Y., Bloch, L., Zolotoyabko, E., 2012a. Inhomogeneity of nacre lamellae on the nanometer length scale. *Crystal Growth & Design* 12 (9), 4574–4579.
- Younis, S., Kauffmann, Y., Pokroy, B., Zolotoyabko, E., 2012b. Atomic structure and ultrastructure of the *Murex troscheli* shell. *Journal of Structural Biology* 180 (3), 539–545.
- Zhang, C., Liu, S., Phelps, T.J., Cole, D.R., Horita, J., Fortier, S.M., Elless, M., Valley, J.W., 1997. Physiochemical, mineralogical, and isotopic characterization of magnetite-rich iron oxides formed by thermophilic iron-reducing bacteria. *Geochimica et Cosmochimica Acta* 61 (21), 4621–4632.
- Zhang, G., Xu, J., 2013. From colloidal nanoparticles to a single crystal: New insights into the formation of nacre's aragonite tablets. *Journal of Structural Biology* 182 (1), 36–43.
- Zhao, L., Schöne, B.R., Mertz-Kraus, R., 2017a. Controls on strontium and barium incorporation into freshwater bivalve shells (*Corbicula fluminea*). *Palaeogeography, Palaeoclimatology, Palaeoecology* 465, 386–394.
- Zhao, L., Schöne, B.R., Mertz-Kraus, R., Yang, F., 2017b. Insights from sodium into the impacts of elevated pCO<sub>2</sub> and temperature on bivalve shell formation. *Journal of Experimental Marine Biology and Ecology* 486, 148–154.
- Zhou, C., Wing Yan Ho, J., Chan, S., Yixin Zhou, J., Dillon Wong, S., Moe, K.S., 2016. Identification of "Pistachio" Colored Pearls treated by Ballerina Pearl Co. *Gems & Gemology* 52 (1), 50–59.

## APPENDIX

## 8. NANOSCALE DEFORMATION PROCESSES REVEALED IN NACRE OF *PINNA NOBILIS* MOLLUSC SHELL

Jiseok Gim<sup>1</sup>, Noah Schnitzer<sup>1</sup>, Laura M. Otter<sup>2</sup>, Yuchi Cui<sup>1</sup>, Sébastien Motreuil<sup>3</sup>, Frédéric Marin<sup>3</sup>,  
Stephan E. Wolf<sup>4,5</sup>, Dorrit E. Jacob<sup>2</sup>, Amit Misra<sup>1</sup>, Robert Hovden<sup>1,6\*</sup>

<sup>1</sup>Department of Materials Science & Engineering, University of Michigan, Ann Arbor, MI, USA

<sup>2</sup>Department of Earth and Planetary Sciences, Macquarie University, Sydney, Australia

<sup>3</sup>Laboratoire Biogéosciences, Université de Bourgogne Franche-Comté (UBFC), Dijon, France

<sup>4</sup>Department of Materials Science & Engineering, Friedrich-Alexander-University Erlangen-Nürnberg (FAU), Erlangen, Germany

<sup>5</sup>Interdisciplinary Centre for Functional Particle Systems (FPS), Friedrich-Alexander University Erlangen-Nürnberg (FAU), Erlangen, Germany.

<sup>6</sup>Applied Physics Program, University of Michigan, Ann Arbor, MI, USA

\*Corresponding Author: hovden@umich.edu

This chapter has been accepted for publication in Nature Communications as:

J. Gim, N. Schnitzer, **L.M. Otter**, Y. Cui, S. Motreuil, F. Marin, S.E. Wolf, D.E. Jacob, A. Misra, R. Hovden (2019): Nanoscale deformation mechanics reveal resilience in nacre of *Pinna nobilis* shell, Nature Communications.

The author's contribution to the publication is as follows: LMO helped acquire some of the TEM data together with JG and NS during her PGRF-funded lab visit and participated in writing and editing the manuscript.

## Abstract

The combination of soft nanoscale organic components with inorganic nanograins hierarchically designed by natural organisms results in highly ductile structural materials that can withstand mechanical impact and exhibit high resilience on the macro- and nano-scale. Our investigation of nacre deformation reveals the underlying nanomechanics that govern the structural resilience and absorption of mechanical energy. Using high-resolution scanning / transmission electron microscopy combined with in-situ indentation, we observe nanoscale recovery of heavily deformed nacre that restores its mechanical strength on external stimuli up to 80 % of its yield strength. Under compression, nacre undergoes deformation of nanograins and non-destructive locking across organic interfaces such that adjacent inorganic tablets structurally join. The locked tablets respond to strain as a continuous material, yet the organic boundaries between them still restrict crack propagation. Remarkably, the completely locked interface recovers its original morphology without any noticeable deformation after compressive contact stresses as large as 1.2 GPa.

## 8.1 Introduction

The inherent trade-off between strength and toughness inspires new design approaches to structural materials with high damage tolerance. While plastic deformation degrades materials' strength and performance lifetime, it is the key attribute for toughness and resistance to fracture. Thus, overcoming the trade-off between toughness, strength, and resilience remains a fundamental design challenge for structural materials (Ritchie, 2011). In this sense, the selection and design of modern high-performance structural materials is driven by optimizing combinations of the mechanical properties and requirements for predictable and non-catastrophic failure (Hofmann et al., 2008; Valiev, 2004). Nature has optimized high-performance materials with unrivalled strength, toughness, and resilience using 3D hierarchical architectures that traverse the atomic, nano-, micro-, to macro-scale with precision that human technology is yet to achieve (Gao et al., 2003).

Among the diverse set of structural biominerals—such as bone (Espinosa et al., 2009), enamel (Nalla et al., 2003), and various biosilica (Gilbert et al., 2005)—to be mimicked for designing new synthetic structural materials, nacre is the prototypical super-material (Espinosa et al., 2009; Meyers et al., 2013; Ritchie, 2011; Wegst et al., 2015; Wegst and Ashby, 2004). After crack initiation, bulk nacre shows a 40-fold higher fracture toughness than the monolithic/single crystal calcium carbonate from which it is constructed (Barthelat et al., 2007; Espinosa et al., 2009; Jackson et al., 1988; Meyers et al., 2008; Sun and Bhushan, 2012). Thus, a central focus has been placed on understanding the principle mechanisms of nacre's excellent mechanical properties to inspire new designs of next-generation high-performance structural materials (Barthelat et al., 2007; Currey, 1977; Espinosa et al., 2009; Espinosa et al., 2011; Evans et al., 2001; Jackson et al., 1988; Li et al., 2004; Li et al., 2006; Meyers et al., 2008; Smith et al., 1999; Song et al., 2003; Wang et al., 2001). However, nacre's ability to undergo limited deformation and dissipate critical stresses before fracture has not yet been quantified nor correlated with nanomechanical processes.

Nacre is constructed from layered interdigitated polygonal (or pseudo-hexagonal) aragonite ( $\text{CaCO}_3$ ) platelets (0.5 to 1  $\mu\text{m}$  thick and 10-20  $\mu\text{m}$  wide), bonded by a thin ( $\sim 5\text{--}30$  nm thick) layer of organic material (the interlamellar membrane). Nacre platelets are either arranged into a brick and mortar like architecture in the sheet nacre of bivalves, or are stacked vertically as columnar nacre in gastropods (Jacob et al., 2008; Kobayashi and Samata, 2006; Nudelman, 2015; Schmidt, 1924). A natural composite material, nacre is reported to consist of roughly 95-98 wt.% aragonite and  $\sim 2\text{--}5$  wt.% biopolymers (Bourrat et al., 2007; Dauphin et al., 2006; Evans et al., 2001; Gu et al., 2017; Jackson et al., 1990; Nudelman, 2015; Smith et al., 1999; Wang et al., 2001). Our measurements herein confirm a  $3.4 \pm 1.0$  wt.% organic fraction for *Pinna nobilis* (Mollusca, Bivalvia). The organic fraction of nacre consists of organic interlamellar membranes (Younis et al., 2012a) and intracrystalline organics embedded in the mineral tablets (Checa et al., 2011; Gries et al., 2009a; Younis et al., 2012a) of  $\sim 5\text{--}20$  nm. Nacre tablets have a textured surface roughness and internal substructure that are both derived from space filling nanogranules (Dauphin, 2001; Hovden et al., 2015; Jacob et al., 2008; Wolf et al., 2016; Yang et al., 2011). The surface contains nano-asperities suspected to play an important role in the prevention of tablet sliding (Barthelat et al., 2006). Surface asperities between opposing nacre tablets occasionally form narrow (20- 50 nm) intrinsic mineral bridges (Checa et al., 2011) without external stress (e.g. Supplementary Figure 8.1) connecting across the interlamellar membrane, while wider (150-200 nm) major intrinsic mineral bridges are thought to be involved in the initial formation of new nacre tablets (Nudelman, 2015; Younis et al., 2012a).

In nacre, Wegst et al. (2015), have suggested that crack bridging and the resulting ‘pull-out’ of mineral bricks is associated with controlled, yet limited, sliding of the aragonite layers over each other and is aided by visco-plastic energy dissipation in the organic layer. Li et al. (2004) and Li et al. (2006) observed the plastic deformation of aragonite surfaces under tensile load at the nanometre level using atomic force microscopy (AFM). However, additional mechanisms for strengthening and toughening have been proposed: resistance from the lamellae nanoroughness (Evans et al., 2001), the organic layer acting as a viscoelastic glue (Espinosa et al., 2011; Gilbert et al., 2005; Smith et al., 1999; Wang et al., 2001), the presence of (pre-existing) mineral bridges (Gu et al., 2017; Meyers et al., 2008; Song et al., 2003), and platelet interlocking at the microscopic level (Espinosa et al., 2011). Direct observation is required to disambiguate the mechanism of nanomechanical deformation of nacre; however, most knowledge of the biomineral toughening process is assembled from microscale tribology (Currey, 1977; Jackson et al., 1988; Wang et al., 2001; Wegst and Ashby, 2004), tensile (Barthelat et al., 2007; Currey, 1977; Espinosa et al., 2009; Espinosa et al., 2011; Evans et al., 2001; Jackson et al., 1988; Smith et al., 1999), or compression (Barthelat et al., 2007; Evans et al., 2001; Menig et al., 2000) testing on bulk specimens. Understanding nanomechanical responses across the 3D hierarchical architectures is critical to understanding how the individual nacre components work together to create properties greater than the sum of their parts (i.e. far exceeding the rule of mixtures, Wegst et al., 2015).

Our investigation of toughening strategies in nacre reveals nanomechanical deformation of organic interfaces, nanocrystallites, and organic inclusions as key to the increased damage tolerance of nacre.



High-resolution scanning / transmission electron microscopy (S/TEM) combined with in-situ nano-indentation (Minor et al., 2006; Stach et al., 2001) has been adapted to biomineral systems to allow sub-nanometre resolution imaging of the nanomechanical deformation processes and provide precise assessment of when and where fracture occurs. We show that during compressive indentation nacre undergoes non-destructive locking where inorganic tablets come into contact across organic interfaces. Remarkably, the completely locked interface recovers its original morphology without any deformation after releasing compression and retains its full mechanical strength. During compression, the aragonite grains and organic inclusions reversibly rotate and deform indicating nanoscale resilience of the nacre tablets. Prior to tablet locking, strain attenuates up to 80 % between the decoupled tablets. However, by 3 % engineering strain of the first tablet, the tablets have locked to redistribute stress continuously across the organic interface and the strain attenuation decreases.

When fracture occurs, we show the organic components restrict crack propagation both within and between tablets, sustaining the overall macroscale architecture through multiple fractures to allow further structural loading. This allows nacre to absorb significantly greater mechanical energy than monolithic aragonite. We report that nacre absorbs roughly 1-3 times more mechanical energy than geological (i.e. non-biogenic) monolithic aragonite before fracture results in structural failure under nanoindentation. This approach provides an energy dissipation measurement that is not derived from a crack-propagating force. In addition, we show that the yield strength measured under nanoscale compression along the c-axis (growth direction) of a single tablet can reach values three times higher (e.g. ~1.1-1.6 GPa) than previously reported for bulk nacre measured with micro-indentation (Barthelat et al., 2006; Barthelat et al., 2007; Currey, 1977; Espinosa et al., 2009; Jackson et al., 1990; Lin, 2008; Menig et al., 2000; Meyers et al., 2008; Ritchie, 2011; Wang et al., 2001).

## 8.2 Materials and methods

### 8.2.1 Sample material

Specimens of the protected Mediterranean *P. nobilis* (Pinnidae, Linnaeus) bivalve species were live collected in the bay of Villefranche-sur-Mer, Département Alpes-Maritimes, France. All necessary permits were acquired from DDTM (Direction Départementale des Territoires et de la Mer) of Alpes-Maritimes department. *P. nobilis* is strongly protected by a European Directive (92/43/CEE). Specimens of the geological monolithic aragonite were mined in Sefrou, Morocco.

### 8.2.2 Sample preparation

After the bivalves were sacrificed, small shell sections were cut from the whole shell measuring 60 cm shell height (Hovden et al., 2015) using a diamond wire saw. To avoid beam damage and amorphisation from ion beam milling, cross-sections for S/TEM were prepared by mechanical wedge polishing (Hovden et al., 2015). This technique provided large-area, electron-transparent specimens with structural stability critical for nanotribology. Nacre samples had thicknesses of  $124 \pm 3$  nm (Figure 8.4a-

c),  $98 \pm 2$  nm (Figure 8.3a), prismatic calcite had a thickness of  $102 \pm 6$  nm (Figure 8.4d-f), monolithic aragonite had a thickness of  $169 \pm 1$  nm (Figure 8.4g-i).

### 8.2.3 Electron microscopy

Real-time observation of the compressive nano-deformation was performed using scanning and transmission electron microscopy (S/TEM). Column pressure in the TEM column at the specimen was  $\sim 1 \times 10^7$  torr. Bright field transmission electron microscopy with 60  $\mu\text{m}$  (for nacre) and 120  $\mu\text{m}$  (for biogenic prismatic calcite) apertures provided contrast of strain contours and performed on a 200 keV JEOL 2010F and Gatan OneView camera enabling frame rates of up to 200 frames per second. Images were captured at 50 frames ( $2048 \times 2048$  pixels) per second for nacre, and at 12.5 frames ( $2048 \times 2048$  pixels) per second for biogenic prismatic calcite and monolithic aragonite. STEM was performed using a JEOL 3100R05 microscope with Cs aberration corrected STEM (300 keV, 22 mrad) and cold field emission gun. A HAADF detector with 120–150 mm camera lengths and a detector angle of 59–74 (inner) – 354–443 mrad (outer) were used to produce Z-contrast images where greyscale intensity is sensitive to the atomic number in the specimen's matrix.

No change was observed in mechanical behaviour measurements with beam exposure: whether the beam was blanked, or the microscope was operated in low-dose STEM or TEM mode. Low-dose methods, beam shuttering, and examination of regions exposed to the beam were used to separate electron beam irradiation from intrinsic phenomena. For STEM measurements, with a typical field of view of 500 nm the electron dose was typically  $\sim 150 \text{ e}^-/\text{\AA}^2$  and dose rates around  $\sim 4 \text{ e}^- \cdot \text{\AA}^{-2} \cdot \text{s}^{-1}$  the material was structurally preserved during imaging. However, for the same imaging conditions at higher magnifications (e.g. 30 nm field of view) the radiation dose increases to  $\sim 2 \cdot 10^5 \text{ e}^-/\text{\AA}^2$  and dose rate to  $\sim 10^3 \text{ e}^- \cdot \text{\AA}^{-2} \cdot \text{s}^{-1}$  which causes the material to show electron irradiation damage localized to the small field of view. Thus, larger fields of view are preferred to minimize dose and provide a large area of observation where fracture may nucleate. Atomic resolution STEM requires a small field of view, on-axis region of interest, and a static specimen which was not achievable during in-situ nanoindentation. This limits atomic imaging during nanoindentation despite the well-aligned instrument's probe limited resolution of  $\sim 1 \text{\AA}$ . For TEM imaging, dose was minimized through use of a heavily diverged beam and a high efficiency camera (DQE of 0.3) with single electron sensitivity and high-readout speed (up to 300 fps). Low-loss electron energy loss spectra (EELS) were acquired at 300 kV with a Gatan Quantum Energy Filter, with 1.5 eV per channel to determine thickness of the specimen. The convergence semi-angle was 22 mrad and the collection semi-angle was approximately 40 mrad. Linear combination of power laws (LCPL) with local background averaging (LBA) was applied to analyse the spectrum image using the Cornell Spectrum Imager (Cueva et al., 2012). Thickness of the specimen is determined from plural scattering in an electron energy loss spectrum, which is defined by  $I_0 = I_{\text{ZLP}} \cdot e^{t/\lambda}$  where  $I_0$  is total plural scattering in electron loss spectrum,  $I_{\text{ZLP}}$  is zero loss peak in the spectrum,  $t$  is the thickness of the nacre, and  $\lambda$  is the wavelength of the incident electron beam, as described in (Egerton, 2011). Relative organic concentration in nacre tablet was formulated by ratio of high-angle elastic electron scattering

intensity, which is defined by  $I_{\text{HAADF}} = t \cdot \sum Z_x^2 \cdot \rho$  where  $I_{\text{HAADF}}$  is the high-angle annular dark field intensity,  $t$  is the thickness of the nacre,  $x$  is a certain element in  $\text{CaCO}_3$  or organic molecule,  $\gamma$  is elastic scattering cross-section ranging from 1.4 to 1.7 and  $\rho$  is the  $\text{CaCO}_3$  or organic molecular density (Supplementary Figure 8.2).

#### 8.2.4 *In-situ nanoindentation*

Nanoindentation experiments were conducted in the TEM column ( $\sim 25^\circ\text{C}$ ,  $10^{-6}$  Torr) using a Hysitron PI-85 PicoIndenter. Load-controlled nanoindentation was performed using cube corner (tip radius =  $\sim 0.1\ \mu\text{m}$ , half-angle =  $35.26^\circ$ , included angle =  $90^\circ$ ) and conospherical (tip radius =  $\sim 1\ \mu\text{m}$ , semi-angle =  $60^\circ$ ) diamond probe tips. Maximum loads varied from 10 to 400  $\mu\text{N}$ . A piezoelectric actuator controlled the specimen position in all three dimensions. During indentation the indenter was fixed, and the specimen was advanced at a rate of 5 nm/s for nacreous aragonite and prismatic calcite and at a rate of 60 nm/s for monolithic aragonite. Force–displacement information and movies were recorded during indentation, and still TEM micrographs were collected between tests. The electrostatic force constant of the transducer was calibrated such that the root-mean-square error fell below  $\sim 10^{-5}\ \mu\text{N}/\text{V}^2$  using Z-axis calibration, which results in the measurement error in force and displacement within  $\pm 5\%$ . The top surface of the tip was aligned vertically to the cross-sectional nacre specimen to achieve uniaxial compression without shear or bending. For all the samples, contact stress is calculated through dividing the measured load by cross-sectional area of the specimen in contact with the indenter tip. This contact area is estimated by multiplying the length of the contact region measured in real-time with S/TEM images and the specimen cross-sectional thickness measured by the ratio of zero loss / total low loss electron energy loss spectrum captured with EELS. Total error of contact stress is calculated by a quadrature of the errors from the contact length measured by human vision ( $\pm 10\%$ ), the specimen thickness estimated by EELS spectrum image ( $\pm 11\%$ ), and the load reported by the nanoindentation software ( $\pm 5\%$ ). The contact area changes through series of indentations (Figure 8.3) due to stage drift (typically 20 - 60 nm). Toughness ( $\text{J}/\text{m}^2$ ) is defined as the absorbed mechanical energy, which can be bounded by integrating the stress-displacement curve to find the energy absorbed per unit area (Figure 8.4j). The tablet engineering strain along the c-axis is defined as the ratio of the reduction of the tablet width (that is, compressive deformation directly under the region of loading) to its initial width (Supplementary Figure 8.6). Strain attenuation is defined as the ratio of the measured tablet engineering strain between the first and the second tablet from the indenter tip contact location (Supplementary Figure 8.6).

#### 8.2.5 *Triboindentation*

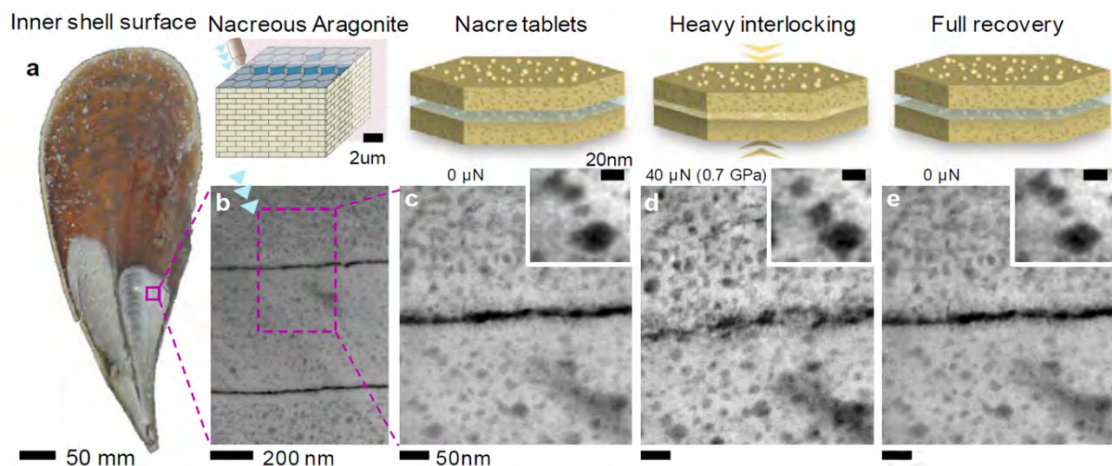
Triboindentation experiments were carried out on bulk biological aragonite, calcite and geological aragonite samples (5 mm  $\times$  5 mm area, 3 mm thick) with polished surfaces to determine the elastic modulus of the materials using a Hysitron TI-950 Triboindenter. During indentation the indenter was fixed, and the specimen was advanced at a rate of 20 nm/s for nacre, prismatic calcite and monolithic aragonite. A Berkovich tip (i.e. three-sided pyramidal diamond tip) was used for nano indentation. Since

the mechanical properties extracted from the indentation are sensitive to the tip geometry, the tip area function has to be calibrated before determining the mechanical properties accurately. This calibration which was conducted using a standard quartz sample. The tip area function was calibrated in the low depth ranges for precise determination of the modulus. Using this area function, nano-indentation experiments were performed on an Al single-crystal to cross check the standard elastic modulus,  $E$ , and hardness,  $H$ , values prescribed by the manufacturer ( $75.1 \pm 5$  % GPa and  $360 \pm 10$  % MPa, respectively). The standard deviation is within 5 % for both these values, validating the tip calibration process.

## 8.2 Results

### 8.2.1 Nanoscale deformation and toughening processes

We observe non-linear elastic nanoscale deformation and toughening processes in nacre under compression using nano-indentation with  $0.04 - 0.2 \mu\text{m}^2$  contact areas approximately normal to the growth direction (c-axis). This surface normal is nacre's strongest direction (Barthelat et al., 2006; Jackson et al., 1988; Meyers et al., 2008), although the monolithic aragonite from which it is comprised is stiffer along the planar direction (Agbaje et al., 2017b). Electron transparent cross-sections from a mature *P. nobilis* specimen (Figure 8.1a) provided the structural stability required for indentation while allowing sub-nanometre resolution imaging (see methods). S/TEM observation revealed a range of strengthening and toughening processes enabled by nacre's hierarchical structure: (i) tablet interlocking, (ii) strain damping, (iii) crack blunting, and (iv) intracrystalline deformation and rotation of nanograins and organics. Despite comprising only a few weight percent (i.e.  $\sim 2$  to 5 wt.%, Bourrat et al., 2007; Dauphin et al., 2006; Evans et al., 2001; Gu et al., 2017; Jackson et al., 1990; Nudelman, 2015; Smith et al., 1999; Wang et al., 2001) of the entire nacre architecture, the organic components of nacre provide a range of functions that absorb the energy of applied loads while remaining highly recoverable even after initial fracture. The ratio of high-angular annular dark-field (HAADF) STEM intensity estimates the total organic volume fraction in *P. nobilis* nacre to be  $7.1 \pm 2.2$  vol. % ( $3.4 \pm 1.0$  wt.%) comprised of  $2.5 \pm 0.3$  vol. % ( $1.2 \pm 0.1$  wt.%) interlamellar and  $4.6 \pm 1.9$  vol. % ( $2.2 \pm 0.9$  wt.%) intracrystalline material (see Supplementary Figure 8.2).



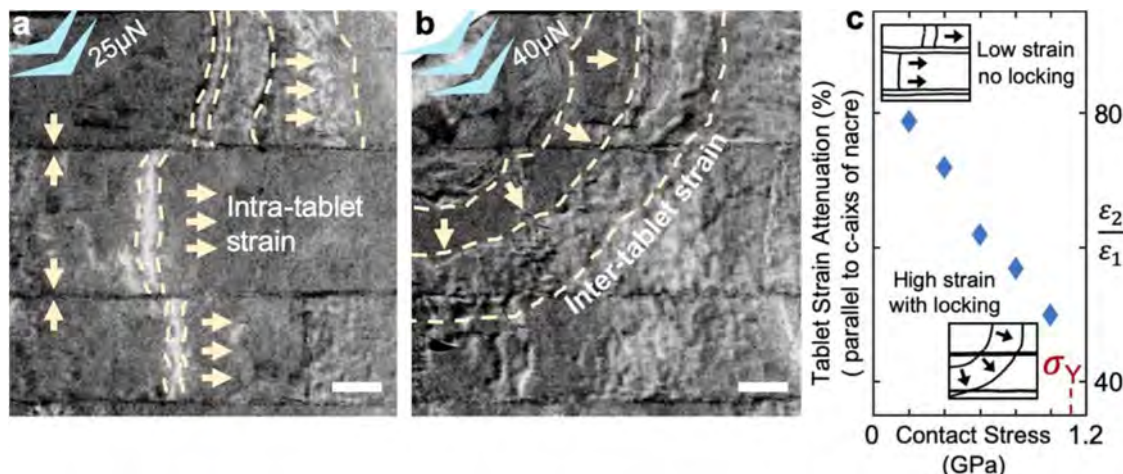
**Figure 8.1: Highly deformed and recovered nacre. a.** Schematic of the inner shell surface of the bivalve mollusc *P. nobilis*, with the investigated area marked by a purple square. **b.** HAADF STEM overview image

of cross-sectional interface of nacre tablets before compression. c. High resolution STEM image of two tablets and their organic interface before compression. d. Tablets heavily interlocked under 40  $\mu\text{N}$  compressive load. e. After indenter is retracted, tablets and organic interface have fully recovered their initial morphology. Insets show the movement of organic inclusions due to the deformation of the tablet and their complete recovery after removing the compressive load.

### 8.2.2 Highly recoverable nacre tablet locking

Nacre's nanoscale organic boundaries and inclusions allow heavily deformed nacre to fully recover its original morphology on the nanoscale (Figure 8.1, Supplementary Figure 8.3, 8.4). Under large compressive loads (e.g. 0.7 GPa in Figure 8.1d), opposing nacre tablets interlock across the mineral-organic interface to form temporary inorganic connections through the joining of asperities. Further, the entire tablet volume compresses resulting in small but discernible deformation of organic inclusions (Figure 8.1). After releasing the load, the mineral connections at the deformed organic interface and the intratablet nanostructure perfectly recover their initial morphology without any sustained deformation (Figure 8.1e, Supplementary Figure 8.3a-d). This remarkable recovery after tablet locking was reproduced and observed across all areas of interest (Supplementary Figure 8.3, 8.4).

Nacre shows mechanical response regimes of high and low compression visible in the strain contours measured during in-situ TEM indentation (Figure 8.2). Low compressive loads applied along the growth direction generate strain contours which propagate transversely within each tablet (Figure 8.2a). Shearing of the interlamellar membranes prevent propagation longitudinally to neighbouring tablets. At higher loads, tablets couple, coming into direct contact with one another and allowing strain contours to spread across tablets radially from the location of indentation (Figure 8.2b). Strain along the c-axis is highest directly below the tip loading and tablet compression (tablet engineering strain) is measurable using interlamellar demarcation (Supplementary Figure 8.6). By  $\sim 3\%$  engineering strain in the first tablet, the contours redistribute continuously and by  $\sim 6\%$  engineering strain, locking is strikingly visible between tablets. Initially, the engineering strain of the first to second tablet along the axis of indentation decreases by over  $\sim 80\%$  when measured using a  $0.1\ \mu\text{m}^2$  contact area. This measurement is only one component of an inhomogeneous strain field that on-average, dissipates away from the point of compression. As greater contact stress is applied, the tablets increasingly lock farther away from the tip and the strain attenuation linearly decreases—the deformability is reduced as the nacre behaves more like a monolithic material (Figure 8.2c). This entire process occurs with elastic processes that are fully repeatable. We note, tablets also exhibit a limited amount of locking for indentation parallel to the tablet plane (Supplemental Figure 8.5). This occurred near the indentation tip where stress is high, and the Poisson effect pushes the compressed tablet against its neighbours. Further away, unlocked tablets accommodate shear deformability at their interface and strain contours are discontinuous. Indentation parallel to the tablet plane was less resilient and typically resulted in unrecoverable brittle fracture (Supplemental Figure 8.5).



**Figure 8.2: Strain propagation confined by organic interfaces. a-b. Bright field TEM (contrast inverted) on the cross-sectional nacreous region under low and high compressive contact stresses. Under low compressive stress, intra-tablet strain contours are generated, and strain propagates independently along each tablet. As the compressive stress is increased, nacre tablets interlock and larger inter-tablet strain contours propagate diagonally between tablets. c. Tablet strain attenuation along the axis of the indentation source. The linear strain dissipation behaviour indicates that the deformability of nacre is weakened as the applied stress is increased. Scale bar 200 nm.**

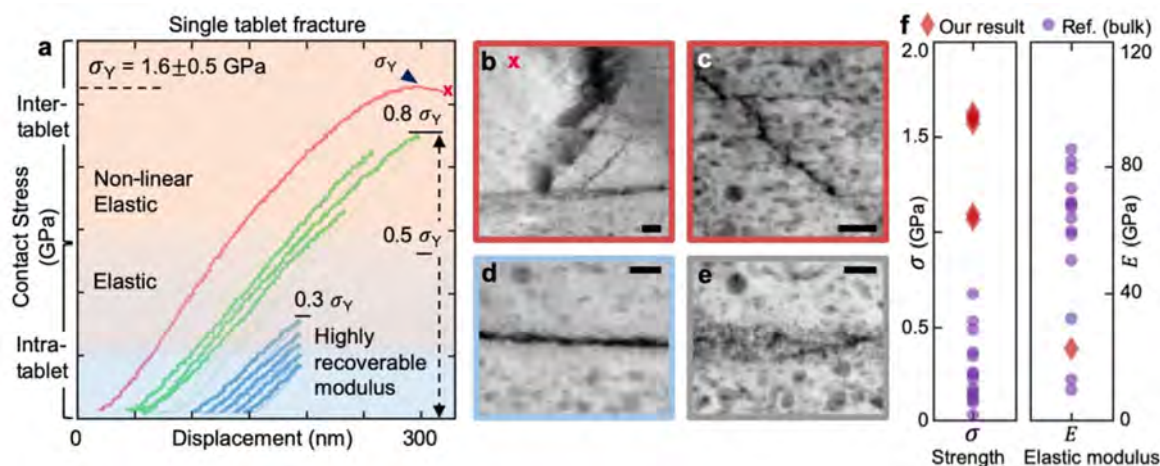
### 8.2.3 Preservation of mechanical strength

During consecutive indentation tests, highly deformed nacre fully recovers under external loads up to ~80 % of its yield contact stress. This can be seen in Figure 8.3a, where the elastic modulus remains unchanged during eight-consecutive compressions (blue and red). As shown in the specimen of Figure 8.3d-e, beyond ~0.8 GPa, nacre begins non-linear elastic deformation—yield is visible from the decreasing slope of the contact stress-displacement curve. However, unlike traditional plastic deformation, the initial structure is preserved after unloading. Full recovery was even observed in highly deformed nacre (e.g. above ~0.8-1.1 GPa) prior to crack formation (Figure 8.1, Supplementary Figure 8.3, 8.4). This preservation of mechanical strength under repeated loading/unloading cycles reflects a non-linear elastic deformation process featuring nanomechanical resilience not present in traditional bulk materials, attributable at least in part to tablet interlocking. The rotation and deformation of organic inclusions and nano-granularity has also been predicted as another mechanism for viscoelasticity (Li et al., 2006). Although structurally recoverable locking of tablets is key to nacre's resilience, in the reported nanoindentation experiments, performed under dry conditions, the absorbed energy appears to primarily occur within the resilient deformation of nanograined tablets that constitute a significant volume fraction (~ 97 %). This process is confirmed in our bright field TEM data, where individual aragonite nanograins change contrast as nanograins reorient and organic inclusions slightly reshape their volume (Supplementary Figure 8.7, Supplementary Movie 1).

The deformation of these nanometre scale organic inclusions with compression of the material accommodates the load while avoiding irrevocable damage to the inorganic matrix (Figure 8.1c-e, also shown in insets of Supplementary Figure 8.3, 8.4, and Supplementary Figure 8.7). Here, nacre's response shows non-linear elastic deformation distinct from that expected in analogous nanocrystalline metals. Unlike nano- or micro-grained metals, which strengthen through reduced mobility of dislocations at grain boundaries (Hall, 1951; Petch, 1953), nacre's proteinaceous organic components

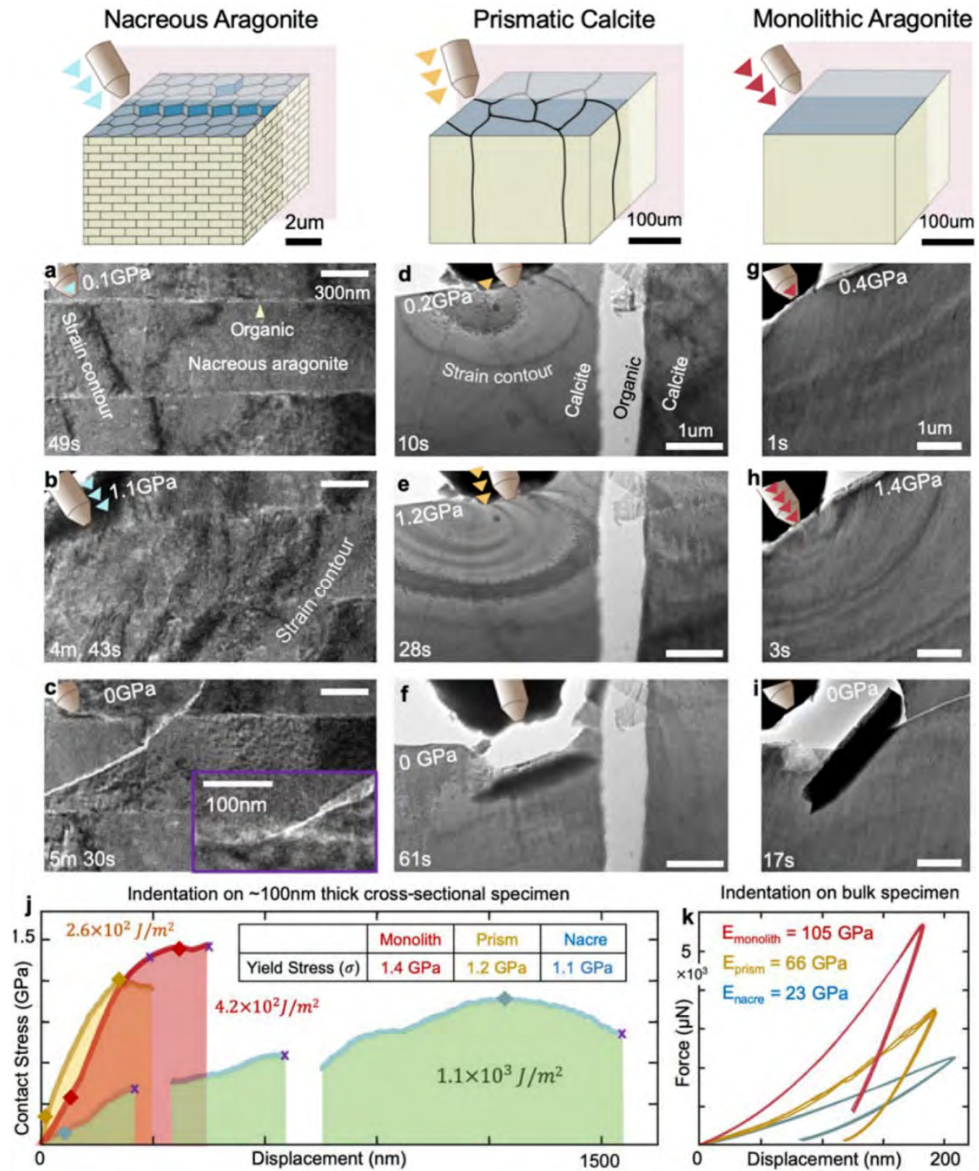


contain flexible molecular bonds that elastically accommodate strain and rotation of nanograins and restoratively return the system to the original state when an external stress is released. This process occurs without the introduction of dislocation pile-up and plastic deformation. Energy absorption during protein stretching / unfolding and subsequent energy release upon refolding of the elastomeric molecules provides high resilience in nacre and similar to that found in bone (Fantner et al., 2005). In contrast, nanocrystalline or nano-twinned metals have lower resilience since they exhibit plasticity via dislocations.



**Figure 8.3: Recoverable mechanical strength of nacre and crack blunting within and between tablets. a.** Nine consecutive *in situ* TEM compression tests on the same nacreous tablet. Three different colour correspond to different contact areas during the series of the compressions. Stage drift caused changes to contact area between indentations. **b.** ADF STEM images after the series of the indentation tests showing a crack blunted by an organic boundary. **c.** ADF STEM image shows crack formed within tablet and blunted by an organic inclusion. **d-e.** ADF STEM images of Nacre tablet compressed by 47  $\mu$ N (55 % of  $\sigma_{Yield}$ ), corresponding to the non-linear elastic regime, structure remains fully recoverable—after deformation nacre still preserves both its initial strength and structure. **f.** Strength and elastic modulus of nacre from contact stress in nanoindentation on the thin cross-sectional specimen in this study and various types of testing – microscale tribology, tensile, compression, and bending– on bulk specimens in previous reports. Scale bar 50 nm.

At failure, the organic components in nacre impede crack propagation both within and between tablets (Figure 8.3b-c, 4c, Supplementary Figure 8.8). The smaller organic inclusions embedded within the inorganic matrix hinder crack propagation within the tablet and were observed to blunt and deflect cracks (Figure 8.3c). The interlamellar membrane likewise hampers propagation between tablets, where cracks often terminate or jump at the interface (Figure 8.3b). After each fracture event, the overall macroscale architecture is preserved and maintains its mechanical properties (Figure 8.4a-c, Supplementary Figure 8.9, Supplementary Movie 2). This extends the damage tolerance of the superstructure beyond a single fracture. In fracture mechanics (Evans and Charles, 1976), the ability to resist fracture is quantified by a fracture toughness when a crack is present. In this complex material local stress states can lead to a variety of mechanisms responsible for the fracture process zone. Here, cracks can be under mixed mode loading conditions, which in general can lead to differences in the energy required for crack extension and make quantification of fracture toughness by nanoindentation challenging. In bulk specimens loaded in mode I, a fracture toughness of 10  $\text{MPa}\cdot\text{m}^{1/2}$  has been reported for nacre, 40-fold larger than that of single crystal aragonite,  $\sim 0.25 \text{ MPa}\cdot\text{m}^{1/2}$  (Barthelat et al., 2007; Barthelat and Espinosa, 2007).



**Figure 8.4: Toughening processes of nacre, prismatic calcite, and monolithic aragonite.** a-c. Bright field TEM images of the cross-sectional nacreous region during *in situ* TEM indentation. The nacreous tablets made contact on the side of the tip (tip diameter:  $\sim 100 \text{ nm}$ ). Inset in (c) shows crack blunting at the organic interface. d-f. Bright field TEM images of the cross-sectional prismatic calcite region during indentation. g-i. Bright field TEM images of non-biogenic, monolithic aragonite during indentation. j. Correlative compressive contact stress vs. displacement curve showing mechanical response of the nacreous, prismatic, and monolithic region. Stress herein is engineering stress calculated by dividing load by cross-sectional area contacted with tip. Total energy dissipation values (area under contact stress-displacement curves) marked. k. Triboindentation on bulk specimens of nacre, prismatic calcite, and monolithic aragonite. Videos provided as Supplemental Material. (See Supplemental Movie 2, 3, 4).

#### 8.2.4 Damage-tolerance of nacre's architecture

On a system level, nacre can sustain several fractures before total failure due to its hierarchical soft-hard matter design. This means the yield stress of nacre is not typically defined by crack initiation. In contrast, prismatic calcite and monolithic aragonite exhibits limited deformation before the yield stress is followed by catastrophic failure or crack runaway (Figure 8.4d-i, Supplementary Figure 8.10, 8.11, Supplementary Movie 3, 4) from cone cracking at indentation. Monolithic aragonite responds to strain with stress contours radiating from the point of contact. Prismatic calcite from the *P. nobilis* mollusc—behaved similar to monolithic aragonite however indentation near an organic interface showed significant attenuation into an adjacent prism (Figure 8.4e). When compared to monolithic calcite

materials, we clearly see nacre's interlamellar membranes reshape compressive strain fields. Both biogenic calcite from the prismatic layer of *P. nobilis* and geological monolithic aragonite were noticeably stiffer than nacre (Figure 8.4k) and typically reached higher yield stresses than nacre (Figure 8.4j). However, nacre's inorganic-organic architecture reliably absorbed 1-3 times more mechanical energy than prismatic calcite and monolithic aragonite before total failure. Integrating the applied stress over the displaced volume of the indenter contact area provides an upper bound on nacre's energy dissipation of  $1.1 \times 10^3 \text{ J/m}^2$ . Here, nanoindentation provides us with true estimates of the energy required to cause fracture(s) that lead to structural degradation. A typical contact stress-displacement curve for nacre often included several intermediate failures, where cracking was halted, nanoscale morphology of nanograins and organic inclusions was preserved, and nacre could undergo further loading without a noticeable change of structure in its mechanical response. Notably, in calcite and monolithic aragonite crack runaway occasionally allowed noticeable energy absorption—however this occurred after the maximum yield stress and resulted in the unrecoverable structural failure typically found in brittle materials.

In-situ nanoindentation enables mechanical behaviour to be measured at the single tablet level, allowing the contributions of the toughening and resilience mechanisms across length scales to be assessed. For instance, while the elastic modulus of nacre and calcite from *P. nobilis* were comparable to previous reports on bulk specimens (Barthelat et al., 2006; Barthelat et al., 2007; Currey, 1977; Fitzer et al., 2015; Jackson et al., 1990; Kunitake et al., 2013; Li et al., 2004; Merkel et al., 2009; Okumura and Gennes, 2001; Song et al., 2003; Stempflé et al., 2010; Sun and Tong, 2007; Wang et al., 2001) (Figure 8.3f, Supplementary Figure 8.12), the measured strength of nano-indented nacre reached values as high as  $1.6 \pm 0.2 \text{ GPa}$ , roughly three times larger than the literature reports for bulk nacre in hydrated and dehydrated specimens (Barthelat et al., 2006; Barthelat et al., 2007; Currey, 1977; Espinosa et al., 2009; Jackson et al., 1990; Lin, 2008; Menig et al., 2000; Meyers et al., 2008; Ritchie, 2011; Stach et al., 2001; Wang et al., 2001). Dehydrated nacre has been shown to have a greater strength and elastic modulus, but lower toughness than hydrated nacre due to the plasticizing of the organic matrix by water (Jackson et al., 1988). Here the *P. nobilis* specimen was sacrificed and dehydrated. In native conditions, the performance of nacre should be even better, we underestimate the recoverability of nacre under conditions of low-pressure, low-hydration and overestimate its tendency to fracture. Typically, nanoindentation in the thin cross-sectional specimens of the nacre and calcite from *P. nobilis* and geological monolithic aragonite also resulted in a yield strength (e.g.  $1.1 \pm 0.1 \text{ GPa}$ ) larger than previously reported bulk values (Figure 8.3f, Supplementary Figure 8.13). The high strength may be attributed to the finite size of the indentation tip and nanoscale size effects of the mechanical response. As previously observed in several materials—including gold nanowires (Wu et al., 2005), polycrystalline thin films (Espinosa et al., 2004), and multi-walled carbon nanotubes (Peng et al., 2008)—the size effects on mechanical properties of nanostructured materials deviate from bulk and necessitate the use of in-situ nanomechanical testing (Bhowmick et al., 2019; Minor and Dehm, 2019).

## Discussion

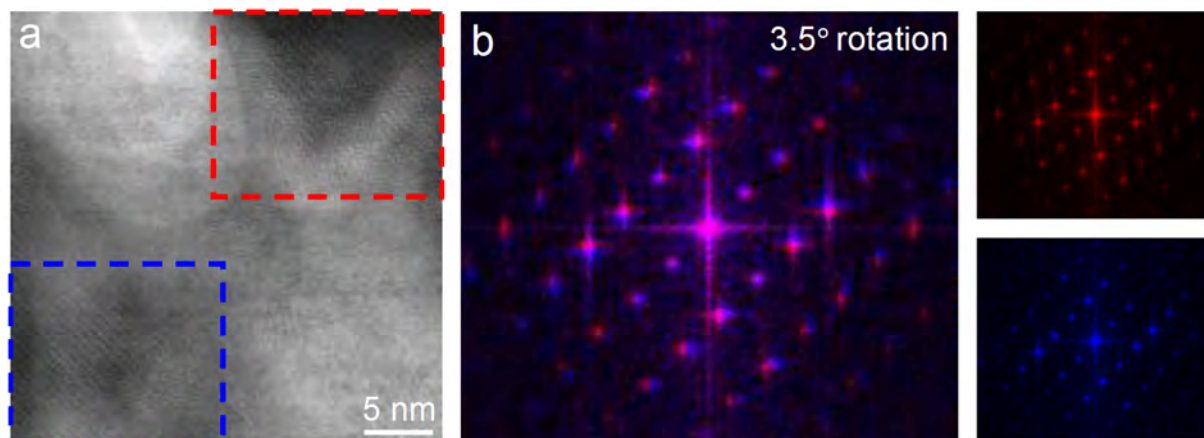
The present *in-situ* S/TEM nanoindentation study illuminates nacre's distinct non-linear elastic deformation processes that provide high resilience. We see how large forces can drive nacre into locked states that allow the material to distribute strain across tablets and recoverably absorb energy through inorganic and organic compression, nanograin reorientation, and the deformation of organic inclusions. After the load is removed, locked nacre completely recovers both its original morphology and mechanical strength. Even after fracture, failure is mitigated through barriers to crack propagation that preserve the macroscale architecture and allow nacre to retain its mechanical properties and further sustain impact. The material's structure and deformation mechanisms allow it to absorb more mechanical energy than geological monolithic aragonite and biogenic prismatic calcite. Using *in-situ* S/TEM nanoindentation, the mechanical properties of the material were tested down to the individual tablets where yield  $\sim 3$  times stronger than bulk measurements were observed. This approach enables investigation of the wider range of evolutionary optimized biomineral to reveal advantages underlying each's nanomechanical design. The study of deformation and fracture under nanoindentation is a subset of the broader fracture phenomena in nacre and other biological materials which may reveal additional nanomechanical responses to external forces such as tensile strain or shear. The observed mechanisms reported in this work may guide theoretical models of deformation behaviour, and the demonstration of *in situ* S/TEM nanoindentation of nacre opens the possibility of other *in situ* S/TEM such as bending, tensile, etc. across a wider range of biological and bio-inspired composites. For nacre under compression, the rich multiscale resilient deformation processes and interlamellar locking inspires new synthetic routes to complex structural materials.

## Acknowledgements

The authors acknowledge the University of Michigan College of Engineering for financial support and the Michigan Centre for Materials Characterization for use of the instruments. S.E.W. acknowledges financial support by an Emmy Noether starting grant issued by the German Research Foundation (DFG, no. WO1712/3-1). We thank Kai Sun for experimental assistance and Anna Son for illustration assistance.

## Supporting material

### *Crystal structure of inorganic bridges*

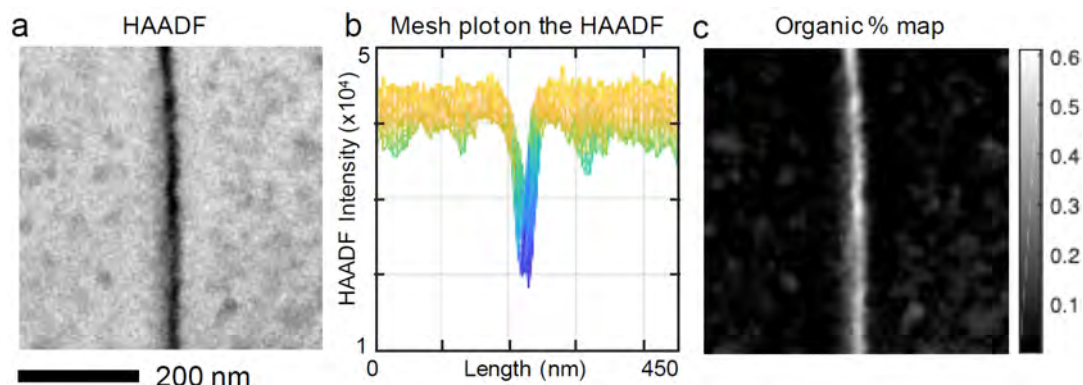


**Supplementary Figure 8.1: Shared crystal orientation between two adjacent nacre tablets. a.** Cross-sectional bright field STEM of a minor connection i.e. intrinsic mineral bridge structure without external stress spanning across the interlamellar membrane showing continuous crystal growth between tablets. **b.** Fast Fourier Transformation of (a) showing a twist angle of 3.5° between the crystallographic orientations of the tablets. This could suggest continuous growth of the tablets from one layer to the next through intrinsic bridges, noted as a possible nacre growth mechanism (Checa et al., 2011; Nudelman, 2015).

### *Quantifying organic concentration from HAADF intensity*

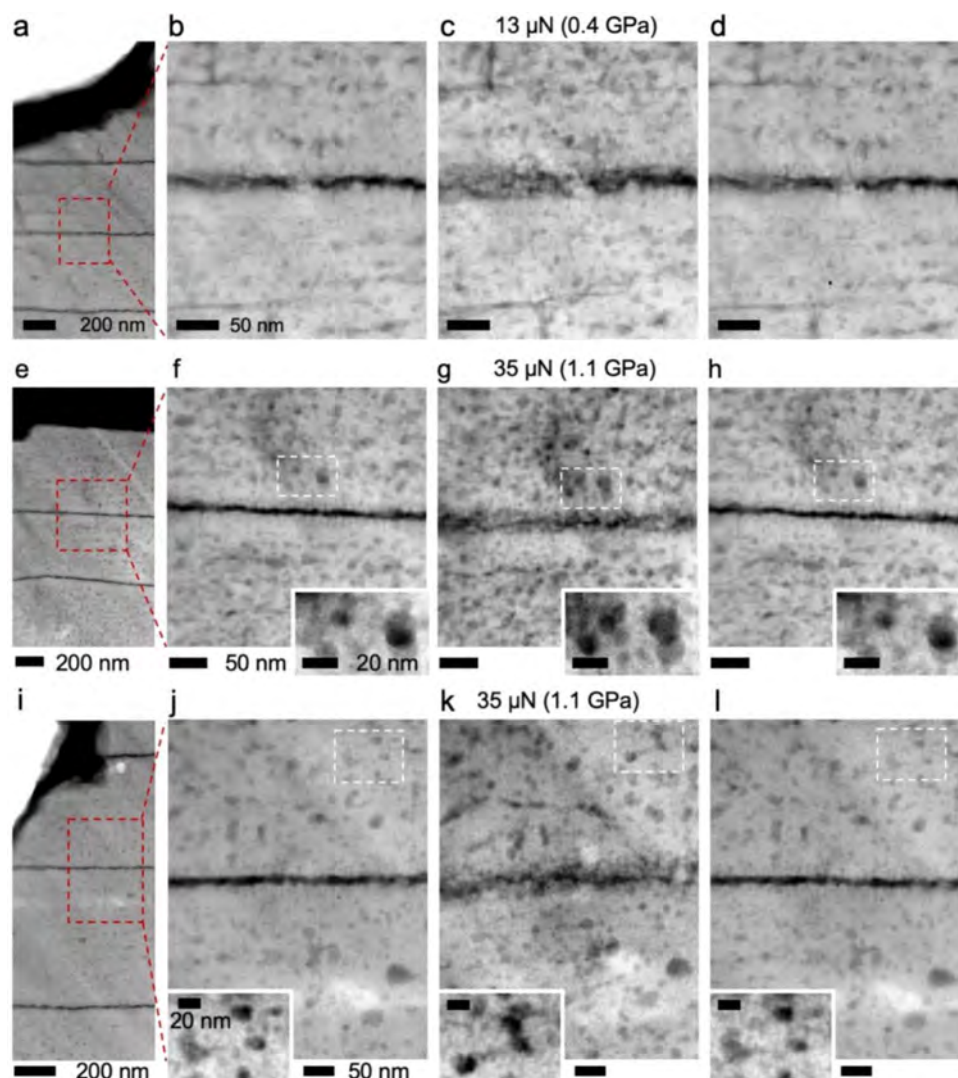
Relative organic concentration in the nacre tablets was formulated by ratio of high-angle elastic electron scattering intensity, which is defined by  $I_{\text{HAADF}} = t \cdot \Sigma Z_x^\gamma \cdot \rho$  where  $t$  is the thickness of nacre,  $\rho$  is the density of the  $\text{CaCO}_3$  or an organic molecule, and  $Z_x$  is the atomic number of an element in  $\text{CaCO}_3$  or an organic molecule. Chitin (Cartwright and Checa, 2007; Suzuki et al., 2009) and lustring (Blank et al., 2003; Shen et al., 1997) are considered as representatives of the organics in nacre because the two proteins are the main components of the matrix protein in nacre of mollusc shells, which consists of amino groups. The collected HAADF signal scales as  $Z_\gamma$  and gamma ranges from 2 for Rutherford scattering at very large angles to 4/3 as described by Lenz-Wentzel expressions for a range of scattering angles from a screened coulomb potential. Typically,  $\gamma$  is around 1.7, and this value was chosen for this calculation (Hovden and Muller, 2012). There is little thickness variation across the cropped 500 nm by 500 nm region of interest, equivalent to the width of the nacre tablets inspected. The intensity measured over vacuum is subtracted from the HAADF intensities and set to a positive value to avoid negative counts, then down-sampled by a factor of 2 to improve signal-to-noise ratio. Total error of organic material fraction is calculated by different threshold values for HAADF intensity of 100 %  $\text{CaCO}_3$ . The volume fraction of organics are converted into the weight fraction by multiplying the density of generic protein (1.35 g/cm<sup>3</sup>) (Fischer et al., 2013) and aragonite (2.95 g/cm<sup>3</sup>) (MacDonald, 1956). The values in the manuscript are averaged from two different region in nacre.





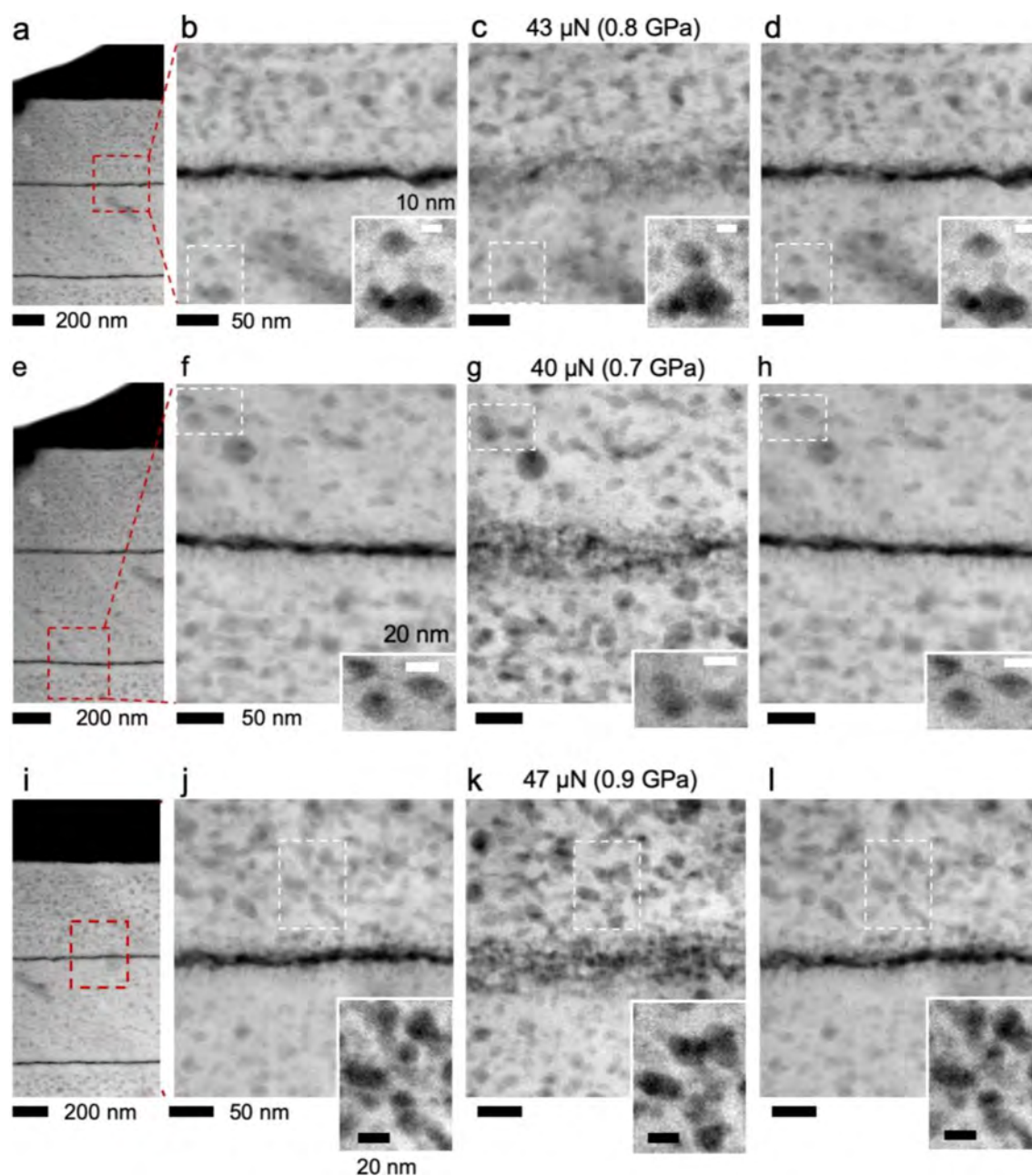
**Supplementary Figure 8.2: Relative organic concentration in nacre tablets using the ratio of high-angle elastic electron scattering intensity. a.** HAADF-STEM showing the overview of the nacreous tablet. The region of interest is cropped to an area of 500 nm by 500 nm, which is equivalent to the width of a nacre tablet. **b.** Mesh plot on HAADF image in a showing the region interest has little thickness variation. **c.** Relative organic component concentration map on the region in a. In this example, organic materials occupy  $6.9 \pm 1.8$  vol. % ( $3.3 \pm 0.8$  wt.%) of nacre composed of  $3.0 \pm 0.5$  vol. % ( $1.4 \pm 0.2$  wt.%) interlamellar and  $3.9 \pm 1.3$  vol. % ( $1.9 \pm 0.6$  wt.%) interorganic.

### *Deformation and recovery of nacre tablets*

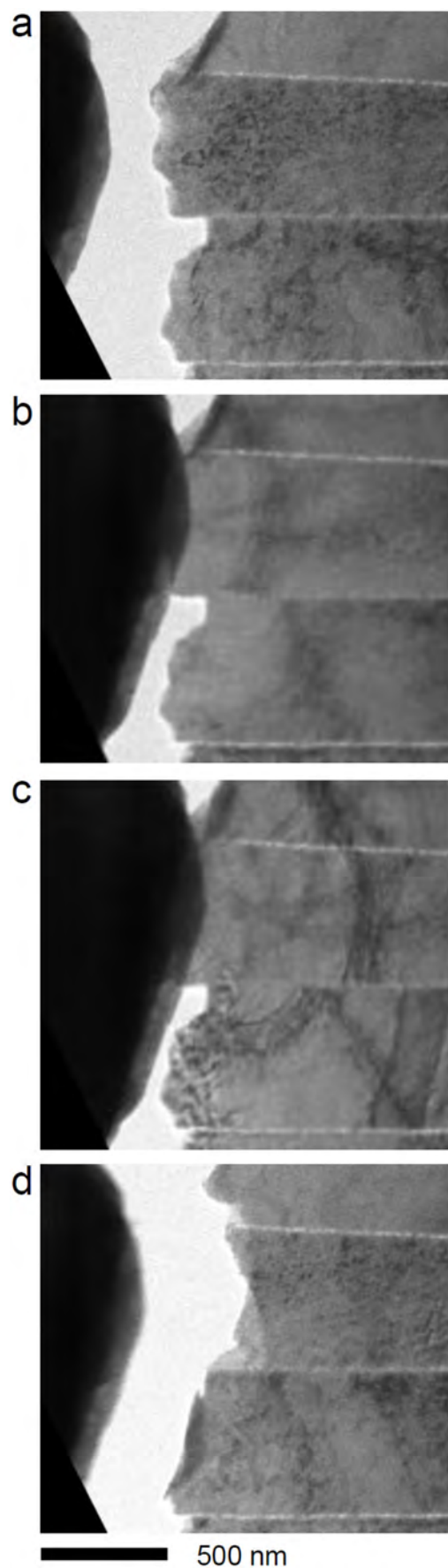


**Supplementary Figure 8.3: Cross-sectional view of nacre deformation and recovery at tablet interfaces using HAADF STEM. a, e, i)** Overview of three different nacre tablets. **b, f, g)** The interlamellar membrane between opposite tablets is well defined before compressive nanoindentation. **c, g, k)** Upon loading, interface interlocks and temporary inorganic connections form. **d, h, l)** After the load is released, the system fully recovers to its initial state. Insets highlight deformation of aragonite grains and organic inclusions as viewed in projection.

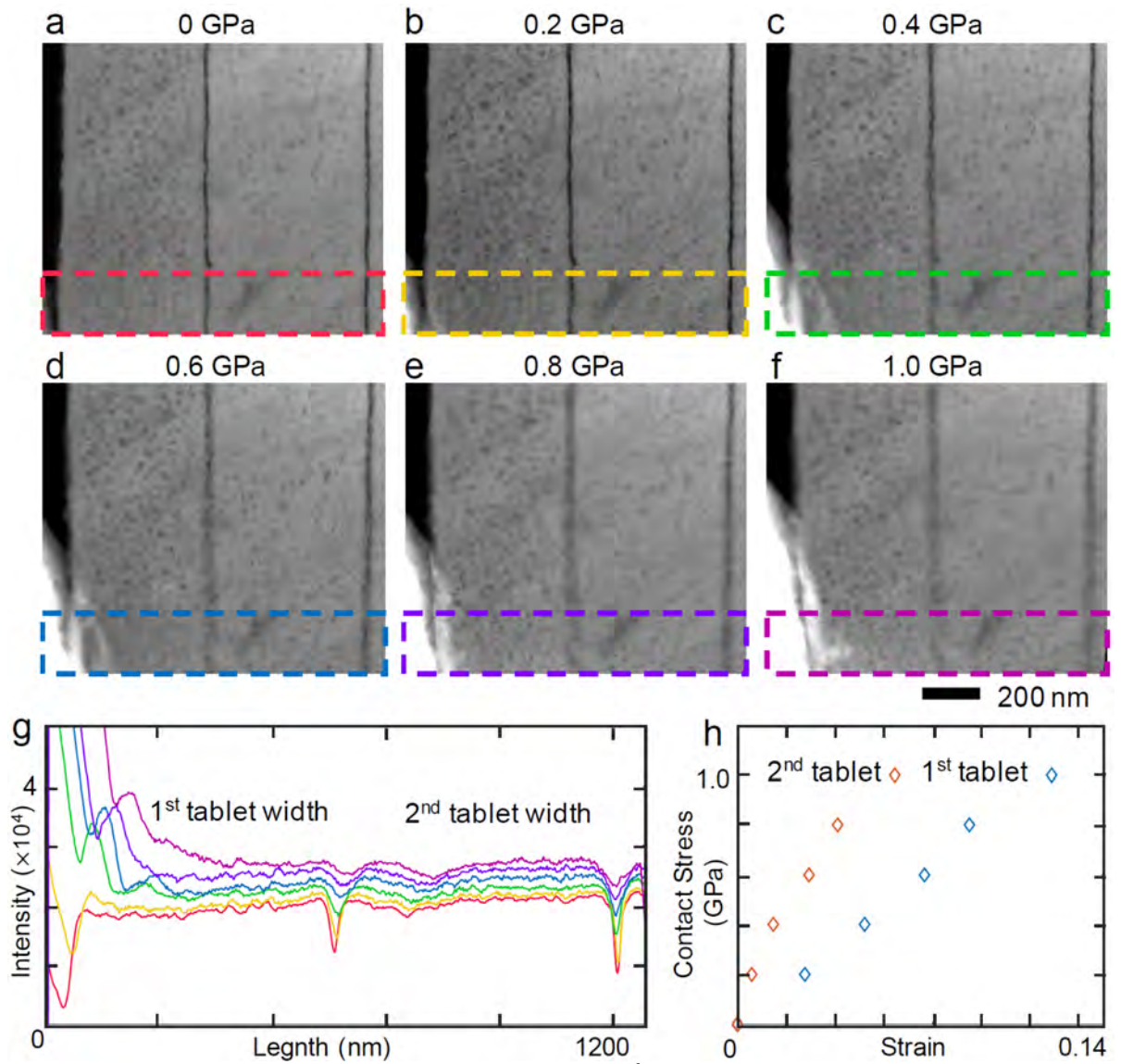




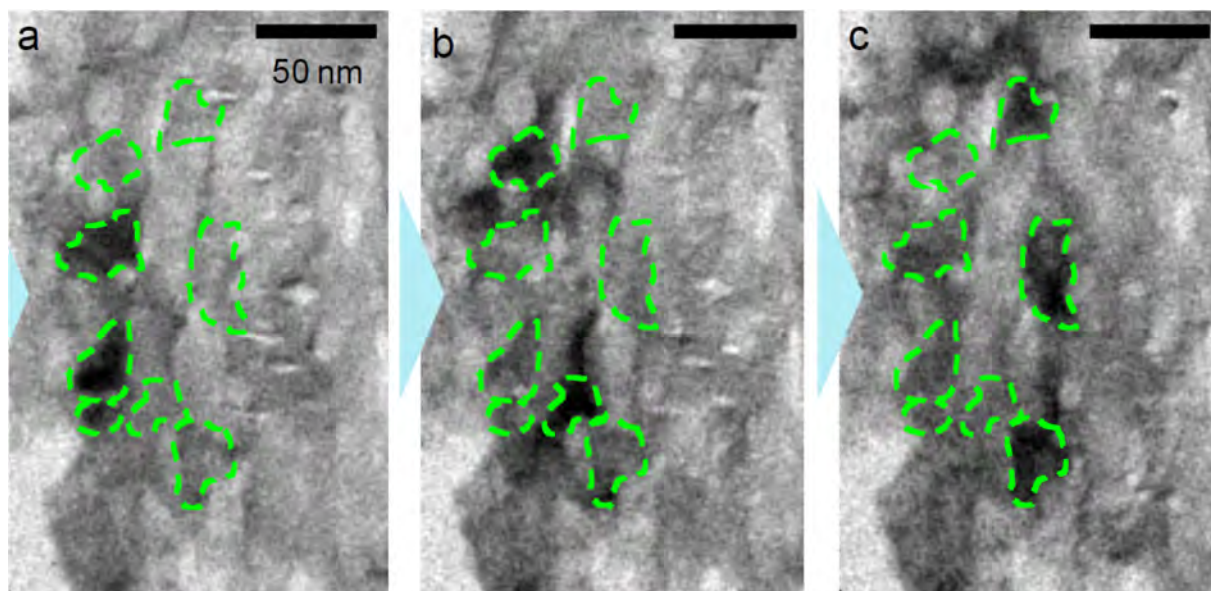
**Supplementary Figure 8.4: Cross-sectional view of nacre deformation and recovery at tablet interfaces using HAADF STEM. a, e, i) Overview of nacre tablets. b, f, g) The interlamellar membrane between tablets is well defined before compressive nanoindentation. c, g, k) Upon loading, interface interlocks and temporary inorganic connections form. d, h, l) After the load is released, the system fully recovers to its initial state. Insets highlight deformation of aragonite grains and organic inclusions as viewed in projection.**



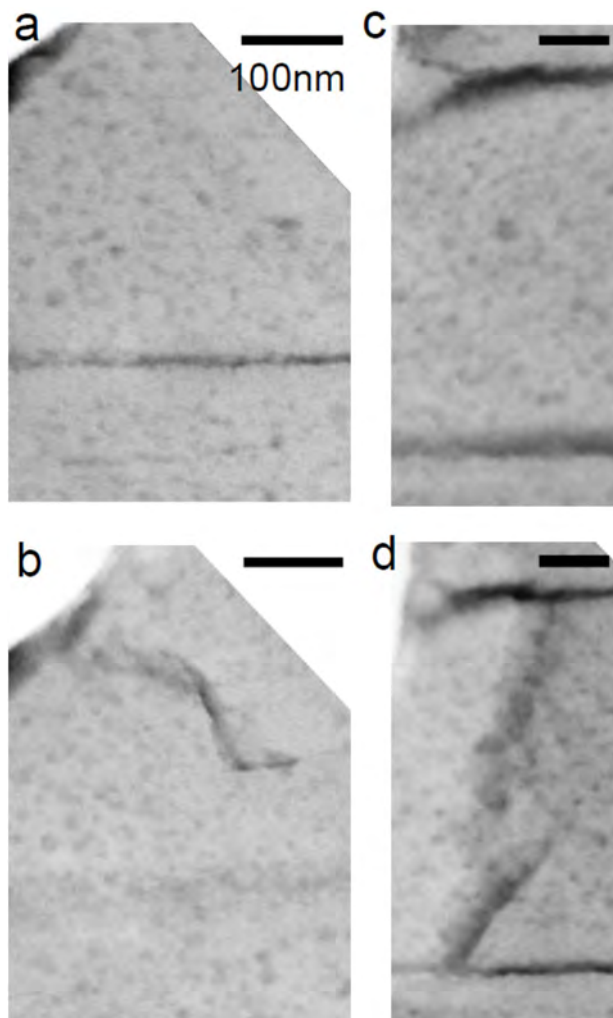
**Supplementary Figure 8.5: *In situ* TEM nanoindentation along a-axis of nacre tablets. (a-d) Compression parallel to the tablet plane showing a limited amount of locking at interface before fracture.**



**Supplementary Figure 8.6: Strain attenuation from 1<sup>st</sup> to 2<sup>nd</sup> tablet from indenter tip. a-f. HAADF-STEM images showing nacreous tablet compressed from 0 GPa to 1.0 GPa. g. HAADF intensity profiles of the cropped area in a-f showing the gradual reduction of the tablet width. h. Contact stress-tablet engineering strain curve plotted based on the ratio of 1<sup>st</sup> and 2<sup>nd</sup> tablet width measured in g. Rotation and deformation of nanograins and crack blunting**

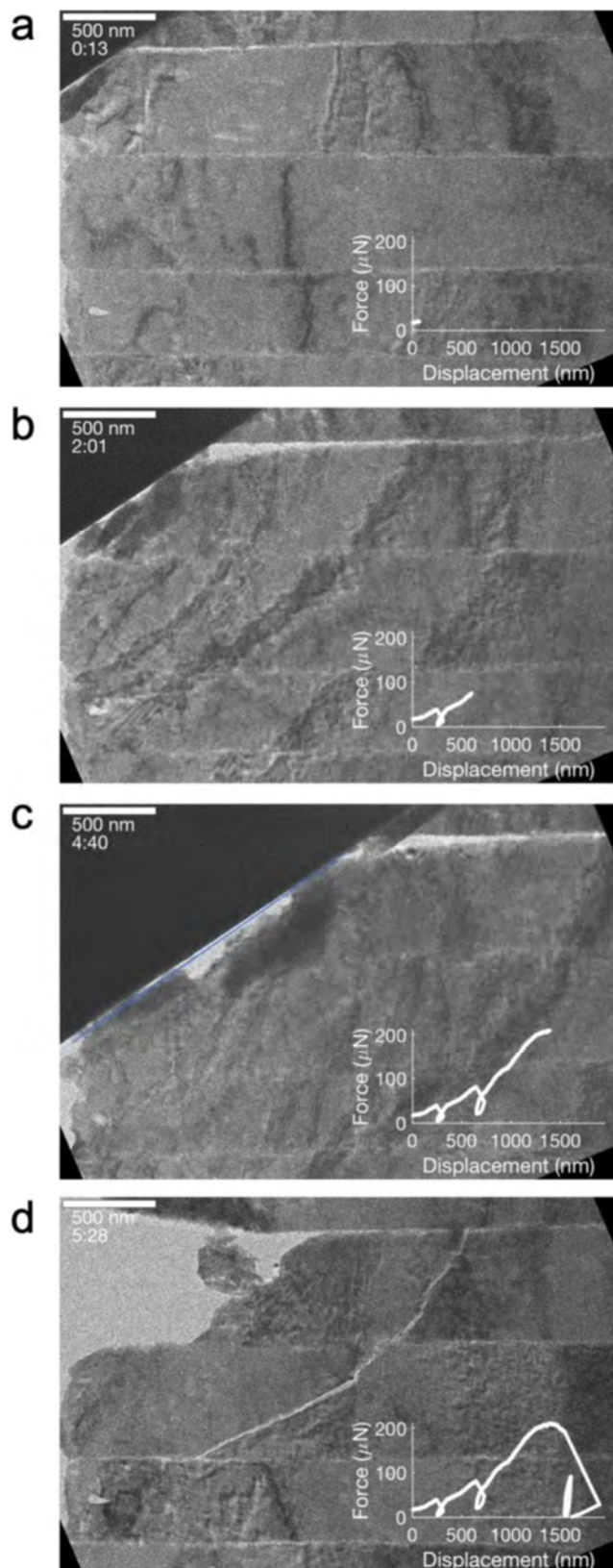


**Supplementary Figure 8.7: Rotation and deformation of aragonite nanograins and organic inclusions in nacre at the nano-scale. a-c. Bright field TEM of the cross-sectional nacreous region after contact with indenter tip (noted by cyan arrow) and continuous compression of the same region. Darkening of grains corresponds to changes in crystallographic orientation. Notably, the organic inclusions of c) have become rounded in morphology compared to a, b. Here, BF-TEM contrast of the thin specimen is sensitive to strain and small changes in crystallographic orientation. The visible darkening of grains (green circles) during indentation are due to nanograin deformation or reorientation from local stresses. The nanogranular response and dynamics are most visible in the Supplemental Movie 1.**



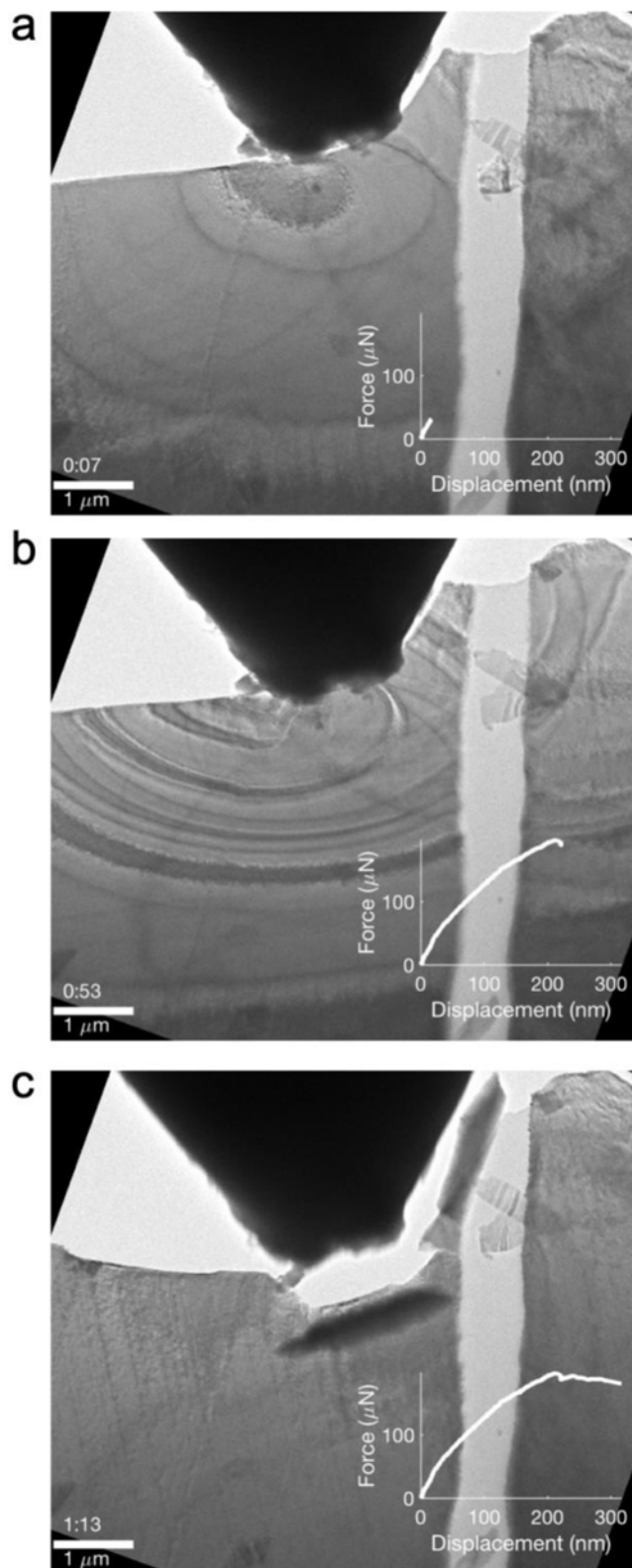
**Supplementary Figure 8.8: Cracks blunted by organic boundaries and inclusions in nacre. a, c.) Nacre structure before compression. After failure cracks propagate and terminate at organic inclusions (b) or terminate at the interlamellar membrane (d).**





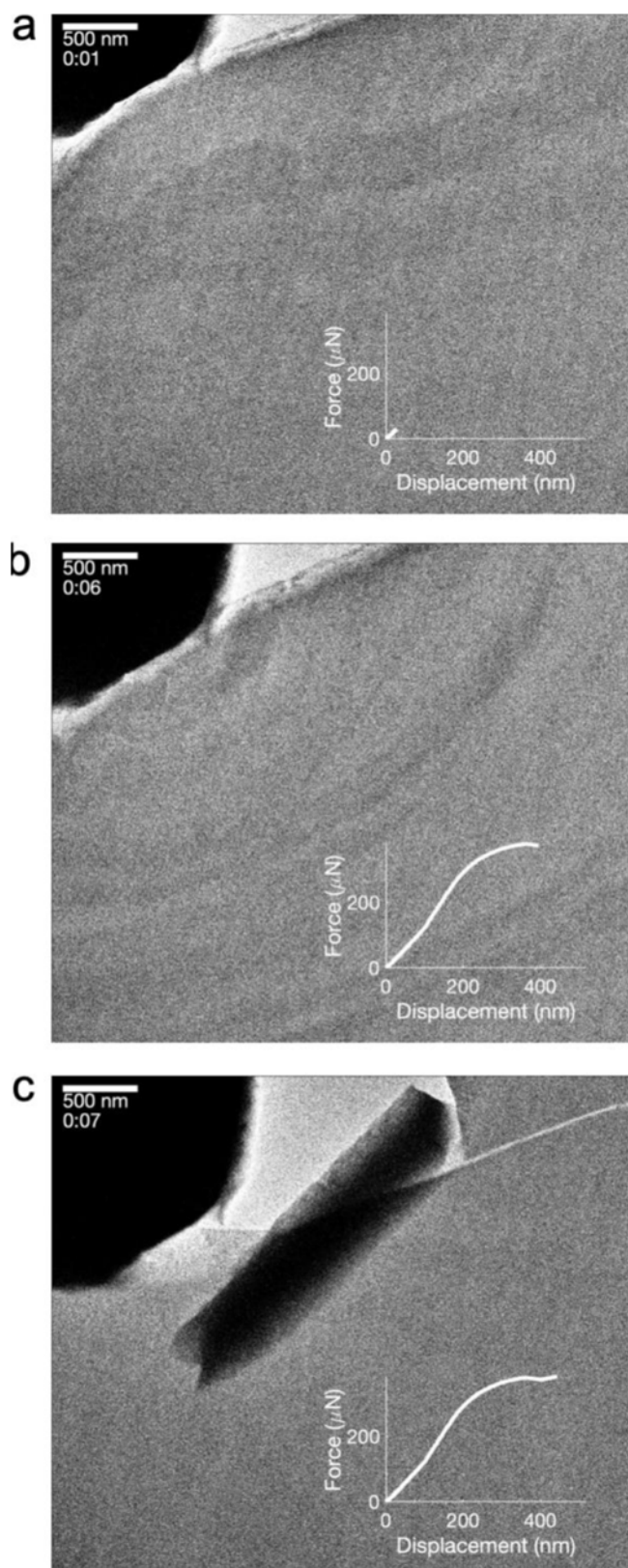
**Supplementary Figure 8.9:** Video stills of nacreous aragonite extracted from an in-situ BF-TEM nanoindentation using a cube corner diamond probe tip. Right-bottom graph in each image are the correlative load–displacement curves. Video content is included as Supplementary Movie 2.



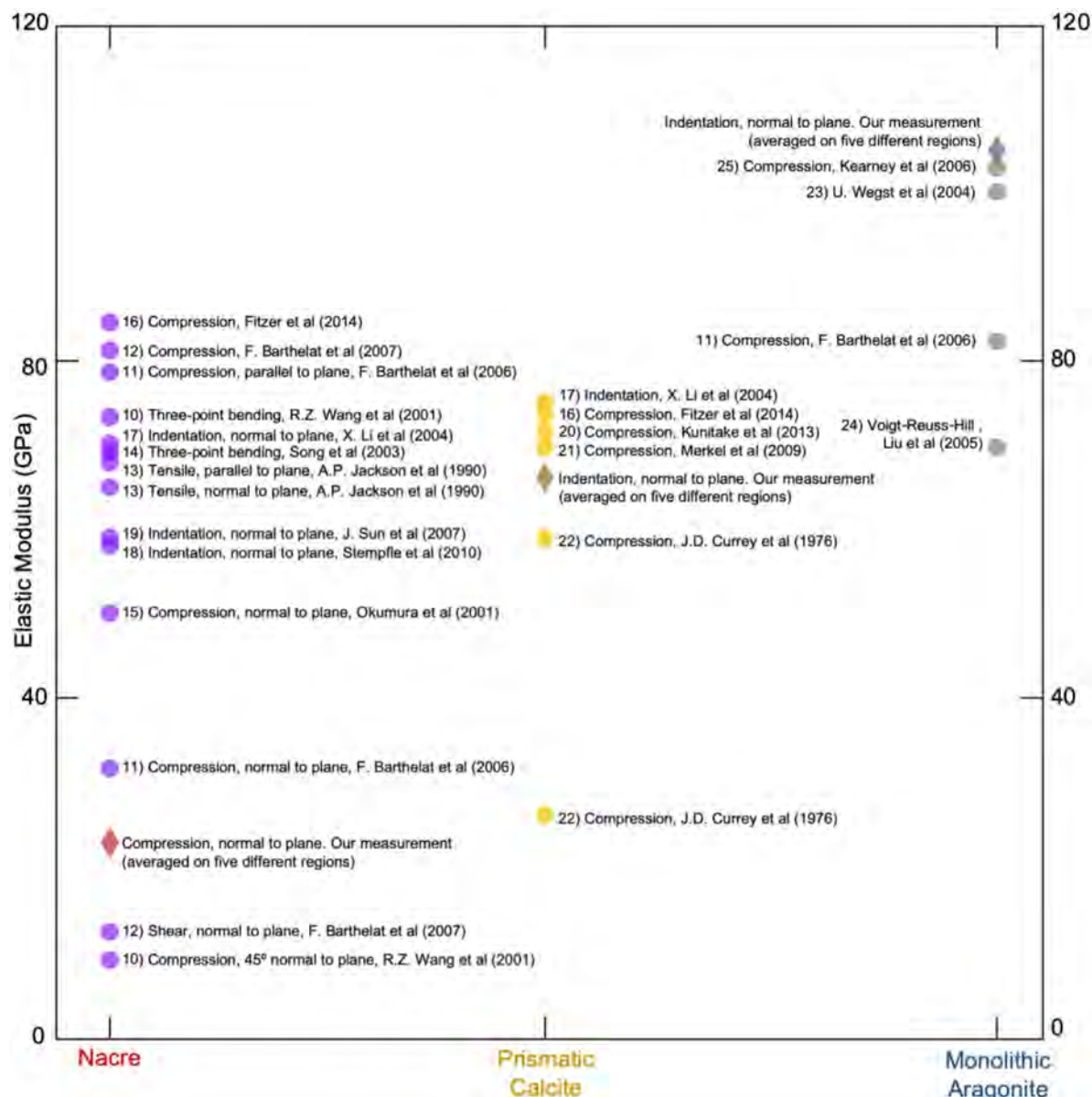


**Supplementary Figure 8.10: Video stills of prismatic calcite extracted from an in-situ BF-TEM nanoindentation using a conospherical diamond probe tip. Right-bottom graph in each image are the correlative load–displacement curves. Video content is included as Supplementary Movie 3.**

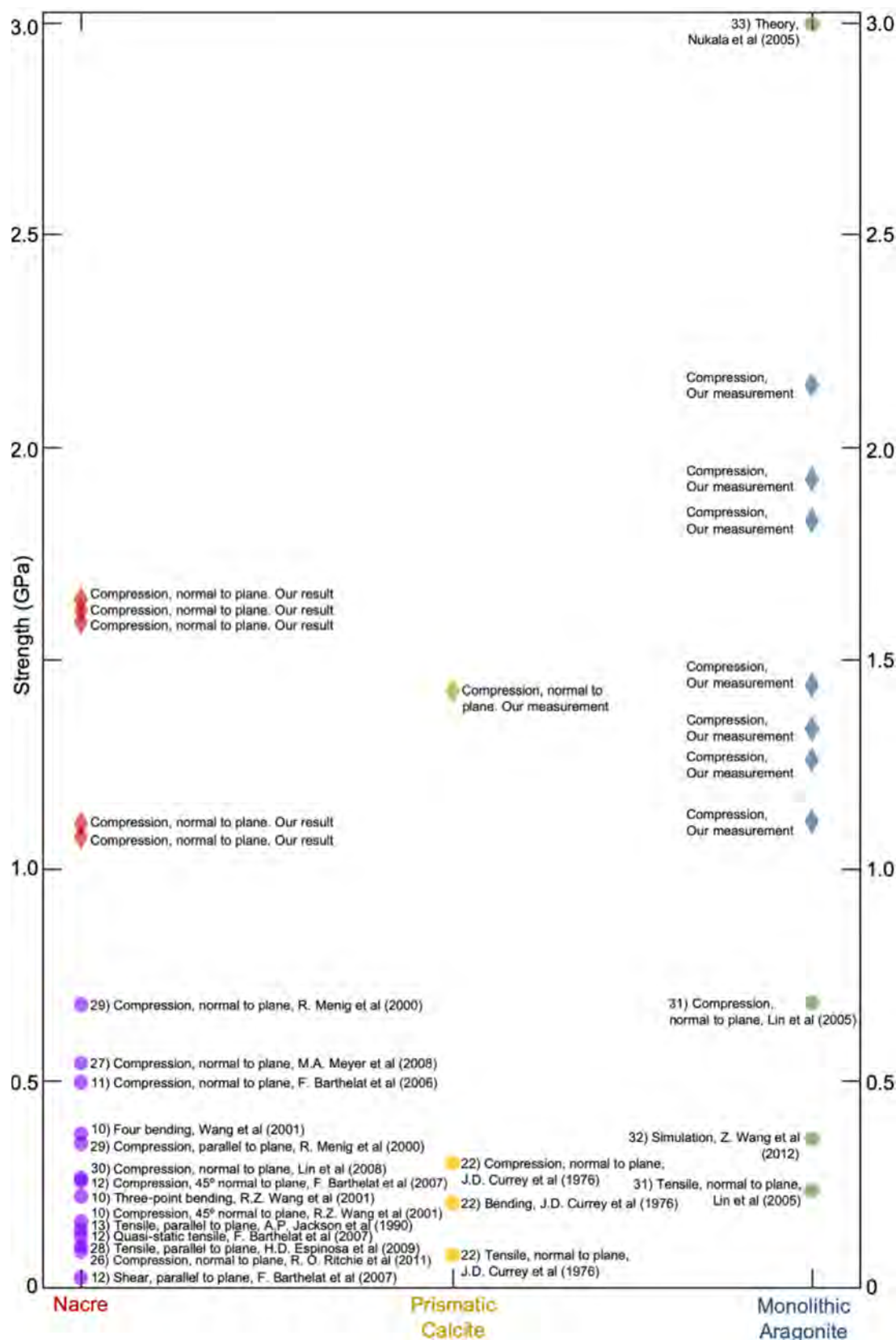
*Comparison of mechanical properties on the cross-sectional and bulk specimen of nacre, prismatic calcite, and geological monolithic aragonite*



**Supplementary Figure 8.11:** Video stills of geological monolithic aragonite extracted from an in-situ BF-TEM nanoindentation using a conospherical diamond probe tip. Right-bottom graphs in each image are the correlative load–displacement curves. Video content is included as Supplementary Movie 4.



**Supplementary Figure 8.12: Literature survey of elastic modulus of nacre, prismatic calcite, and monolithic aragonite.** Both the cross-sectional nanoindentation measurements taken in this study, and previous reports on the bulk properties of the materials are shown (Barthelat et al., 2006; Barthelat et al., 2007; Currey, 1977; Fitzer et al., 2015; Jackson et al., 1990; Kearney et al., 2006; Kunitake et al., 2013; Li et al., 2004; Merkel et al., 2009; Okumura and Gennes, 2001; Song et al., 2003; Stempfle et al., 2010; Sun and Tong, 2007; Wang et al., 2001; Wegst and Ashby, 2004). Values from the literature are averages that represent each test type.



**Supplementary Figure 8.13: Literature survey of strength of nacre, prismatic calcite, and monolithic aragonite. Both the cross-sectional nanoindentation measurements taken in this study, and previous reports on the bulk properties of the materials are shown (Barthelat et al., 2006; Barthelat et al., 2007; Currey, 1977; Espinosa et al., 2009; Lin, 2008; Liu et al., 2005; Menig et al., 2000; Meyers et al., 2008; Nukala and Simunovic, 2005; Ritchie, 2011; Wang et al., 2001; Wang et al., 2012). Values from the literature are averages that represent each test type.**

## 9. ARCHITECTURE OF *ANOTEROPORA LATIROSTRIS* (BRYOZOA, CHEILOSTOMATA) AND IMPLICATIONS FOR THEIR BIOMINERALIZATION

Dorrit E. Jacob<sup>1\*</sup>, Bernhard Ruthensteiner<sup>2</sup>, Patrick Trimby<sup>3+</sup>, Hadrien Henry<sup>1,4</sup>, Silviu O. Martha<sup>5</sup>, Jan  
Leitner<sup>6</sup>, Laura M. Otter<sup>1</sup>, Joachim Scholz<sup>5</sup>

<sup>1</sup>Department of Earth and Planetary Sciences, Macquarie University, Sydney NSW 2109 Australia

<sup>2</sup>Zoologische Staatssammlung München, Münchhausenstraße 21, 81247 München, Germany

<sup>3</sup>Australian Centre for Microscopy and Microanalysis, The University of Sydney, Sydney, New South  
Wales 2006, Australia

<sup>+</sup>present address: Oxford Instruments Nanoanalysis, High Wycombe, UK

<sup>4</sup>Australian Research Council Centre of Excellence for Core to Crust Fluid System (CCFS)/ GEMOC

<sup>5</sup>Senckenberg Forschungsinstitute und Naturmuseen, Marine Evertibraten III, Senckenberganlage 25,  
Frankfurt, Germany

<sup>6</sup>Max Planck Institute for Chemistry, Particle Chemistry, Hahn-Meitner-Weg 1, Mainz, Germany

\*Corresponding Author: dorrit.jacob@mq.edu.au

This chapter has been published in Scientific Reports as:

D.E. Jacob, B. Ruthensteiner, P. Trimby, H. Henry, S. O. Martha, J. Leitner, **L. M. Otter**, and J. Scholz  
(2019): Architecture of *Anoteropora latirostris* (Bryozoa, Cheilostomata) and implications for their  
biomineralization, Scientific Reports Vol. 9, No. 1, pp. 1-13. Doi.org/10.1038/s41598-019-47848-4.  
Open Access at: <https://www.nature.com/articles/s41598-019-47848-4>.

The author's contribution to the publication is as follows: LMO conducted SEM and BSE imaging with  
subsequent analysis of skeleton wall thickness and, further, contributed to the final version of the  
manuscript.



## Abstract

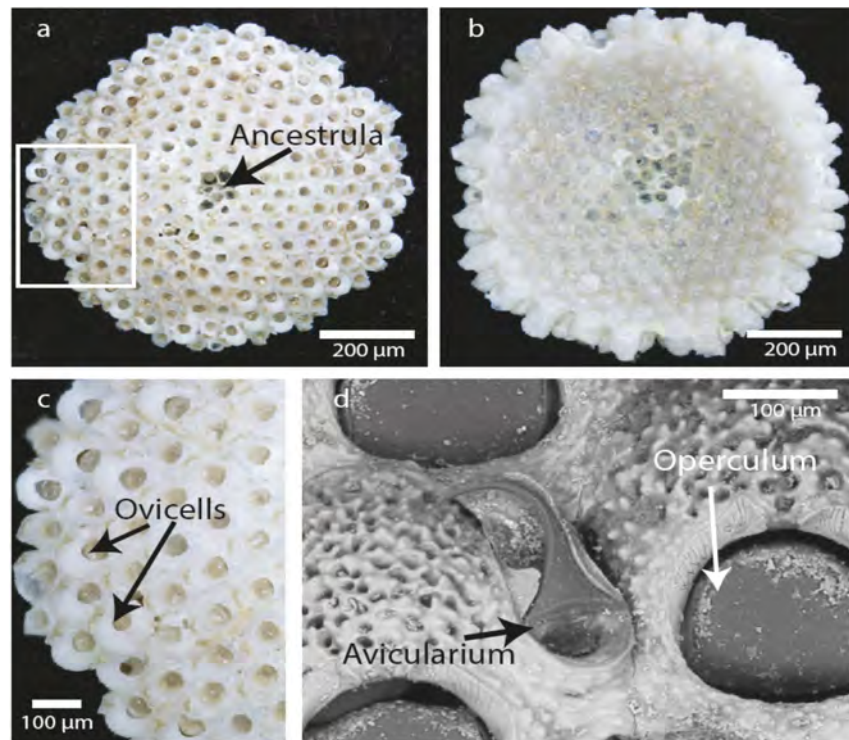
Cheilostome Bryozoa *Anoteropora latirostris*, a colonial marine invertebrate, constructs its skeleton from calcite and aragonite. This study presents firstly correlated multi-scale electron microscopy, micro-computed tomography, electron backscatter diffraction and NanoSIMS mapping. We show that all primary, coarse-grained platy calcitic lateral walls are covered by fine-grained fibrous aragonite. Vertical lateral walls separating autozoid chambers have aragonite only on their distal side. This type of asymmetric mineralization of lateral walls results from the vertical arrangement of the zooids at the growth margins of the colony and represents a type of biomineralization previously unknown in cheilostome bryozoans. NanoSIMS mapping across the aragonite-calcite interface indicates an organic membrane layer between both mineral phases, likely representing an organic template for biomineralization of aragonite on the calcite layer. Analysis of crystallographic orientations show a moderately strong crystallographic preferred orientation (CPO) for calcite (7.4 times random orientation) and an overall weaker CPO for aragonite (2.4 times random orientation) with a high degree of twinning (45 %) of the aragonite grains. The calculated Young's modulus for the CPO map shows a weak mechanical direction perpendicular to the colony's upper surface facilitating this organism's strategy of clonal reproduction by fragmentation along the vertical zooid walls.

## 9.1 Introduction

Bryozoans represent a diverse phylum of mostly marine, colonial suspension feeding animals, present in nearly 7,000 recent and about 20,000 fossil species in all types of marine habitats from the intertidal to the deep sea, and the Polar Regions towards the tropics. The phylum is unique in consisting exclusively of clonal animals. Colonies form by repeated budding of physically connected and intercommunicating modules called “zooids” (Huxley, 1852). Zooids are polymorphic and may be subdivided into ‘autozooids’, i.e. zooids responsible for feeding of the colony, and various ‘heterozooids’, which have specialised functions other than feeding (Ryland, 1979). Heterozooids include, for example, polymorphs responsible for active and passive defence (avicularia and spines), cleaning (vibracula) and colony stability (kenozooids). The modular construction allows two different levels of morphological analysis: that of the zooids and zooid chambers, and another of the budding and packaging of zooids to form various types of colonies (McKinney and Jackson, 1991). Bryozoan skeletal hard parts, consisting of calcite and/or aragonite (Rucker and Carver, 1969; Taylor et al., 2008) are abundant throughout the geological record since the Ordovician (Taylor and Sendino, 2010), which makes them interesting as potential paleo-environmental and -climatic proxy archives (Key et al., 2013; Lombardi et al., 2008; O'Dea and Okamura, 1999; Smith and Key, 2004), as well as ‘sentinels’ of ocean acidification (Durrant et al., 2013; Lombardi et al., 2011; Smith, 2014). Furthermore, they are an ideal group for the study of evolution, since they are abundant and morphologically complex. Most are sessile, calcify and laminarily encrust all types of substrata or grow erect. Death assemblages are commonly preserved *in situ* and reflect life assemblages (McKinney and Jackson, 1991).

A prerequisite for evaluating and deciphering the environmental information potentially stored in bryozoan skeletal hard parts, however, is to better understand their skeletal architecture at the micro- to nano-scale and their biomineralization mechanisms (Taylor et al., 2015). In this study, we present a detailed characterization of the internal structure and biomineral architecture of colonies of recent *Anoteropora latirostris*, a bryozoan that is free-living and does not encrust with their basal colonial surface. The genus *Anoteropora* (Canu and Bassler, 1927) belongs to the suborder Cheilostomata which is the most diverse one of recent bryozoans, represented by about 5000 extant species (Bock and Gordon, 2013), and showing the highest developed polymorphism among all Bryozoa.

Most of the marine bryozoans calcify and laminarily encrust all types of substrata or grow erect and attached with the base to a substratum. In contrast, some cheilostomes developed colonies that are not fixed to a substratum. While modern free-living bryozoans are motile and usually have cup-shaped colonies (lunulitiform) with the openings (orifices) in the autozooidal wall on the convex frontal (apical) surface similar to *Anoteropora latirostris* (Figure 9.1a), the latter is not motile, but fixed to the substrate via rootlets (Cook and Chimonides, 1983). Traditionally, studies on lunulitiform bryozoans have focused on free-living families, which, in terms of morphology, are ‘anaskan’-grade cheilostomes lacking a frontal shield. Superficially very similar to free-living ‘anascans’, yet less well-studied, are ‘ascophoran’-grade lunulitiform bryozoans, such as *Anoteropora latirostris*. Colonies of *Anoteropora latirostris* are unilaminar, the autozooids are elongate and extend vertically from the frontal (apical) to the basal surface (Figure 9.1b). Brood chambers (ovicells) (Figure 9.1c) and avicularia (Figure 9.1d) are present (Cook and Chimonides, 1994; Harmer, 1957).



**Figure 9.1: General aspects of *Anoteropora latirostris* Silén (1947). (a) Apical (frontal) view of colony indicating the ancestrula (damaged in this individual). White rectangle shows the area of close-up in (c). (b) Basal view of colony. (c) Margin of colony with ovicellate autozooids. (d) SEM image of adventitious avicularium between two ovicellate autozooids, the orifices of which are closed by opercula. (a–c) SMF 60000; (d) SMF 60001 (see Supplementary Table A.1).**

## 9.2 Materials and methods

### 9.2.1 Systematic account

The study object, *Anoteropora latirostris* (Silén, 1947), is a cheilostome bryozoan of the family Mamilloporidae (Canu and Bassler, 1927) that has cupshaped colonies anchored by rhizoids (rootlets) that emanate from the concave basal surface. Autozooids (feeding zooids) are hexagonal in outline and arranged in rows radiating from the centrally located ancestrula (initial zooid, Figure 9.1a, b). *A. latirostris* has a calcified frontal shield with occasional marginal pores and with a large central circular opening (orifice, Figure 9.1d) for passage of the lophophore and tentacles. One avicularium (specialized defence zooid) is positioned on the surface of each autozooid (Figure 9.1d) and has an acute, outwardly curved distal end. In infertile autozooids, the avicularium is located distolateral or distal of the orifice, while in fertile autozooids, it occurs lateral of the brood chamber (ovicell, Figure 9.1c). The single avicularium occurring both in fertile and infertile autozooids allows unequivocal identification of the species as *A. latirostris*. *A. latirostris* is widespread in the Indian Ocean from the Cape of Good Hope to the southern Red Sea and the Malacca Strait (Cook and Chimonides, 1994).

### 9.2.2 Collection and repository of material

In total 240 colonies of the motile bryozoan species *Anoteropora latirostris* (Silén, 1947) have been used for this study (Supplementary Table A.1). 239 of those were studied by light microscope and 16 specimens were chosen for SEM study. Micro-CT was carried out on 2 samples and one each was chosen for NaonSIMS and EBSD. The material was collected in March 1987 during RV Meteor expedition 5/2 “Mindik” from dredged sediment in the Gulf of Aden (Nellen, 1996). All material is from stations 236 KD (12° 21'24.01"N; 43° 26'53.99"E) and 283 KU (12° 30'54"N, 44° 47'42"E). Both stations represent shallow banks of 35–45 m (236 KD) and 70 m (283 KU) depth and the seabed was covered with coarse carbonate sands and gravels, shells and coral debris. This type of shallow water sediments was not sampled elsewhere during this expedition, as the main goal was to explore the deep-sea habitats. See Supplementary Figure 9.7 and Supplementary Methods for details on sampling locations and collection. The sample material was preserved in 4 % formalin on board and were watered and transferred to 70 % ethanol upon arrival in Frankfurt, and later dried. No further sample preparation other than breaking or cutting of the colonies was carried out prior to analysis. All samples are stored at the Senckenberg Natural History Museum (SNG) in Frankfurt am Main (SMF 60000–6001819) and the Bavarian State Collection of Zoology in Munich (ZSM20190252-ZSM20190253).

### 9.2.3 Sample preparation, light and electron microscopy

A Leica MZ12.5 stereomicroscope with a maximum magnification of 120-x was used for choosing suitable colony fragments for SEM imaging. SEM images of uncoated fragments were produced using a Tescan Vega 3 scanning electron microscope equipped with a low-vacuum chamber at the Senckenberg am Meer (SMW) in Wilhelmshaven, Germany (Figure 9.1d). Specimens imaged at the SGN (Figure 9.4, Supplementary Figure 9.3) were coated in gold/palladium (20/80) and using a

Camscan CS 24 SEM producing secondary electron images. BSE images of sectioned and polished colonies were obtained using a JEOL JXA 8200 electron probe microanalyser (EPMA) at the University of Mainz, Germany. Specimens were imaged using 15 kV acceleration voltage, 8 nA beam current at a working distance of 11 mm. BSE images were merged using Photoshop CS5 and skeleton thickness was measured using ImageJ. For NanoSIMS mapping, colonies were embedded in epoxy resin, sectioned and polished at Max-Planck Institute for Chemistry, Mainz, Germany following routine methods.

#### 9.2.4 X-ray micro-CT

X-ray micro-computed tomography (micro-CT) scans were produced using a Phoenix nanotom m (GE Measurement & Control, Wunstorf, Germany). One specimen was scanned at a voltage of 120 kV and a current of 80  $\mu$ A for 1600 projections over 53 minutes. Two specimens previously used for EBSD analysis (see below) were scanned at a voltage of 130 kV and a current of 90  $\mu$ A for 1440 projections over 48 minutes. Data sets (voxel size 4.44  $\mu$ m for the untreated specimen, 3.04  $\mu$ m for the EBSD treated specimens) were further processed using Amira 6.4 (Thermo Fisher Scientific, Hillsboro, Oregon, USA). Surface models were produced by threshold segmentation. Endocasts of zooid chambers were segmented semi-manually. For the Supplementary video the EBSD section was co-registered with the 3D-CT data set largely following the procedure outlined by Handschuh et al. (2013).

#### 9.2.5 Electron backscatter diffraction

EBSD was carried out on one sectioned and polished colony of *A. latirostris* using a Zeiss Ultra Plus field emission gun scanning electron microscopy (FEG SEM) equipped with an Oxford Instruments Nordlys Nano EBSD detector. Crystallographic preferred orientation (CPO) maps were acquired using the AZtec software v3.0 and were processed using the Channel5 data processing software. Diffraction patterns were collected using an accelerating voltage of 15 kV, a beam current of  $\sim$ 10 nA, a detector resolution of  $336 \times 256$  pixels and at a rate of 40 patterns per second.

In total, 7 separate maps were combined to form a transect across the full colony width, with a measurement spacing of 200 nm. The indexing rate across the full area was typically 90–95 % in the areas without significant porosity.

Grain sizes as observed by TEM are usually in the nanometre range in biominerals (Jacob et al., 2008; Jacob et al., 2011), hence the chosen ‘grain’ size cut-off for EBSD defines domains of several crystallographically well-aligned nanograins, rather than individual aragonite grains and depends on the spatial resolution of the method.

EBSD data were processed using the MTEX toolbox for Matlab (Bachmann et al., 2010; Hielscher and Schaeber, 2008). Measurement bearing a mean angular deviation (MAD) value greater than 1.3 were discarded. Grains were computed using a  $10^\circ$  cut-off angle. Grains smaller than 10 pixels were discarded to prevent bias caused by potential indexing errors. The remaining grains were then smoothed and missing data within grains were interpolated.

Data are plotted in pole figures (Figure 9.7a–c), which are stereograms with axes defined by an external reference frame using the direction tangential (X) and perpendicular to the convex surface of the colony (Y) and the axis normal to the X-Y plane (Z). Accumulation of points around a specific direction in the pole figures (pole maxima) shows a degree of texture in the polycrystalline material, quantified according to the colour scales in the figures. For calcite ( $N_{\text{grains}} = 556$ ), an orientation density function (ODF) with a bandwidth of  $10^\circ$  was calculated using the mean orientation of each grain (i.e. one point per grain pole figure). For aragonite ( $N_{\text{grains}} = 11,389$ ), as twinning is occurring, all EBSD measurements were considered for the ODF calculation ( $N_{\text{measurements}} = 1,037,343$ ; bandwidth =  $10^\circ$ ). The resulting ODFs were then plotted on a lower hemisphere, equal area projection. Contours represent multiples of a uniform distribution.

The twinning percentage was defined as  $100 \cdot ((N - N_t) / N)$  with  $N$  the number of grains computed without taking twinning into account and  $N_t$  the number of grains computed by taking twinning into account. Twin boundaries for aragonite were defined as a  $63.8^\circ \pm 5^\circ$  rotation around the  $[001]$  axis. The strength of the crystallographic preferred orientation is usually estimated using the J-index (Bunge, 2013) and the M-index (Skemer et al., 2005). For a fabric with random (strong) crystallographic orientation, the J-index will approach one (infinity), while the M-index trends towards zero (one). Here, we determined a J-index of 11.8 for calcite (1.23 for aragonite) and an M-index of 0.48 (0.02 for aragonite).

Orientation maps (Figure 9.6c) are plotted using the Channel5 software and are coloured according to the inverse pole figure colour schemes for aragonite and calcite (insets), showing the crystallographic direction parallel to the map's Y (vertical) direction. For orthorhombic aragonite, areas in red have their crystallographic  $[001]$  axis pointing up or down the map, green denotes the  $[100]$  axis and blue the  $[010]$  axis. For rhombohedral calcite, areas in red have their crystallographic  $[0001]$  axis pointing up (North) or down (South) in the map, green denotes the  $[01\bar{1}0]$  and blue the  $[10\bar{1}0]$  axis.

The Young's modulus in Figure 9.7d was calculated using the Voigt-Reuss averaging scheme for the aggregate elastic constant with the single crystal elastic constants for calcite (Chen et al., 2001) and for aragonite (Liu et al., 2005). The maximum anisotropy for the Young's modulus was calculated as  $200 \cdot (Y_{\text{max}} - Y_{\text{min}}) / (Y_{\text{max}} + Y_{\text{min}})$  with  $Y_{\text{max}}$  and  $Y_{\text{min}}$  the maximum and minimal values (in GPa), respectively.

#### 9.2.6 NanoSIMS analysis

NanoSIMS analyses in this study were carried out with the NanoSIMS 50 ion probe (Hoppe et al., 2013) at the Max-Planck-Institute for Chemistry, Mainz, Germany. The Cameca NanoSIMS 50 ion probe is a secondary ion mass spectrometer designed for high spatial resolution isotope measurements with high sensitivity and simultaneous detection of up to 5 (NanoSIMS 50) isotopes. All measurements were performed in “ion imaging” mode, by rastering a primary Cs-beam (100 nm diameter,  $\sim 1$  pA) over several regions of interest. Prior to analysis, selected sample areas were pre-sputtered with a high current primary beam ( $\sim 20$  pA) to remove the gold coating. Secondary ion images of  $^{12}\text{C}^-$ ,  $^{12}\text{C}^{14}\text{N}^-$ , and  $^{28}\text{Si}^-$

from selected sample areas ( $10 \times 10 \mu\text{m}^2$  and  $15 \times 15 \mu\text{m}^2$ , respectively) were acquired in multi-collection mode.

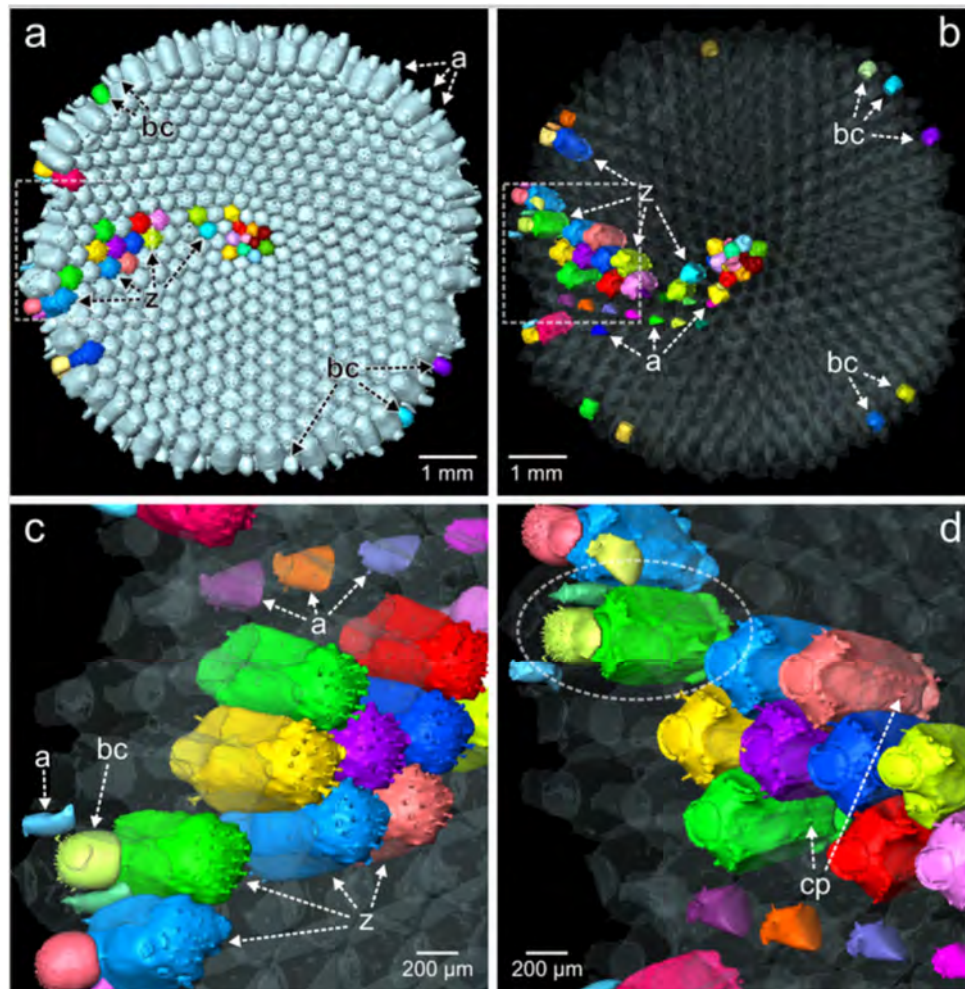
Two to three image planes ( $256 \times 256$  pixels) were recorded for each analysis area with integration times of 10 ms/pixel each. The ion counting rates were corrected for quasi-simultaneous arrivals (QSA) with correction factors according to Slodzian et al. (2004) and Hillion et al. (2008). Corrections were applied individually for each region of interest. For data reduction and processing, in-house software developed at the MPIC was used. Since the sample was embedded in epoxy resin, care was taken to identify potential contamination from the epoxy on the secondary ion images of  $^{12}\text{C}^-$  and  $^{12}\text{C}^{14}\text{N}^-$ . For this, two locations in the epoxy (Supplementary Table A.2), away from the sample, were measured and  $^{12}\text{C}^{14}\text{N}^- / ^{12}\text{C}^-$  ratios obtained there were compared with those on the sample to monitor potential contamination of the sample area with epoxy resin. One of the seven areas measured (B\_a\_01#C) was identified as contaminated in this way and rejected (Supplementary Table A.2).

## 9.3 Results

### 9.3.1 Colony morphology via X-ray Micro Computed Tomography (Micro-CT)

Micro-CT images (including a 3D animation provided as Supplementary Video) allow accurate imaging of individual zooidal chambers and study of the zooid chamber and interconnection between zooids. Figure 9.2 shows the shape and general alignment of different zooid chambers and brood chambers in the colony with the endocast rendered transparent. Autozooidal chambers are block-shaped with rounded edges (marked as ‘z’ in Figure 9.2), while avicularian chambers (marked as ‘a’) are smaller and flat ovoid-shaped. Brood chambers (marked as ‘bc’) are commonly present in autozooids at the distal edge of a colony (Figure 9.1c). They are partly immersed, globular, and closed by the opercula. These opercula are clearly visible in most autozooids of the colonies studied, but are rarely preserved after death, thus indicating that the material used here is from live-collected and/or recently alive individuals. Connecting pores near the bottom of each autozooid (Figure 9.2d) are used for interzooidal communication across the colony. Adventitious avicularia are connected with both the ‘host’ autozooid and the distally adjacent autozooid (Figures 9.1d, 9.2c).

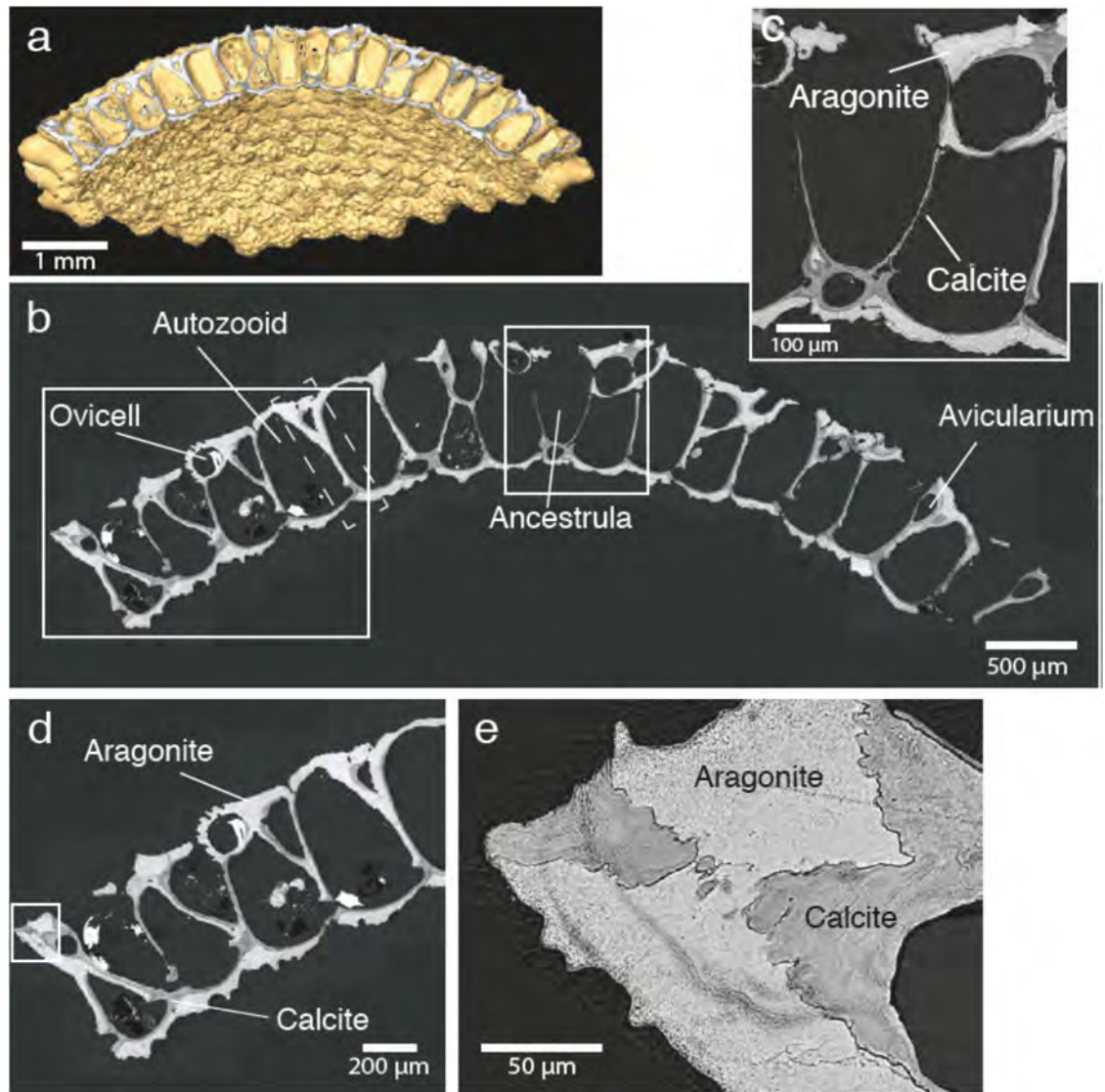




**Figure 9.2:** Endocasts from microCT of a colony of *Anoteropora latirostris* Silén (1947) (sample SMF 60002 from station 283 KU); (a) Basal view of endocast with separated (coloured) zooid chambers. (b–d) Separated zooid chambers shown opaque and remaining endocast transparent. (b) Apical (frontal) view of endocast. (c) Basal view of marginal part of colony. (d) Apical (frontal) view of marginal part of colony; dashed rectangle in (b) outlines the enlarged areas shown in (c, d); dashed ellipse outlines the chamber of one autozooid and the brood cavity and avicularian chamber associated with the same autozooid. Abbreviations: a – avicularian chamber; bc – brood chamber; cp – connecting pore, z – autozooidal chamber.

### 9.3.2 Micron-scale architecture and mineral phase composition

Backscattered electron (BSE) imaging of colonies sectioned through their centre (Figures 9.3a and Supplementary Figure 9.1, 9.2) show that most walls in the colony consist of two mineral phases distinguishable by their different greyscales (Figure 9.3b–e), which are indicative of different compositions (Benedix et al., 2014). These phases were identified as calcite (darker grey) and aragonite (light grey) via Electron Backscatter Diffraction (EBSD) analysis.

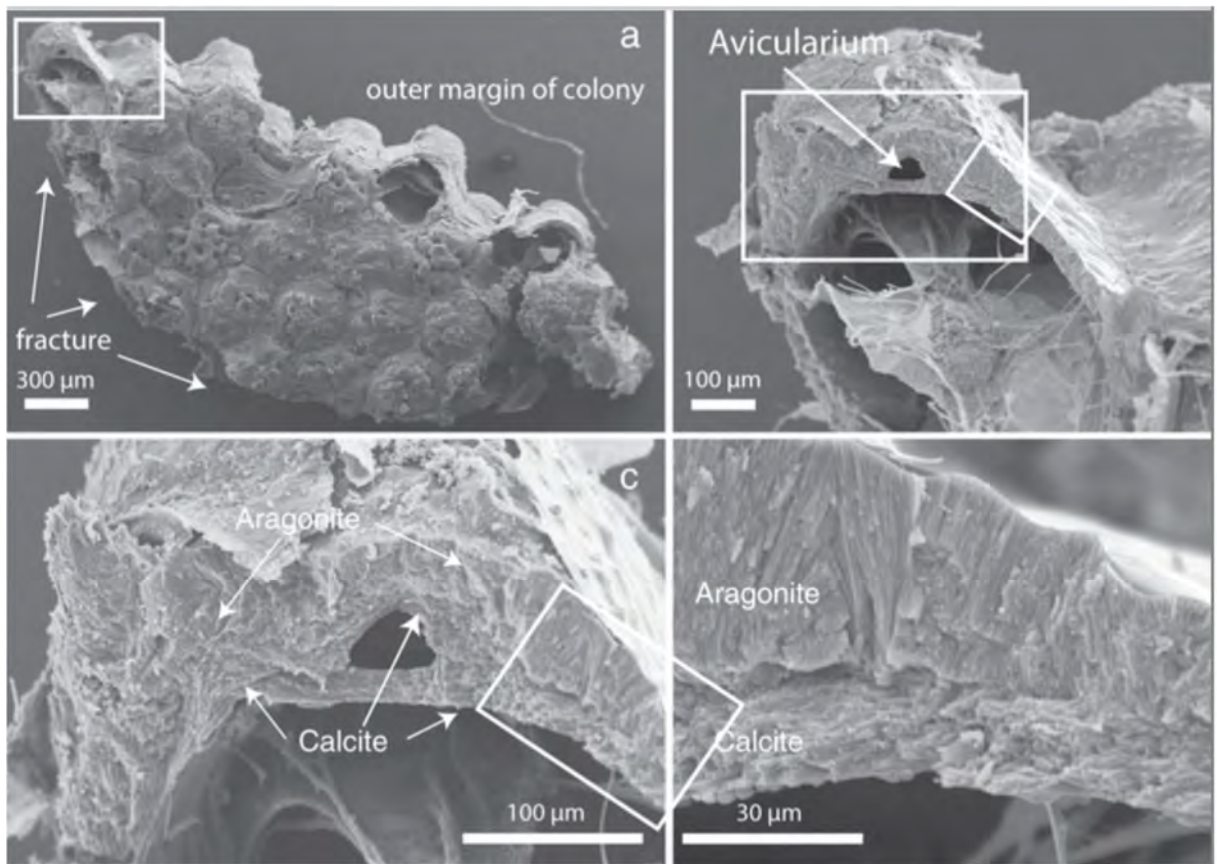


**Figure 9.3: Mineralogy of *Aoteropora latirostris*.** (a) Sectioned colony micro-CT overlay with BSE image of the polished cross-section shown in (c). (b) Close-up of ancestrula (central) area outlined by rectangle in (c) highlighting calcite in dark grey and aragonite in light grey. (d) Close-up of marginal area outlined by rectangle in (b). (e) Close-up BSE image of area outlined by rectangle in (d) showing calcite (dark grey) and aragonite (light grey) wall components. Dashed line in (c) outlines the area investigated by EBSD (Figure 9.6).

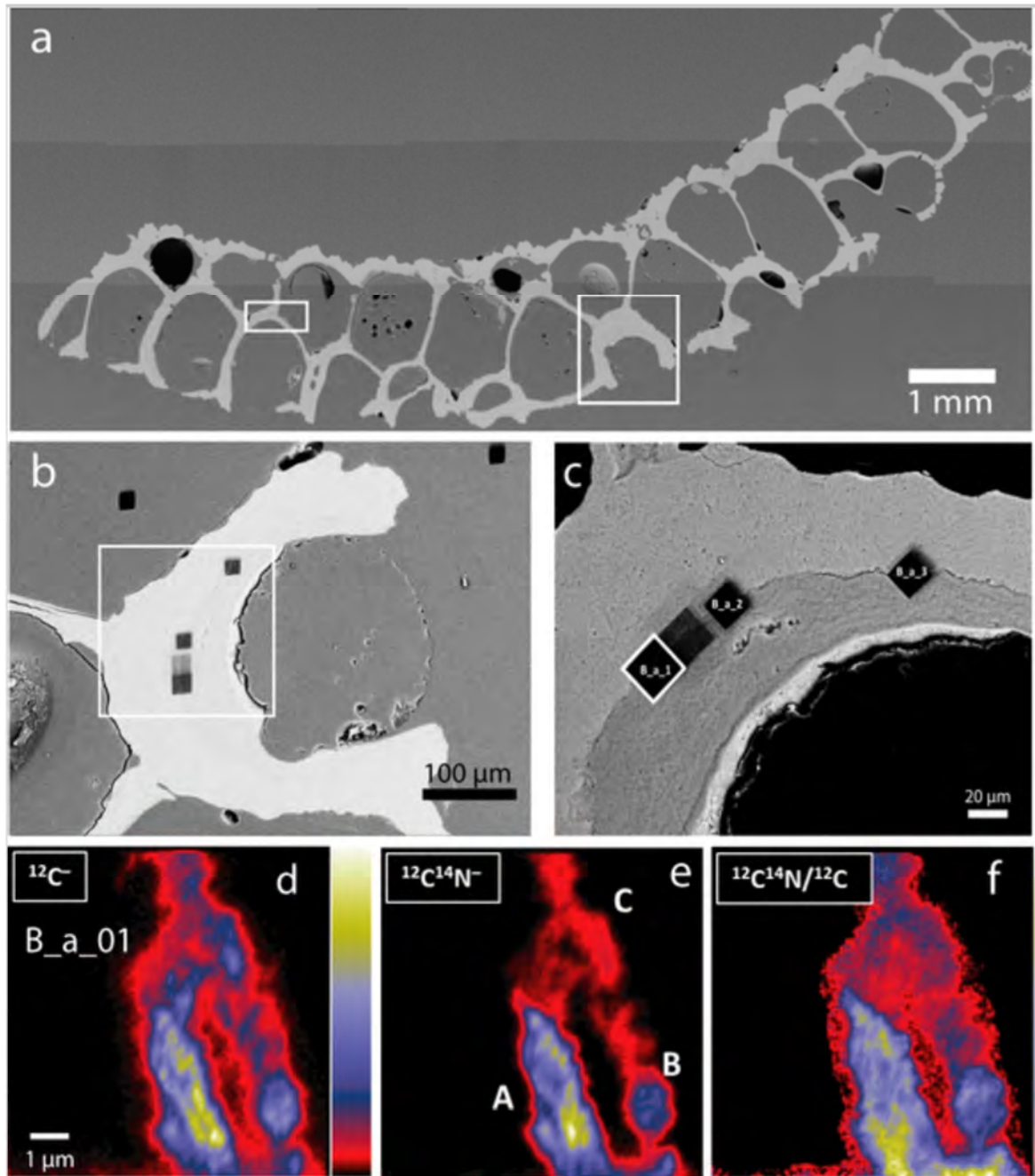
In detail, the different units of each mineralized zooid chamber consist of a specific combination of aragonite and calcite as verified through SEM study of sixteen different colonies (Supplementary Table A.1): judging from the sections we studied, the outside layer of the wall of the colony consists of fibrous aragonite (Figures 9.3c, 9.4, Supplementary Figures 9.2, 9.3). The inner layer of the basal and (most) apical walls, which face the zooid, consist of platy calcite (Figures 9.3c, 9.4b, Supplementary Figures 9.2, 9.3). All vertically oriented interzooidal walls consist, in regard to the centre of the colony, of a distal layer of aragonite and a proximate layer of platy calcite. All walls are therefore bimineralic and, in addition to calcite, contain a secondary fibrous aragonite layer. The calcitic walls are generally thinner than the aragonite walls (see Supplementary Figure 9.1 for measurements in one of the colonies: calcite layer – 3–35 µm in thickness, 5–45 µm for aragonitic walls, occasionally up to 80 µm). Boundaries between calcitic and aragonitic walls are irregular and can be crenulated (Figure 9.3e). To investigate whether an organic membrane separates these two mineral phases, we employed NanoSIMS mapping. This method combines the advantage of submicron spatial resolution as is required here, with minimal



additional sample preparation, thus reducing the risk of artefacts. Carbon and nitrogen distribution maps by NanoSIMS analysis across the calcite-aragonite interface (Figure 9.5a–c) show significantly increased signals for these elements along the interface (Figure 9.5d–f, Supplementary Figure 9.4), which is a clear indication for the presence of a thin organic layer between calcite and aragonite.



**Figure 9.4:** SEM images of a skeleton of *Aoteropora latirostris* (sample SMF 60004). (a) Basal view of broken marginal piece of colony. (b) Fractured cross-section through autozoid near the basal wall (close-up of area marked with a rectangle in (a)) showing a fracture through three of the six walls defining the autozoid chamber. Outer marginal wall contains an avicularium; parietal and retractor muscles traverse the autozoid chamber. White rectangles indicate close-up areas shown in (c) - large rectangle and (d) - small rectangle. (c) Marginal wall shows platy calcite on the inside and enclosing the avicularium (cf. Figure 9.3c) and fibrous aragonite on the outside. (d) Close-up of the lateral wall area marked with a rectangle in (c) and (b) consisting of a thick layer of fibrous aragonite and a thin layer of platy calcite towards the autozoid chamber.

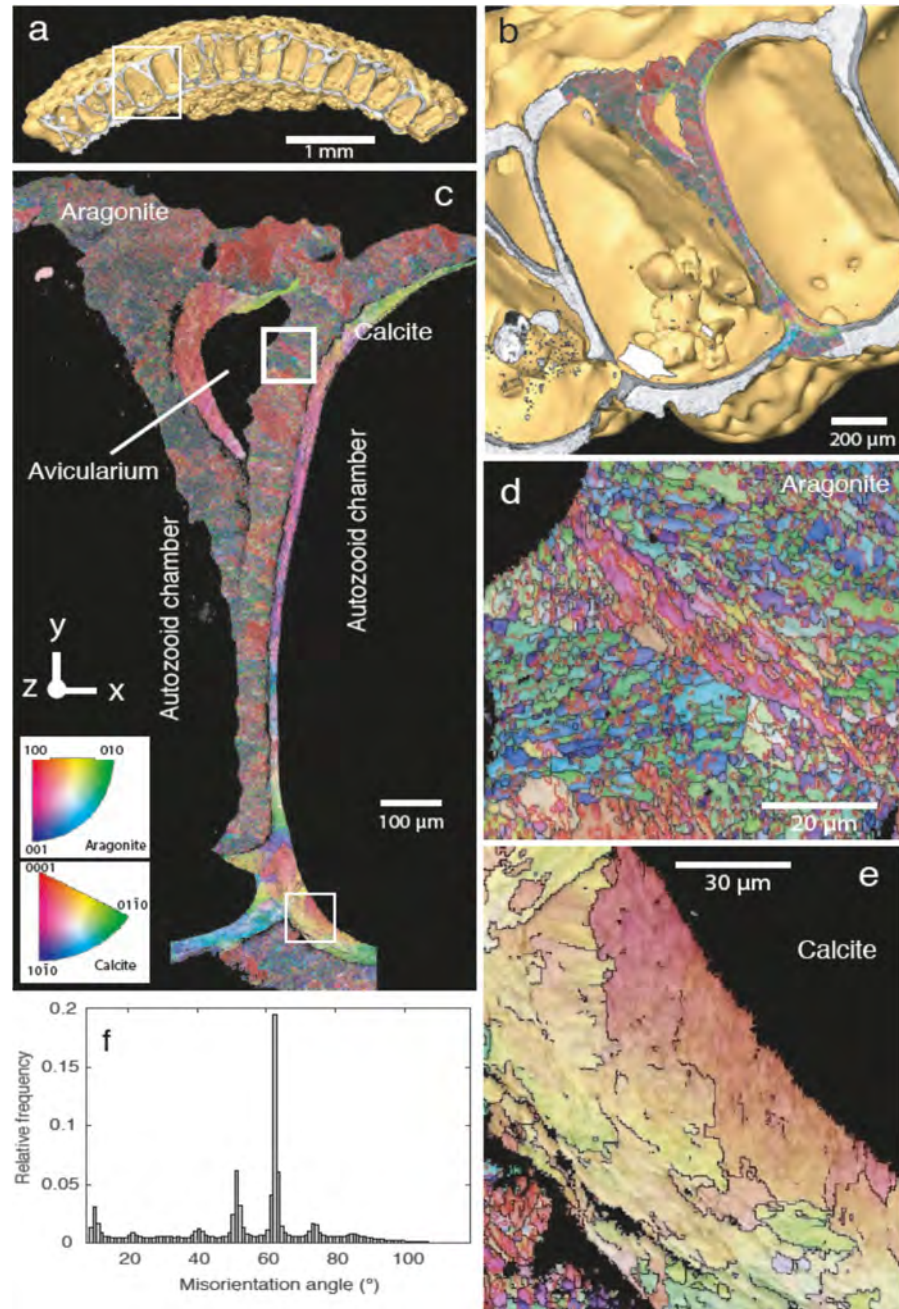


**Figure 9.5:** SEM images and NanoSIMS maps of sectioned and polished epoxy embedded *Anoteropora latirostris* colony. (a–c) Show the areas mapped by NanoSIMS after analyses at the interface between calcite (dark grey in c) and aragonite (light grey in c). Two maps in the epoxy resin were measured for comparison (see Supplementary Table A.2). (d–f) NanoSIMS maps for area outlined by white rectangle in (c): (d) Carbon concentrations (measured as  $^{12}\text{C}^-$ ), (e) nitrogen concentrations (measured as  $^{12}\text{C}^{14}\text{N}^-$ ) and (f) C/N ratios show higher concentrations along the interface between aragonite and calcite than on either side of it (compare colour scale to the right of d), indicating the presence of an organic membrane along the interface. NanoSIMS maps are each  $15 \times 15 \mu\text{m}^2$ , for quantitative data see Supplementary Table A.2.

The interzoooidal walls at the apex of the colony, representing the central area including the ancestrula and thus the oldest part of the colony, are damaged or missing in many specimens (Figure 9.1a, Supplementary Figure 9.2). However, in colonies where these are preserved, the walls delineating the ancestrula are purely calcitic and lack the aragonite layer (Figure 9.3c), which contrasts with the interzoooidal walls of subsequent generations of colony modules (radially away from the centre) in the same samples. Crystallographic orientation of calcite and aragonite grains via Electron Backscatter Diffraction (EBSD). An entire transect of the sectioned and polished colony was analysed by EBSD

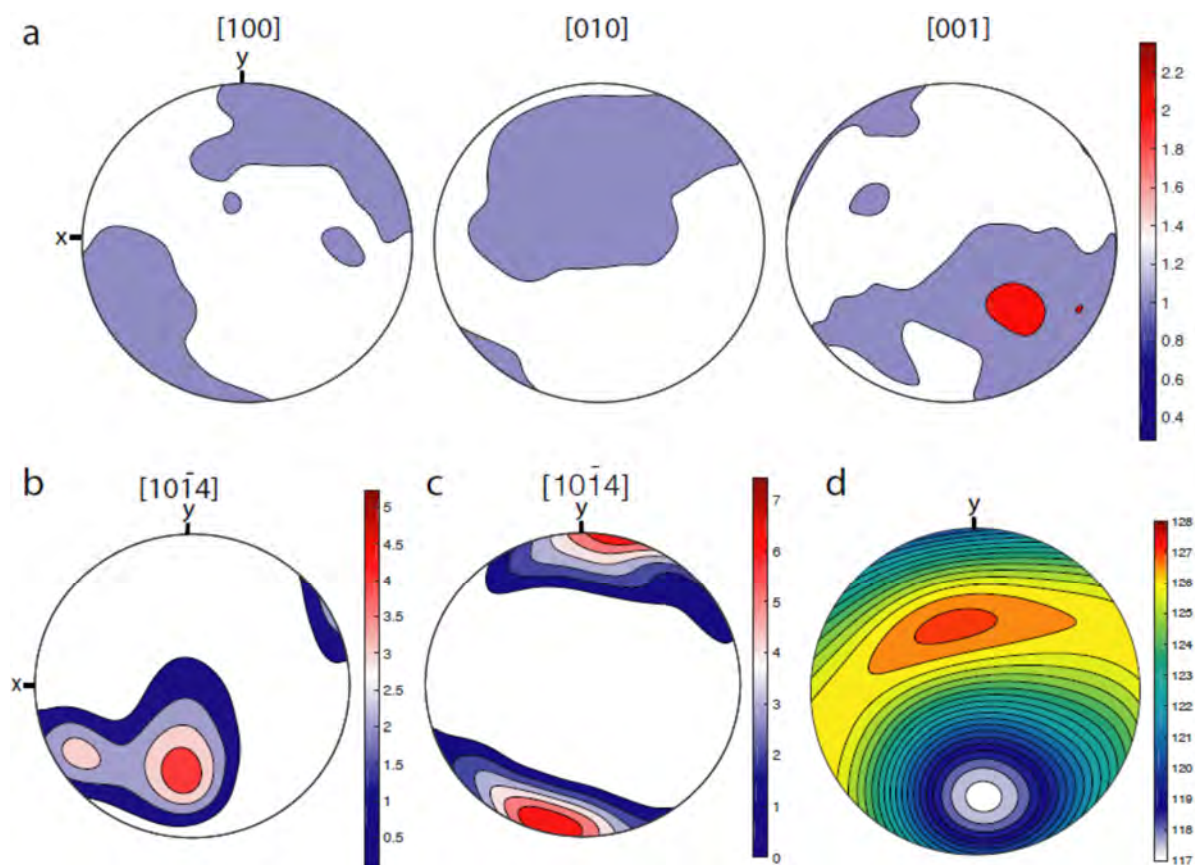


(Figure 9.3c: white dashed rectangle, Figure 9.6b). The resulting crystallographic orientation map for aragonite and calcite grains in Figure 9.6b, c and Supplementary Figure 9.6 is coloured according to the inverse pole figure colour schemes for aragonite and calcite (insets), assuming the reader's perspective. For aragonite and for calcite, areas in red have their crystallographic c-axis pointing north or south in the map. Green denotes the a-axis in aragonite and the calcite  $[01\bar{1}0]$  axis, while blue is the aragonite b-axis, and the  $[10\bar{1}0]$  axis in calcite, respectively. Intermediate colours are crystallographic orientations intermediate to these three.



**Figure 9.6: Crystallographic preferred orientations in the skeleton of *Anoteropora latirostris*.** (a) Sectioned colony micro-CT overlay with BSE image of the polished cross-section shown in Figure 9.3c. (b) Close-up of area outlined by rectangle in (a) overlay with crystallographic orientation map from Electron backscatter diffraction analysis (EBSD). (c) Orientation map of a lateral vertical wall segment of the colony (see also Supplementary Figure 9.2 for high resolution map). (d) close-up of an aragonitic segment outlined by rectangle in (c). Red grain boundaries are twin boundaries, colours as in the scale in (c). (e) close-up of a calcitic segment outlined by rectangle in (c). (f) Histogram of misorientation angles between aragonitic grains in (c) show pronounced maxima for the main twinning angles in aragonite at around 63° and 52°.

The maps allow grain size analysis for both mineral phases and show that these differ significantly between calcite and aragonite in the colony walls: While calcite grains are relatively large (Figure 9.6e), mostly around 600  $\mu\text{m}$ , occasionally up to 1400  $\mu\text{m}$ , aragonite grains are predominantly less than 100  $\mu\text{m}$  in size (Figure 9.6d, Supplementary Figure 9.7). Twinning was not observed in calcite, while a significant proportion of aragonite grains (i.e. 45 %) are twinned with a misorientation angle of  $64^\circ$  (Figure 9.6f), which is close to the angle of twinning on  $\{110\}$  in aragonite. Aragonite shows a predominantly small-grained fraction ( $\sim 75 \mu\text{m}^2$ ). Calcite grain sizes are distributed over a large range between  $\sim 50 \mu\text{m}^2$  and  $\sim 1,3 \text{ mm}^2$  with no significant maximum (Supplementary Figure 9.7). Calcite and, to a lesser extent, aragonite show significant intra-grain misorientation as indicated by the changing colours in Figure 9.6c–e. This is a typical feature in biominerals and an effect of the particulate nature of the grains (Agbaje et al., 2017b), sometimes referred to as ‘mesocrystals’ (Bergström et al., 2015; Wolf et al., 2016). Aragonite crystals show a weaker crystal preferred orientation (Figure 9.7a) than calcite crystals (Figure 9.7a, b).



**Figure 9.7:** Pole figures for aragonite and calcite in the skeleton of *Aoteropora latirostris* Silén (1947). (a) pole figure for aragonite crystals across the entire orientation map in Figure 9.6c showing the orientation of the prism axis (N = 1,037,343). (b) calcite orientations in the avicularium wall (see Figure 9.6c) and (c) across the entire orientation map in Figure 9.6c. (d) Young's modulus (in GPa) for the entire orientation map.

The growth face of any calcite crystal is usually the face of the cleavage rhombohedron, normal to the  $[10\bar{1}4]$  axis and with a constant angle of  $44^\circ$  to the calcite c-axis. The pole figures for calcite across the complete orientation map show a relatively strong alignment (five multiples of uniform distribution) of the  $[10\bar{1}4]$  axis (Figure 9.7b). In the wall of the avicularium (Figure 9.1d), the calcite  $[10\bar{1}4]$  axis is oriented sub-orthogonal to the surface of the colony (close to the y-direction; mostly red colours in



Figure 9.6c) and has a stronger alignment (seven multiples; Figure 9.7c) compared to that of the overall orientation map for the transect. The orientation of the calcite crystals along the entire vertical interzooidal wall changes gradually from an alignment of the c-axis close to the y-axis (orthogonal to the surface of the colony, Figure 9.6a, b) at the surface and the underside of the colony (mostly green colours in Figure 9.6c) via an orientation pointing more to the reader (z-direction, mostly red-purple colours in Figure 9.6c).

## 9.4 Discussion

### 9.4.1 Bimineralic bryozoan skeletons

Little is known about the ultrastructure and the biomineralization processes of bryozoan skeletons compared to the sizeable body of work available on other phyla such as molluscs, cnidarians or echinoderms. Cheilostome bryozoans are known since the Late Jurassic and originally had monomineralic calcitic skeletons. Their mineralogy diversified with many cheilostome clades convergently evolving aragonitic or bimineralic calcitic-aragonitic skeletons by the Late Cretaceous (Taylor et al., 2009). In bimineralic species, the aragonitic parts typically comprise the outer surfaces of the colony walls (Benedix et al., 2014; Taylor et al., 2008) and/or the frontal shield. This is similar for *A. latirostris*, where an aragonite layer covers the entire surface of the colony (Figure 9.3c). In addition to this, in this species we observe aragonite layers also along the lateral walls of each zooidal chamber (Figures 9.3, 9.4, Supplementary Figures 9.2, 9.3). Taking into account the general growth direction of the colony, namely from the centre (apex) radially to the margins, the aragonitic layers on the vertical interzooidal walls are precipitated distally (Figure 9.3b–d), thereby resulting in the colony being radial symmetrical whereas the zooids are not. We found these zooid walls with an aragonite layer covering the calcite wall on the distal side of the zooid chamber in all *A. latirostris* colonies that we studied (see Supplementary Table A.1 and Methods for a full list of studied specimens) and interpret them as primary and integral parts of the *A. latirostris* skeleton. We consider it unlikely that this feature could be a result of diagenesis, because all colonies show intact opercula (Figure 9.1d), indicating that they were alive or recently alive at the time of sampling. Furthermore, the aragonite layer composes one side of the wall to its full height and with relatively constant thickness, which is typical for a regular architectural element of the skeleton, whereas diagenetic aragonite could be expected to form more random morphologies and cavity fillings.

### 9.4.2 Ultrastructure and mechanical properties

Ultrastructures in bimineralic bryozoan skeletons usually differ according to their mineralogy (Cheetham et al., 1969; Kobayashi and Akai, 1994; Tavener-Smith and Williams, 1972; Taylor et al., 2009) and the same is observed for *A. latirostris* here: Calcitic structures have platy or lamellar morphology, while aragonites show a fibrous fabric (Figure 9.4b, c). Unlike calcite, aragonite grains are most often crystallographically twinned (Figure 9.6d), which is a common observation for aragonites in biominerals (Agbaje et al., 2017b; Kobayashi and Akai, 1994).

Unlike the shells of some molluscs, where several hierarchical orders can be identified (Dauphin and Denis, 2000; Otter et al., 2019) the *A. latirostris* skeleton does not show a pronounced hierarchy of distinct architectural units. Aragonite fibres and calcite platelets show a crystallographic preferred orientation (CPO), but not as strong as in bivalve shells: Areas of similar colouration in the orientation map (Figure 9.6c) show domains of crystallites with very similar orientation for both minerals. Pole figures (Figure 9.7) show a relatively strong preferred orientation for the calcitic crystallographic  $[10\bar{1}4]$  of up to 7.4 times uniform (uniform equals random orientation) (Figure 9.7a, b) and a weaker preferred orientation for  $[001]$  of aragonite of 2.4 times uniform. Compared to the textural strength of bivalve shells, which can have textural strengths of 12.5 times uniform (Agbaje et al., 2017b; Chateigner et al., 2000), these maxima are weak in *A. latirostris*.

In mollusc shells the strongly controlled CPO across the entire shell maximizes their mechanical properties by creating a plane of (quasi-) isotropy of the Young's modulus for the otherwise anisotropic crystals, thus maximizing the stiffness coefficients in all directions across this plane in the shell (Agbaje et al., 2017b; Chateigner et al., 2000; Ouhenia et al., 2008). In aragonitic mollusc shells, this mechanical effect is further enhanced by a spread of the crystal orientation angle due to extensive twinning. Aragonite grains in the *A. latirostris* skeleton show a high degree of twinning (45 % of all grains in Figure 9.6c have at least one twin boundary), but the textural strength of aragonite (2.4 times uniform; Figure 9.7a) and calcite (5–7.4 times uniform; Figure 9.7b, c) taken individually is much weaker compared to the bivalve *T. derasa* (12.5 times uniform, Agbaje et al., 2017b). Nevertheless, the combination of the two mineralogically different layers in the skeleton results in a similar, even slightly higher range of values of 117 to 126.5 GPa for the Young's modulus (compared to 80 to 106 GPa in *T. derasa*, Agbaje et al., 2017b). The anisotropy of the Young's modulus for the *A. latirostris* skeleton results in a value of 7.8 %, thus, it is significantly more isotropic in all directions than for the shell of *T. derasa* (28 %, Agbaje et al., 2017b).

A noteworthy and significant difference between the Young's modulus for shells of the bivalve *T. derasa* and the skeleton of the bryozoan *A. latirostris*, however, is that the stiffest direction in the further is perpendicular to the shell's dorsal surface (perpendicular to the growth lines in *T. derasa*, Agbaje et al., 2017b), whereas this direction (i.e. perpendicular to the colony's apical surface) is the weakest in *A. latirostris*. It could be speculated that this difference in mechanical properties likely supports the function of the mineralized parts of these organisms: Molluscs most likely developed their architectural design aiming at optimizing mechanical isotropy as a strategy in resistance to predators that may have provided a significant evolutionary advantage. *A. latirostris* colonies, on the other hand, proliferate by fragmentation of the colony along the interior vertical walls between zooids (O'Dea et al., 2008) and maintaining the weak mechanical direction perpendicular to the colony's apical surface in this species is potentially a strategy to facilitate this fragmentation process.

#### 9.4.3 Insights into the biomineralization processes

We observed that the spatial distribution pattern of aragonite coating on calcite walls, and the construction of the walls follows a strikingly symmetrical pattern on colonial and on zooid level with only the distal side of the vertical zooidal walls layered with aragonite (Figure 9.3). The regular arrangement and thickness of the aragonite layers and the freshness of the sample material excludes a diagenetic origin and therefore raises the question about how these walls are formed.

A unifying principle of biomineralization is that the minerals nucleate and grow with the support of an organic template, which promotes biomineralization by minimizing surface energies and provides binding sites for calcium (Weiner and Dove, 2003). The central organic cuticular layer (Håkansson, 1973) observed in compound walls in bryozoan skeletons is thought to act as such a biomineralization template, but similar organic cuticles have never been described between calcite and aragonite layers in walls. NanoSIMS distribution maps for carbon and nitrogen across the calcite-aragonite interface (Figure 9.5a, b) show significantly increased signals for these elements along the interface (Figure 9.5c–e, Supplementary Figure 9.4), which is a clear indication for the presence of a thin organic layer between calcite and aragonite. This strongly suggests that the general principles of biomineralization as observed in marine invertebrates, such as nucleation and growth of crystals involving an organic template (Weiner and Dove, 2003), may also hold for bryozoans.

Macroscopically, colonial growth of *Anoteropora latirostris* proceeds radially, starting from the centrally located ancestrular zooid (Figure 9.1a), which is also the only zooid composed solely of calcite (Fig. 9.3c). This suggests that calcite is the primary  $\text{CaCO}_3$  phase, which is secreted from the epithelial cells of the hypostegal coelom of the zooid in each of the zooid chambers. Most of the remaining skeleton, however, is aragonitic: Aragonite makes up the outer layer of the extrazooidal basal walls, of the apical walls as well as most of the distal parts of the lateral walls (Figures 9.3, 9.4, Supplementary Figures 9.3, 9.4). This suggests that aragonite is a secondary phase, secreted from the cells of a tissue layer covering the exterior of the colony in its entirety (i.e. frontal, basal walls and lateral margins of the colony).

The asymmetric distribution of aragonite only at the distal side of each autozooid chamber (Figure 9.3) can be understood by studying the radial growth mechanism of the colony: In a living colony, growth of the colony occurs via budding and internal separating of a single autozooid into two individuals (McKinney and Jackson, 1991). Thereby, the distal lateral vertical walls of each newly formed autozooid chamber comprise the margin of the growing colony and are therefore in direct contact with the exterior tissue that covers the entire colony. Hence, we conclude from our observations that *A. latirostris* possesses two different types of calcifying tissue, one being the epithelial tissue of the autozooidal hypostegal coelom, which produces calcite and the other being the tissue covering the colony which produces aragonite. Such cellular differentiation, as suggested here, would follow observations made in bivalves, where the regulation of which polymorph of calcium carbonate - aragonite or calcite - forms

during shell growth is achieved by cellular differentiation (Marie et al., 2012), and cell secretion plasticity is retained to accommodate shell repair processes (Hüning et al., 2016).

This bimineralic calcification pattern is significantly different to what has been documented for other bimineralic bryozoan species so far. Typically, secondary aragonitic layers are limited to the frontal shields in bimineralic colonies, such as *Pentapora fascialis* (Benedix et al., 2014), but do not comprise the vertical interzooidal walls. The difference in growth form between this species and *A. latirostris* is that the latter has a lunulitiform (cup-shaped) mode of growth, and the colony only consists of one zooid layer. Budding at the margins of the cup-shaped colony exposes the distal sides of newly formed calcitic interzooidal walls to the aragonite-forming exterior tissue, unlike in *Pentapora fascialis* where only the frontal surfaces (the frontal shields) for the bilateral two-zooid-layer colony are exposed for aragonite formation.

## **Acknowledgements**

The authors are grateful to Kei Matsuyama (Wilhelmshaven) for help with SEM imaging at the SMW. Michael Türkay (1948–2015) and Andreas Allspach (SNG Frankfurt) are thanked for providing the material used in this study. The authors acknowledge the facilities and the scientific and technical assistance of the Microscopy Australia at the Australian Centre for Microscopy & Microanalysis at the University of Sydney. This study received funding through ARC Future Fellowship grant FT120100462 (D.E.J.).

## Supporting material

**Supplementary Table 9.1: List of colonies of *Anoteropora latirostris* used in this study.**

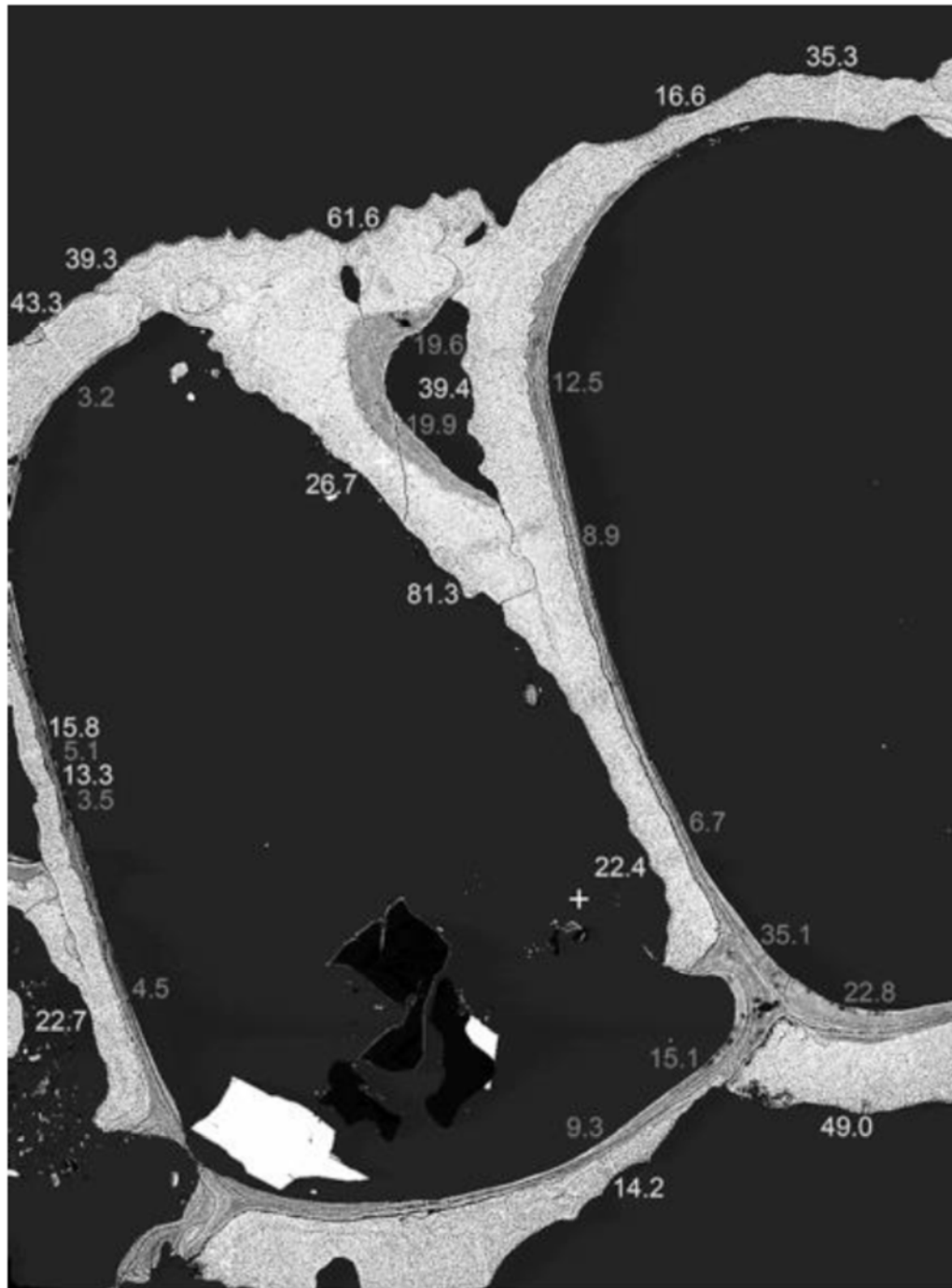
SAMPLE NUMBER	COLONIES	STATION	USED FOR
SMF 60000	1	283 KU	Macrophotos (Figure 9.1a–c)
SMF 60001	1	283 KU	SEM (Figure 9.1d)
SMF 60002	1	283 KU	Micro-CT (Figure 9.2a, b)
SMF 60003	1 (sectioned)	283 KU	EBSD, Micro-CT, NanoSIMS (Figure 9.3a–e)
SMF 60004	1 (fragment)	236 KD	SEM (Figure 9.4a–b)
SMF 60005	1 (sectioned)	283 KU	NanoSIMS
SMF 60006	3	283 KU	SEM (unfigured)
SMF 60007	1	283 KU	SEM (unfigured)
SMF 60008	1	283 KU	SEM (unfigured)
SMF 60009	1	283 KU	SEM (unfigured)
SMF 60010	3 (fragments)	283 KU	SEM (unfigured)
SMF 60011	1	236 KD	Macrophotos (unfigured)
SMF 60012	1	236 KD	Prestudy
SMF 60013	3	283 KU	Prestudy
SMF 60014	33 fragments	283 KU	Prestudy
SMF 60015	5 fragments	283 KU	Prestudy
SMF 60016	79 fragments	283 KU	Prestudy
SMF 60017	43 fragments	283 KU	Prestudy
SMF 60018	45 fragments	236 KD	Prestudy
SMF 60019	1	236 KD	Prestudy, SEM
ZSM 20190252	3 (2 fragmented)	283 KU	SEM (Suppl. Figure 9.3a–h)
ZSM 20190253	10	283 KU	Prestudy

**Supplementary Table 9.2: Measured  $\text{CN}^-/\text{C}^-$  and  $\text{Si}^-/\text{C}^-$  ratios for four sample areas and selected sub-regions (denoted by A, B and C for the respective fields, see Figure 9.5 and Supplementary Figure 9.4). All errors are 1 sigma. Note the ratios for the epoxy references are distinct from those for all maps across the aragonite-calcite boundary indicating that the analyses are free of epoxy contamination. Only exception is B\_a\_01#C, which is identical to epoxy and was therefore excluded from the discussion.**

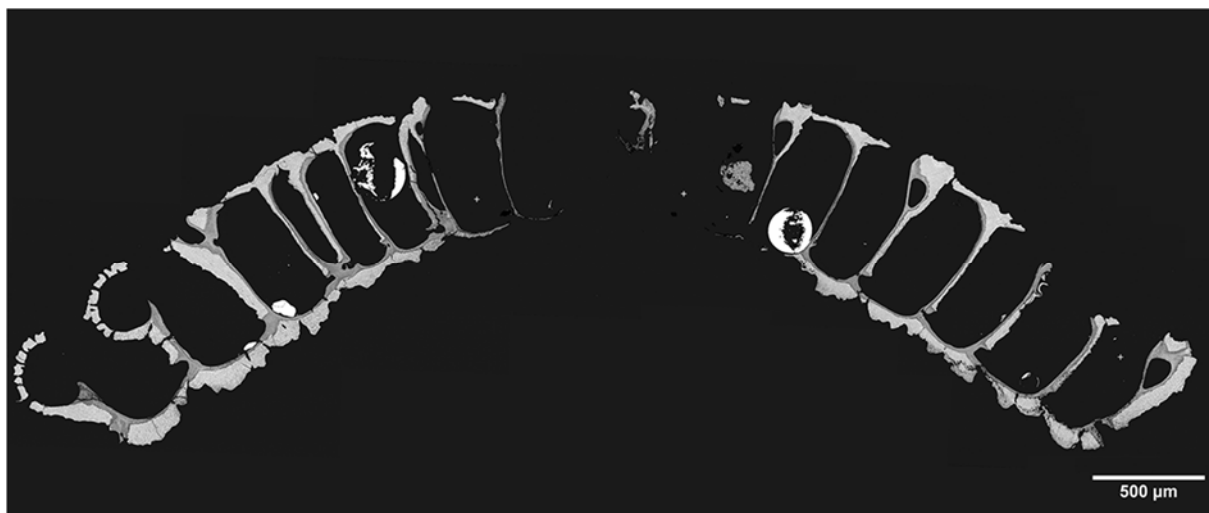
	$^{12}\text{C}^{14}\text{N}^-/^{12}\text{C}^-$	ERR	$^{28}\text{Si}^-/^{12}\text{C}^- (\times 10^{-3})$	ERR ( $\times 10^{-3}$ )
B_a_01#A	2.31	0.01	4.11	0.11
B_a_01#B	1.48	0.01	3.20	0.23
B_a_01#C	0.70	0.01	6.21	0.28
B_a_02	1.56	0.01	9.01	0.34
B_a_03#A	4.14	0.01	6.15	0.11
B_a_03#B	2.10	0.01	10.24	0.23
B_b_1	6.27	0.02	13.20	0.28
Epoxy_reference_1	0.68	0.0003	0.062	0.003
Epoxy_reference_2	0.53	0.0002	0.035	0.001

<sup>#</sup>For SiC, the respective ion ratios are typically  $>3 \times 10^{-1}$

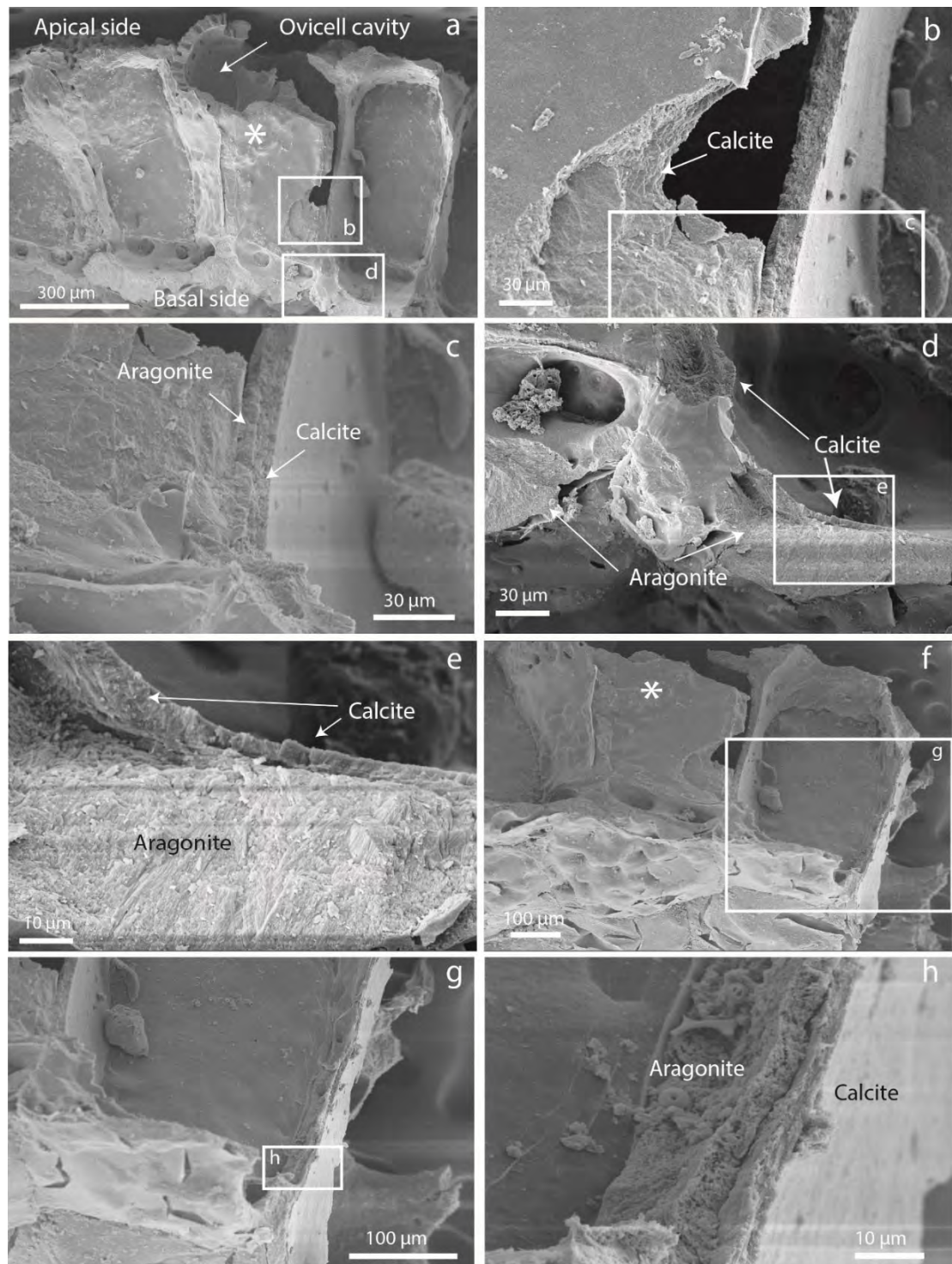




Supplementary Figure 9.1: BSE image of a sectioned and polished colony of *Aoteropora latirostris* with measurements of wall thicknesses for calcitic (dark grey) and aragonitic layers (light grey). Area analysed is the same as the one mapped by EBSD, for location see Figure 9.6a (dashed outline).

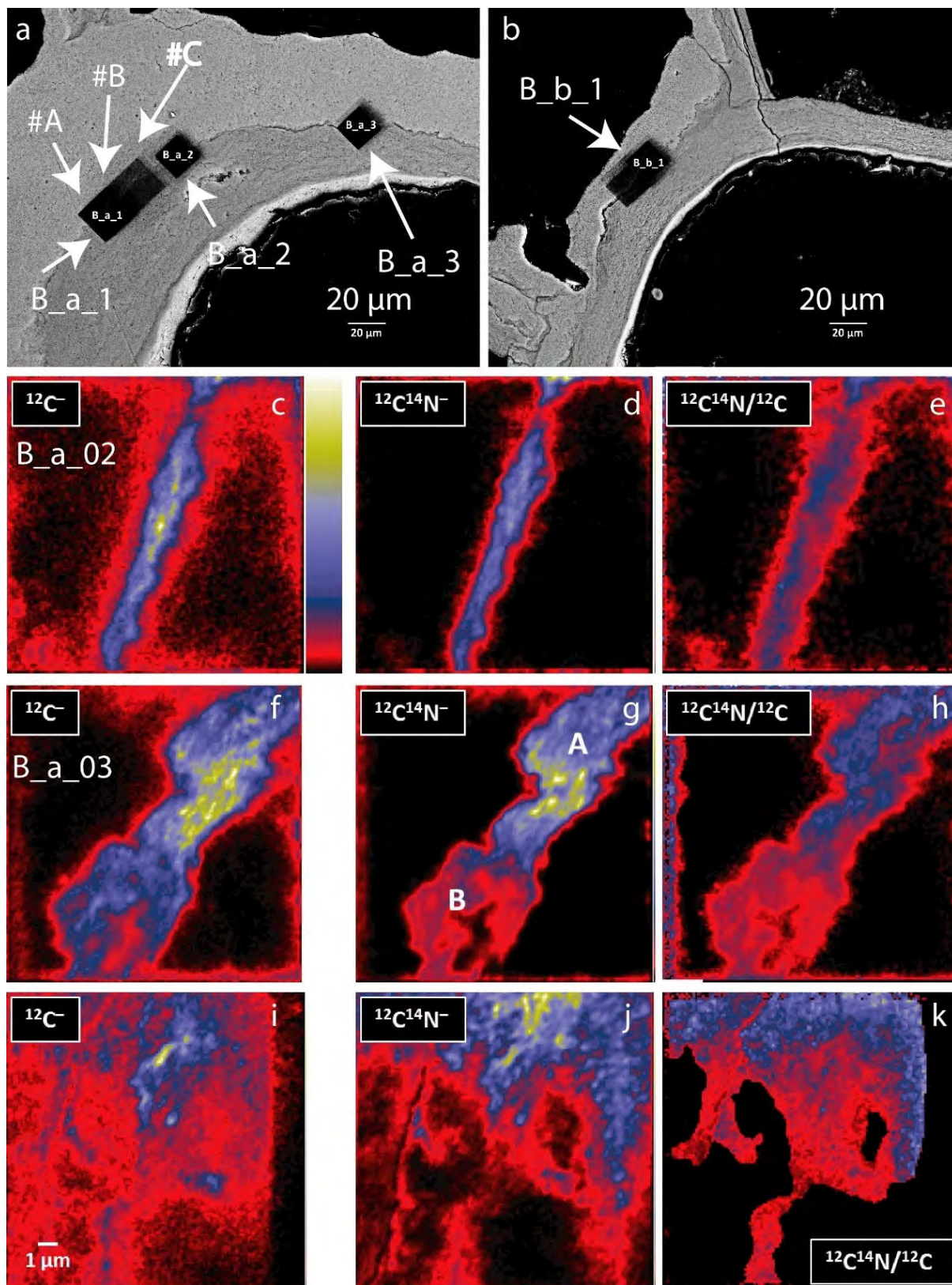


**Supplementary Figure 9.2: Backscatter Electron image of polished section of sample SMF60007. Note the distribution of aragonite (light grey) consistently on the distal side of the lateral walls. Calcite in dark grey. Ancestrula area in this colony is not preserved in this section through the centre.**

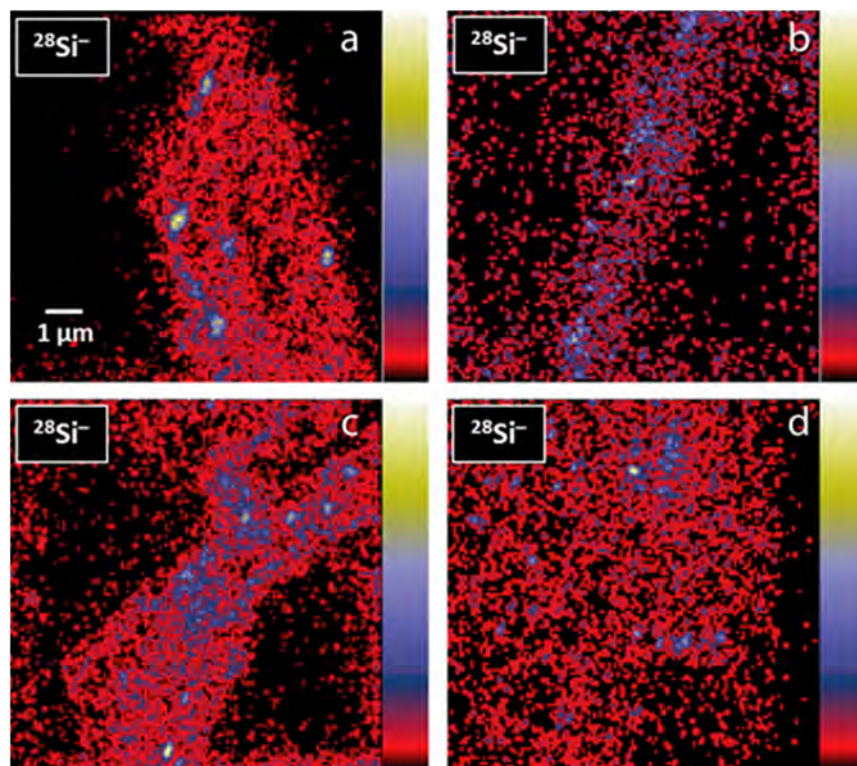


**Supplementary Figure 9.3: SEM images showing fractured walls defining the chambers of individual autozooids (Sample ZSM20190252). (a)** Broken piece of colony showing several zooid chambers and their delineating skeletal walls. The same area is depicted at a slightly different angle in (f) – refer to asterisk for orientation. Note that the fracture surface runs in steps towards the reader relative to the imaged surface. In this way, the autozooid chamber on the right in (a) reveals the bottom-wall in addition to the fractured lateral walls, while the adjacent chamber to the left shows the top-wall of this chamber (towards the reader) in the image plane. **(b)** Close-up of area marked by white rectangle ‘b’ in (a) showing the fractured top-wall revealing the typical platy morphology of the calcitic top-wall. **(c)** Close-up of the lateral wall in (b) marked with rectangle ‘c’ shows the distal side of the wall consisting of aragonite. **(d)** Close-up of the basal area of the autozooid chamber marked with rectangle ‘d’ in (a) showing the innermost platy calcite wall, overlain by fibrous aragonite towards the outside of the colony. **(e)** Further magnification of area marked with rectangle ‘e’ in (d). **(f)** overview image of the fractured wall around the autozooid chamber depicted in (a) focussing on the lateral wall on the right. **(g)** Close-up of area marked by rectangle ‘g’ in (f), and **(h)** further magnification of area in rectangle ‘h’ in (g) showing the bimineralic lateral wall with the distal part of the wall consisting of aragonite, in analogy to the lateral wall architecture shown in (c).



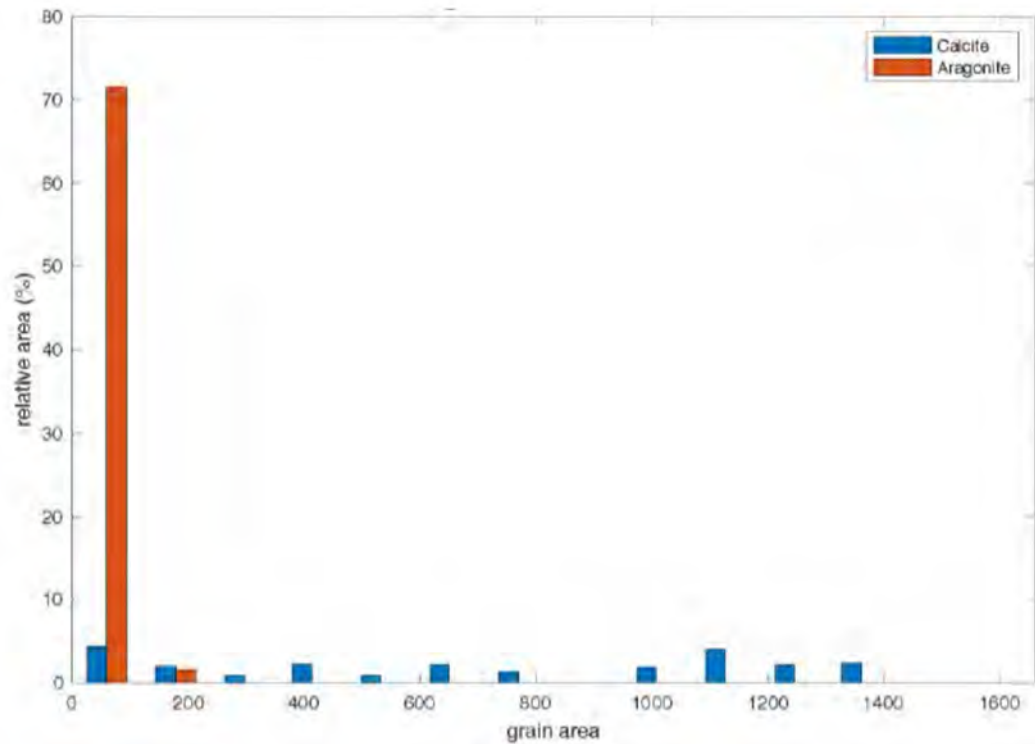


Supplementary Figure 9.4: BSE images and NanoSIMS maps of the sectioned and polished specimen in epoxy (a) close-up of the areas B\_a\_2 and B\_a\_3 mapped by NanoSIMS after analysis (for area B\_a\_1 see Figure 9.5) at the boundary between calcite (dark grey) and aragonite (light grey). (b) close-up of area B\_b\_1 (for general locations see Figure 9.7). NanoSIMS analysed areas show up as dark grey squares of  $15 \times 15 \mu\text{m}^2$  each. NanoSIMS maps (mirrored) for carbon (c), nitrogen (d) and calculated carbon/nitrogen ratios (e) for area B\_a\_2. (f) to (k) show respective maps for areas B\_a\_3 and B\_b\_1. Colour scale next to (c) indicates signal intensities.

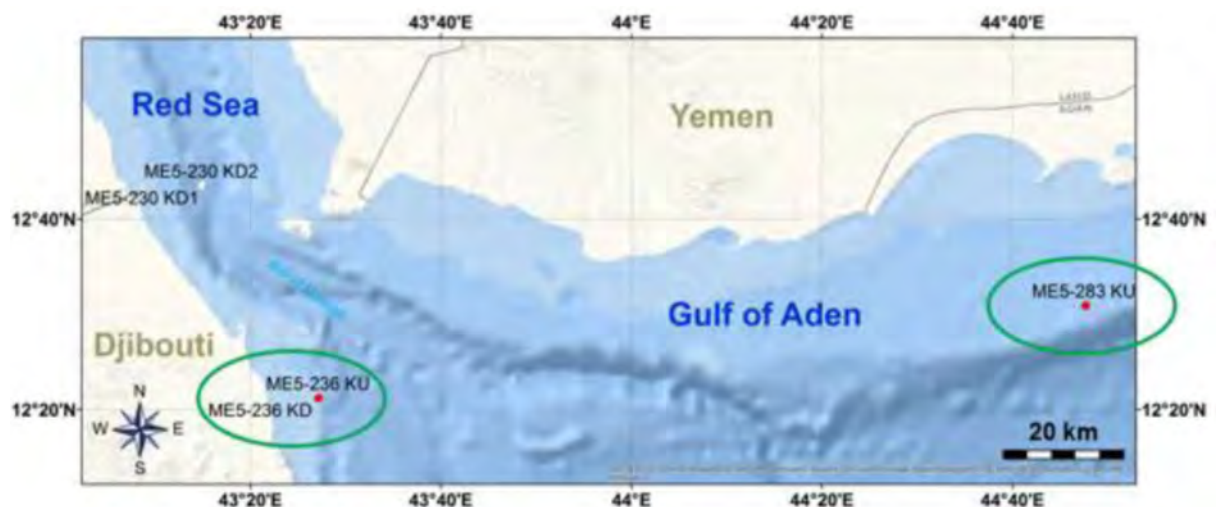


Supplementary Figure 9.5: NanoSIMS maps (mirrored) of  $^{28}\text{Si}^-/^{12}\text{C}^-$  for areas B\_a\_01 (a), B\_a\_02 (b), B\_a\_02 (c) and B\_b\_1 (d) showing very low concentrations in each of these maps, attesting to the absence of contamination during surface polishing of the area.





**Supplementary Figure 9.6:** Grain sizes in micrometre of calcite (blue) and aragonite (red) grains for the segment mapped by EBSD. Note the variable and large sizes of calcites versus the mostly small-sized aragonite grains.



**Supplementary Figure 9.7:** Map of the sampling stations during RV Meteor expedition 5/2 “Mindik” in March 1987 in the Gulf of Aden with the sampling stations of material used for this study indicated as red dots inside green ellipses. Map modified after template map by M. Sonnewald.

### *Supplementary methods*

Sample collection in March 1987 during RV Meteor expedition 5/2 “Mindik” from dredged sediment in the Gulf of Aden. Focus of this cruise was the investigation of deep-sea fauna in the aphotic zone of the Red Sea and the two stations where bryozoans were collected are the only two in shallow waters. The general depth range covered was approximately 300 to 2300 m. Shallow banks at 40-80 m depth were trawled on only two occasions in order to provide comparative data to understand the differences between shallow and deep waters of the region, and to investigate whether there were any shallow water

immigrants to the deep Red Sea. These two trawls were those that contained *Anoteropora latirostris* materials.

The Gulf of Aden areas investigated were characterized by low standing stocks of plankton but high production rates, as it is typical for subtropical and tropical oceanic regions.

The official report on cruise Me5/2 “Mindik” does not provide any information on water parameters such as temperature. The hydrographic bottle data obtained in the Gulf of Aden during the cruise do not provide any data on the two shallow water stations but focus on stations situated in the aphotic zone (Verch et al. 1989). A site situated near to station Me5-283 KU recorded at 77 m depth a temperature of 24.54 °C, and the salinity 36.194 ppt. (Đuriš 2007).

#### *Stations and sampling:*

##### Me5-283 Ku

Indian Ocean: Gulf of Aden, interior part of the Gulf of Aden, (12° 30.9' N 44° 47.7' E - 12°31.2' N 44° 48.4' E)

76 m water depth, 16.3.1987, 11:52 - 12:12, Beam Trawl

##### Me5-236 KD

Indian Ocean: Gulf of Aden, Bab-el-Mandeb, (12° 21.4' N 43° 26.9' E - 12°20.6' N 43°27.3'E)

45 m water depth, 6.3.1987, 13:30 - 13:45, Dredge Trawl

Two types of gear were used for sampling at these stations: a beam trawl with a two metre frame and a net of 1 cm minimum mesh size in the cod end, (Me5-283 Ku) and a hard bottom dredge in which the net of 1 cm mesh size was protected by a chain-sack (Me5-236 KD). The gear was not deployed unless a suitable smooth bottom profile of an appropriate dredging distance was found. All sieve residues were preserved with 4 % formalin on board. Upon arrival in Frankfurt am Main (Senckenberg Institute), the samples were watered and transferred to 70 % Ethanol, and dried later for sorting smaller macrobenthos.